博 士 論 文

Full-Field Simulation for Sonic Boom Propagation through Real Atmosphere

（実在大気中のソニックブーム伝播に関する全空間解析）

山 下　　礼

Doctoral Thesis

Full-Field Simulation for Sonic Boom Propagation through Real Atmosphere

Rei Yamashita

Department of Advanced Energy
Graduate School of Frontier Sciences
The University of Tokyo

February, 2016

Contents

Nomenclature

Roman Symbols

a_n	:	velocity normal to wave front
A	:	Jacobian matrix or ray tube area
c	:	speed of sound
D	:	maximum diameter
e	:	total energy per unit volume
e_{vO_2}, e_{vN_2}	:	vibrational energy of O_2 and N_2 per unit volume
E, F, G	:	inviscid flux vectors
E_v, F_v, G_v	:	viscous flux vectors
$\widetilde{F}$	:	inviscid flux vector at cell interface
g	:	acceleration of gravity
h	:	altitude
h_a	:	absolute humidity
h_r	:	relative humidity
H	:	axi-symmetric inviscid term
H_v	:	axi-symmetric viscous term
I	:	unit matrix
J	:	Jacobian
$\dot{m}$	:	mass flux
m_i	:	pressure gradient of segment i (Appendix)
M	:	Mach number
n_s	:	number of molecular species
L	:	length of body
p	:	pressure
$\widetilde{p}$	:	pressure flux
Pr	:	Prandtl number
q	:	primitive variables

Q	:	conservative variables
R	:	gas constant
Re	:	Reynolds number
s	:	flux limiter function
S	:	source term
$S(x)$	:	cross-sectional area at x coordinate
S_C	:	correction term for gravity term
S_G	:	gravity term
S_W	:	translational-vibrational relaxation term
t	:	time
$\vec{t}$	:	unit vector tangential to surface of body
T	:	temperature
T_{01}	:	triple point temperature
T_{vO_2}, T_{vN_2}	:	vibrational temperature of O_2 and N_2
u, v, w	:	velocity components
$\vec{U}$	:	velocity vector
V_n	:	velocity component normal to cell interface
w_{vO_2}, w_{vN_2}	:	translational-vibrational relaxation term of O_2 and N_2
$w_{v,\,max}$	:	maximum value of translational-vibrational relaxation term
x_n, y_n, z_n	:	unit vector components normal to cell interface
x, y, z	:	Cartesian coordinates
x, r, θ	:	cylindrical coordinates

Greek Symbols

α	:	angle of flow velocity from x direction
β	:	temperature lapse rate
β_r	:	relaxation coefficient
γ	:	ratio of specific heat
$\Delta e_{tr,\,\max}$	:	maximum increase in translational energy per unit volume
Δp	:	pressure fluctuation from atmospheric pressure
Δp_i	:	pressure rise at the boundary of segments i and i–1 (Appendix)
$\Delta p_{\max}$	:	pressure rise
Δt_{ex}	:	exchange time of translational-vibrational energy

Δt_{rt}	:	rise time
$\varepsilon_{O_2}, \varepsilon_{N_2}$	:	mole ratio of air of O_2 and N_2
$\theta_{O_2}, \theta_{N_2}$	:	characteristic vibrational temperature of O_2 and N_2
κ	:	thermal conductivity
λ	:	spectral radius
λ_{Di}	:	time duration of segment *i* (Appendix)
μ	:	viscous coefficient
μ_M	:	Mach angle
$\mu_{M\,\mathrm{mod}}$	:	modified Mach angle
ρ	:	density
τ	:	viscous shear stress
τ_{O_2}, τ_{N_2}	:	relaxation time of O_2 and N_2
ϕ	:	scalar quantity
ξ, η, ζ	:	generalized coordinates

Subscript

0	:	ground
1	:	value just before shock wave
a	:	atmosphere
L, *R*	:	left-side and right-side values at cell interface
∞	:	freestream value at flight altitude

Superscript

eq	:	thermal equilibrium
*	:	nondimensional variable

Chapter 1

Introduction

1.1 Sonic Boom

Shock waves generated from a supersonic or hypersonic flight object propagate through the atmosphere down to the ground. Consequently, the rapid pressure rises caused by the shock waves generate significant impacts including explosive sounds on the ground. This phenomenon is known as sonic boom [1], which occurs primarily due to an aircraft flying faster than the speed of sound [2] and a meteorite falling to the earth [3, 4].

Figure 1.1 shows a schematic of sonic boom propagation from the near field around a supersonic aircraft to the far field reaching the ground. Multiple shock waves generated from a fuselage and wings are consolidated into an N-shaped waveform (N-wave) in the far field, and as a result the explosive sound occurs twice on the ground [5]. For the sonic boom problem, the overland civil supersonic flight has been restricted, and there has been no civil supersonic aircraft after the Concorde was retired in 2003 [6]. The International Civil Aviation Organization (ICAO) [7] presently deliberates an international standard in which the allowable level of sonic boom is determined to realize an overland supersonic flight. To formulate the clear international standard, sonic boom intensity in various flight and atmospheric conditions must be precisely predicted. Therefore, research activities of sonic boom including not only the sonic boom minimization [8, 9] but also the development of accurate prediction methods for sonic boom [10, 11] are accelerated. Moreover, to validate the accuracy of sonic boom predictions, several flight tests for sonic boom were recently conducted by NASA [12, 13] and the Japan Aerospace Exploration Agency (JAXA) [14, 15].

Sonic boom researches on supersonic aircrafts have been significantly advanced, whereas those on hypersonic aircrafts have been hardly conducted. However, the development of hypersonic aircrafts is recently accelerated [16, 17], and the sonic boom problem must be addressed not only in supersonic aircrafts but also in hypersonic aircrafts [18]. Sonic boom intensity of a hypersonic aircraft may be weaker than that of a supersonic aircraft because of the following reason: The cruising altitude of the hypersonic

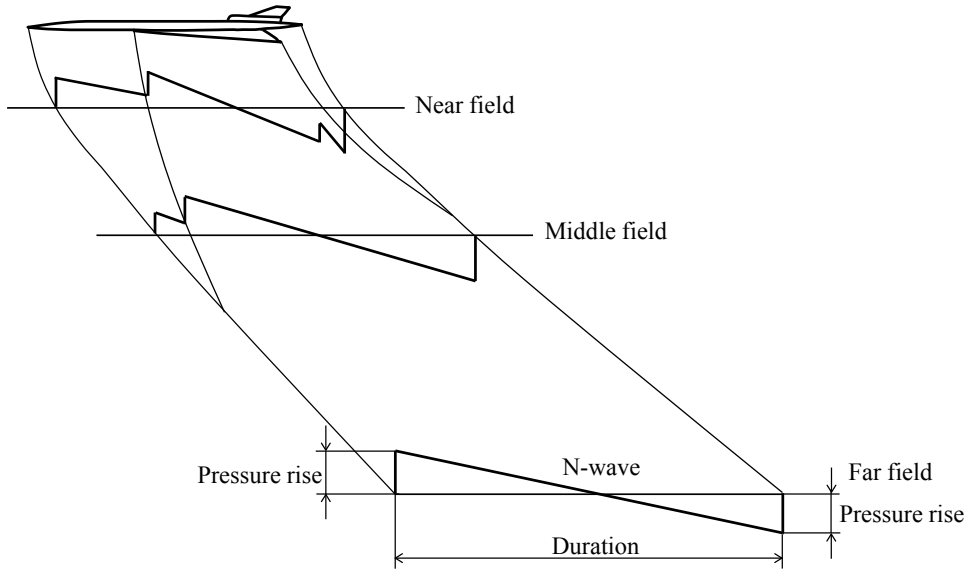

Fig. 1.1 Schematic of sonic boom propagation generated from supersonic aircraft.

aircraft is assumed to be higher than that of the supersonic aircraft, and the distance of sonic boom propagation to the ground increases with increasing the flight altitude. However, sonic boom propagation from hypersonic aircrafts cannot be precisely predicted because the existing prediction methods for sonic boom based on the weak shock theory [19] do not consider the strong nonlinearity and thermochemical nonequilibrium in hypersonic flow regimes [20]. Therefore, the accurate prediction method considering these effects must be constructed to evaluate sonic boom intensity generated from hypersonic aircrafts.

Sonic boom is generated from not only an aircraft flying faster than the speed of sound but also a meteorite falling to the earth. Ten-thousand near-earth asteroids are presently observed [21], and there is always the possibility of a meteorite falling. In fact, the big meteorite events were observed near the Marshall Islands in 1994 [22], Indonesia in 2009 [23], and Chelyabinsk, Russia in 2013 [24–27]. In particular, the Chelyabinsk event was well known because the significant damage was caused by the meteorite falling. The Chelyabinsk meteorites exploded several times, and small fragments generated by the explosions fell to the ground. At that time, strong shock waves were generated from not only the meteorites exploding but also their hypersonic flights, and they propagated toward the ground. Consequently, the sonic boom rather than the direct impact of the fragments caused the significant damage including not only the destruction of the building but also the human damage. Extrapolated from the measurement of the window breakage in Chelyabinsk, the pressure rise caused by the shock wave was estimated to be 3.2±0.6 kPa [24]. Hence, it can be seen that the sonic boom intensity in the Chelyabinsk meteorite was much stronger than that in a supersonic aircraft (e.g., the pressure rise generated by the Concorde flying at the cruising speed was approximately 95 Pa [6]). Because the proportion of the population area on the earth is low, a natural disaster, as well as the Chelyabinsk event, was not observed in

the past century. However, it is thought that the meteorite of the same size as that of Chelyabinsk falls to the earth once in a decade [27, 28]; thus, there is always the possibility of a natural disaster caused by a meteorite falling. From these facts, it is important to evaluate the influence of meteorite impacts including sonic boom and to anticipate hazard meteorites. However, the sonic boom prediction of a hypersonic meteorite has been mainly predicted by the self-similar solution [29, 30], without consideration of the atmospheric effects such as atmospheric stratification, viscosity, and thermochemical nonequilibrium. In addition, the existing prediction methods based on the weak shock theory [19] cannot be applied to the sonic boom prediction of the hypersonic meteorite because of the strong nonlinearity and thermochemical nonequilibrium in a hypersonic flow regime [20]. Therefore, the accurate prediction method must be constructed to precisely predict sonic boom propagation generated from hypersonic meteorites as well as that generated from hypersonic aircrafts.

1.2 Existing prediction methods for sonic boom

Sonic boom intensity depends on the configuration of flight object, the flight and atmospheric conditions, and the ground geometry [2]. In particular, the atmospheric effects such as atmospheric stratification [31], molecular relaxation [32, 33], and atmospheric turbulence [34–36] significantly affect the sonic boom intensity because the sonic boom propagates for quite a long distance until it reaches the ground. Therefore, the accurate prediction of sonic boom with consideration of all such effects is challenging but essential for evaluating the perceived loudness of sonic boom. Thus far, the prediction methods for sonic boom have been mainly developed to realize a low-boom supersonic aircraft [8, 9], and the predictions have been conducted in three different fields: the near field around a supersonic aircraft, the far field reaching the ground, and the caustic-vicinity field [37] where the shock waves are focused due to accelerations, maneuvers, and low-supersonic flights. In this section, the representative prediction methods in each field and the limitation of the application are described.

1.2.1 Near field

As a three-dimensional aircraft configuration and strong nonlinearity must be considered in the near field, near-field pressure waveforms have been obtained by experiments or Computational Fluid Dynamics (CFD). The experiments are categorized into two types: wind tunnel [38, 39] and ballistic range [40] experiments. The experimental techniques using wind tunnels have been already established, and the experimental results have been used to validate the accuracy of computation [41]. However, the influence of a sting to which the experimental model is attached cannot be ignored in the wind tunnel experiments. In

contrast, such a sting is unnecessary in ballistic range experiments because the free flight of the model is conducted. For this reason, the ballistic range experiments have been conducted, although the experimental technique should be further improved because the flight control including the angle of attack is difficult. In addition, CFD analysis [42] is often performed not only to obtain near-field waveforms but also to evaluate the flow field around the body. However, the computational results may be somewhat different from the experimental results because of the complexity of the flow fields around three-dimensional aircraft configurations. Thus, the CFD methods for precisely predicting sonic boom intensity have been studied [43, 44].

1.2.2 Far field

It is difficult to precisely predict sonic boom propagation for quite a long distance in the real atmosphere because sonic boom intensity depends on various effects such as geometrical spreading, nonlinearity, and atmospheric effects [33]. Hence, far-field waveforms have been obtained by simplified prediction methods based on the weak shock theory formulated by Whitham [19], in which a shock wave is treated as a sound wave, and the propagation speed at any point is modified by the isentropic wave theory to consider the nonlinear effect; i.e., the propagation speed is assumed to be a sum of the local speed of sound and the change of velocity. In addition, a shock wave is determined by the area-balancing technique: if two Mach lines intersect with each other, the bisector is treated as a shock wave. According to the Whitham's theory, the pressure rise of weak shock wave in the far field decreases as the power –3/4 of radial distance from the body axis (according to the Lin's self-similar solution, the pressure rise of strong shock wave decreases as the power –2 of radial distance [29]). Although sonic boom intensity can be roughly predicted by the Whitham's solution, the accuracy is inadequate for evaluating the perceived loudness of sonic boom because of the following two reasons: First, the strong nonlinearity in the near field around a flight object cannot be considered by the solution. Second, the atmospheric effects such as atmospheric stratification, molecular relaxation, and viscosity cannot be considered. Thus, several prediction methods, in which the weak shock theory is extended to the more practical use, have been proposed.

The waveform parameter method invented by Thomas [45] is a representative prediction method for sonic boom. In this method, far-field waveforms can be predicted by extrapolating the near-field waveform that is obtained by the experiment or CFD [46], and the wave propagation is computed in consideration of several effects including geometrical spreading, nonlinearity, and atmospheric stratification (see Appendix for details). However, the rise time of sonic boom, which is one of the most important parameters for evaluating sonic boom intensity, cannot be predicted by the waveform parameter method because the shock wave is treated as a discontinuity; i.e., the shock wave has no thickness. Although the formation mechanism

of rise time has not been well clarified, it is thought that the molecular relaxation and thermoviscous dissipation including the fluid friction and thermal conduction have significant effects on the formation of rise time [32]. Hence, several prediction methods of rise time, in which the molecular relaxation and thermoviscous dissipation are considered, have been proposed. These methods are categorized into two approaches. One is the frequency domain approach [47], wherein the relaxation effects are considered in the frequency domain while the wave propagation is computed in the time domain. The other is the time domain approach based on the augmented Burgers equation [48], wherein the wave propagation with the relaxation effects is computed in the time domain. Recently, the method of solving the augmented Burgers equation is often used to predict far-field waveforms, including not only the pressure rise but also the rise time.

Accuracy of the prediction methods was recently evaluated by comparison with the Drop test for Simplified Evaluation of Non-symmetrically Distributed sonic boom #1 (D-SEND#1) [14] conducted by JAXA. As a result, the latest prediction method of solving the augmented Burgers equation [48] was the best possible way to predict the sonic boom intensity, including not only the pressure rise but also the rise time. However, the discrepancies between predictions and flight test measurements were significantly changed according to the flight and atmospheric conditions [49], because of the following two reasons: First, the effects of molecular relaxation and thermoviscous dissipation were treated as simplified models, and the treatments might not be adequate for analyzing sonic boom propagation in various flight and atmospheric conditions because these effects have not been fully clarified, although they have been investigated by one-dimensional numerical and asymptotic analyses [50]. Second, the effect of atmospheric turbulence [34–36], which causes the ragged distortion of the waveform behind the shock wave, was not considered because it cannot be well modeled. Therefore, the effects of molecular relaxation, thermoviscous dissipation, and atmospheric turbulence should be further investigated, and the prediction method considering the detailed models of these effects must be constructed to precisely predict sonic boom propagation through the real atmosphere.

1.2.3 Caustic-vicinity field

Acoustic rays that indicate the propagation paths of shock waves converge in accelerations [51], maneuvers [52], and low-supersonic flights [53]. Consequently, the envelop surface of the rays forms a caustic cusp, at which the sonic boom intensity becomes approximately three times larger than that without the focusing of the rays. This phenomenon is known as focused sonic boom [54]. In order to predict focused sonic boom, the diffraction effect caused by atmospheric stratification with altitude must be considered. Because the far-field prediction methods such as the waveform parameter method cannot

consider the diffraction effect, focused sonic boom has been analyzed by other prediction methods of solving the progressive wave equation [55], Khokhlov–Zabolotskaya (KZ) equation [56], nonlinear Tricomi equation [57] and so on. The accuracies of these methods were evaluated by comparison with the flight test, known as the Superboom Caustic Analysis and Measurement Project (SCAMP) [12] at NASA. As a result, the latest prediction method of solving the lossy nonlinear Tricomi equation [58] was the best possible way to evaluate the focused sonic boom, and the focusing strength was in good agreement with the flight test results. However, because the lossy nonlinear Tricomi equation does not incorporate the important effects of geometrical spreading and atmospheric stratification, the accuracy of the prediction may significantly differ in the flight and atmospheric conditions. In addition, the attenuation characteristics of the evanescent wave [57, 58] under the caustic region have not been fully clarified, although this wave is assumed to decay exponentially toward the ground. Therefore, the flight test, known as the Farfield Investigation of No boom Threshold (FaINT) [13] at NASA, was conducted to evaluate sonic boom cutoff phenomena [53] in the caustic-vicinity field, where the shock waves do not reach the ground because of an increase in atmospheric temperature toward the ground.

1.2.4 Limitation of application

Sonic boom waveforms generated from supersonic aircrafts in several flight and atmospheric conditions can be predicted by the existing prediction methods. However, these methods are based on the weak shock theory, and even complex phenomena are treated as simplified models. Thus, the applications of these methods are limited, and there are four big issues as follows. First, the accuracy of the rise time prediction is not necessarily adequate because the molecular relaxation and thermoviscous dissipation are evaluated as simplified models, and the effect of atmospheric turbulence cannot be well considered, as described in section 1.2.2. Second, the prediction of focused sonic boom in the caustic-vicinity field is conducted without consideration of the important effects such as geometrical spreading and atmospheric stratification, and the prediction accuracy of the evanescent wave is not adequate, as described in section 1.2.3. Third, the prediction methods based on the weak shock theory cannot be applied to sonic boom propagation generated from hypersonic flight objects because of the following reason: The area-balancing technique [19] for determining the weak shock waves cannot be applied to the strong shock waves with strong nonlinearity. In addition, the formation process of rise time significantly differs in supersonic and hypersonic flow regimes because the effects of molecular relaxation and chemical nonequilibrium in the hypersonic flow regime are much stronger than those in the supersonic flow regime. Forth, the variation in the circumferential direction around the body axis cannot be considered, and the ground effects [59, 60], including the ground reflection and ground topography, are treated as simplified models in the exciting prediction methods. For these

reasons, the applications of the existing prediction methods are limited, and they must be further improved to precisely predict sonic boom intensity in various flight, atmospheric, and ground conditions. Moreover, considering the fact that the several flight tests for sonic boom measurements were recently conducted, high-precision numerical flight experiments should be conducted in concert with the flight tests. Therefore, instead of the simplified prediction methods using the weak shock theory, the rigorous prediction method based on the CFD, i.e., the full-field simulation method [61, 62] seems to be a valid approach not only for analyzing sonic boom propagation through the real atmosphere but also for realizing numerical flight experiments (see next section for details).

1.3 Full-field simulation

1.3.1 Introduction of full-field simulation method

Full-field simulation [61, 62] represents CFD analysis for sonic boom predictions, wherein the entire flow field including the near, far, and caustic-vicinity fields is solved as a single computational domain. This simulation has the potential for considering various flight, atmospheric, and ground conditions because of the following three reasons: First, even complex effects such as molecular relaxation, viscosity, chemical nonequlibrium, and turbulence can be incorporated by modifying the governing equations [63–65], although the rigorous physics-based models of these effects must be constructed as needed. Second, the three-dimensional structure of a shock wave can be clarified because this method can consider the variation in the circumferential direction around the body axis. Third, the ground effects, including not only the ground reflection but also the ground topography, are precisely predicted because even a complex geometry, as well as an aircraft configuration, can be analyzed by the CFD methods [66, 67]. For these reasons, the full-field simulation method seems to be a powerful tool for precisely predicting sonic boom propagation in the realistic environmental conditions and for clarifying the complex sonic boom phenomena that have not been well clarified. Moreover, this simulation holds promise for conducting numerical flight experiments, wherein flight tests for sonic boom measurements are precisely reproduced.

CFD analysis for sonic boom propagation in the far field has been conducted by solving the one-dimensional, spherical-symmetric, and axi-symmetric equations [68–70]. However, the resolution of the shock wave was not necessarily adequate, and the computational load was very high. In addition, there is no precedent for three-dimensional CFD analysis considering atmospheric stratification. Therefore, the following three problems must be improved to perform full-field simulation in the real atmosphere. First, the computational approach for considering atmospheric stratification must be constructed. In the case of compressible CFD analysis, the flow field is generally discretized by the computational grid and is solved by the Riemann solver [71]. Consequently, the change caused by atmospheric stratification with altitude is

treated as a discontinuity in the Riemann solver, and nonphysical waves are generated. Thus, a computational approach for avoiding this change must be constructed because such an approach has not yet been proposed. Second, the solution-adapted grid over the entire flow field must be constructed to precisely capture shock waves [72]. Because the shock-wave angles change with the atmospheric temperature, the grid angles must be changed according to the propagation directions of the shock waves in the stratified atmosphere; thus, the three-dimensional solution-adapted grid must be constructed. Third, the computational load must be reduced as much as possible because the computational domain ranges over quite a long distance, and the thermal nonequilibrium flow analysis [68, 69] with high computational load is essential for predicting the rise time. With those in mind, the framework of the full-field simulation method is developed to analyze sonic boom propagation through the real atmosphere in this study.

1.3.2 Roadmap for formulation of full-field simulation method

Figure 1.2 shows the roadmap for constructing the framework of the full-field simulation method. The roadmap is composed of three phases. The first phase is the formulation of the full-field simulation method including the computational approach, the method of constructing the solution-adapted grid, and the segmentation method of a computational domain. The computational approach is formulated to simulate sonic boom propagation including five important effects as follows:

- **Geometrical spreading**: the attenuation effect due to the geometrical spreading of a wave with increasing distance from a generation source.
- **Nonlinearity**: the effect of wave steepening that is caused by the difference in the propagation speed of waves.
- **Atmospheric stratification**: the atmospheric effect due to variation in atmospheric properties with altitude.
- **Molecular relaxation (thermal nonequilibrium)**: the relaxation effect due to translational-vibrational energy exchange.
- **Viscosity**: the dissipation effect due to the fluid friction and thermal conduction.

If the computational approach considering these five effects is formulated, the extension of this approach is assumed to be relatively easy because the full-field simulation is based on the CFD. The method of constructing the solution-adapted grid is formulated so as to meet the following three requirements. First, shock waves must not intersect with the grid lines; thus, the grid lines in the entire computational domain must align with the shock waves. Second, the grid resolution near the shock waves must be adequately high. Third, the number of grid points must be reduced as much as possible because the computational domain ranges over quite a long distance. The segmentation method of a computational domain is constructed to

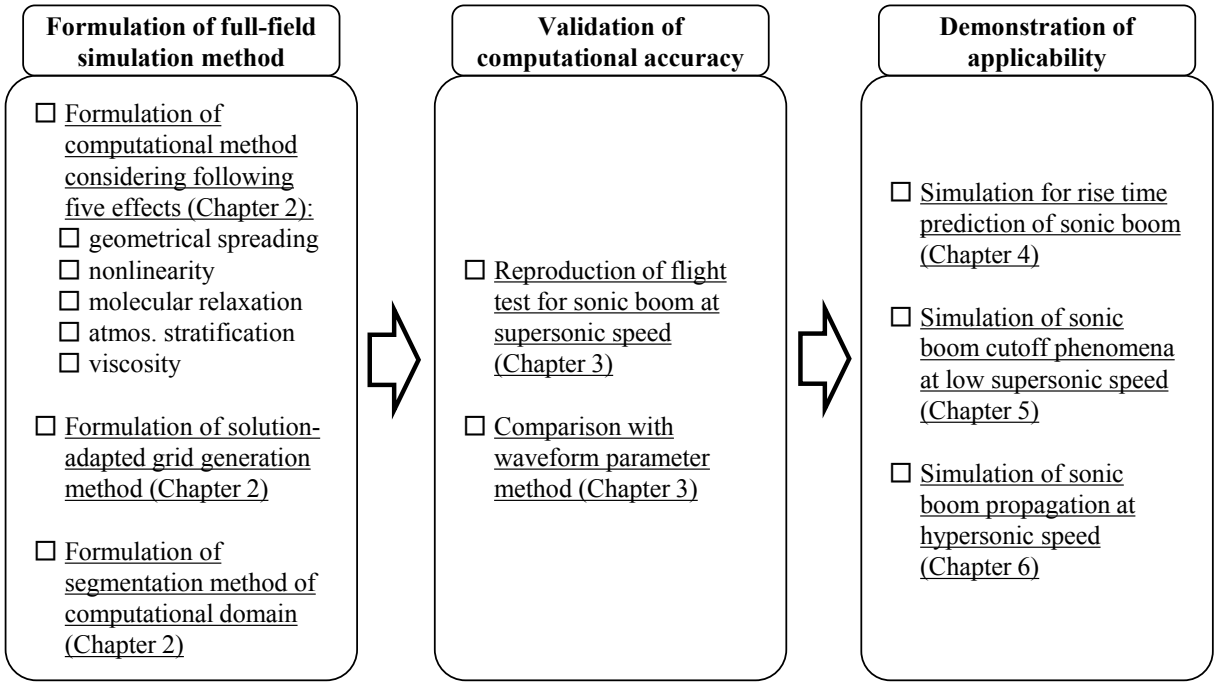

Fig. 1.2 Roadmap for constructing framework of full-field simulation method.

reduce the computational load and to improve the efficiency of computation.

The second phase is the validation of computational accuracy. Full-field simulation is performed to reproduce the flight test, and the simulation results are validated by comparison with the results of the waveform parameter method, which is a representative prediction method for sonic boom, and the flight test data. Consequently, the reproducibility of the flight test for sonic boom in the real atmosphere is investigated.

The third phase is the demonstration of the applicability to the analysis of complex sonic boom phenomena that have not been well clarified. First, full-field simulation with the thermal nonequilibrium is performed to investigate the formation mechanism of rise time as described in section 1.2.2. Second, full-field simulation is performed to analyze sonic boom cutoff phenomena [53] generated from a low supersonic flight object, including focused sonic boom in the caustic-vicinity field as described in section 1.2.3. Third, full-field simulation is performed to investigate sonic boom characteristics in hypersonic flow regimes as described in section 1.1. Consequently, the usefulness of full-field simulation method is investigated as a valid approach for analyzing sonic boom characteristics at all speeds including nonequilibrium characteristics and for clarifying sonic boom phenomena that cannot be investigated in the existing prediction methods.

When all three phases shown in Fig. 1.2 are accomplished, it can be said that the framework of the full-field simulation method is constructed. For the practical use of the framework, the appropriate computational method including the governing equations is selected according to the application and is

extended as needed. Consequently, the full-field simulation can precisely reproduce sonic boom propagation in various flight, atmospheric, and ground conditions; thus, numerical flight experiments can be conducted by the full-field simulation.

1.4 Objectives

Based on the above discussion, the objectives of this study are to formulate the framework of the full-field simulation method for sonic boom, according to the roadmap shown in Fig. 1.2, and to clarify sonic boom phenomena as follows:

- Formation mechanism of rise time due to molecular relaxation in uniform and stratified atmospheres.
- Sonic boom characteristics at low supersonic speeds, including cutoff phenomena in the caustic-vicinity field.
- Sonic boom characteristics at hypersonic speeds, including waveform transition of sonic boom according to flight Mach number.

Consequently, sonic boom phenomena that have not been well clarified become better understood, and the full-field simulation method becomes a powerful tool for precisely predicting sonic boom propagation through the real atmosphere and for realizing numerical flight experiments.

1.5 Outline of this thesis

An outline of this thesis is as follows. In chapter 2, the full-field simulation method is described. In chapter 3, the accuracy of full-field simulation is validated by comparison with the results of the waveform parameter method and the D-SEND#1 [14] flight test conducted by JAXA. In chapters 4 to 6, full-field simulation is performed to demonstrate the applicability of the full-field simulation method and to clarify sonic boom phenomena that cannot be investigated in the existing prediction methods. In chapter 4, full-field simulation is performed to investigate the effect of molecular relaxation on the sonic boom waveform and the formation mechanism of rise time in the uniform and stratified atmospheres. In chapter 5, full-field simulation is performed to analyze sonic boom propagation at low supersonic speeds, including sonic boom cutoff phenomena, and to investigate the applicability of this simulation to the analysis of focused sonic boom in the caustic-vicinity field. In chapter 6, full-field simulation is performed to clarify the waveform transition in a hypersonic flow regime and to investigate the applicability to sonic boom propagation from a hypersonic flight object. In chapter 7, the conclusion is described.

Chapter 2

Full-Field Simulation Method

2.1 Outline

In this chapter, the full-field simulation method is described. What must be necessary for realizing full-field simulation is to precisely predict sonic boom propagation in the entire flow field and to reduce the computational load as much as possible. For the requirements above, the full-field simulation method is formulated in this chapter. The flow solver considering the important effects on sonic boom propagation is formulated in sections 2.2 and 2.3. The method of constructing a solution-adapted grid to capture shock waves in the entire flow field is described in section 2.4. The segmentation method of a computational domain for reducing the computational load is explained in section 2.5. Then, the computational procedure of full-field simulation is described in section 2.6.

2.2 Governing equations

In order to precisely analyze sonic boom propagation, the governing equations must be formulated with consideration of physical effects such as geometrical spreading, nonlinearity, molecular relaxation and so on. As full-field simulation is based on the CFD, various physical effects can be incorporated by modifying the governing equations. However, because the computational domain in the full-field simulation ranges over quite a long distance, the computational load must be reduced as much as possible. Therefore, the different equations, where the minimum required effects are considered, are solved according to the application. Because the computational approach is the same regardless of the governing equations, two representative equations are only described in this chapter. One is the full three-dimensional equations including all effects considered in this study, i.e., the effects of geometrical spreading, nonlinearity, molecular relaxation, atmospheric stratification, and viscosity. The detailed explanation of these effects on sonic boom propagation is described in section 1.3.2 of chapter 1. The other is the axi-symmetric equations derived by assuming axi-symmetry in the full three-dimensional equations.

2.2.1 Full three-dimensional equations

Dimensional form in Cartesian coordinates

Full-field simulation based on the CFD can be performed by solving the primitive equations of fluid dynamics, i.e., the Navier-Stokes equations. In the Navier-Stokes equations, the nonlinear wave steepening and viscous dissipation are expressed by the convective and viscous terms, respectively. The geometrical spreading of waves can be considered by three-dimensional analysis, and horizontally atmospheric stratification can be incorporated by adding the gravity term for maintaining the state of hydrostatic equilibrium to the governing equations. In addition, the molecular relaxation can be considered by adding the thermal nonequilibrium model, in which conservation equations for vibrational energy are incorporated. The full three-dimensional equations including all the above effects are as follows:

$$\frac{\partial Q}{\partial t}+\frac{\partial E}{\partial x}+\frac{\partial F}{\partial y}+\frac{\partial G}{\partial z}=\frac{\partial E_v}{\partial x}+\frac{\partial F_v}{\partial y}+\frac{\partial G_v}{\partial z}+S_G+S_W \tag{2.1}$$

$$Q=\begin{bmatrix}\rho\\ \rho u\\ \rho v\\ \rho w\\ e\\ e_{vO_2}\\ e_{vN_2}\end{bmatrix},E=\begin{bmatrix}\rho u\\ \rho u^2+p\\ \rho uv\\ \rho uw\\ (e+p)u\\ e_{vO_2}u\\ e_{vN_2}u\end{bmatrix},F=\begin{bmatrix}\rho v\\ \rho uv\\ \rho v^2+p\\ \rho vw\\ (e+p)v\\ e_{vO_2}v\\ e_{vN_2}v\end{bmatrix},G=\begin{bmatrix}\rho w\\ \rho uw\\ \rho vw\\ \rho w^2+p\\ (e+p)w\\ e_{vO_2}w\\ e_{vN_2}w\end{bmatrix} \tag{2.2}$$

$$E_v=\begin{bmatrix}0\\ \tau_{xx}\\ \tau_{xy}\\ \tau_{xz}\\ \beta_x\\ 0\\ 0\end{bmatrix},F_v=\begin{bmatrix}0\\ \tau_{yx}\\ \tau_{yy}\\ \tau_{yz}\\ \beta_y\\ 0\\ 0\end{bmatrix},G_v=\begin{bmatrix}0\\ \tau_{zx}\\ \tau_{zy}\\ \tau_{zz}\\ \beta_z\\ 0\\ 0\end{bmatrix} \tag{2.3}$$

$$S_G=\begin{bmatrix}0\\ 0\\ \rho g\\ 0\\ \rho g v\\ 0\\ 0\end{bmatrix},S_W=\begin{bmatrix}0\\ 0\\ 0\\ 0\\ 0\\ w_{vO_2}\\ w_{vN_2}\end{bmatrix} \tag{2.4}$$

$$\beta_x = \tau_{xx}u + \tau_{xy}v + \tau_{xz}w + \kappa\frac{\partial T}{\partial x}$$
$$\beta_y = \tau_{yx}u + \tau_{yy}v + \tau_{yz}w + \kappa\frac{\partial T}{\partial y} \tag{2.5}$$
$$\beta_z = \tau_{zx}u + \tau_{zy}v + \tau_{zz}w + \kappa\frac{\partial T}{\partial z}$$

where the full three-dimensional equations are composed of the conservation equation for mass, three conservation equations for momentum, conservation equation for total energy, and two conservation equations for vibrational energies with respect to O_2 and N_2. Q is the conservative variables, E, F, and G are the inviscid flux vectors, E_v, F_v, and G_v are the viscous flux vectors, S_G is the gravity term, and S_W is the translational-vibrational relaxation term. In the Cartesian coordinates (x, y, z), x is the streamwise direction, y is the vertically downward direction, and z is the horizontal direction. u, v, and w are the velocity components in the x, y, and z directions, respectively. ρ is the density, p is the pressure, T is the temperature, τ_{ij} ($i, j = x, y$, and z) is the viscous shear stress, κ is the thermal conductivity, e is the total energy per unit volume, e_{vO_2} and e_{vN_2} are the vibrational energies of O_2 and N_2 per unit volume, respectively. w_{vO_2} and w_{vN_2} are the translational-vibrational relaxation terms of O_2 and N_2, respectively. The acceleration of gravity is g = 9.80665 m/s^2.

The viscous stress tensor is calculated as

$$\begin{bmatrix} \tau_{xx} & \tau_{xy} & \tau_{xz} \\ \tau_{yx} & \tau_{yy} & \tau_{yz} \\ \tau_{zx} & \tau_{zy} & \tau_{zz} \end{bmatrix} = \begin{bmatrix} \frac{2}{3}\mu\left(2\frac{\partial u}{\partial x} - \frac{\partial v}{\partial y} - \frac{\partial w}{\partial z}\right) & \mu\left(\frac{\partial u}{\partial y} + \frac{\partial v}{\partial x}\right) & \mu\left(\frac{\partial w}{\partial x} + \frac{\partial u}{\partial z}\right) \\ & \frac{2}{3}\mu\left(2\frac{\partial v}{\partial y} - \frac{\partial w}{\partial z} - \frac{\partial u}{\partial x}\right) & \mu\left(\frac{\partial w}{\partial y} + \frac{\partial v}{\partial z}\right) \\ sym. & & \frac{2}{3}\mu\left(2\frac{\partial w}{\partial z} - \frac{\partial u}{\partial x} - \frac{\partial v}{\partial y}\right) \end{bmatrix} \tag{2.6}$$

where μ is the viscous coefficient.

The total energy of ideal gas is described as

$$e = \frac{\rho RT}{\gamma - 1} + e_{vO_2} + e_{vN_2} + \frac{\rho}{2}\left(u^2 + v^2 + w^2\right) \tag{2.7}$$

where the ratio of specific heat is γ = 1.4. Assuming an air, the gas constant is R = 287 J/(K·kg).

The equation of the state of ideal gas is described as follows:

$$p = \rho RT \tag{2.8}$$

In the thermal nonequilibrium model, the vibrational energy is evaluated by the harmonic oscillation model [20] as

$$e_{vs} = \frac{\varepsilon_s \rho R \theta_s}{\exp(\theta_s / T_{vs}) - 1} \quad (\mathrm{s} = O_2, N_2) \tag{2.9}$$

$$e_{vs}{}^{eq} = \frac{\varepsilon_s \rho R \theta_s}{\exp(\theta_s / T) - 1} \quad (\mathrm{s} = \mathrm{O_2}, \mathrm{N_2}) \tag{2.10}$$

where the mole ratios of air for O_2 and N_2 are ε_{O_2} = 0.233 and ε_{N_2} = 0.767, respectively, and the characteristic vibrational temperatures for O_2 and N_2 are θ_{O_2} = 2273.0 K and θ_{N_2} = 3393.0 K, respectively [68]. The translational–rotational energy modes are assumed to be in the local equilibrium, and the translational and rotational temperatures are evaluated as the common temperature T. The translational–vibrational energy modes are assumed to be in the nonequilibrium, and the vibrational temperatures of O_2 and N_2 are evaluated as T_{vO_2} and T_{vN_2}, respectively. In the case of sonic boom propagation for quite a long distance, a shock wave is slowly relaxed by the effect of molecular relaxation, i.e., the translational–vibrational energy exchange. Thus, the translational–vibrational relaxation in the adiabatic transition is evaluated by the Landau-Teller relaxation model [73] as

$$w_{vs} = \frac{e_{vs}{}^{eq} - e_{vs}}{\tau_s} \quad (\mathrm{s} = \mathrm{O_2}, \mathrm{N_2}) \tag{2.11}$$

where τ_{O_2} and τ_{N_2} are the vibrational relaxation time of O_2 and N_2, respectively, and are evaluated by the Bass et al's formula [74] as

$$\frac{1}{\tau_{O_2}} = \frac{2\pi p}{p_0}\left(24 + 4.04 \times 10^4 h_a \frac{0.02 + h_a}{0.391 + h_a}\right) \tag{2.12}$$

$$\frac{1}{\tau_{N_2}} = \frac{2\pi p}{p_0}\left\{\left(\frac{T_0}{T}\right)^{\frac{1}{2}}\left[9 + 280 h_a \exp\left(-4.17\left\{\left(\frac{T_0}{T}\right)^{\frac{1}{3}} - 1\right\}\right)\right]\right\} \tag{2.13}$$

where the units of τ_{O_2} and τ_{N_2} are second, T_0 = 293.15 K, and p_0 = 101.3 kPa. The absolute humidity h_a is derived as

$$h_a = h_r \frac{p_{sat}/p_0}{p/p_0} = p_0\left(\frac{h_r}{p}\right)\left(\frac{p_{sat}}{p_0}\right) \tag{2.14}$$

$$\log_{10}\left(\frac{p_{sat}}{p_0}\right) = -6.8346\left(\frac{T_{01}}{T}\right)^{1.261} + 4.6151 \tag{2.15}$$

where h_r is the relative humidity, and the units of h_a and h_r are %. The triple point temperature is T_{01} = 273.16 K. As can be seen from Eqs. (2.12) and (2.13), the relaxation time depends on the pressure, temperature, and absolute humidity.

Nondimensional form in Cartesian coordinates

Nondimensional variables are defined as

$$x^* \equiv \frac{x}{L}, \quad y^* \equiv \frac{y}{L}, \quad z^* \equiv \frac{z}{L}, \quad u^* \equiv \frac{u}{u_\infty}, \quad v^* \equiv \frac{v}{u_\infty}, \quad w^* \equiv \frac{w}{u_\infty},$$

$$t^* \equiv \frac{t}{L/u_\infty}, \quad \rho^* \equiv \frac{\rho}{\rho_\infty}, \quad p^* \equiv \frac{p}{\rho_\infty {u_\infty}^2}, \quad T^* \equiv \frac{T}{T_\infty}, \quad \mu^* \equiv \frac{\mu}{\mu_\infty}, \quad g^* \equiv \frac{g}{{u_\infty}^2/L}, \tag{2.16}$$

$$e^* \equiv \frac{e}{\rho_\infty {u_\infty}^2}, \quad {e_{vO_2}}^* \equiv \frac{e_{vO_2}}{\rho_\infty {u_\infty}^2}, \quad {e_{vN_2}}^* \equiv \frac{e_{vN_2}}{\rho_\infty {u_\infty}^2}, \quad {\tau_{O_2}}^* \equiv \frac{\tau_{O_2}}{L/u_\infty}, \quad {\tau_{N_2}}^* \equiv \frac{\tau_{N_2}}{L/u_\infty}$$

where superscript * denotes nondimensional variable, subscript ∞ denotes freestream variable at the flight altitude, and L is the reference length. Substituting Eq. (2.16) into Eq. (2.1), the nondimensional form is described as

$$\frac{\partial Q^*}{\partial t^*} + \frac{\partial E^*}{\partial x^*} + \frac{\partial F^*}{\partial y^*} + \frac{\partial G^*}{\partial z^*} = \frac{1}{\mathrm{Re}}\left(\frac{\partial {E_v}^*}{\partial x^*} + \frac{\partial {F_v}^*}{\partial y^*} + \frac{\partial {G_v}^*}{\partial z^*} \right) + {S_G}^* + {S_W}^* \tag{2.17}$$

where the Reynolds number Re is defined as follows:

$$\mathrm{Re} = \frac{\rho_\infty u_\infty L}{\mu_\infty} \tag{2.18}$$

The equation of the state of ideal gas is also nondimensionalized, and the gas constant is described as

$$R^* = \frac{1}{\gamma {M_\infty}^2} \tag{2.19}$$

where the freestream Mach number is defined as follows:

$$M_\infty = \frac{u_\infty}{\sqrt{\gamma R T_\infty}} \tag{2.20}$$

The viscous coefficient is evaluated by Sutherland's formula:

$$\mu^* = \frac{{c_1}^* {T^*}^{\frac{3}{2}}}{T^* + {c_2}^*} \tag{2.21}$$

$${c_1}^* = \frac{1.458 \times 10^{-6}}{\mu_\infty}\sqrt{T_\infty}, \quad {c_2}^* = \frac{110.4}{T_\infty} \tag{2.22}$$

The thermal conductivity is described as

$$\kappa^* = \frac{\mu^*}{(\gamma - 1){M_\infty}^2 \,\mathrm{Pr}} \tag{2.23}$$

where the Prandtl number is Pr = 0.72 of air.

Nondimensional form in generalized coordinates

Using the chain rule, Eq. (2.17) is transformed from Cartesian coordinates (x, y, z) to generalized coordinates (ξ, η, ζ) as

$$\frac{\partial \hat{Q}}{\partial t}+\frac{\partial \hat{E}}{\partial \xi}+\frac{\partial \hat{F}}{\partial \eta}+\frac{\partial \hat{G}}{\partial \zeta}=\frac{1}{\mathrm{Re}}\left(\frac{\partial \hat{E}_v}{\partial \xi}+\frac{\partial \hat{F}_v}{\partial \eta}+\frac{\partial \hat{G}_v}{\partial \zeta}\right)+\hat{S}_G+\hat{S}_W \tag{2.24}$$

$$\hat{Q}=\frac{Q}{J},\quad \hat{E}=\frac{1}{J}\left(E\xi_x+F\xi_y+G\xi_z\right),\quad \hat{F}=\frac{1}{J}\left(E\eta_x+F\eta_y+G\eta_z\right),\quad \hat{G}=\frac{1}{J}\left(E\zeta_x+F\zeta_y+G\zeta_z\right) \tag{2.25}$$

$$\hat{E}_v=\frac{1}{J}\left(E_v\xi_x+F_v\xi_y+G_v\xi_z\right),\quad \hat{F}_v=\frac{1}{J}\left(E_v\eta_x+F_v\eta_y+G_v\eta_z\right),\quad \hat{G}_v=\frac{1}{J}\left(E_v\zeta_x+F_v\zeta_y+G_v\zeta_z\right) \tag{2.26}$$

$$\hat{S}_G=\frac{S_G}{J},\quad \hat{S}_W=\frac{S_W}{J} \tag{2.27}$$

where subscripts x, y, and z denote the partial derivatives with respect to x, y, and z, respectively. The metrics such as ξ_x and the Jacobian J are calculated as

$$\begin{aligned}
&\xi_x=J\left(y_\eta z_\zeta-y_\zeta z_\eta\right),\quad \xi_y=J\left(z_\eta x_\zeta-z_\zeta x_\eta\right),\quad \xi_z=J\left(x_\eta y_\zeta-x_\zeta y_\eta\right),\\
&\eta_x=J\left(y_\zeta z_\xi-y_\xi z_\zeta\right),\quad \eta_y=J\left(z_\zeta x_\xi-z_\xi x_\zeta\right),\quad \eta_z=J\left(x_\zeta y_\xi-x_\xi y_\zeta\right),\\
&\zeta_x=J\left(y_\xi z_\eta-y_\eta z_\xi\right),\quad \zeta_y=J\left(z_\xi x_\eta-z_\eta x_\xi\right),\quad \zeta_z=J\left(x_\xi y_\eta-x_\eta y_\xi\right)
\end{aligned} \tag{2.28}$$

$$J^{-1}=x_\xi\left(y_\eta z_\zeta-y_\zeta z_\eta\right)+x_\eta\left(y_\zeta z_\xi-y_\xi z_\zeta\right)+x_\zeta\left(y_\xi z_\eta-y_\eta z_\xi\right) \tag{2.29}$$

where subscripts ξ, η, and ζ denote the partial derivatives with respect to ξ, η, and ζ, respectively. The partial derivatives are evaluated by the second-order central difference.

2.2.2 Axi-symmetric equations

Dimensional form in cylindrical coordinates

Assuming a uniform atmosphere in the entire flow field around an axi-symmetric body, the full three-dimensional equations described as Eq. (2.1) can be simplified as follows. Eq. (2.1) is transformed from Cartesian coordinates (x, y, z) to cylindrical coordinates (x, r, θ), and the velocity in the rotational direction (θ direction) and the partial derivatives with respect to θ are assumed to be zero. As a result, the axi-symmetric equations are derived as

$$\frac{\partial Q}{\partial t}+\frac{\partial E}{\partial x}+\frac{\partial F}{\partial r}+H=\frac{\partial E_v}{\partial x}+\frac{\partial F_v}{\partial r}+H_v+S_W \tag{2.30}$$

$$Q=\begin{bmatrix}\rho\\ \rho u\\ \rho v\\ e\\ e_{vO_2}\\ e_{vN_2}\end{bmatrix},E=\begin{bmatrix}\rho u\\ \rho u^2+p\\ \rho uv\\ (e+p)u\\ e_{vO_2}u\\ e_{vN_2}u\end{bmatrix},F=\begin{bmatrix}\rho v\\ \rho uv\\ \rho v^2+p\\ (e+p)v\\ e_{vO_2}v\\ e_{vN_2}v\end{bmatrix},H=\begin{bmatrix}\rho v/r\\ \rho uv/r\\ \rho v^2/r\\ (e+p)v/r\\ e_{vO_2}v/r\\ e_{vN_2}v/r\end{bmatrix} \tag{2.31}$$

$$E_v = \begin{bmatrix} 0 \\ \tau_{xx} \\ \tau_{xr} \\ \beta_x \\ 0 \\ 0 \end{bmatrix}, F_v = \begin{bmatrix} 0 \\ \tau_{rx} \\ \tau_{rr} \\ \beta_r \\ 0 \\ 0 \end{bmatrix}, H_v = \begin{bmatrix} 0 \\ \tau_{xr}/r \\ 2\mu\left(\frac{\partial v}{\partial r} - \frac{v}{r}\right)\Big/ r \\ \beta_r/r \\ 0 \\ 0 \end{bmatrix} \tag{2.32}$$

$$S_W = \begin{bmatrix} 0 \\ 0 \\ 0 \\ 0 \\ w_{vO_2} \\ w_{vN_2} \end{bmatrix} \tag{2.33}$$

$$\begin{aligned} \beta_x &= \tau_{xx} u + \tau_{xr} v + \kappa \frac{\partial T}{\partial x} \\ \beta_r &= \tau_{rx} u + \tau_{rr} v + \kappa \frac{\partial T}{\partial r} \end{aligned} \tag{2.34}$$

where H and H_v are the axi-symmetric inviscid and viscous terms, respectively. u and v are the velocities in the x and r directions, respectively. The gravity term S_G is excluded because atmospheric stratification cannot be considered in axi-symmetric analysis.

The viscous stress tensor is calculated as

$$\begin{bmatrix} \tau_{xx} & \tau_{xr} \\ \tau_{rx} & \tau_{rr} \end{bmatrix} = \begin{bmatrix} \frac{2}{3}\mu\left(2\frac{\partial u}{\partial x} - \frac{\partial v}{\partial r} - \frac{v}{r}\right) & \mu\left(\frac{\partial u}{\partial r} + \frac{\partial v}{\partial x}\right) \\ \mu\left(\frac{\partial u}{\partial r} + \frac{\partial v}{\partial x}\right) & \frac{2}{3}\mu\left(2\frac{\partial v}{\partial r} - \frac{\partial u}{\partial x} - \frac{v}{r}\right) \end{bmatrix} \tag{2.35}$$

The total energy of the ideal gas is described as

$$e = \frac{\rho R T}{\gamma - 1} + e_{vO_2} + e_{vN_2} + \frac{\rho}{2}\left(u^2 + v^2\right) \tag{2.36}$$

The equation of the state of ideal gas given by Eq. (2.8) and the thermal nonequilibrium model given by Eqs. (2.9) to (2.15) are used.

Nondimensional form in generalized coordinates

As in the full three-dimensional equations, the axi-symmetric equations given by Eq. (2.30) are nondimensionalized and transformed from cylindrical coordinates (x, r) to generalized coordinates (ξ, η) as

$$\frac{\partial \hat{Q}}{\partial t} + \frac{\partial \hat{E}}{\partial \xi} + \frac{\partial \hat{F}}{\partial \eta} + \hat{H} = \frac{1}{\mathrm{Re}}\left(\frac{\partial \hat{E}_v}{\partial \xi} + \frac{\partial \hat{F}_v}{\partial \eta} + \hat{H}_v\right) + \hat{S}_W \tag{2.37}$$

$$\hat{Q} = \frac{Q}{J}, \quad \hat{E} = \frac{1}{J}\left(E\xi_x + F\xi_r\right), \quad \hat{F} = \frac{1}{J}\left(E\eta_x + F\eta_r\right), \quad \hat{H} = \frac{H}{J} \tag{2.38}$$

$$\hat{E}_v = \frac{1}{J}\left(E_v\xi_x + F_v\xi_r\right), \quad \hat{F}_v = \frac{1}{J}\left(E_v\eta_x + F_v\eta_r\right), \quad \hat{H}_v = \frac{H_v}{J} \tag{2.39}$$

$$\hat{S}_W = \frac{S_W}{J} \tag{2.40}$$

where subscripts x and r denote the partial derivatives with respect to x and r, respectively. The metrics and Jacobian are calculated as

$$\xi_x = Jr_\eta, \quad \xi_r = -Jx_\eta, \quad \eta_x = -Jr_\xi, \quad \eta_r = Jx_\xi \tag{2.41}$$

$$J^{-1} = x_\xi r_\eta - x_\eta r_\xi \tag{2.42}$$

where subscripts ξ and η denote the partial derivatives with respect to ξ and η, respectively. The partial derivatives are evaluated by the second-order central difference.

2.3 Computational approach of solving governing equations

2.3.1 Discretization of convective terms

In the case of full-field simulation, shock waves must be precisely captured in the entire flow field, and the computational load should be reduced as much as possible. Thus, the Finite Volume Method (FVM), which possesses the conservation properties of mass, momentum, and energy, is used to capture discontinuities such as shock waves. In the FVM, the computational domain is discretized into finite control volumes, and the flow properties in each cell are computed. In this study, the numerical fluxes of the convective terms are evaluated by the Simple High resolution Upwind Scheme (SHUS) [75] because this scheme is not only simple but also accurate for capturing shock waves. The SHUS scheme is classified into the group of Advection Upstream Splitting Method (AUSM) [76] type scheme. The flux of AUSM type scheme, which is one of the Flux Vector Splitting (FVS) methods [77], is described as

$$\widetilde{F} = \frac{\dot{m} + |\dot{m}|}{2}\Phi_L + \frac{\dot{m} - |\dot{m}|}{2}\Phi_R + \widetilde{p}N \tag{2.43}$$

$$\Phi = \begin{bmatrix} 1 \\ u \\ v \\ w \\ (e+p)/\rho \\ e_{vO_2}/\rho \\ e_{vN_2}/\rho \end{bmatrix}, \quad N = \begin{bmatrix} 0 \\ x_n \\ y_n \\ z_n \\ 0 \\ 0 \\ 0 \end{bmatrix} \tag{2.44}$$

where (x_n, y_n, z_n) is the unit vector normal to the cell interface. $\dot{m}$ and $\widetilde{p}$ are the mass and pressure fluxes at

the cell interface, respectively. Subscripts L and R show left-side and right-side values at the cell interface, respectively. The AUSM type scheme is divided by the difference of the evaluation method for the mass and pressure fluxes. In the SHUS scheme, the mass flux is evaluated by Roe's Finite Difference Splitting (FDS) scheme [71] as

$$\dot{m} = \frac{1}{2}\left\{ (\rho V_n)_L + (\rho V_n)_R - \left|\overline{V}_n\right|\Delta\rho - \frac{\left|\overline{M}+1\right| - \left|\overline{M}-1\right|}{2}\overline{\rho}\Delta\overline{V}_n - \frac{\left|\overline{M}+1\right| + \left|\overline{M}-1\right| - 2\left|\overline{M}\right|}{2\overline{c}}\Delta p \right\} \tag{2.45}$$

$$V_n = x_n u + y_n v + z_n w \tag{2.46}$$

$$\Delta q = q_L - q_R (q = V_n, \rho, p) \tag{2.47}$$

$$\overline{q} = \frac{q_L + q_R}{2} \tag{2.48}$$

$$\overline{M} = \frac{\overline{V}_n}{\overline{c}} \tag{2.49}$$

$$\overline{c} = \sqrt{\gamma\overline{p}/\overline{\rho}} \tag{2.50}$$

and the pressure flux is evaluated as

$$\widetilde{p} = \beta_L p_L + \beta_R p_R \tag{2.51}$$

$$\beta_L = \begin{cases} \frac{1}{4}(2 - M_L)(M_L + 1)^2 & if\ |M_L| < 1 \\ \frac{1}{2}(M_L + |M_L|)/|M_L| & otherwise \end{cases} \tag{2.52}$$

$$\beta_R = \begin{cases} \frac{1}{4}(2 + M_R)(M_R - 1)^2 & if\ |M_R| < 1 \\ \frac{1}{2}(M_R - |M_R|)/|M_R| & otherwise \end{cases} \tag{2.53}$$

$$M_{L/R} = (V_n)_{L/R}/\overline{c} \tag{2.54}$$

The SHUS scheme of first-order accuracy is extended to third-order accuracy by the Monotone Upstream-centered Schemes for Conservation Law (MUSCL) interpolation [78]. The MUSCL interpolation is described as

$$\begin{aligned} (q_L)_{i+\frac{1}{2}} &= q_i + \left\{ \frac{s}{4}\left[(1-\sigma s)\Delta_R + (1+\sigma s)\Delta_L\right] \right\}_i \\ (q_R)_{i+\frac{1}{2}} &= q_{i+1} - \left\{ \frac{s}{4}\left[(1-\sigma s)\Delta_L + (1+\sigma s)\Delta_R\right] \right\}_{i+1} \end{aligned} \tag{2.55}$$

where $(\Delta_L)_i = q_{i+1} - q_i$, $(\Delta_R)_i = q_i - q_{i-1}$, $\sigma = 1/3$ for third-order accuracy, and s is the flux limiter function. In this study, the slope limiter proposed by Van Albada et al. [79] is used as

$$s = \frac{2\Delta_L\Delta_R + \varepsilon}{(\Delta_L)^2 + (\Delta_R)^2 + \varepsilon} \tag{2.56}$$

where ε is a small, positive value. The MUSCL interpolation at the other boundaries i–1/2, j±1/2, and k±1/2

can be described as in the same way described above.

2.3.2 Discretization of viscous terms

The viscous terms are evaluated by second-order central difference. Using the chain rule, the first derivatives are calculated as

$$\begin{aligned}\phi_x &= \xi_x\phi_\xi + \eta_x\phi_\eta + \zeta_x\phi_\zeta \\ \phi_y &= \xi_y\phi_\xi + \eta_y\phi_\eta + \zeta_y\phi_\zeta \\ \phi_z &= \xi_z\phi_\xi + \eta_z\phi_\eta + \zeta_z\phi_\zeta\end{aligned} \tag{2.57}$$

where ϕ is a scalar quantity. ϕ_ξ, ϕ_η, and ϕ_ζ are discretized as

$$\begin{aligned}\left(\phi_\xi\right)_{i+\frac{1}{2}} &= \frac{1}{2}\left(\phi_{i+1,j,k} - \phi_{i-1,j,k}\right) \\ \left(\phi_\eta\right)_{i+\frac{1}{2}} &= \frac{1}{2}\left[\left(\phi_\eta\right)_i + \left(\phi_\eta\right)_{i+1}\right] \\ &= \frac{1}{4}\left(\phi_{i,j+1,k} - \phi_{i,j-1,k} + \phi_{i+1,j+1,k} - \phi_{i+1,j-1,k}\right) \\ \left(\phi_\zeta\right)_{i+\frac{1}{2}} &= \frac{1}{2}\left[\left(\phi_\zeta\right)_i + \left(\phi_\zeta\right)_{i+1}\right] \\ &= \frac{1}{4}\left(\phi_{i,j,k+1} - \phi_{i,j,k-1} + \phi_{i+1,j,k+1} - \phi_{i,j-1,k+1}\right)\end{aligned} \tag{2.58}$$

The derivatives at the other boundaries i–1/2, j±1/2, and k±1/2 can be evaluated as in the same way described above.

2.3.3 Evaluation of translational-vibrational relaxation term

In the case of thermal nonequilibrium flow analysis, the robustness of computation must be improved because the translational-vibrational relaxation time is generally much faster than the time scale of the flow. Thus, the translational-vibrational relaxation term S_W is evaluated by the diagonal implicit method [80], which is derived by simplifying the point implicit method [81]. The diagonal implicit method is derived as follows. Assuming the one-dimensional Euler equations with the relaxation term, the discretized form in the generalized coordinates is written as

$$\Delta\hat{Q}_i = -\Delta t\left(\hat{E}^n_{i+1/2} - \hat{E}^n_{i-1/2} - \hat{S}_{W_i}{}^{n+1}\right) \tag{2.59}$$

where the relaxation term is defined implicitly and is evaluated as follows:

$$\hat{S}_{W_i}{}^{n+1} = \hat{S}_{W_i}{}^{n} + \frac{\partial\hat{S}_{W_i}{}^{n}}{\partial\hat{Q}_i}\Delta\hat{Q}_i \tag{2.60}$$

Substituting Eq. (2.60) into Eq. (2.59),

$$\left(I - \Delta t \hat{Z}_i^n\right)\Delta \hat{Q}_i = -\Delta t\left(\hat{E}_{i+1/2}^n - \hat{E}_{i-1/2}^n - \hat{S}_{Wi}{}^n\right) \tag{2.61}$$

$$\hat{Z}_i^n = \frac{\partial \hat{S}_{Wi}{}^n}{\partial \hat{Q}_i} \tag{2.62}$$

where I is a unit matrix. In the point implicit method, Eq. (2.61) is solved by the matrix inversion of $\left(I - \Delta t \hat{Z}_i^n\right)$, and as a result the robustness can be improved. However, the matrix inversion involves the high computational load. If the steady solution is needed, the final solution does not depend on this matrix. Therefore, in the diagonal implicit method, the matrix can be diagonalized as follows:

$$\left(I - \Delta t \hat{Z}_i^n\right) \approx \left[I + diag\left(\frac{\Delta t}{\tau_s}\right)\right] \quad (\mathrm{s} = \mathrm{O_2}, \mathrm{N_2}) \tag{2.63}$$

$$\frac{1}{\tau_s} = \beta_r \left[\sum_i \left(\frac{\partial w_{vs}}{\partial \rho_i}\right)^2\right]^{1/2} \quad (\mathrm{s} = \mathrm{O_2}, \mathrm{N_2}) \tag{2.64}$$

where β_r is the relaxation coefficient. Moreover, Eq. (2.64) can be approximately evaluated as

$$\frac{1}{\tau_s} \approx \beta_r \times n_s \times \left|\frac{w_{vs}}{\rho_s}\right| \quad (\mathrm{s} = \mathrm{O_2}, \mathrm{N_2}) \tag{2.65}$$

where n_s is the number of molecular species. In the diagonal implicit method, the robustness can be improved, and the matrix inversion is unnecessary; thus, the increase of computational load is avoided. The relaxation coefficient is set to $\beta_r = 10$ in this study.

2.3.4 Evaluation of gravity term and correction term

To consider the stratified atmosphere such as the standard atmosphere [82] defined by the International Organization for Standardization (ISO), the hydrostatic equilibrium must be maintained as

$$\frac{dp_a}{dh} = -g\rho_a \tag{2.66}$$

where subscript a denotes the atmospheric value, and h is the altitude. Thus, the full three-dimensional equations described in Eq. (2.1) incorporate the gravity term. If $u = v = w = 0$ in Eq. (2.1), the hydrostatic equilibrium is strictly maintained. However, the flow field is discretized by the computational grid and is solved by the Riemann solver [71]. Consequently, the change caused by atmospheric stratification with altitude is treated as a discontinuity in the Riemann solver, and nonphysical waves are generated because the hydrostatic equilibrium cannot be strictly maintained. In general, the Riemann solver cannot distinguish between the change by atmospheric stratification and the fluctuation by waves in the compressible fluid. Thus, the nonphysical waves must not be generated. To avoid this generation, the authors proposed the new numerical correction method [62, 83]. The following is the description of this method.

From the Taylor series expansion of Eq. (2.66),

$$\frac{\Delta p_a}{\Delta h} = -g\rho_a + O(\Delta h^2) \tag{2.67}$$

where the second term in the right-hand side is a discretization error. If the error is ignored, the nonphysical waves are generated because the state of hydrostatic equilibrium cannot be strictly maintained. The governing equations given by Eq. (2.24) are discretized as

$$\left(\frac{\partial \hat{Q}}{\partial t} + \frac{\partial \hat{E}}{\partial \xi} + \frac{\partial \hat{F}}{\partial \eta} + \frac{\partial \hat{G}}{\partial \zeta}\right)_{i,j,k} = \left[\frac{1}{\mathrm{Re}}\left(\frac{\partial \hat{E}_v}{\partial \xi} + \frac{\partial \hat{F}_v}{\partial \eta} + \frac{\partial \hat{G}_v}{\partial \zeta}\right) + \hat{S}_G + \hat{S}_W + S_C\right]_{i,j,k} \tag{2.68}$$

where the correction term S_C is added for cancelling the discretization error. If the grid spacing is zero, S_C is a zero vector. In the numerical correction method, the gravity term is treated as a source term, and the correction term is evaluated as follows:

1) The freestream conditions in the stratified atmosphere, where $u = u_\infty$, $v = w = 0$, $T = T_{vO_2} = T_{vO_2} = T_a(h)$, and $p = p_a(h)$, are set in the entire computational domain including the entire boundaries.
2) The numerical fluxes are computed, and the correction term is derived to conserve the freestream conditions in the stratified atmosphere as

$$S_{C,i,j,k} = \left[\left(\frac{\partial \hat{E}}{\partial \xi} + \frac{\partial \hat{F}}{\partial \eta} + \frac{\partial \hat{G}}{\partial \zeta}\right) - \frac{1}{\mathrm{Re}}\left(\frac{\partial \hat{E}_v}{\partial \xi} + \frac{\partial \hat{F}_v}{\partial \eta} + \frac{\partial \hat{G}_v}{\partial \zeta}\right) - \hat{S}_G - \hat{S}_W\right]_{i,j,k} \tag{2.69}$$

3) The derived correction term is evaluated as the constant value in the simulation.

Using the numerical correction method above, the fluctuation components from the freestream conditions in the stratified atmosphere are substantially calculated. The usefulness of this method is investigated as described in section 3.3.4 of chapter 3.

2.3.5 Time integration method

Sonic boom waveforms in the far field are assumed to be steady, unless atmospheric variability is considered. Thus, the time integration is performed by the first-order Matrix Free Gauss-Seidel (MFGS) [84, 85] implicit method, which is derived from the Lower-Upper Symmetric-Gauss-Seidel (LU-SGS) [86] implicit method. The MFGS method is derived as follows. When the Euler implicit method is applied to Eq. (2.24) and the ξ direction is only assumed,

$$\Delta \hat{Q}_i = -\Delta t\left(\hat{E}^{n+1}_{i+1/2} - \hat{E}^{n+1}_{i-1/2} - \hat{S}_i\right) \tag{2.70}$$

$$\begin{aligned} \hat{E}^{n+1}_{i+1/2} &= \hat{E}^{n}_{i+1/2} + \Delta \hat{E}_{i+1/2} \\ \hat{E}^{n+1}_{i-1/2} &= \hat{E}^{n}_{i-1/2} + \Delta \hat{E}_{i-1/2} \end{aligned} \tag{2.71}$$

where $\hat{S}$ is the source term including the viscous terms, gravity term, and translational-vibrational relaxation term. In the MFGS method, $\Delta \hat{E}_{i+1/2}$ and $\Delta \hat{E}_{i-1/2}$ are described as

$$\Delta\hat{E}_{i+1/2} = \left(\hat{A}^{+}\Delta\hat{Q}\right)_i + \left(\hat{A}^{-}\Delta\hat{Q}\right)_{i+1}$$
$$\Delta\hat{E}_{i-1/2} = \left(\hat{A}^{+}\Delta\hat{Q}\right)_{i-1} + \left(\hat{A}^{-}\Delta\hat{Q}\right)_i \tag{2.72}$$

Here, $\hat{A}^{\pm}$ is approximately evaluated as follows:

$$\hat{A}^{\pm} = \frac{\hat{A} \pm \lambda\hat{E}}{2} \tag{2.73}$$

$$\hat{A} = \frac{\partial\hat{E}}{\partial\hat{Q}} \tag{2.74}$$

$$\lambda = u\xi_x + v\xi_y + w\xi_z + c\left|\nabla\xi\right| \tag{2.75}$$

where $\hat{A}$ is the Jacobian matrix, and λ is the spectral radius. In addition, $\left(\hat{A}^{\pm}\Delta\hat{Q}\right)_i$ can be approximately evaluated as follows:

$$\left(\hat{A}^{\pm}\Delta\hat{Q}\right)_i = \frac{\hat{E}\left(\hat{Q}_i + \Delta\hat{Q}_i\right) - \hat{E}\left(\hat{Q}_i\right) \pm \lambda_i\Delta\hat{Q}_i}{2} \tag{2.76}$$

Combining Eqs. (2.71) and (2.72),

$$\hat{E}^{n+1}_{i+1/2} - \hat{E}^{n+1}_{i-1/2} = \hat{E}^{n}_{i+1/2} - \hat{E}^{n}_{i-1/2} + \left(\hat{A}^{+}\Delta\hat{Q}\right)_i - \left(\hat{A}^{-}\Delta\hat{Q}\right)_i + \left(\hat{A}^{-}\Delta\hat{Q}\right)_{i+1} - \left(\hat{A}^{+}\Delta\hat{Q}\right)_{i-1} \tag{2.77}$$

Substituting Eq. (2.76) into Eq. (2.77),

$$\begin{aligned}\hat{E}^{n+1}_{i+1/2} - \hat{E}^{n+1}_{i-1/2} &= \hat{E}^{n}_{i+1/2} - \hat{E}^{n}_{i-1/2} + \lambda_i\Delta\hat{Q}_i - \frac{\lambda_{i+1}\Delta\hat{Q}_{i+1} + \lambda_{i-1}\Delta\hat{Q}_{i-1}}{2} \\ &+ \frac{\hat{E}\left(\hat{Q}_{i+1} + \Delta\hat{Q}_{i+1}\right) - \hat{E}\left(\hat{Q}_{i+1}\right)}{2} - \frac{\hat{E}\left(\hat{Q}_{i-1} + \Delta\hat{Q}_{i-1}\right) - \hat{E}\left(\hat{Q}_{i-1}\right)}{2}\end{aligned} \tag{2.78}$$

and assuming the isentropic flow, i.e., $\hat{Q}_{i+1} = \hat{Q}_{i-1} = \hat{Q}_i$,

$$\begin{aligned}\hat{E}^{n+1}_{i+1/2} - \hat{E}^{n+1}_{i-1/2} &= \hat{E}^{n}_{i+1/2} - \hat{E}^{n}_{i-1/2} + \lambda_i\Delta\hat{Q}_i - \frac{\lambda_{i+1}\Delta\hat{Q}_{i+1} + \lambda_{i-1}\Delta\hat{Q}_{i-1}}{2} \\ &+ \frac{\hat{E}\left(\hat{Q}_i + \Delta\hat{Q}_{i+1}\right) - \hat{E}\left(\hat{Q}_i + \Delta\hat{Q}_{i-1}\right)}{2}\end{aligned} \tag{2.79}$$

Substituting Eq. (2.79) into Eq. (2.70) and rearranging,

$$\begin{aligned}\left\{\frac{1}{\Delta t} + \lambda_i\right\}\Delta\hat{Q}_i &= \hat{S}_i - \left(\hat{E}^{n}_{i+1/2} - \hat{E}^{n}_{i-1/2}\right) - \frac{\hat{E}\left(\hat{Q}_i + \Delta\hat{Q}_{i+1}\right) - \lambda_{i+1}\Delta\hat{Q}_{i+1}}{2} \\ &+ \frac{\hat{E}\left(\hat{Q}_i + \Delta\hat{Q}_{i-1}\right) + \lambda_{i-1}\Delta\hat{Q}_{i-1}}{2}\end{aligned} \tag{2.80}$$

The discretized forms in the η and ζ directions can be obtained as in the same way described above. As can be seen from Eq. (2.80), $\Delta\hat{Q}_i$ can be calculated by scalar division without matrix inversion; this is the specific advantage of the MFGS method. In this study, the number of iteration is twice in one time step.

2.4 Solution-adapted grid generation

In order to precisely predict sonic boom intensity, there are three requirements for the computational grids. First, shock waves must not intersect with the grid lines; thus, the grid lines in the entire computational domain must align with the shock waves. Second, the grid resolution near the shock waves must be adequately high. Third, the number of grid points must be reduced as much as possible because the computational domain ranges over quite a long distance. For the requirements above, the method of constructing a solution-adapted grid in the entire computational domain is proposed [62, 87]. In this study, full-field simulation is performed to solve the flow fields around three axi-symmetric models: the N-Wave Model (NWM) [14] without the tail fins used in the D-SEND#1 flight test (Chapters 3 and 4), the

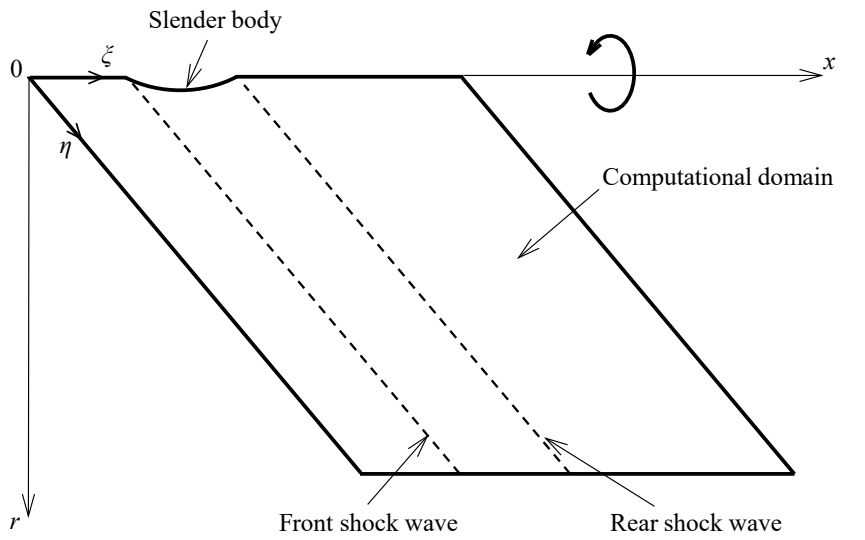

(a) Axi-symmetric slender body

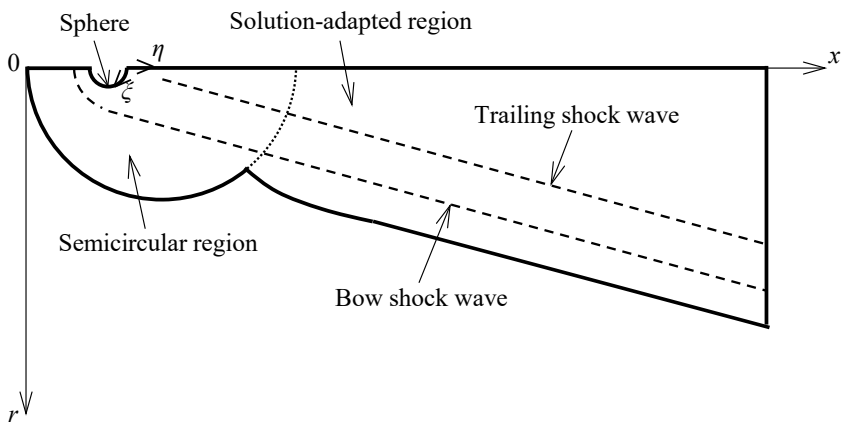

(b) Sphere

Fig. 2.1 Outline of entire computational grid.

axi-symmetric paraboloid (Chapter 5), and the sphere (Chapter 6). Thus, the computational grid is divided into two types for the axi-symmetric slender and spherical bodies. Figure 2.1 shows the outline of the solution-adapted grids. As shown in Fig. 2.1(a), the solution-adapted grid for the slender body is constructed to align the grid lines with the front and rear shock waves. As shown in Fig. 2.1(b), the solution-adapted grid for the sphere is composed of two regions. One is the semicircular region in the near filed around the sphere, where the outer boundary has a semicircular shape. The other is the solution-adapted region in the far-field, where the grid lines are aligned with the bow and trailing shock waves. The locations of the minimum grid spacing in the ξ direction are set as those of the shock waves. To reduce the computational load, the grid spacing in the η direction is increased as the distance from the axis of symmetry increases. The three-dimensional grid is basically constructed by rotating the two-dimensional grid around the axis of symmetry from 0° to –180°. However, the shock-wave angles depending on the atmospheric temperature change with altitude, and thus the two-dimensional solution-adapted grid on each rotational plane is constructed. The grid spacing in the rotational direction is equal regardless of the rotational direction and is increased with increasing radial distance.

The method of constructing the solution-adapted grid is the same in two-dimensional and three-dimensional grids as follows.

(i) A preliminary grid is constructed. Because the shock wave weakens as the distance from the axis of symmetry increases, the shock-wave angle in the far field approaches the Mach angle [88]:

$$\mu_M = \arcsin\frac{1}{M_\infty} \tag{2.81}$$

Thus, the grid angles of the initial grid in the far field are set as the Mach angle.

(ii) The preliminary computation is performed by the preliminary grid.

(iii) The locations of the shock waves are detected by the computational results. The locations can be identified as those of the extreme values of pressure or pressure gradient. As the identification method differs according to the object shape, the detailed method is described in each chapter.

(iv) The computational grid is reconstructed to align the grid lines with the shock waves, as shown in Fig. 2.2. When the computational grid for the slender body is reconstructed, the streamwise coordinate is only changed; i.e., the radial coordinate is not changed. To make the grid lines smooth, the grid angles in the far field are changed every five or ten points.

If the grid lines of the reconstructed grid are not close to those of the preliminary grid, they may not be precisely aligned with the shock waves. Thus, the computational grid is reconstructed several times, according to the above procedures. However, in this regard, the change in the grid angle is small in the far field excluding the near and caustic-vicinity fields, and the reconstruction in the far field is usually conducted only once.

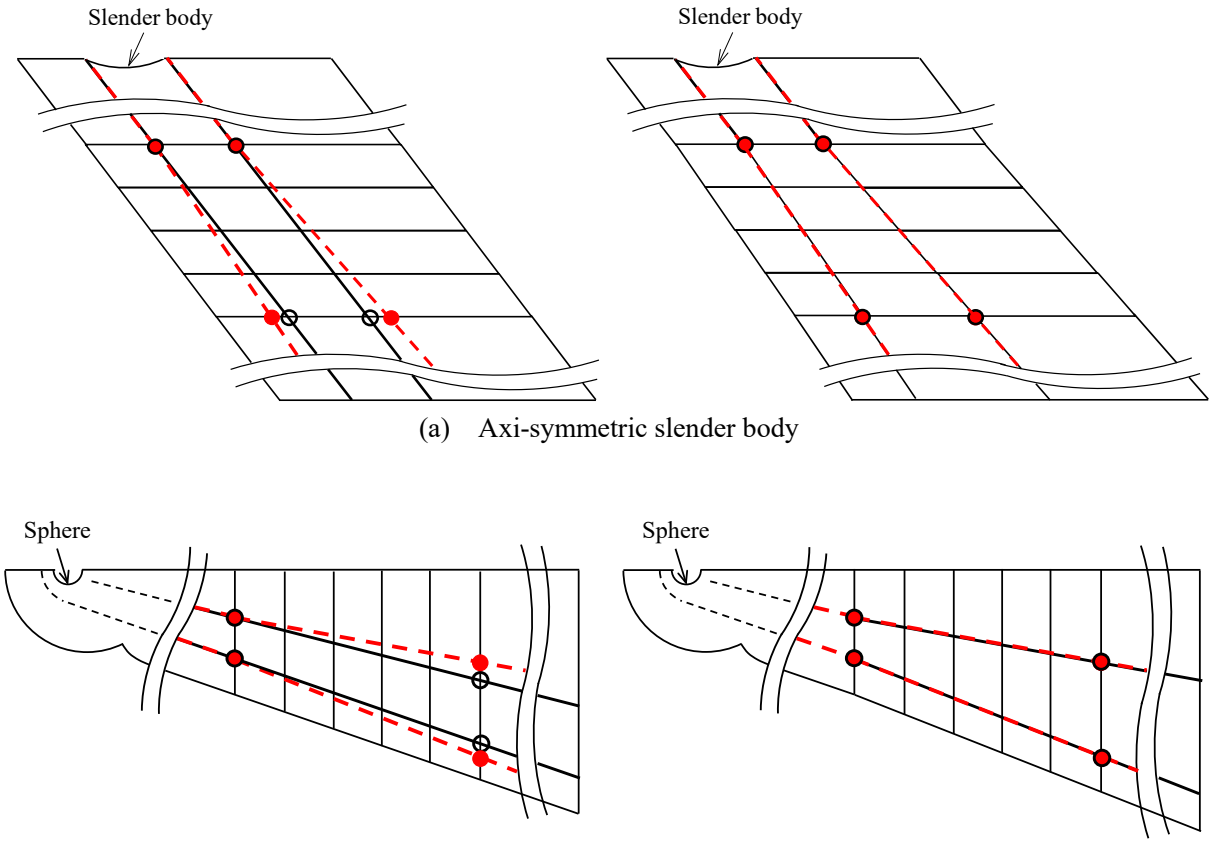

Fig. 2.2 Method of reconstructing solution-adapted grid, where black and red lines show grid lines and traces of shock waves, respectively (Left: preliminary grid, Right: reconstructed grid).

2.5 Segmentation of computational domain

As the computational domain of full-field simulation ranges over quite a long distance, the computational load must be reduced as much as possible. To improve the efficiency of computation, the computational domain is split into a sequence of subdomains. Figure 2.3 shows the outline of the subdomain and the extended region in the case of the slender body. When the subdomain (n) is computed, the extended region (n) is computed simultaneously to prevent the influence of the outer boundary condition in the subdomain (n). The distance of the extended region (n) is large enough to prevent the influence of the outer boundary condition from reaching the subdomain (n). The time step in each subdomain with the extended region is changed to perform the efficient computation and is decided by the preliminary computation. In the thermal nonequilibrium flow analysis, the relaxation time at low altitudes is too short to calculate the flow field in the long time step, even if the implicit algorithms for the time integration and the relaxation term are used. Thus, the time step is shortened as the altitude decreases.

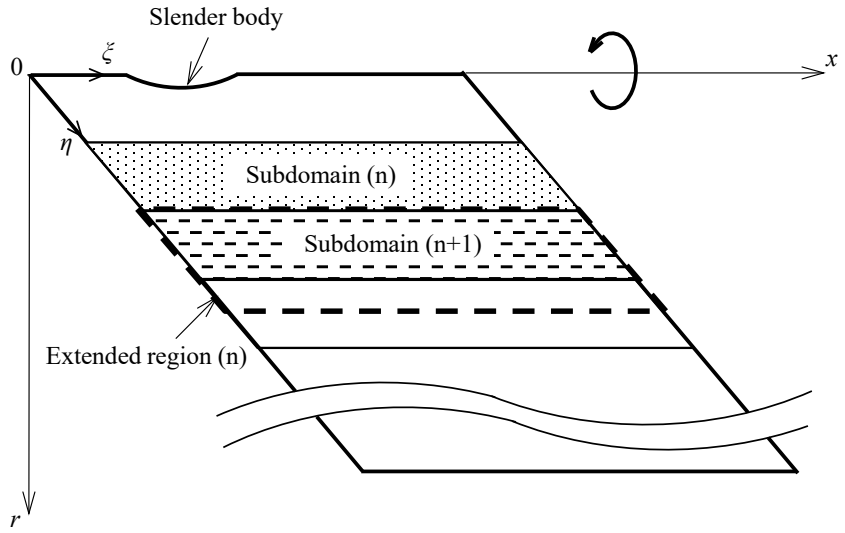

Fig. 2.3 Outline of subdomain and extended region in the case of slender body

2.6 Computational procedure

The computational procedure of full-field simulation is divided into two stages. First is the solution-adapted grid generation to align the grid lines with the shock waves. Second is the computation using the solution-adapted grid over the entire flow field. Figure 2.4 shows the flowchart of computational procedure for full-field simulation [61]. The computational procedure is as follows.

(i) The computational grid is set in the subdomain (n) with the extended region (n).

(ii) Numerical simulation is performed.

(iii) The applicability of the grid to the flow field is investigated. If the grid lines are not aligned with the shock waves, the solution-adapted grid is reconstructed as described in section 2.4, and the computation in the same subdomain is performed again.

(iv) The computational domain is moved to the next subdomain until the computation in the entire flow field is finished.

According to the above procedure, the solution-adapted grid in the entire flow field is constructed. Thereafter, the final computation is performed by the solution-adapted grid, according to the above procedure except for step (iii).

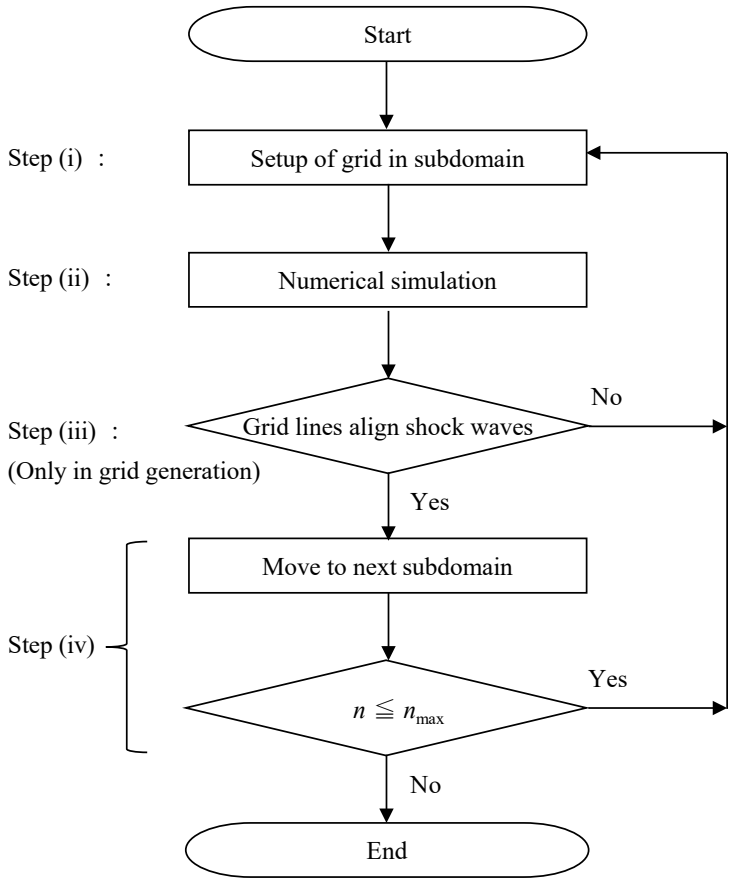

Fig. 2.4 Flowchart of computational procedure [61].

Chapter 3

Validation of Computational Accuracy

3.1 Outline of this chapter

In this chapter, the usefulness of full-field simulation is investigated as an approach to precisely predict sonic boom propagation through the real atmosphere. The first ever direct reproduction of the flight test for sonic boom is performed, and the simulation results are analyzed to investigate the effectiveness of the solution-adapted grid and the validity of the numerical correction method for considering atmospheric stratification. Moreover, the computational accuracy of full-field simulation is validated by comparison with the results of the waveform parameter method [45], which is a representative prediction method for sonic boom, and the D-SEND#1 flight test data [15]. The contents of this chapter were already published in [61, 89].

3.2 Computational methods

3.2.1 Computational conditions

Computational model

A simple computational model is suitable not only for the simplicity of the analysis, but also for reducing the computational load, and the accuracy of full-field simulation should be validated by comparison with the flight test data. Thus, the computational model was set as the N-Wave Model (NWM) [15], which was one of the D-SEND#1 flight test models designed by JAXA. Figure 3.1 shows the configuration of the NWM without the tail fins. The length of the body is L = 5.6 m. To reduce the computational load, the tail fins attached to the NWM were excluded in the full-field simulation, and the model was considered as an axi-symmetric body. Although the tail fins were expected to hardly affect the far-field waveform, the influence of these fins should be investigated in the future work.

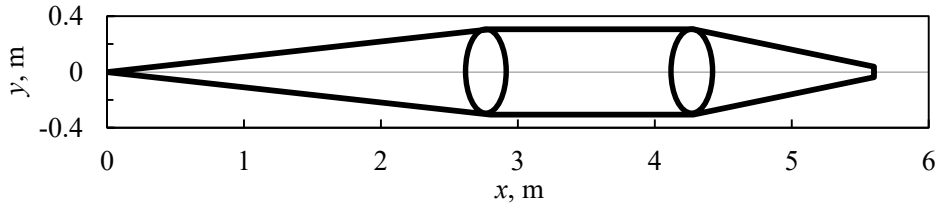

Fig. 3.1 N-Wave Model (NWM) without tail fins.

Flight conditions

The computational conditions were set in accordance with the conditions of the D-SEND#1 flight test. The flight Mach number was $M_\infty = 1.43$, and the flight altitude was $h = 6{,}039$ m. Although the D-SEND#1 flight tests were conducted in free fall as shown in Fig. 3.2(a), a steady level flight was assumed in full-field simulation as shown in Fig. 3.2(b) [61], because of the following reason: it is convenient for the simulation to assume the equivalent condition, in which a stationary body exists in a supersonic flow and the wave propagation is affected by atmospheric stratification in the same way as in the free fall case. When the flight Mach number was approximately 1.4, the ray path in free fall was approximately 45° to the direction of the free fall, and that in the level flight was approximately 45° to the flight direction. Therefore, the ray path to the observation point in the free fall was almost equivalent to that in the level flight beneath the flight object, and atmospheric stratification had the same effect on the wave propagation. The validity of this assumption is described in section 3.2.6.

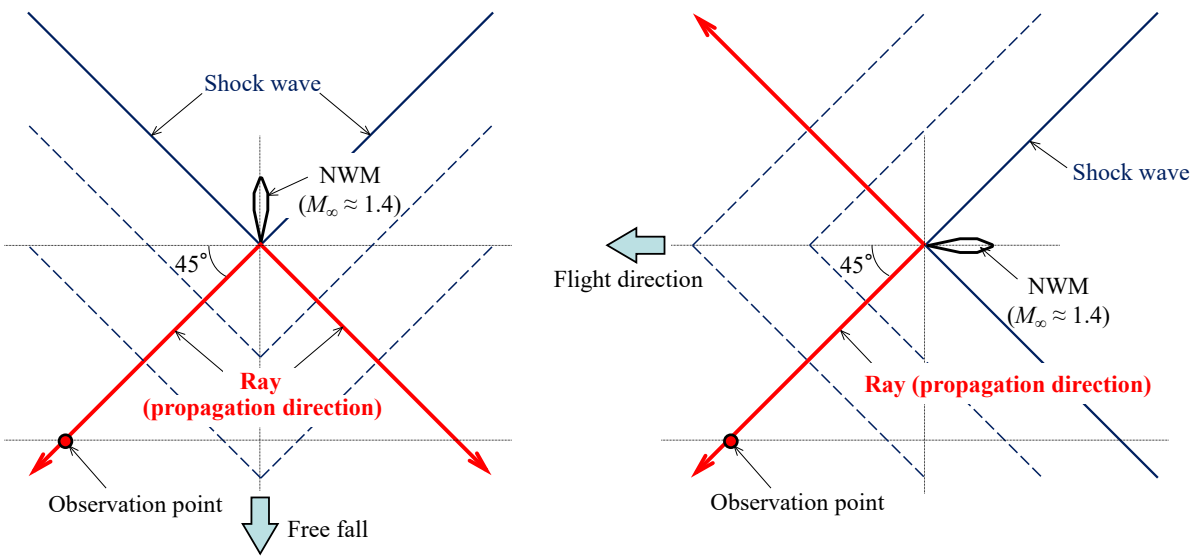

(a) Free fall (D-SEND#1 flight test) (b) Level flight (full-field simulation)

Fig. 3.2 Analogy between free fall and level flight when flight Mach number is approximately 1.4.

Atmospheric conditions

Figure 3.3 shows the atmospheric model [89] and the meteorological data [15] observed in the D-SEND#1 flight test. The atmospheric model was based on the meteorological data and was similar to the ISO standard atmosphere [82], except for the temperature lapse rate and the location of the change in its rate. The atmospheric temperature was set as

$$T_a = T_0 - \beta h \quad (h \le 6.75km) \tag{3.1}$$

$$T_a = const \quad (h \ge 6.75km) \tag{3.2}$$

where subscript a denotes the atmospheric property. The atmospheric temperature at the ground is T_0 = 275.95 K, and the temperature lapse rate is β = 7.2 km/K. The unit of h is kilometer. The atmospheric pressure and density were calculated by the equation of the state of ideal gas as

$$p_a = \rho_a R T_a \tag{3.3}$$

and the hydrostatic equation as

$$\frac{dp_a}{dh} = -g\rho_a \tag{3.4}$$

Consequently, the atmospheric pressure was obtained as follows:

$$\frac{p_a}{p_0} = \left(\frac{T_a}{T_0}\right)^{\frac{g}{\beta R}} \quad (h \le 6.75km) \tag{3.5}$$

$$\frac{p_a}{p_c} = \exp\left(-\frac{g}{RT_c}(h - 6.75)\right) \quad (h \ge 6.75km) \tag{3.6}$$

where the atmospheric pressure at the ground is p_0 = 101.25 kPa. Subscript c denotes the atmospheric property at h = 6.75 km, where the temperature lapse rate β changes. The relative humidity at each altitude was set as the linearly-interpolated value of the meteorological data. Figures 3.4 shows the relaxation time

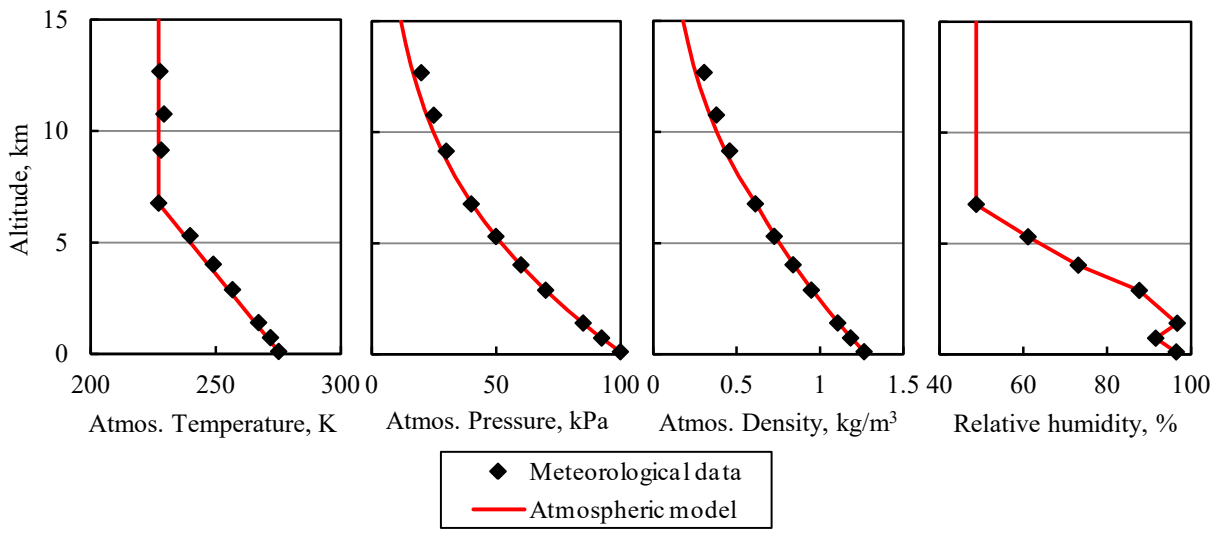

Fig. 3.3 Atmospheric model based on meteorological data.

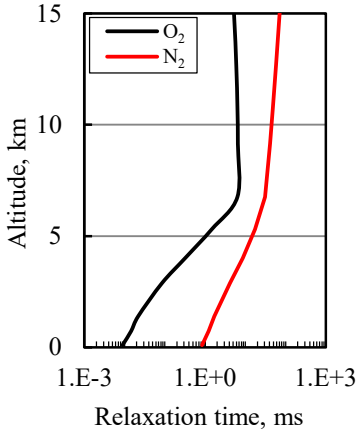

Fig. 3.4 Relaxation time in atmospheric condition.

Table 3.1 Computational conditions

	Case A	Cases B–D
Computational model	NWM (L = 5.6 m)	
Flight Mach number	M_∞ = 1.43	
Flight altitude	h = 6.039 km	
Flight condition	Steady level flight	
Atmosphere	Uniform	Stratification
Computational domain	r/L = 0–1090	

in the atmospheric conditions, which are calculated by the Bass et al.'s formula [74] given by Eqs. (2.12) and (2.13). As can be seen in Fig. 3.4, the relaxation time at low altitudes shortens as the altitude decreases, and the relaxation time of N_2 is longer than that of O_2 in the entire domain. When axi-symmetric analysis assuming the uniform atmosphere was performed, the atmospheric conditions were set as the uniform properties of atmosphere at the flight altitude.

Table 3.1 shows the computational conditions. The flow solver in each case and the computational domain are explained in sections 3.2.2 and 3.2.3, respectively.

3.2.2 Flow solver

The four types of governing equations were solved to analyze the effectiveness of the solution-adapted method described in section 2.4 of chapter 2, the validity of the numerical correction method for considering atmospheric stratification described in section 2.3.4 of chapter 2, and the accuracy of full-field simulation including the reproducibility of all physical effects that are considered in this study.

Equation A: Axi-symmetric Euler equations

Sonic boom propagation through the uniform atmosphere was analyzed by solving the axi-symmetric Euler equations as

$$\frac{\partial Q}{\partial t}+\frac{\partial E}{\partial x}+\frac{\partial F}{\partial r}+H=0 \tag{3.7}$$

$$Q=\begin{bmatrix}\rho\\ \rho u\\ \rho v\\ e\end{bmatrix}, E=\begin{bmatrix}\rho u\\ \rho u^2+p\\ \rho uv\\ (e+p)u\end{bmatrix}, F=\begin{bmatrix}\rho v\\ \rho uv\\ \rho v^2+p\\ (e+p)v\end{bmatrix}, H=\begin{bmatrix}\rho v/r\\ \rho uv/r\\ \rho v^2/r\\ (e+p)v/r\end{bmatrix} \tag{3.8}$$

$$e=\frac{\rho RT}{\gamma-1}+\frac{\rho}{2}\left(u^2+v^2\right) \tag{3.9}$$

where geometrical spreading and nonlinearity are considered. The accuracy of simulation, including the effectiveness of the two-dimensional solution-adapted method, is investigated by comparison with the result of the waveform parameter method.

Equation B: Three-dimensional Euler equations with gravity term

Sonic boom propagation through the stratified atmosphere was analyzed by solving the three-dimensional Euler equations with the gravity term as

$$\frac{\partial Q}{\partial t}+\frac{\partial E}{\partial x}+\frac{\partial F}{\partial y}+\frac{\partial G}{\partial z}=S_G \tag{3.10}$$

$$Q=\begin{bmatrix}\rho\\ \rho u\\ \rho v\\ \rho w\\ e\end{bmatrix}, E=\begin{bmatrix}\rho u\\ \rho u^2+p\\ \rho uv\\ \rho uw\\ (e+p)u\end{bmatrix}, F=\begin{bmatrix}\rho v\\ \rho uv\\ \rho v^2+p\\ \rho vw\\ (e+p)v\end{bmatrix}, G=\begin{bmatrix}\rho w\\ \rho uw\\ \rho vw\\ \rho w^2+p\\ (e+p)w\end{bmatrix}, S_G=\begin{bmatrix}0\\ 0\\ \rho g\\ 0\\ \rho g v\end{bmatrix} \tag{3.11}$$

$$e=\frac{\rho RT}{\gamma-1}+\frac{\rho}{2}\left(u^2+v^2+w^2\right) \tag{3.12}$$

where atmospheric stratification in addition to geometrical spreading and nonlinearity are considered. The accuracy of simulation, including the effectiveness of the three-dimensional solution-adapted method and the validity of the numerical correction method, is investigated by comparison with the result of the waveform parameter method.

Equation C: Three-dimensional Euler equations with gravity term and thermal nonequilibrium

In order to evaluate the perceived loudness of sonic boom, the rise time of sonic boom must be predicted. In the case of full-field simulation based on the CFD, a shock wave is considered as a discontinuity; i.e., the thickness of the shock wave that is of the order of several mean free paths cannot be resolved. However, because the shock wave significantly weakens with the propagation distance from a generation source, that in the far field is almost the same as a compression wave without a discontinuity. In addition, the molecular relaxation, i.e., thermal nonequilibrium mainly affects the weak shock wave on the length scale much larger than the mean free path, resulting in the formation of rise time. Therefore, the rise time of sonic boom can be analyzed by full-field simulation with the thermal nonequilibirium. With that in mind, the inviscid, thermal nonequilibrium flow analysis in the stratified atmosphere was performed by solving the following equations:

$$\frac{\partial Q}{\partial t}+\frac{\partial E}{\partial x}+\frac{\partial F}{\partial y}+\frac{\partial G}{\partial z}=S_G+S_W \tag{3.13}$$

$$Q=\begin{bmatrix}\rho\\ \rho u\\ \rho v\\ \rho w\\ e\\ e_{vO_2}\\ e_{vN_2}\end{bmatrix},E=\begin{bmatrix}\rho u\\ \rho u^2+p\\ \rho uv\\ \rho uw\\ (e+p)u\\ e_{vO_2}u\\ e_{vN_2}u\end{bmatrix},F=\begin{bmatrix}\rho v\\ \rho uv\\ \rho v^2+p\\ \rho vw\\ (e+p)v\\ e_{vO_2}v\\ e_{vN_2}v\end{bmatrix},G=\begin{bmatrix}\rho w\\ \rho uw\\ \rho vw\\ \rho w^2+p\\ (e+p)w\\ e_{vO_2}w\\ e_{vN_2}w\end{bmatrix},S_G=\begin{bmatrix}0\\ 0\\ \rho g\\ 0\\ \rho gv\\ 0\\ 0\end{bmatrix},S_W=\begin{bmatrix}0\\ 0\\ 0\\ 0\\ 0\\ w_{vO_2}\\ w_{vN_2}\end{bmatrix} \tag{3.14}$$

$$e=\frac{\rho RT}{\gamma-1}+e_{vO_2}+e_{vN_2}+\frac{\rho}{2}\left(u^2+v^2+w^2\right) \tag{3.15}$$

where molecular relaxation in addition to geometrical spreading, nonlinearity, and atmospheric stratification are considered.

Equation D: Three-dimensional Navier-Stokes equations with gravity term and thermal nonequilibrium (full three-dimensional equations)

It is thought that not only the molecular relaxation but also the viscosity affects the rise time of sonic boom. Hence, the viscous, thermal nonequilibrium flow analysis in the stratified atmosphere was performed by solving the following equations:

$$\frac{\partial Q}{\partial t}+\frac{\partial E}{\partial x}+\frac{\partial F}{\partial y}+\frac{\partial G}{\partial z}=\frac{\partial E_v}{\partial x}+\frac{\partial F_v}{\partial y}+\frac{\partial G_v}{\partial z}+S_G+S_W \tag{3.16}$$

$$E_v = \begin{bmatrix} 0 \\ \tau_{xx} \\ \tau_{xy} \\ \tau_{xz} \\ \beta_x \\ 0 \\ 0 \end{bmatrix}, F_v = \begin{bmatrix} 0 \\ \tau_{yx} \\ \tau_{yy} \\ \tau_{yz} \\ \beta_y \\ 0 \\ 0 \end{bmatrix}, F_v = \begin{bmatrix} 0 \\ \tau_{zx} \\ \tau_{zy} \\ \tau_{zz} \\ \beta_z \\ 0 \\ 0 \end{bmatrix} \tag{3.17}$$

$$e = \frac{\rho RT}{\gamma - 1} + e_{vO_2} + e_{vN_2} + \frac{\rho}{2}\left(u^2 + v^2 + w^2\right) \tag{3.18}$$

where Q, E, F, G, S_G, and S_W are given by Eq. (3.14). In Eq. (3.16), all physical effects that are considered in this study are included. However, viscosity is assumed to hardly affect sonic boom waveforms except for the rise time, and the rise time is not formed when the shock wave is strong in the near field. Thus, for reducing the computational load, the viscous terms were not considered in the near field around the body (i.e., subdomain (0) described in section 3.2.3). The accuracy of the thermal nonequilibrium flow analysis, including the rise time, is investigated by comparison with the D-SEND#1 flight test data.

Table 3.2 shows physical effects included in each case where the different governing equations were solved. The computational approach of solving the governing equations is explained in section 2.3 of chapter 2.

Table 3.2 Physical effects that are considered in each case

	Case A	Case B	Case C	Case D
Governing equation	Equation A	Equation B	Equation C	Equation D
Geometrical spreading	✓	✓	✓	✓
Nonlinearity	✓	✓	✓	✓
Atmospheric stratification	–	✓	✓	✓
Molecular relaxation	–	–	✓	✓
Viscosity	–	–	–	✓

3.2.3 Computational domain

Figure 3.5 shows the outline of the entire computational domain around the NWM. The computational domain was set from r/L = 0 to 1090 (r = 0 m to 6,104 m). To reduce the computational load, the computational domain in the radial direction was split into several subdomains with extended regions (see section 2.5 of chapter 2 for details). Table 3.3 shows the range of the subdomains with the extended regions. In the case of stratified atmosphere, the boundary condition at the surface of the body must be evaluated by considering the change caused by atmospheric stratification and the fluctuation caused by waves in the

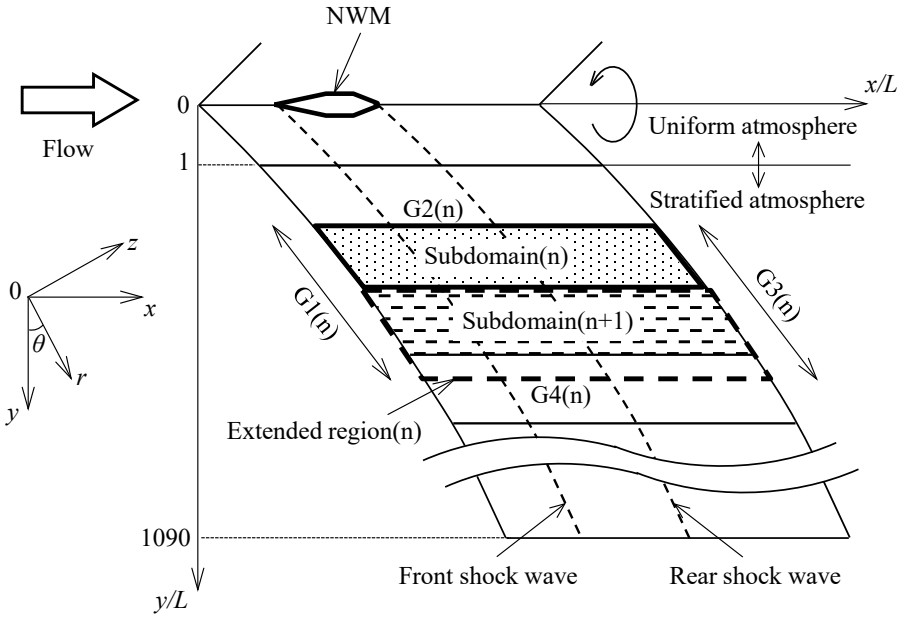

Fig. 3.5 Outline of entire computational domain around NWM.

Table 3.3 Range of subdomain(n) with extended region(n)

Atmosphere	n	*r/L*
Uniform	0	0–10.0
	1	1.0–15.5
	2	5.0–21.3
Case A: Uniform	3	10.0–24.4
Cases B – D: Stratification	4	13.8–30.0
	5	20.0–40.0
	6–110	30–50, 40–60, …, 1070–1090

compressible fluid. However, these two terms cannot be distinguished, and simple extrapolation such as that used in the unstratified atmosphere is not necessarily adequate. To improve this problem, the uniform atmosphere at the flight altitude was assumed for the near field around the NWM, i.e., the subdomain (0) with the extended region (0). Assuming the uniform atmosphere, axi-symmetric analysis instead of three-dimensional analysis can be performed and is suitable for reducing the computational load. Therefore, axi-symmetric analysis was performed in the subdomain (0) with the extended region (0).

3.2.4 Boundary conditions

Slip and isothermal wall boundary conditions

The surface of the body was treated as the slip and isothermal boundary conditions:

$$\begin{aligned} \vec{U}_{j=1} &= \left[\left(2\vec{U}_{j=2} - \vec{U}_{j=3}\right)\cdot\vec{t}\right]\cdot\vec{t} \\ p_{j=1} &= p_{j=2} \\ T_{j=1} &= T_{vO_2,j=1} = T_{vN_2,j=1} = T_\infty \end{aligned} \tag{3.19}$$

where $\vec{U}$ is the velocity vector, and $\vec{t}$ is the unit vector tangential to the surface of the body. Subscript ∞ denotes the freestream value at the flight altitude, and subscript $j = 1$ denotes the index of grid points at the surface of the body. The density was calculated by the equation of the state of ideal gas given by Eq. (2.8).

Axi-symmetric boundary conditions

The axi-symmetric boundary at $r = 0$ was treated as the axi-symmetric boundary conditions:

$$Q_{j=1} = Q_{j=2}\text{, but } v_{j=1} = 0 \tag{3.20}$$

Freestream boundary conditions

G1(n) and G4(n) shown in Fig. 3.5 were treated as the freestream boundary conditions:

Uniform atmosphere:

$$\begin{aligned} u &= u_\infty \\ v &= 0 \\ w &= 0 \\ p &= p_\infty \\ T &= T_{vO_2} = T_{vN_2} = T_\infty \end{aligned} \tag{3.21}$$

Stratified atmosphere:

$$\begin{aligned} u &= u_\infty \\ v &= 0 \\ w &= 0 \\ p &= p_a(h) \\ T &= T_{vO_2} = T_{vN_2} = T_a(h) \end{aligned} \tag{3.22}$$

In the case of stratified atmosphere, the boundary condition at G4(n), as well as the surface of the body, must be set by considering the change caused by atmospheric stratification and the fluctuation caused by waves in the compressible fluid. However, these two terms cannot be distinguished by simple extrapolation such as that used in the unstratified atmosphere and nonreflective boundary conditions [91]. Therefore,

G4(n) was treated as the freestream boundary conditions, and the extended region (n) was simultaneously computed when the subdomain (n) was computed. The radial distance of the extended region (n) was large enough to prevent the influence of the boundary conditions at G4 (n) from reaching the subdomain (n). In the D-SEND#1 flight test [14], the pressure waveforms were obtained at h = 500 m, and thus the pressure signal observed in the flight test was not affected by the ground reflection. Therefore, the ground reflection was not considered in the simulation.

Outflow boundary conditions

G3(n) was evaluated by the zeroth-order extrapolation as

$$Q_{i=i\max} = Q_{i=i\max-1} \tag{3.23}$$

where subscript $i = i\max$ denotes the index of grid points at G3(n).

Interpolating boundary conditions

G2(n) excluding G2(0) was treated as the interpolating boundary conditions:

Uniform atmosphere:

$$Q_n = Q_{n-1} \tag{3.24}$$

Stratified atmosphere:

$$\begin{aligned} u_n &= u_{n-1} \\ v_n &= v_{n-1} \\ w_n &= w_{n-1} \\ p_n &= p_a(h) + \Delta p_{n-1} \\ T_n &= T_a(h) + \Delta T_{n-1} \\ T_{vO_2,n} &= T_a(h) + \Delta T_{vO_2,n-1} \\ T_{vN_2,n} &= T_a(h) + \Delta T_{vN_2,n-1} \end{aligned} \tag{3.25}$$

where Δp, ΔT, ΔT_{vO_2}, and ΔT_{vN_2} are the fluctuation components from the freestream conditions. Subscript n denotes the subdomain's number.

Plane-symmetric boundary conditions

The fluxes on the x-y plane were calculated, and the plane-symmetric boundary conditions were set as follows:

$$\begin{aligned} Q_{k=1} &= Q_{k=3}, \text{ but } \; w_{k=1} = -w_{k=3} \\ Q_{k=k\max} &= Q_{k=k\max-2}, \text{ but } \; w_{k=k\max} = -w_{k=k\max-2} \end{aligned} \tag{3.26}$$

where subscripts $k = 2$ and $k\max-1$ denote the indexes of grid points on the x-y plane.

3.2.5 Computational grid and computational load

Figure 3.6 and 3.7 show the two-dimensional and three-dimensional computational grids, respectively, in the near field around the NWM. The computational grids were constructed to align the grid lines with the front and rear shock waves, as described in section 2.4 of chapter 2. The locations of the front and rear shock waves were identified as those of the highest and second-highest pressure gradients in the streamwise directions, respectively. The minimum grid spacing in the streamwise direction was 5.6 mm at the locations of the front and rear shock waves, and that in the radial direction was 5.6 mm at the surface of the body. The grid spacing in the radial direction was increased with the radial distance in the region of $r/L < 30$, and that normalized by the length of the body was 2 in the region of $r/L > 30$. To make the grid lines smooth, the grid angles in the far field were changed when the radial distance normalized by the length of the body was increased by at least 10. Table 3.4 shows the number of grid points. In the Cases A to C, the Grids 2A and 3A were constructed according to the procedure described in sections 2.4 and 2.6 of chapter 2. In the Case D, the Grid 3A obtained in the Case C was used because the viscosity was assumed to hardly affect the sonic boom waveform excluding the rise time. The grid convergence in the Cases A and C was confirmed by comparison with results using grids with twice the number of the Grid 2A or 3A. Computational grids except for these two were constructed by adding the internal dividing points to the Grid 2A or 3A. Table 3.5 shows the grid convergence. As can be seen in Table 3.5, the grid convergence was adequate for evaluating the pressure rise of the front shock wave.

The full-field simulation was performed by the HITACHI SR16000 System (yayoi) [92] in the Information Technology Center, The University of Tokyo. The performance of the processor is 980.48 GFlops per node, and one node was used. Table 3.6 shows the computational time when the Grids 2A and 3A were used.

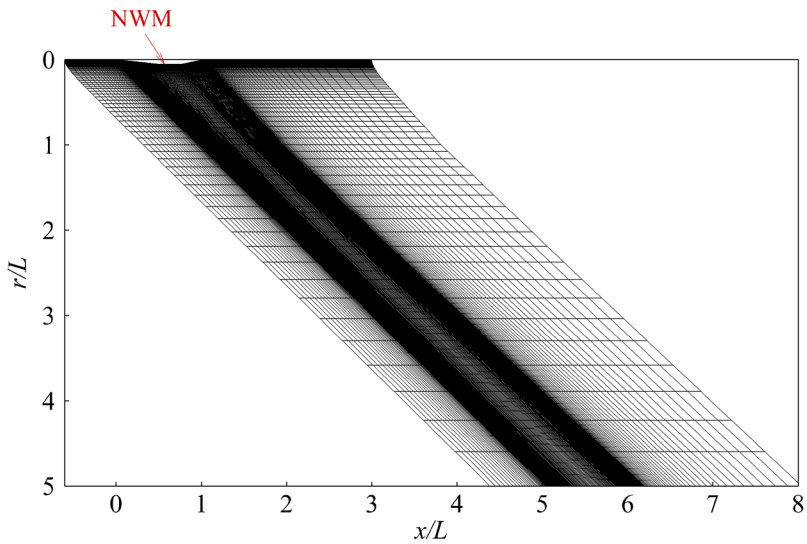

Fig. 3.6 Two-dimensional solution-adapted grid in the near field (CaseA).

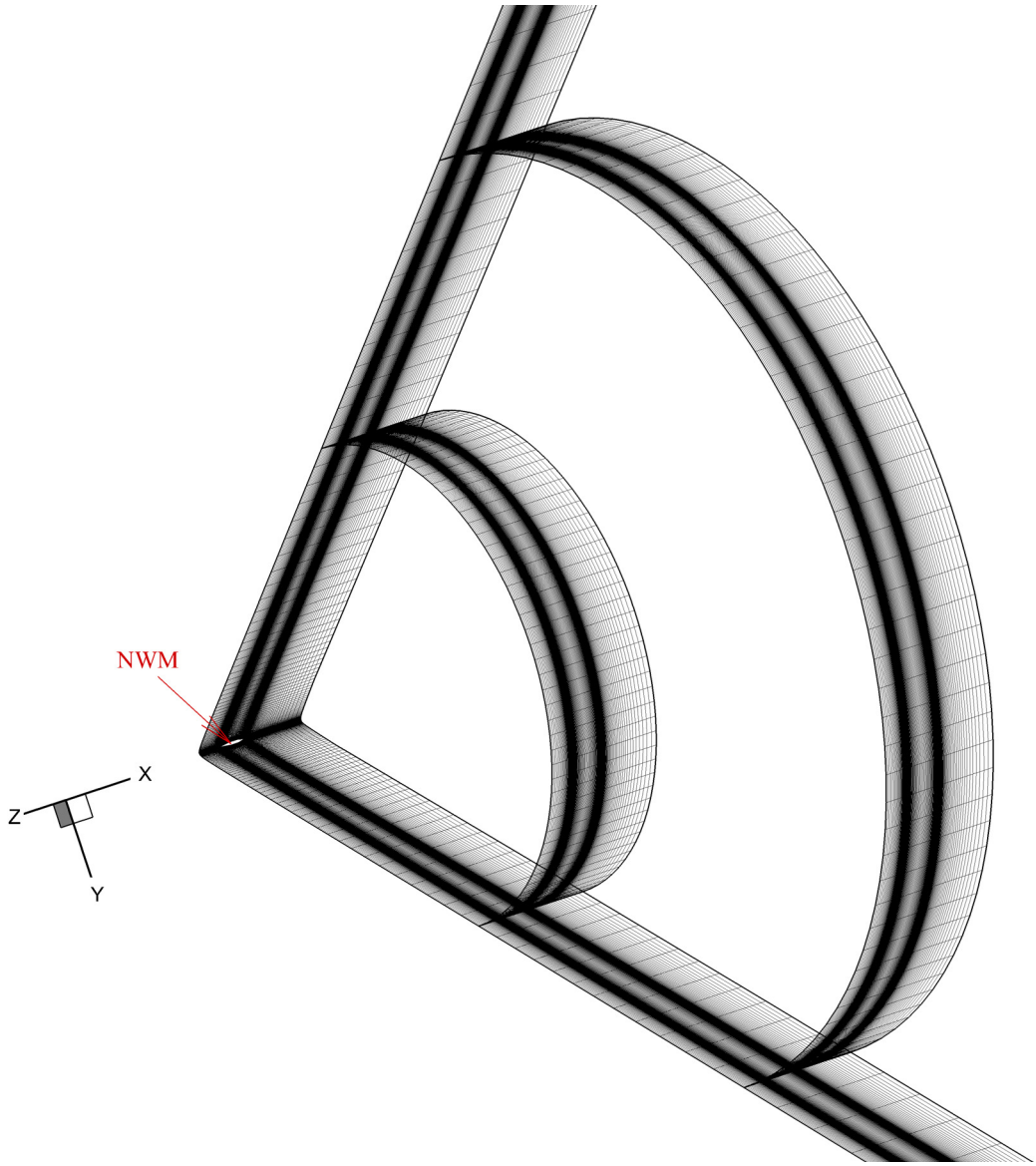

Fig. 3.7 Three-dimensional solution-adapted grid in the near field (Case B).

Table 3.4 Number of grid points

Solver	Grid name	Streamwise direction	Radial direction	Rotational direction
2D (axi-symmetric)	Grid 2A	231	641	–
	Grid 2B	461	641	–
	Grid 2C	231	1281	–
3D	Grid 3A	231	641	53
	Grid 3B	461	641	53
	Grid 3C	231	1281	53
	Grid 3D	231	641	103

Table 3.5 Difference in pressure rise of front shock wave relative to Grid 2A or 3A

Location	Grid name	Case A	Case C
$r/L = 1$	Grid 2B	1.7 %	–
	Grid 2C	2.0 %	–
$r/L = 1078$ ($\theta = 0°$)	Grid 2B or 3B	1.3 %	0.4 %
	Grid 2C or 3C	0.02 %	0.04 %
	Grid 3D	–	0.2 %

Table 3.6 Computational time in Grids 2A and 3A

	Case A	Case B	Case C	Case D
Solution-adapted grid generation	3.5 h	23 h	47 h	–
Final computation	1.5 h	20 h	42 h	43 h

3.2.6 Waveform parameter method

To validate the accuracy of simulation, the sonic boom prediction was also conducted by the waveform parameter method [45], which is a representative prediction method for sonic boom. In this method, the pressure fluctuation is derived from the conservation of the Blokhintsev energy invariant in the geometric acoustics, and the nonlinear effect on the waveform distortion is considered by the isentropic wave theory. The detailed explanation of this method is described in Appendix. In this study, the sonic boom predictions in the uniform and stratified atmospheres were conducted to validate the accuracy of simulation in the Cases A and B. Thus, the flight and atmospheric conditions were set as those used in the Cases A and B. The location of the input waveforms was set to $r/L = 10$. Comparing the results obtained from an input waveform at $r/L = 5$ with those from the input waveform at $r/L = 10$, the difference in the pressure rise of the front shock wave at $r/L = 1078$ was less than 0.1 % in the Cases A and B. Thus, the results of the waveform parameter method hardly depended on the location of the input waveform.

The validity of the assumption of the level flight instead of the free fall, as described in section 3.2.1, was investigated by the waveform parameter method, in which the flight and atmospheric conditions other than the flight direction were the same as those used in the Case B, and the location of the input pressure waveform was set to $r/L = 10$. Consequently, in the case of level flight relative to free fall, the pressure rise of the front shock wave beneath the body at $h = 500$ m increased by 2.0 %, and the intervals between the front and rear shock waves decreased by 0.6 %. Therefore, the assumption of the level flight instead of the free fall had the negligible effect on the far-field waveform.

3.3 Computational results

Simulation results obtained from Grids 2A and 3A are analyzed in this section because the grid convergence was already confirmed in section 3.2.5. To validate the accuracy of full-field simulation, the pressure waveforms of the simulation are compared with those of the waveform parameter method (WPM) and the D-SEND#1 flight test [15].

3.3.1 Pressure fluctuation in the near field

Figures 3.8 and 3.9 show the two-dimensional and three-dimensional distributions of the pressure fluctuation Δp in the near fields around the body in the Case B, respectively. The distributions in the near fields were the same in all cases, where the different governing equations were solved. Physical phenomena around the NWM were composed of six waves: the shock waves at the leading and trailing edges, the expansion waves at the front and rear ends of the cylindrical part of the body, the compression waves at the front cone, and the compression waves for the pressure restoration between the expansion waves.

Figure 3.10 shows the pressure waveforms at r/L = 10 in the Cases A and D, where the horizontal axis represents the relative time calculated by the streamwise distance from the front shock wave and the flight velocity. The relative time is set to zero when the pressure fluctuation becomes the tenth part of the pressure rise of the front shock wave. As shown in Fig. 3.10, the pressure fluctuation is caused by the six waves generated from the body, and the waveform shape is the same in Cases A and D. Therefore, it can be seen that the atmospheric stratification, molecular relaxation and viscosity hardly affect the near-field waveforms.

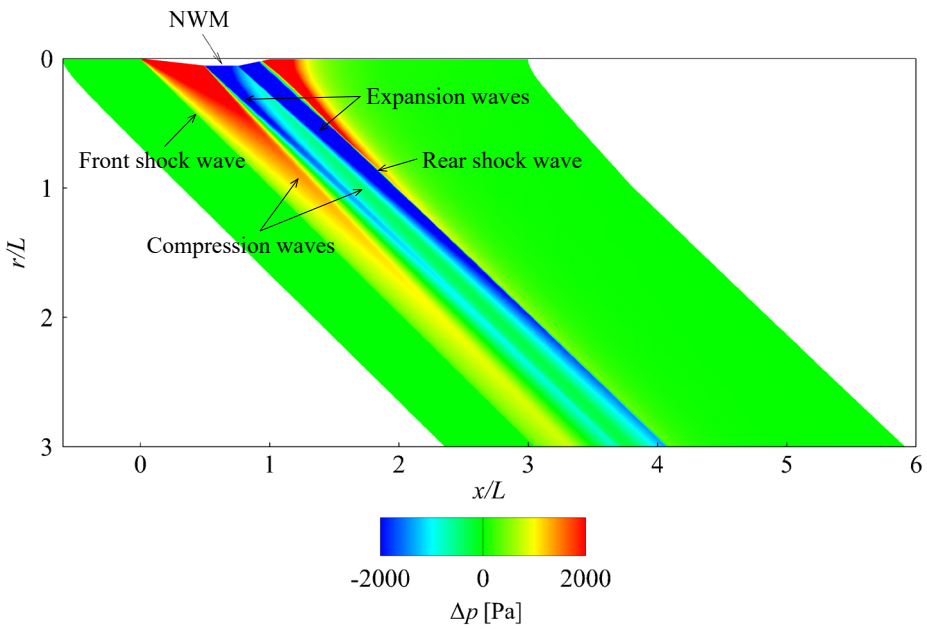

Fig. 3.8 Two-dimensional pressure distribution in the near field (Case B).

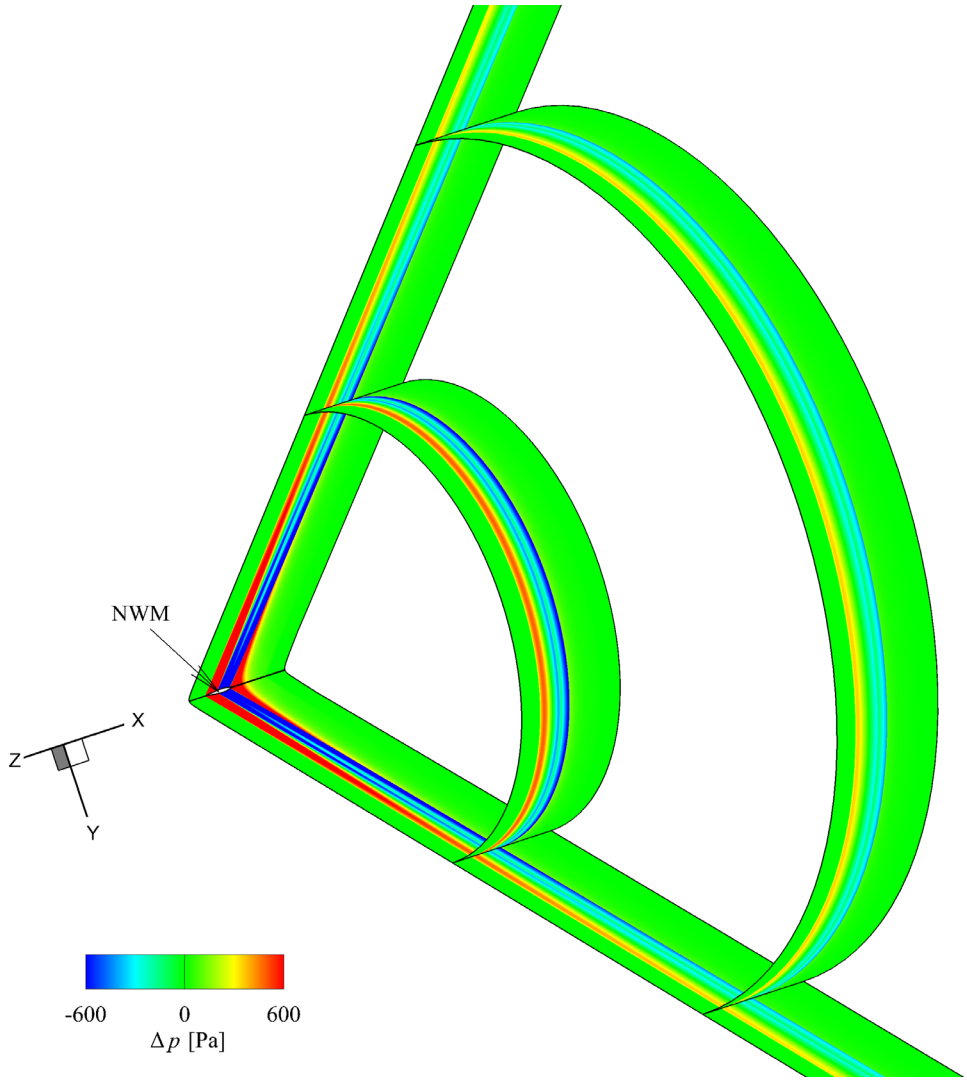

Fig. 3.9 Three-dimensional pressure distribution in the near field (Case B).

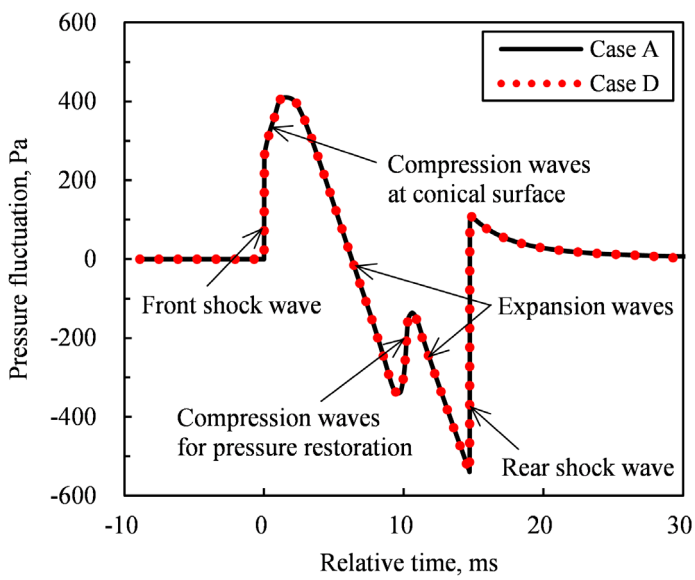

Fig. 3.10 Pressure waveforms at *r*/*L* = 10 on the symmetry plane beneath the body.

3.3.2 Three-dimensional shock-wave configuration

Figure 3.11 shows the distributions of the pressure rise Δp_{max} at the front shock-wave surface in the Case B. In Fig. 3.11(a), the distribution is described from $\theta = 0°$ to 360°, considering the symmetry with respect to the *x-y* plane. The change in pressure rise at an altitude of 6,750 m is influenced by the change in the atmospheric temperature gradient, as shown in Fig. 3.3. However, because the change increases with increasing the horizontal distance from the *x-y* plane, it is assumed to be caused by numerical errors resulting from the low grid resolution in the rotational direction around the body axis. Although the grid resolution must be improved to analyze the region including the local change in the atmospheric properties, the change is assumed to have little effect on the sonic boom propagation under the body. As shown in Fig. 3.11, the full-field simulation successfully reproduces sonic boom propagation through the real atmosphere, because of the following reason: the shock-wave configuration distorted by atmospheric stratification with altitude is captured, although it is close to the Mach cone. In addition, the pressure rise in the upward direction decreases rapidly, whereas that in the downward direction decreases slowly because the atmospheric pressure increases with decreasing altitude, and the convergence of the rays strengthens as the atmospheric temperature and the shock-wave angle increase toward the ground. These results show that the

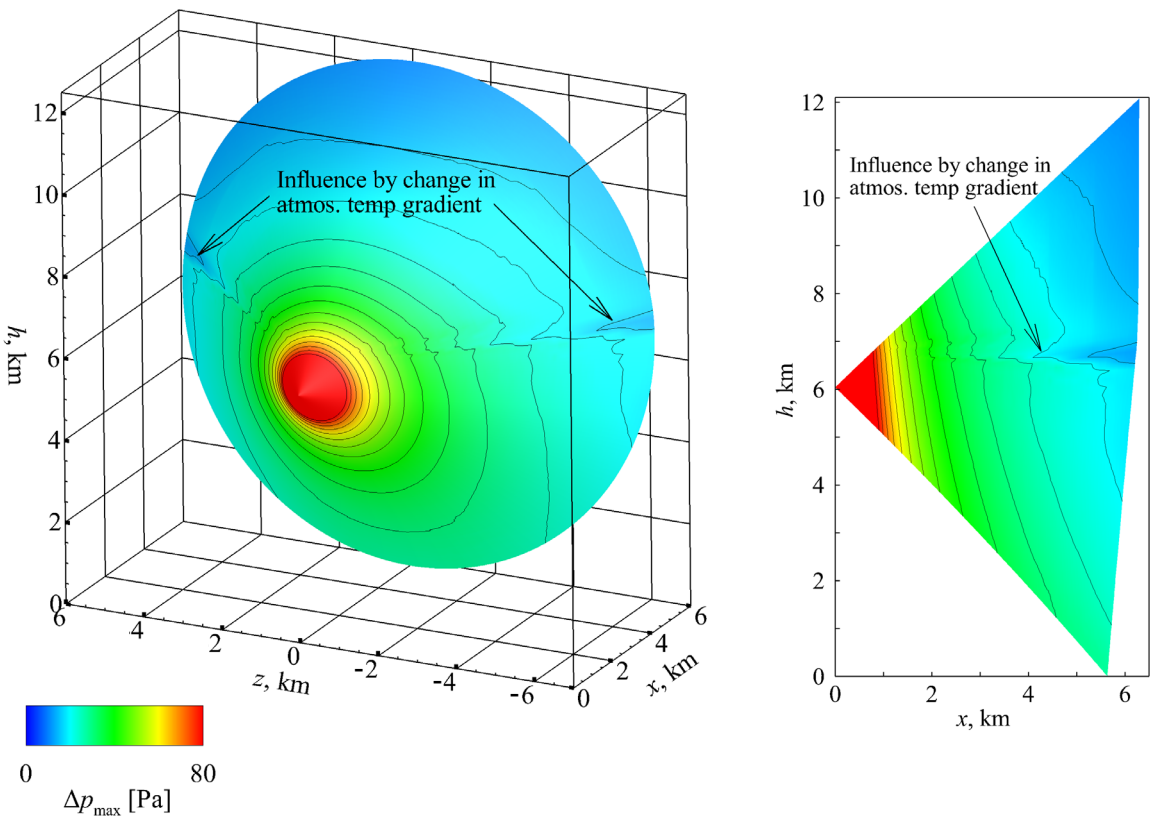

(a) Three-quarter view (b) Side view

Fig. 3.11 Pressure rise distributions at front shock-wave surface (Case B).

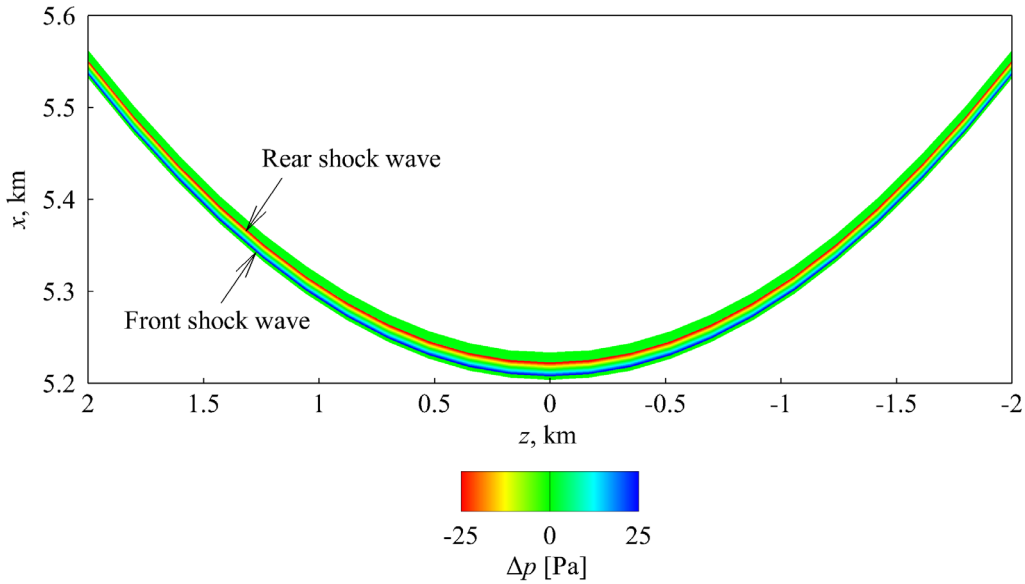

Fig. 3.12 Pressure fluctuation at *h* = 500 m, where aspect ratio is 4:1 (Case B).

variation of the pressure rise in the entire flow field was well predicted by the full-field simulation. Thus, it can be seen that the solution-adapted method that was proposed in this study is reasonable, and this simulation is powerful for clarifying the three-dimensional structure of the shock wave and the attenuation characteristics of sonic boom propagation through the real atmosphere.

Figure 3.12 shows the pressure fluctuation Δp at h = 500 m in the Case B, where the aspect ratio is 4:1 to improve the clarity of the footprint shapes. These shapes are close to hyperbolas, and the pressure fluctuation decreases as the horizontal distance increases. The results show that the extent of the influence of sonic boom can be clarified by the full-field simulation. Moreover, the ground effects, including not only the ground reflection but also the ground topography, can be analyzed by the simulation because of the following reason: Several methods using an orthogonal grid have been proposed to analyze the flow field around the complex geometry such as an aircraft [66, 67], and they can be used to reproduce the realistic ground topography. Therefore, it can be seen that the full-field simulation is promising for clarifying sonic boom propagation in realistic environmental conditions, including ground effects.

3.3.3 Computational accuracy of axi-symmetric Euler analysis in uniform atmosphere (Case A)

Simulation results in the Case A, where the axi-symmetric Euler equations were solved in the uniform atmosphere, were analyzed by comparison with the results of the waveform parameter method. Consequently, the accuracy of simulation, including the effectiveness of the two-dimensional solution-adapted method, was clarified as follows: Figure 3.13 shows the pressure waveforms at r/L = 1078

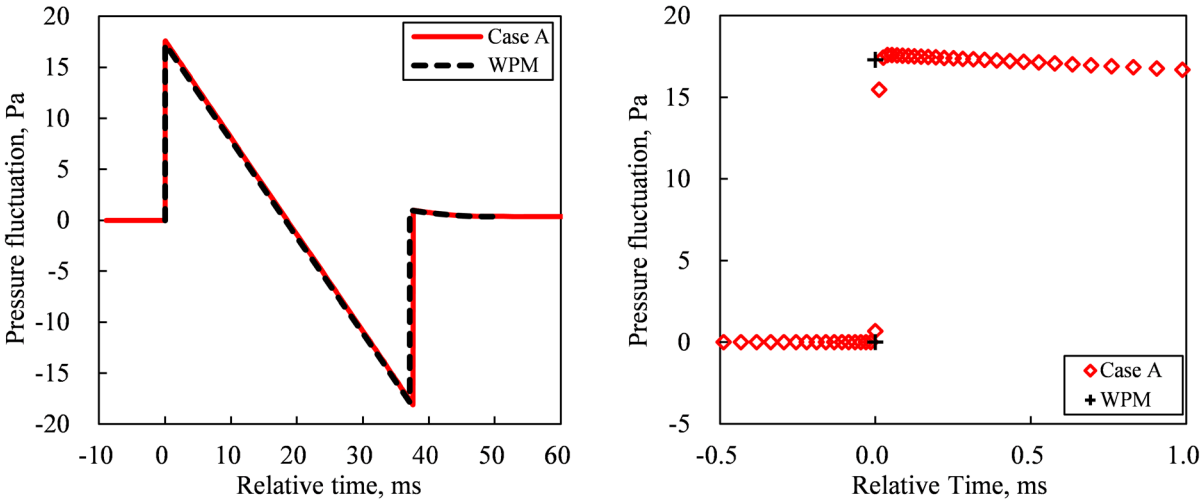

(a) Overall view (b) Closeup of front shock wave

Fig. 3.13 Pressure waveforms at *r*/*L* = 1078 (Case A).

in the Case A. As shown in Fig. 3.13(a), all of the waves generated from the body are consolidated into an N-shaped waveform (N-wave) by the nonlinear effect. In the Euler analysis, the thickness of a shock wave is zero theoretically, and the rapid pressure fluctuation caused by the shock wave should be ideally captured by two grid points. However, the resolution of the shock wave is reduced when the shock wave crosses into the grid lines. Therefore, to precisely capture the shock waves, the grid lines must be strictly aligned with the shock waves, and it can be seen that the shock wave is highly resolved when the shock wave is captured by a few grid points. As shown in Fig. 3.13(b), the front shock wave is captured by four grid points because the solution-adapted grid is strictly aligned with the front shock wave; thus, the solution-adapted grid is powerful for precisely capturing the shock wave in the entire flow field. Moreover, the pressure waveform of the simulation is in good agreement with that of the waveform parameter method, and the difference in the pressure rise of the front shock wave $\Delta p_{\max}$ was 1.7 %. Therefore, the full-field simulation considering the effects of geometrical spreading and nonlinearity in the uniform atmosphere reached the same level of accuracy as the waveform parameter method, which is often used to predict sonic boom intensity.

Figure 3.14 shows the variation in the pressure rise of the front shock wave $\Delta p_{\max}$ in the Case A. In the uniform atmosphere, the pressure rise is attenuated by the effect of geometrical spreading of the shock wave with increasing radial distance from the axis of symmetry. Because the effect weakens as the radial distance increases, the pressure rise in the near field decreases rapidly, whereas that in the far field decreases slowly. The attenuation characteristics of the simulation are in good agreement with those of the waveform parameter method. Therefore, it can be seen that the full-field simulation is useful for investigating the characteristics of sonic boom propagation in the entire flow field.

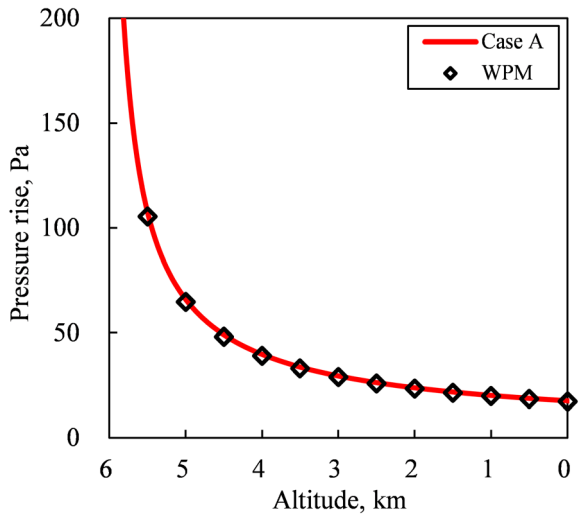

Fig. 3.14 Pressure rise of front shock wave in uniform atmosphere (Case A).

3.3.4 Computational accuracy of three-dimensional Euler analysis in stratified atmosphere (Case B)

Simulation results in the Case B, where the three-dimensional Euler equations with the gravity term were solved in the stratified atmosphere, were analyzed by comparison with the results of the waveform parameter method. Consequently, the accuracy of simulation, including the validity of the numerical correction method for considering atmospheric stratification and the effectiveness of the three-dimensional solution-adapted method, was clarified as follows: Figure 3.15 shows the pressure waveforms at h = 5,500 m on the symmetry plane beneath the body in the Case B. Without the correction term, the pressure in front of the front shock wave decreases toward the ground; i.e., the uniform flow in the stratified atmosphere is not maintained even in front of the front shock wave because the state of hydrostatic equilibrium is not strictly maintained and the nonphysical waves are generated (see section 2.3.4 of chapter 2 for details). On the other hand, with the correction term, the pressure in front of the front shock wave does not change; i.e., the variation in the pressure is only caused by the physical waves generated from the body. Therefore, it can be seen that the numerical correction method that was constructed in this study is useful for avoiding the generation of the nonphysical waves in the Riemann solver.

Figure 3.16 shows the pressure waveforms at h = 500 m on the symmetry plane beneath the body in the Case B. The number of grid points resolving the front shock wave in the Case B is slightly larger than that in the Case A, because of the following reason: The three-dimensional grid in the Case B was reconstructed only once to align the grid lines with the shock wave, although the two-dimensional grid in the Case A was reconstructed several times. However, the rapid pressure fluctuation of the front shock wave is captured by five grid points. Furthermore, the waveform shape in the simulation is macroscopically the same as that in

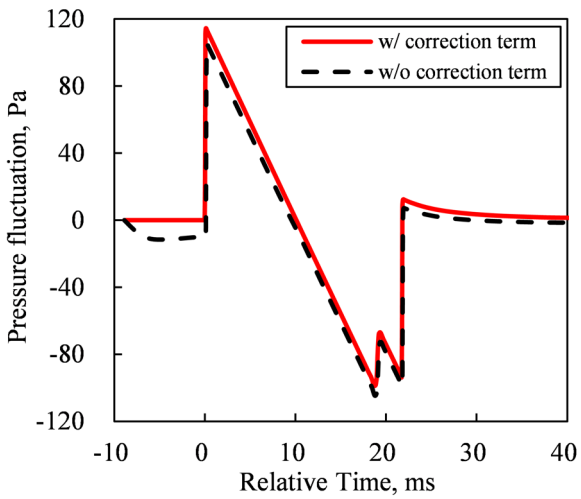

Fig. 3.15 Pressure waveforms at *h* = 5,500 m on the symmetry plane beneath the body (Case B).

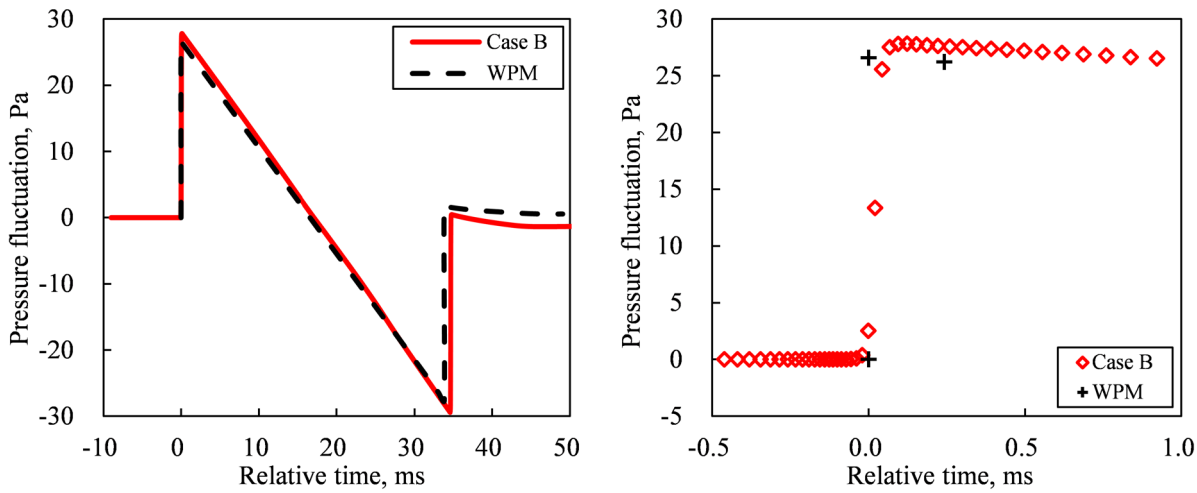

(a) Overall view (b) Closeup of front shock wave

Fig. 3.16 Pressure waveforms at *h* = 500 m on the symmetry plane beneath the body (Case B).

the waveform parameter method, and the difference in the pressure rise of the front shock wave Δp_{max} was 4.6 %. Therefore, the accuracy of the full-field simulation not only in the uniform atmosphere but also in the stratified atmosphere is adequate for evaluating sonic boom intensity.

Figure 3.17 shows the variation in the pressure rise of the front shock wave Δp_{max} on the symmetry plane beneath the body in the Case B. In the stratified atmosphere, the pressure rise is changed by the effects of not only geometrical spreading but also atmospheric stratification. Consequently, the pressure rise in the stratified atmosphere decreases more slowly than that in the uniform atmosphere because the atmospheric properties increase with decreasing altitude. The attenuation characteristics of the simulation are in good agreement with those of the waveform parameter method. Therefore, it can be seen that the full-field

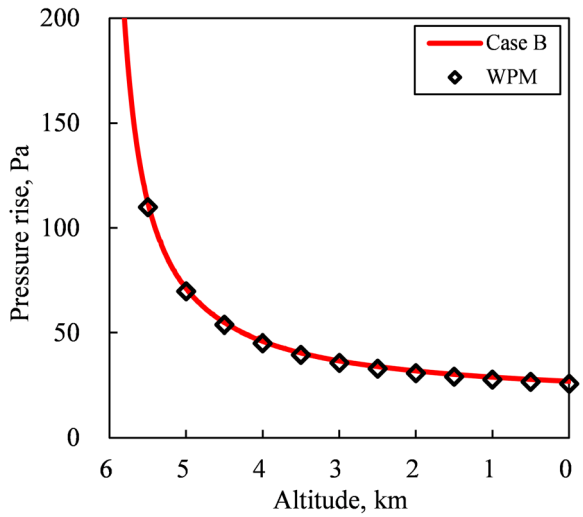

Fig. 3.17 Pressure rise of front shock wave on the symmetry plane beneath the body in stratified atmosphere (Case B).

simulation is quite helpful in understanding the characteristics of sonic boom propagation in the stratified atmosphere.

3.3.5 Computational accuracy of three-dimensional thermal nonequilibrium flow analysis in stratified atmosphere (Cases C and D)

Simulation results in the Cases C and D, where the inviscid and viscous, thermal nonequilibrium flow analyses were conducted in the stratified atmosphere, were analyzed by comparison with the D-SEND#1 flight test data. Consequently, the accuracy of simulation, including the rise time that was formed by the effects of molecular relaxation and viscosity, was clarified as follows: Figure 3.18 shows the pressure waveforms at h = 500 m on the symmetry plane beneath the body in the Cases C and D. Note that the measurement error of the D-SEND#1 flight test hardly affected the pressure waveform because the sonic boom measurement was conducted by the microphone and the AD converter which have a margin of measurement error of ±0.06dB and ±0.03dB, respectively. As can be seen in Fig. 3.18, the rapid pressure fluctuation of the shock waves in the Cases C and D is smoothed by the effect of molecular relaxation, although that in the Case B is not smoothed as shown in Fig. 3.16 (the detailed effect of molecular relaxation on the wave profile is described in next chapter). The pressure waveforms of the simulation are the same in the Cases C and D; i.e., the viscosity hardly affects the sonic boom intensity. The result shows that the effect of molecular relaxation on the rise time is much stronger than that of viscosity. The pressure waveform of the simulation is macroscopically the same as that of the flight test, although the pressure behind the front and rear shock waves in the flight test was assumed to be increased by the atmospheric

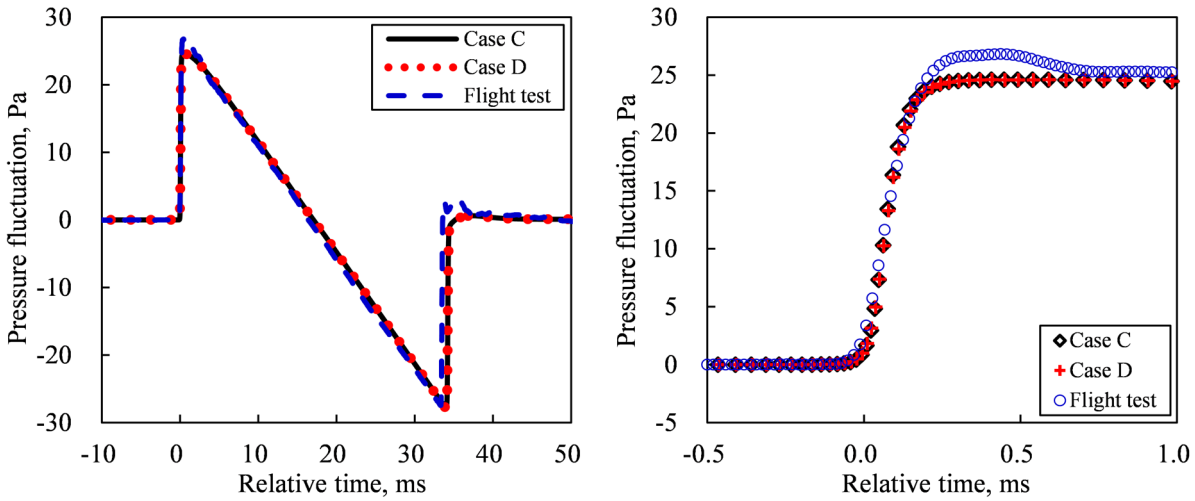

(a) Overall view (b) Closeup of front shock wave

Fig. 3.18 Pressure waveforms at h = 500 m on the symmetry plane beneath the body (Cases C and D).

turbulence [14], which often causes a ragged distortion of waveform behind a shock wave, i.e., an increase or decrease of pressure fluctuation [34–36]. Comparing the simulation results in the Case D with the flight test data, the difference in the pressure rise of the front shock wave $\Delta p_{\max}$ was –8.2 %, and that in the rise time Δt_{rt}, which was defined as the relative time when $\Delta p = \Delta p_{\max}$, was –7.0 %, because of the following reason: The flight and atmospheric conditions in the simulation were not exactly the same as those in the D-SEND#1 flight test. In particular, the pressure behind the front shock wave in the flight test was assumed to be increased by the atmospheric turbulence that was not considered in the simulation. Although the atmospheric turbulence effect should be investigated in the future work, the pressure gradient caused by the front shock wave in the simulation agrees well with that in the flight test, and the difference in the pressure gradient $\Delta p_{\max}/\Delta t_{rt}$ was –1.3 %; thus, not only the pressure rise of sonic boom but also its rise time was precisely predicted by the full-field simulation with the thermal nonequilibrium, in which the detailed model of molecular relaxation with respect to O_2 and N_2 was considered. Therefore it can be seen that the accuracy of full-field simulation is adequate for evaluating sonic boom propagation through the real atmosphere.

3.4 Summary of this chapter

In this chapter, the first-ever direct reproduction of the flight test for sonic boom was successful, and the usefulness of full-field simulation was investigated by comparison with the waveform parameter method and the flight test data. The results are summarized as follows.

- The three-dimensional structure of the shock wave distorted by atmospheric stratification was successfully captured, and the attenuation characteristics of sonic boom propagation could be investigated by the simulation results.
- The solution-adapted method was a valid approach because the shock wave was highly resolved by the solution-adapted grid. The numerical correction method for considering atmospheric stratification was useful for avoiding the generation of nonphysical waves caused by the Riemann solver.
- The full-field simulation not only in the uniform atmosphere but also in the stratified atmosphere was the same level of accuracy as the waveform parameter method, which is a representative prediction method for sonic boom. Moreover, the pressure gradient caused by the front shock wave was in good agreement with the D-SEND#1 flight test data. Thus, it can be seen that not only the pressure rise of sonic boom but also its rise time was precisely predicted by the full-field simulation.

These results show that the accuracy of full-field simulation is adequate for analyzing sonic boom propagation through the real atmosphere.

Chapter 4

Full-Field Simulation for Rise Time Prediction

4.1 Outline of this chapter

In chapters 4 to 6, full-field simulation is performed to clarify sonic boom phenomena that have not been well clarified and to demonstrate the applicability of the simulation. In this chapter, full-field simulation is performed to investigate the effect of molecular relaxation on the wave profile and the formation mechanism of rise time in the uniform and stratified atmospheres. The rise time of sonic boom is mainly formed by the effects of molecular relaxation with respect to O_2 and N_2. However, these effects are treated as simplified models in the existing prediction methods, and the accuracy of the rise time prediction may not be adequate for evaluating sonic boom intensity in various flight and atmospheric conditions, because of the following reason: The discrepancies between predictions and flight test measurements were significantly changed by variation in the flight and atmospheric conditions [49]. Moreover, the detailed effect of molecular relaxation has not been clarified particularly in the realistic wave propagation, although it has been investigated by one-dimensional numerical and asymptotic analyses [50]. Therefore, the prediction method considering the detailed model of molecular relaxation is needed, and the effect of molecular relaxation should be further investigated. In the previous chapter, the rise time was precisely predicted by full-field simulation with the thermal nonequilibrium, in which the detailed model of molecular relaxation was incorporated. Therefore, full-field simulation is quite helpful in clarifying the formation mechanism of rise time. In this chapter, not only the sonic boom waveform but also the magnitude of translational-vibrational energy exchange is investigated to clarify the effect of molecular relaxation on the wave profile and the formation mechanism of rise time. The contents of this chapter were already published in [90].

4.2 Computational methods

The simulation results obtained in the previous chapter are quite helpful in analyzing the formation mechanism of rise time because the configuration of the NWM is very simple. However, the rise time prediction in the uniform atmosphere is not performed in the previous chapter. To investigate the effect of molecular relaxation on the wave profile, the analysis of rise time in the uniform atmosphere is more convenient than that in the stratified atmosphere because the relaxation time in the freestream condition of uniform atmosphere is the constant value. Therefore, the additional simulation assuming the uniform atmosphere is performed in this chapter, and the formation mechanism of rise time is investigated by the simulation results and those obtained in the previous chapter. The following is the explanation of the additional simulation that is conducted in this chapter.

4.2.1 Computational conditions

The computational model was the NWM without the tail fins shown in Fig. 3.1. The flight Mach number was M_∞ = 1.43, and a steady level flight instead of free fall was assumed, as described in section 3.2.1 of chapter 3. To investigate variation in the wave profile according to the atmospheric conditions, the uniform properties of atmosphere at h = 6.039 km, 3 km, and 0 km were set by using the atmospheric model based on the meteorological data of the D-SEND#1 flight test (see section 3.2.1 of chapter 3 for details). Tables 4.1 and 4.2 show the computational conditions and the atmospheric conditions at each altitude, respectively. The flow solver in each case and the computational domain are explained in sections 4.2.2 and 4.2.3, respectively. The relaxation time in the freestream condition of uniform atmosphere is calculated by the Bass et al.'s formula given by Eqs. (2.12) and (2.13).

Table 4.1 Computational conditions

	Cases E–G
Computational model	NWM (L = 5.6 m)
Flight Mach number	M_∞ = 1.43
Flight condition	Steady level flight
Atmosphere	Uniform (see Table 4.2 for details)
Computational domain	r/L = 0–1090

Table 4.2 Atmospheric conditions at each altitude

	h = 6.039 km	h = 3 km	h = 0 km
Temperature, K	232.39	254.31	275.95
Pressure, kPa	44.875	68.773	101.25
Density, kg/m3	0.673	0.942	1.28
Relative humidity, %	54.9	86.1	97.3
Relaxation time of O_2, ms	3.26	0.0967	0.00824
Relaxation time of N_2, ms	24.1	4.49	0.798

4.2.2 Flow solver

The additional simulation was performed by solving the axi-symmetric Euler equations with the thermal nonequilibrium as follows.

Equation E: Axi-symmetric Euler equations with thermal nonequilibirium

$$\frac{\partial Q}{\partial t}+\frac{\partial E}{\partial x}+\frac{\partial F}{\partial r}+H=S_W \tag{4.1}$$

$$Q=\begin{bmatrix}\rho\\ \rho u\\ \rho v\\ e\\ e_{vO2}\\ e_{vN2}\end{bmatrix},E=\begin{bmatrix}\rho u\\ \rho u^2+p\\ \rho uv\\ (e+p)u\\ e_{vO2}u\\ e_{vN2}u\end{bmatrix},F=\begin{bmatrix}\rho v\\ \rho uv\\ \rho v^2+p\\ (e+p)v\\ e_{vO2}v\\ e_{vN2}v\end{bmatrix},H=\begin{bmatrix}\rho v/r\\ \rho uv/r\\ \rho v^2/r\\ (e+p)v/r\\ e_{vO2}v/r\\ e_{vN2}v/r\end{bmatrix},S_W=\begin{bmatrix}0\\ 0\\ 0\\ 0\\ w_{vO2}\\ w_{vN2}\end{bmatrix} \tag{4.2}$$

$$e=\frac{\rho RT}{\gamma-1}+e_{vO_2}+e_{vN_2}+\frac{\rho}{2}\left(u^2+v^2\right) \tag{4.3}$$

where geometrical spreading, nonlinearity, and molecular relaxation are considered. To separate the effects of molecular relaxation with respect to O_2 and N_2, the equations were solved in the following three cases.

- Case E: Molecular relaxation of O_2 was only considered (e_{vN_2} was set to zero).
- Case F: Molecular relaxation of N_2 was only considered (e_{vO_2} was set to zero).
- Case G: Molecular relaxation of O_2 and N_2 was considered.

Table 4.3 shows the physical effects that were considered in each case. The computational approach of solving the governing equations is described in section 2.3 of chapter 2.

Table 4.3 Physical effects that are considered in each case

	Case E	Case F	Case G
Governing equation	Equation E ($e_{vN_2} = 0$)	Equation E ($e_{vO_2} = 0$)	Equation E
Geometrical spreading	✓	✓	✓
Nonlinearity	✓	✓	✓
Atmos. stratification	–	–	–
Viscosity	–	–	–
Molecular relaxation	O_2	N_2	O_2+N_2

4.2.3 Computational domain and computational grid

The computational domain and the boundary conditions were the same as those described in sections 3.2.3 and 3.2.4 of chapter 3, respectively. The solution-adapted grids were also constructed on the same conditions as those described in section 3.2.5 of chapter 3. The simulation was performed by the Grid 2A shown in Table 3.4.

4.3 Computational results

Simulation results are analyzed to clarify the effect of molecular relaxation on the wave profile and the formation mechanism of rise time. Note that the weak shock wave in the far field is almost the same as the compression wave without a discontinuity, and the molecular relaxation affects the weak shock wave on the length scale much larger than the mean free path. As the pressure distribution in the near field was the same regardless of the governing equations, the explanation is left out here (see section 3.3.1 of chapter 3 for details).

4.3.1 Molecular relaxation of O_2 in uniform atmosphere (Case E)

Figures 4.1–4.3 show the waveforms of pressure, density, and temperature at r/L = 1078 in the Case E. In these figures, the relative time is calculated by the streamwise distance and the flight velocity, and it is set to zero when the pressure fluctuation becomes the tenth part of the pressure rise of the front shock wave. To clarify the effect of molecular relaxation, the waveforms in the Case A, where the thermal equilibrium was assumed, are depicted in Figs. 4.1–4.3. As shown in these figures, the waveforms in the thermal nonequilibrium differ from those in the thermal equilibrium and are changed with the atmospheric conditions. Although the pressure and density change in the same way as the translational temperature regardless of the atmospheric conditions, the difference between the translational and vibrational

temperatures changes with the atmospheric conditions, because of the following reason: The relaxation time decreases with decreasing altitude as shown in Table 4.2, and the exchange velocity of the translational-vibrational energy increases with decreasing the relaxation time; thus, the effect of molecular relaxation significantly changes with the atmospheric conditions. Note that the variation in the vibrational temperature was caused by the translational-vibrational energy exchange, which was evaluated by the Landau-Teller relaxation model as

$$w_{vs} = \frac{e_{vs}^{eq} - e_{vs}}{\tau_s} \quad (\mathrm{s} = \mathrm{O_2}, \mathrm{N_2}) \tag{4.4}$$

where the vibrational energy was evaluated by Eqs. (2.9) and (2.10), and the relaxation time was evaluated by Eqs. (2.12) and (2.13). Therefore, the evaluation of the relaxation term given by Eq. (4.4) is quite helpful in analyzing the effect of molecular relaxation according to the atmospheric conditions.

Figure 4.4 shows the magnitude of the translational-vibrational relaxation term at r/L = 1078 in the Case E. In the case of uniform atmosphere at h = 6.039 km, the translational-vibrational energy exchange follows the rapid increase in the translational energy caused by the shock wave, and the magnitude of the energy exchange slowly decreases, as shown in Fig. 4.4(a). Consequently, the pressure fluctuation correlated with the fluctuation of translational energy is widely decreased behind the shock wave as shown in Fig. 4.1(a), although the rise time is not formed because of the following reason: The wave profile is changed by two effects, i.e., the nonlinear effect that makes a wave steepening and the effect of molecular relaxation that makes a wave relaxing. If the effect of molecular relaxation is stronger than the nonlinear effect, the wave profile is smoothed, and the rise time is formed. On the other hand, if the effect of molecular relaxation is weaker than the nonlinear effect, the wave profile is not smoothed, and the rise time is not formed. When the translational-vibrational energy exchange is slowly induced as shown in Fig. 4.4 (a), the magnitude of the energy exchange just behind the shock wave is too small to form the rise time because the effect of molecular relaxation is weaker than the nonlinear effect. For the expansion waves between the front and rear shock waves, the constant amount of vibrational energy is converted to the translational energy because the translational energy is linearly decreased by the expansion waves. However, because the energy exchange caused by the front shock wave lasts for approximately 20–30 ms, the magnitude of the energy exchange slowly decreases. In the case of uniform atmosphere at h = 3 km, the magnitude of energy exchange behind the shock waves is rapidly increased, and then it is rapidly decreased, as shown in Fig. 4.4(b). That is, the significant energy exchange converges just behind the shock wave. Consequently, the pressure fluctuation just behind the shock wave is decreased as shown in Fig. 4.1(b), and the rise time is formed because the effect of molecular relaxation is stronger than the nonlinear effect. In the case of uniform atmosphere at h = 0 km, the exchange velocity of the translational-vibrational energy is very fast as shown in Fig. 4.4(c), and the pressure fluctuation just behind the shock wave is significantly decreased

as shown in Fig. 4.1(c), although the exchange velocity is too fast to form the long rise time. The result shows that there exists the appropriate exchange velocity to form the long rise time. Therefore, it can be seen that the effect of molecular relaxation on the wave profile was strongly related to the exchange velocity of the translational-vibrational energy and the magnitude of the energy exchange.

Figure 4.5 shows the variation in the pressure and the magnitude of the translational-vibrational relaxation term near the front shock wave. To clarify the transition of the waveforms, the vertical axes represent the nondimensional values calculated using the maximum values. In the case of uniform atmosphere at h = 6.039 km, the pressure waveform and the magnitude of the relaxation term are hardly changed by the molecular relaxation as shown in Fig. 4.5(a), although the pressure fluctuation is decreased as shown in Fig. 4.1(a). In the case of uniform atmosphere at h = 3 km, the pressure waveform is smoothed in the order of the highest pressure to the lowest one as the radial distance increases, as shown in Fig. 4.5(b). The exchange velocity decreases with increasing the radial distance because the rapid increase in the translational energy just behind the front shock wave is relaxed by the effect of molecular relaxation. In the case of uniform atmosphere at h = 0 km, the pressure gradient caused by the front shock wave is decreased as the radial distance increases because the exchange velocity is significantly fast, as shown in Fig. 4.5(c). As a result, the exchange velocity decreases somewhat with increasing the radial distance. Therefore, it can be seen that the wave profile near the shock wave is significantly changed according to the variation in the atmospheric conditions.

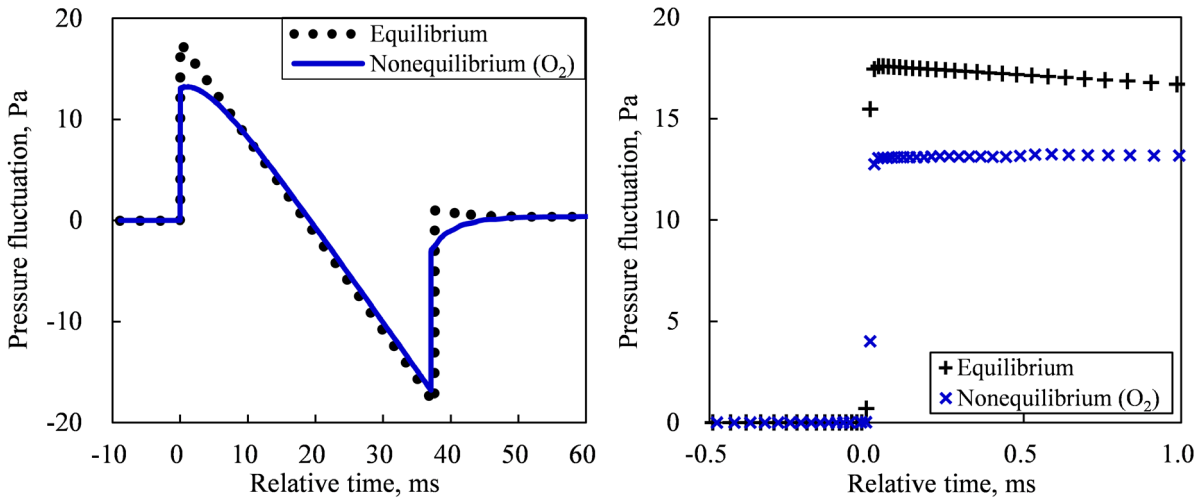

(a) Uniform atmosphere at h = 6.039 km

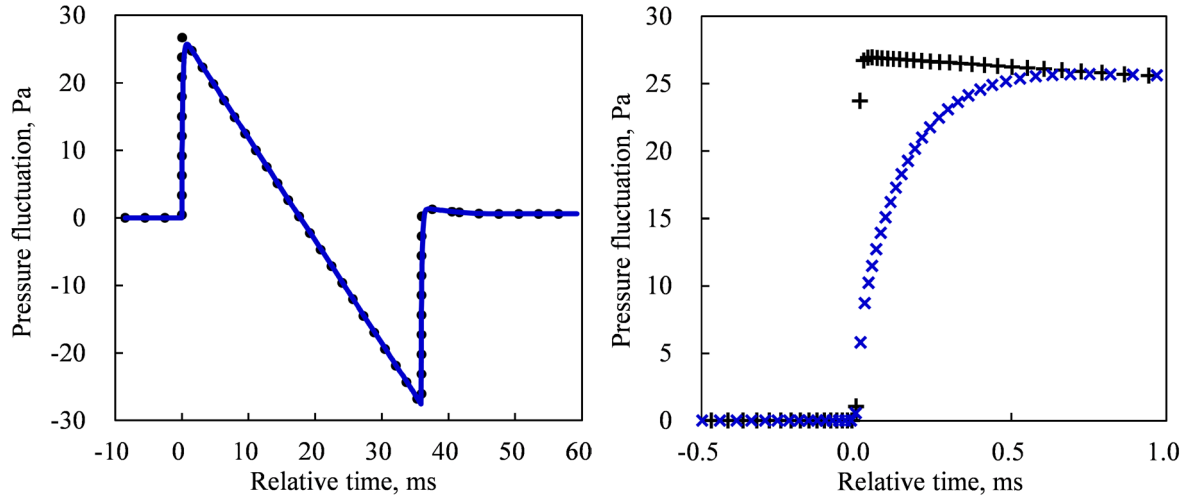

(b) Uniform atmosphere at h = 3 km

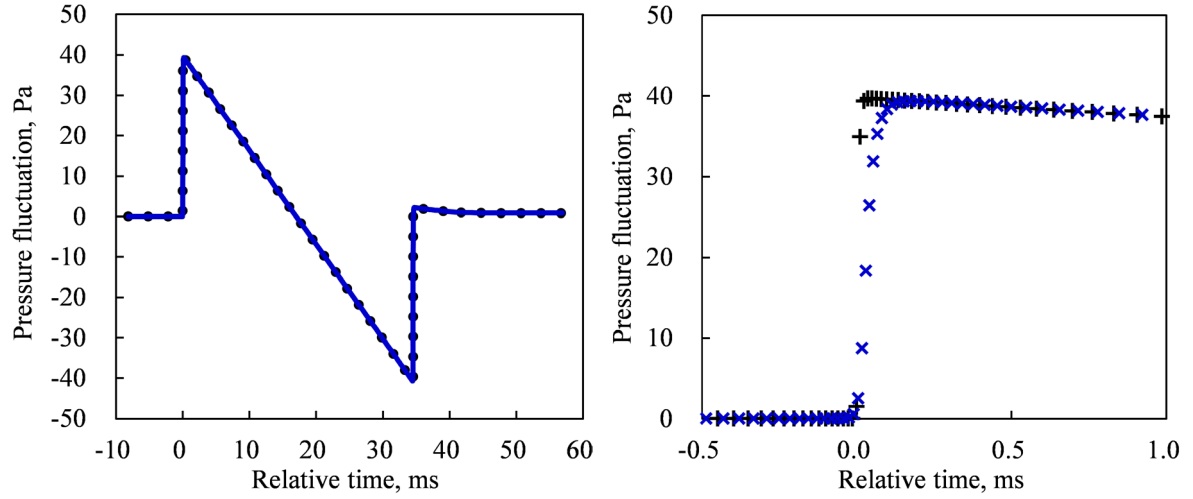

(c) Uniform atmosphere at h = 0 km

Fig. 4.1 Pressure waveforms at r/L = 1078 in Case E where molecular relaxation of O_2 is considered (Left: overall view, Right: Closeup of front shock wave).

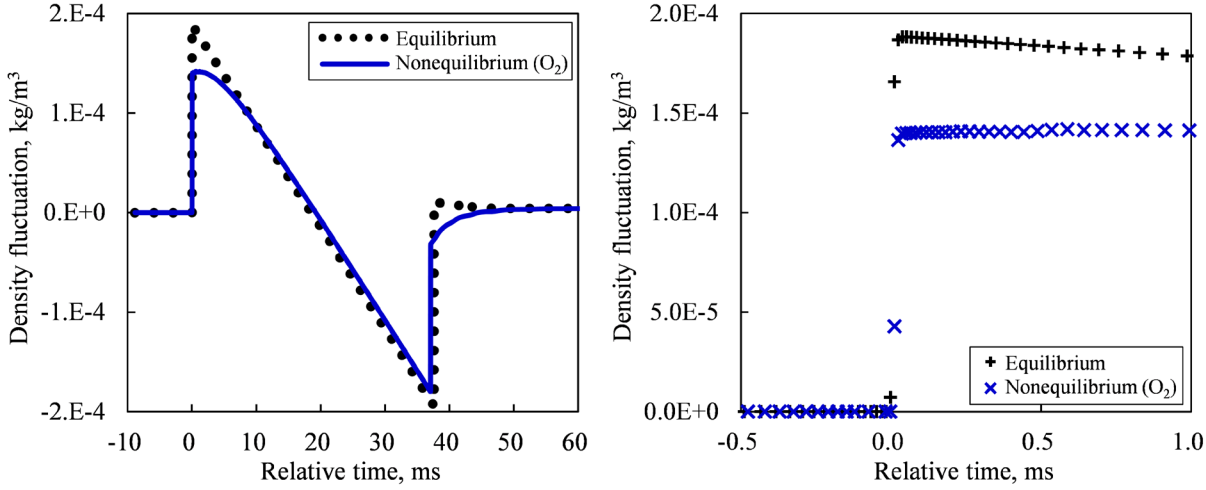

(a) Uniform atmosphere at h = 6.039 km

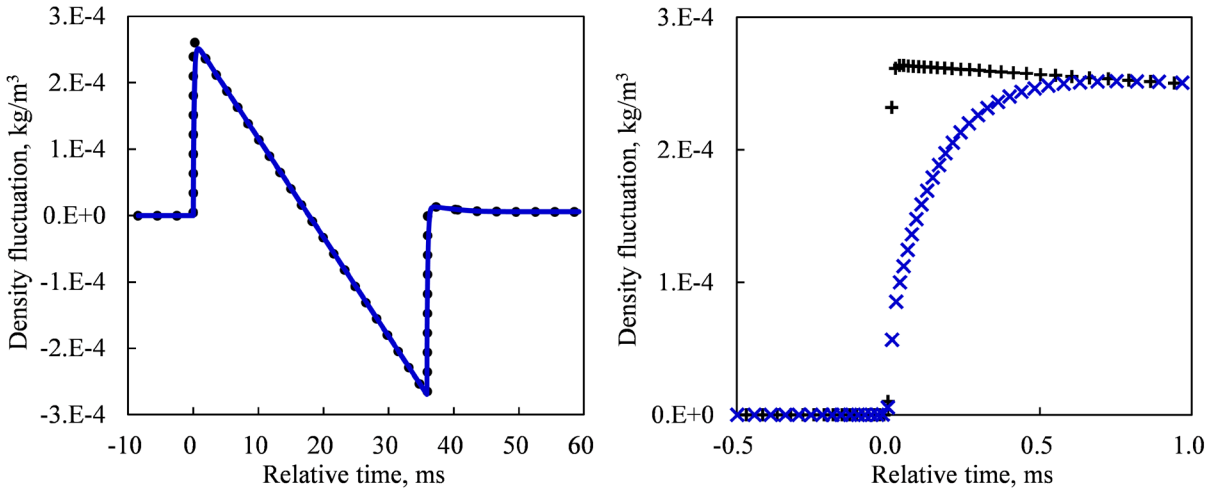

(b) Uniform atmosphere at h = 3 km

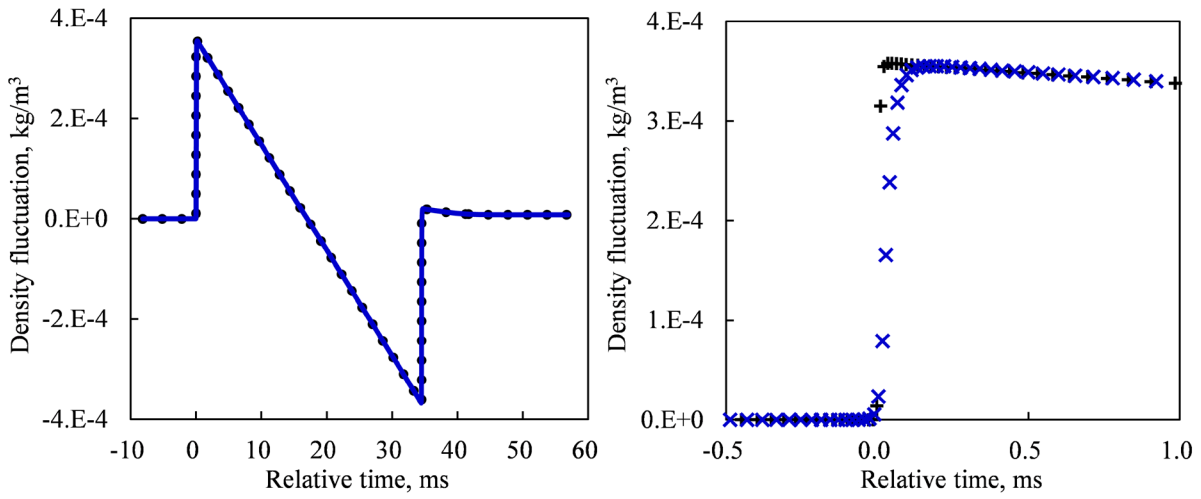

(c) Uniform atmosphere at h = 0 km

Fig. 4.2 Density waveforms at r/L = 1078 in Case E where molecular relaxation of O_2 is considered (Left: overall view, Right: Closeup of front shock wave).

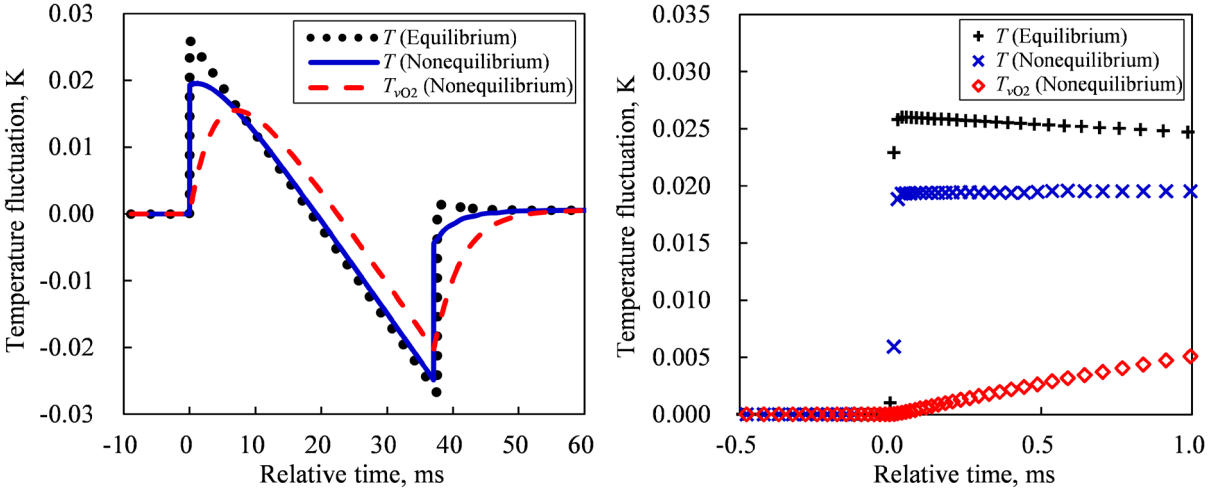

(a) Uniform atmosphere at h = 6.039 km

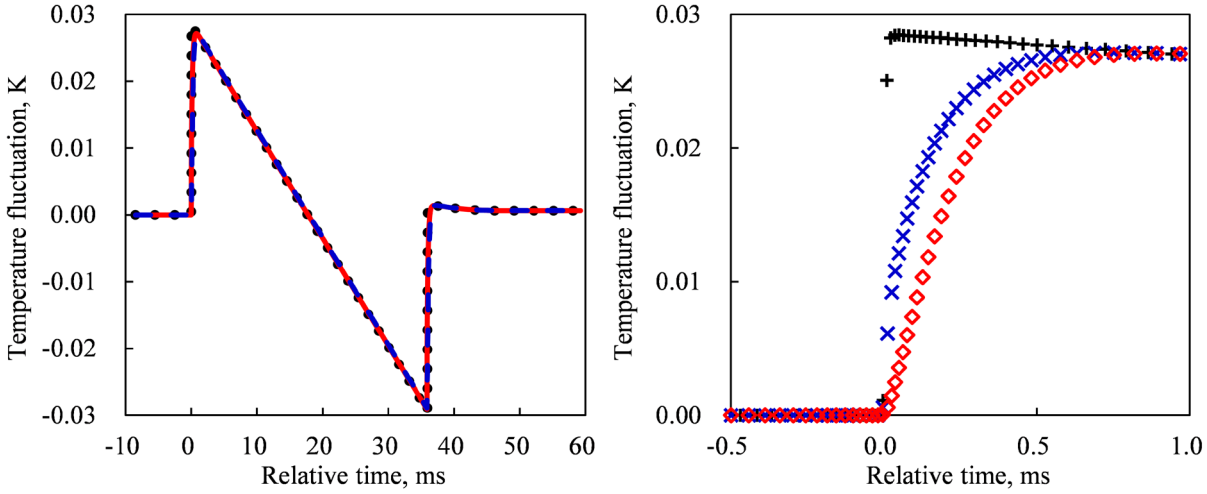

(b) Uniform atmosphere at h = 3 km

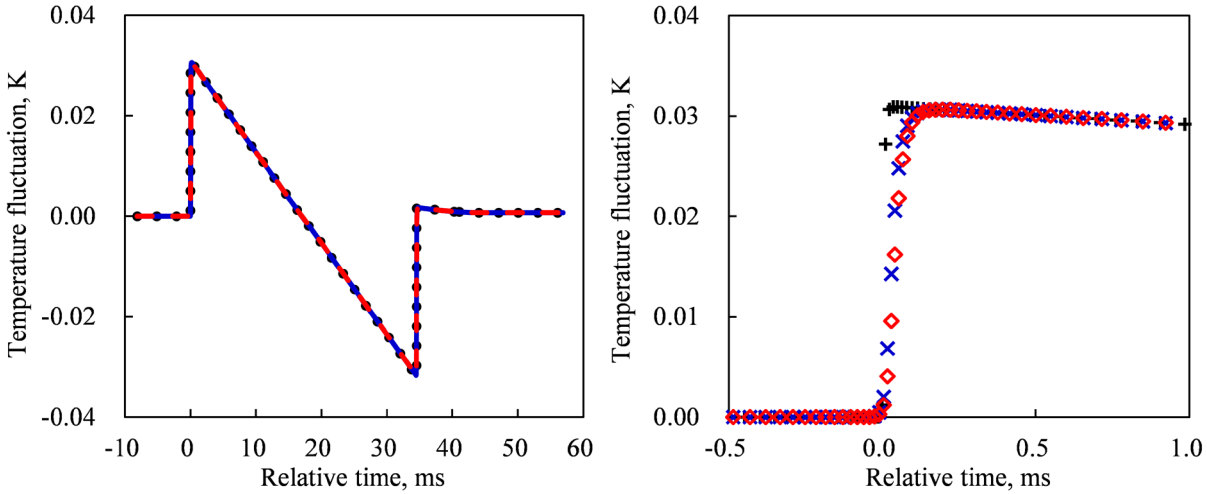

(c) Uniform atmosphere at h = 0 km

Fig. 4.3 Temperature waveforms at r/L = 1078 in Case E where molecular relaxation of O_2 is considered (Left: overall view, Right: Closeup of front shock wave).

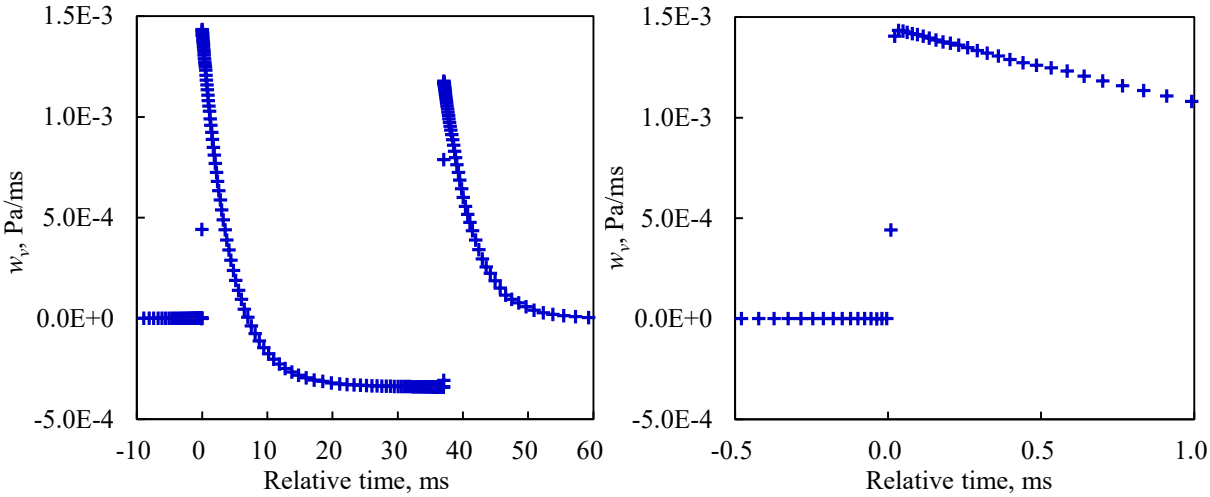

(a) Uniform atmosphere at h = 6.039 km

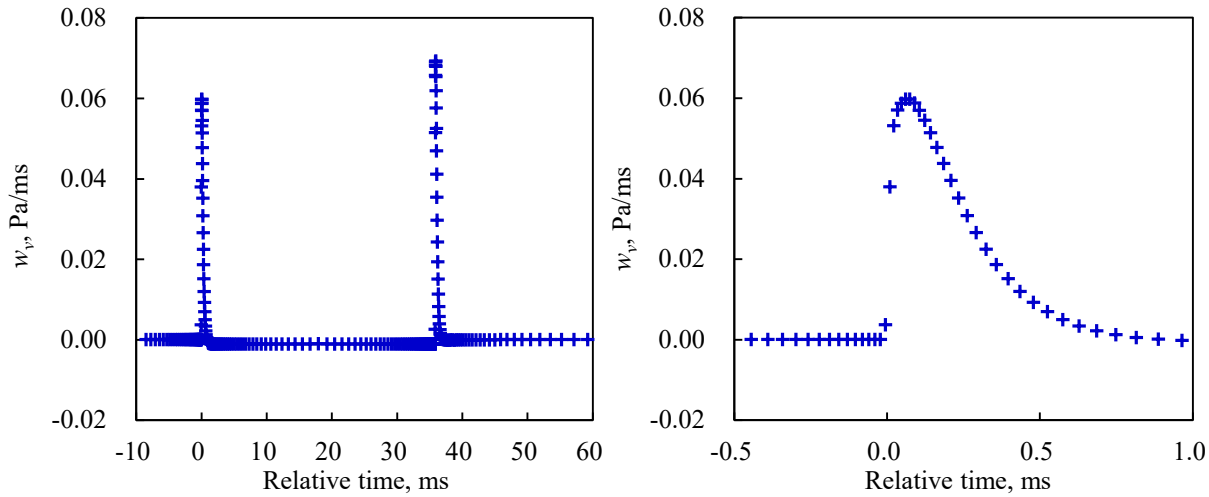

(b) Uniform atmosphere at h = 3 km

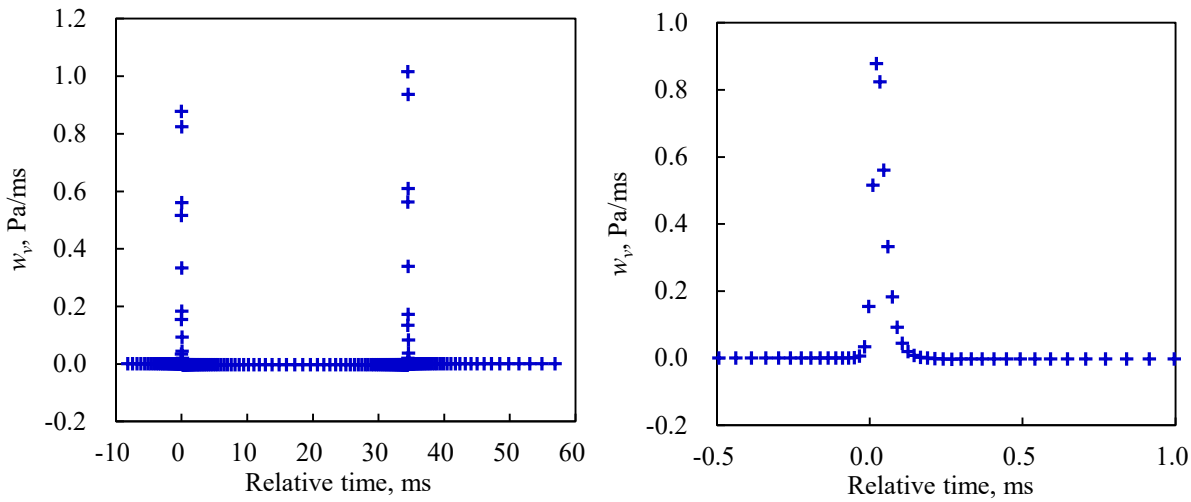

(c) Uniform atmosphere at h = 0 km

Fig. 4.4 Magnitude of relaxation term of O_2 at r/L = 1078 in Case E where molecular relaxation of O_2 is considered (Left: overall view, Right: Closeup of front shock wave).

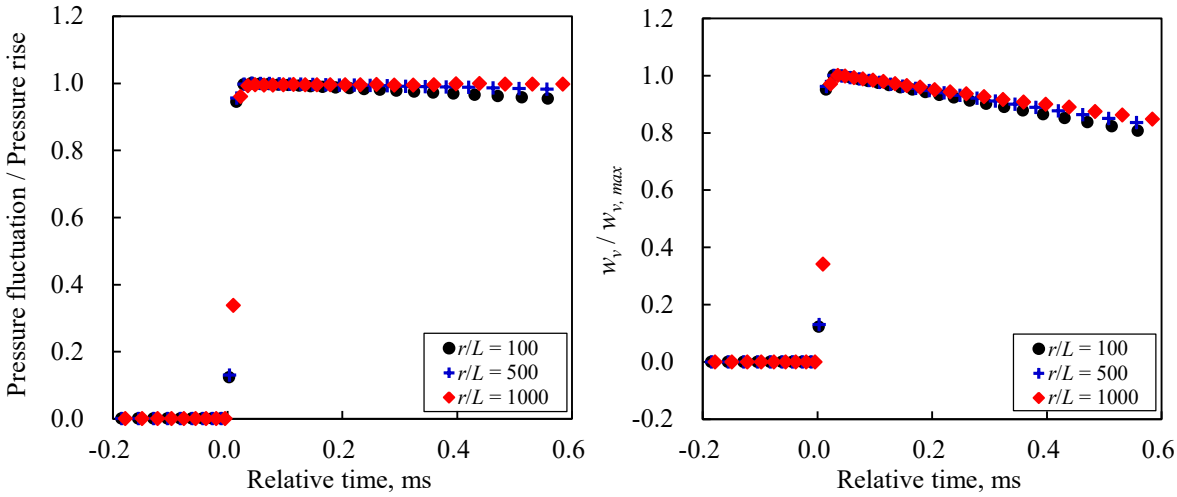

(a) Uniform atmosphere at h = 6.039 km

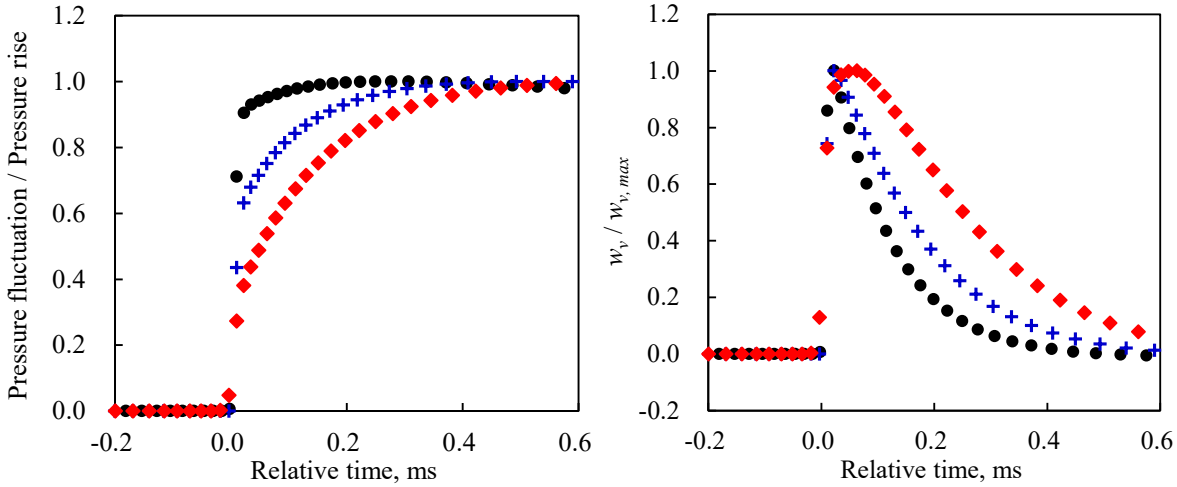

(b) Uniform atmosphere at h = 3 km

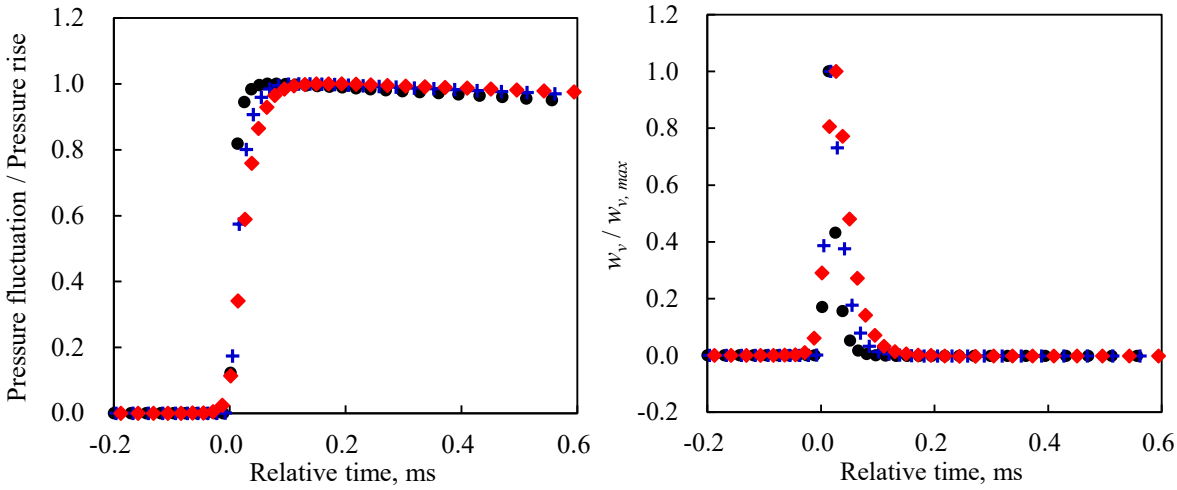

(c) Uniform atmosphere at h = 0 km

Fig. 4.5 Variation in pressure waveform and relaxation term of O_2 near front shock wave in Case E where molecular relaxation of O_2 is considered (Left: pressure, Right: relaxation term of O_2).

4.3.2 Molecular relaxation of N_2 in uniform atmosphere (Case F)

Figures 4.6 and 4.7 show the pressure waveforms and the magnitude of the translational-vibrational relaxation term, respectively, at r/L = 1078 in the Case F, as well as those shown in Figs. 4.1 and 4.4. Note that the relaxation time of N_2 is approximately one to two orders of magnitude greater than that of O_2, as shown in Table 4.2. As the relaxation time of N_2, as well as that of O_2, decreases with decreasing altitude, the exchange velocity of the translational-vibrational energy increases; thus, the wave profile differs according to the atmospheric conditions. In the case of uniform atmosphere at h = 6.039 km, the exchange velocity is very slow, and the translational energy is hardly decreased by the energy exchange, as shown in Fig. 4.7(a). Consequently, the variation in the relaxation term is similar to that in the pressure, and the pressure waveform in the thermal nonequilibrium is almost the same as that in the thermal equilibrium as shown in Fig. 4.6(a). The results show that the molecular relaxation of N_2 in the uniform atmosphere at h = 6.039 km hardly affects the pressure waveform. In the case of uniform atmosphere at h = 3 km, the translational energy is decreased by the energy exchange, although the exchange velocity of the translational-vibrational energy is slow, as shown in Fig. 4.7(b). Consequently, the pressure fluctuation is widely decreased by the molecular relaxation as shown in Fig. 4.6(b), although the rise time is not formed because the effect of molecular relaxation is weaker than the nonlinear effect. The transition of the wave profile caused by the molecular relaxation of N_2 at h = 3 km is similar to that caused by the molecular relaxation of O_2 at h = 6.039 km as shown in Fig. 4.1(a), because the order of the relaxation time is the same in both cases as shown in Table 4.2. In the case of uniform atmosphere at h = 0 km, the exchange velocity is faster than that at h = 3 km as shown in Fig. 4.7(c), and the pressure fluctuation is partially decreased behind the shock wave as shown in Fig. 4.6(c). However, because the effect of molecular relaxation just behind the shock wave is weaker than the nonlinear effect, the rise time is hardly formed. These results show that the effect of molecular relaxation of N_2, as well as that of O_2, is changed by the variation in the relaxation time. Therefore, the effect of molecular relaxation on the wave profile can be classified by the length of the relaxation time (see next section for details).

Figure 4.8 shows the variation in the pressure and the magnitude of the translational-vibrational relaxation term near the front shock wave in the Case F, as well as those shown in Fig. 4.5. In the cases of uniform atmosphere at h = 6.039 km and 3 km, the pressure waveform and the magnitude of the relaxation term are hardly changed by the molecular relaxation as shown in Figs. 4.8(a) and (b), because the effect of molecular relaxation just behind the shock wave is weaker than the nonlinear effect. In the case of uniform atmosphere at h = 0 km, the pressure waveforms are smoothed in the region of the highest pressure as the radial distance increases, as shown in Fig. 4.8(c).

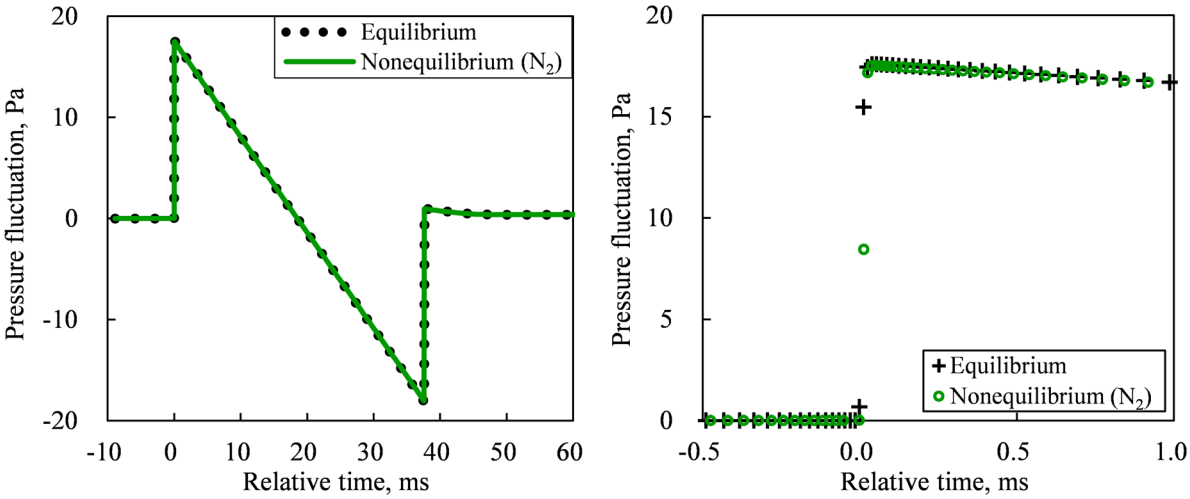

(a) Uniform atmosphere at h = 6.039 km

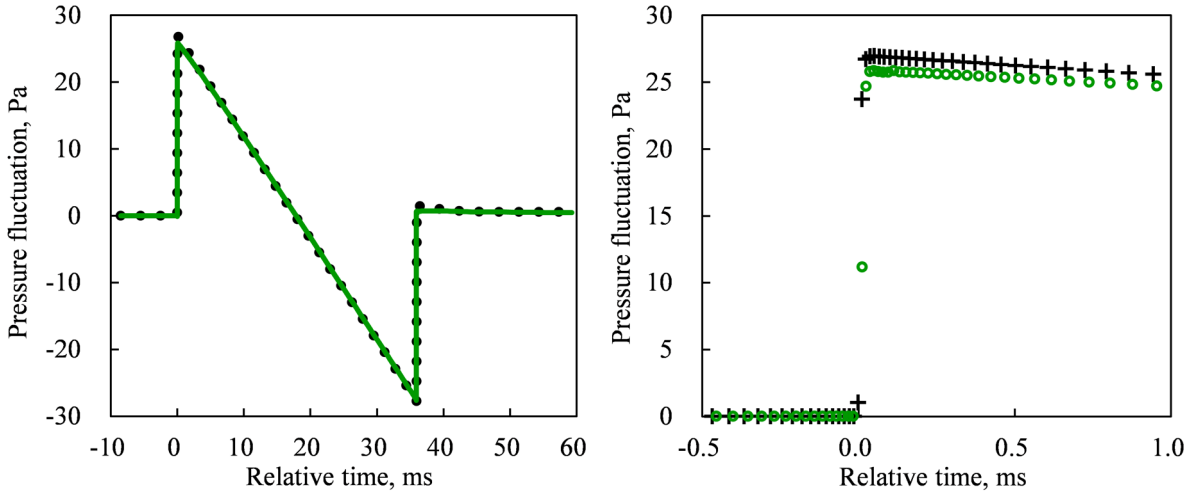

(b) Uniform atmosphere at h = 3 km

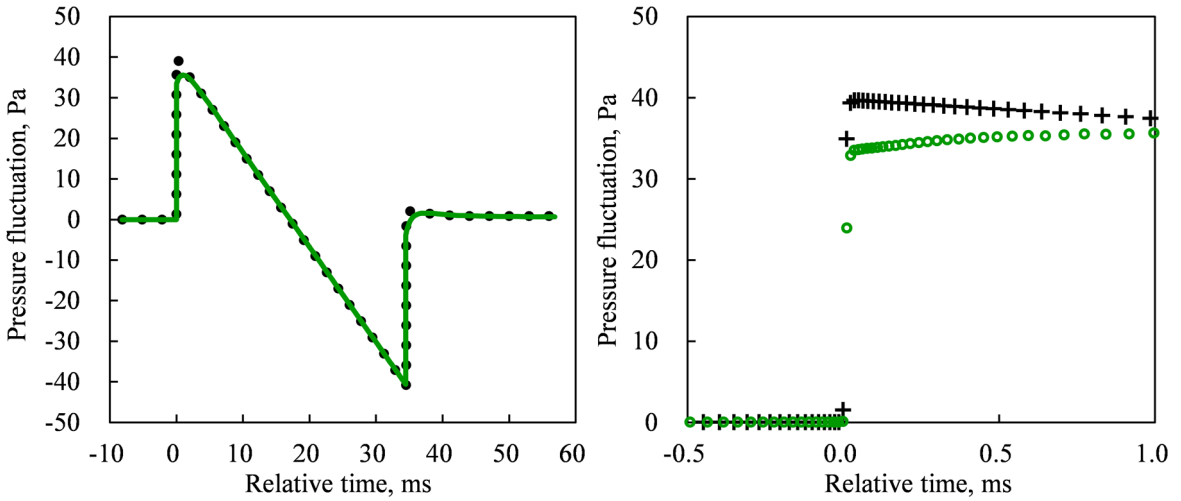

(c) Uniform atmosphere at h = 0 km

Fig. 4.6 Pressure waveforms at r/L = 1078 in Case F where molecular relaxation of N_2 is considered (Left: overall view, Right: Closeup of front shock wave).

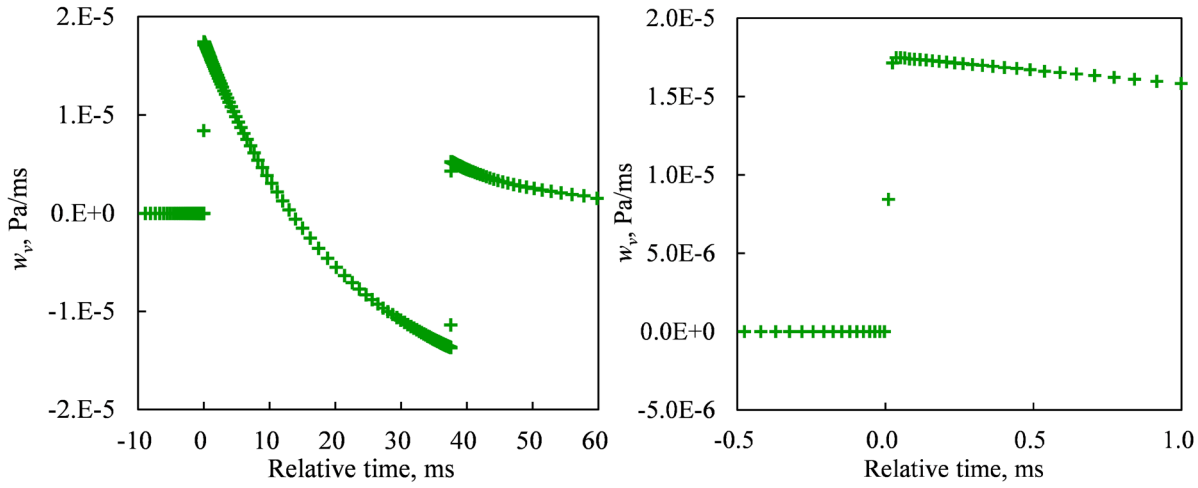

(a) Uniform atmosphere at h = 6.039 km

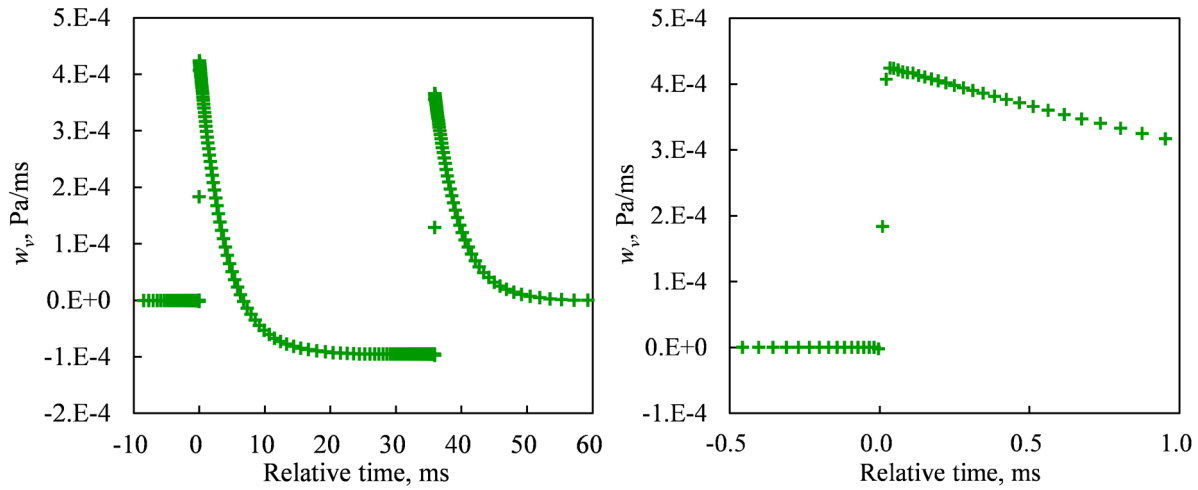

(b) Uniform atmosphere at h = 3 km

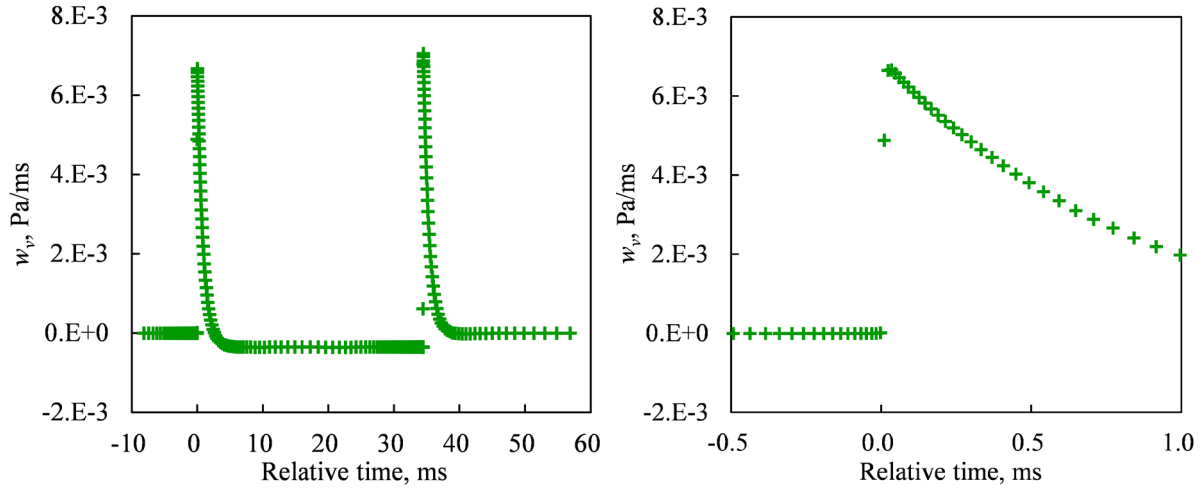

(c) Uniform atmosphere at h = 0 km

Fig. 4.7 Magnitude of relaxation term of N_2 at r/L = 1078 in Case F where molecular relaxation of N_2 is considered (Left: overall view, Right: Closeup of front shock wave).

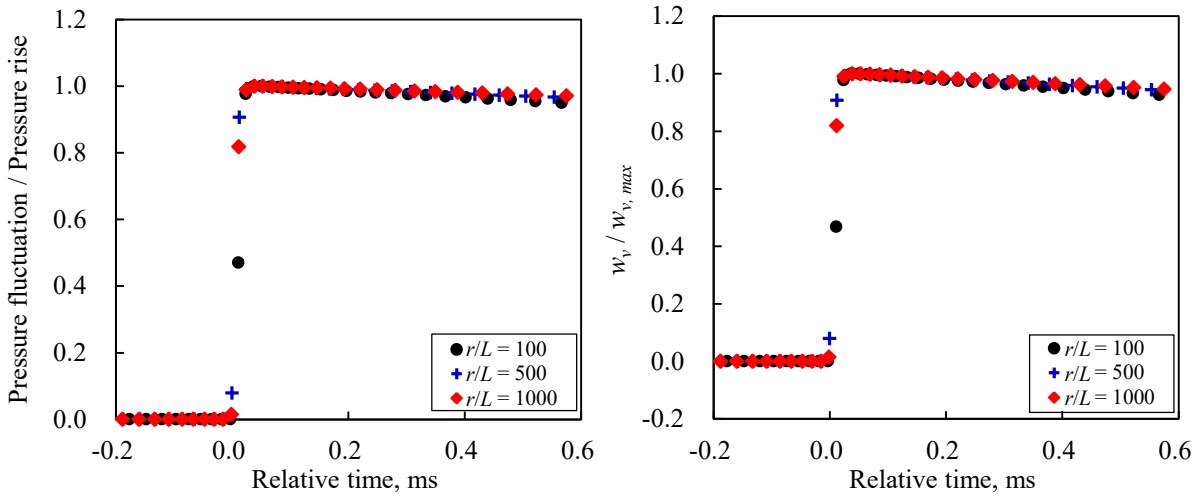

(a) Uniform atmosphere at h = 6.039 km

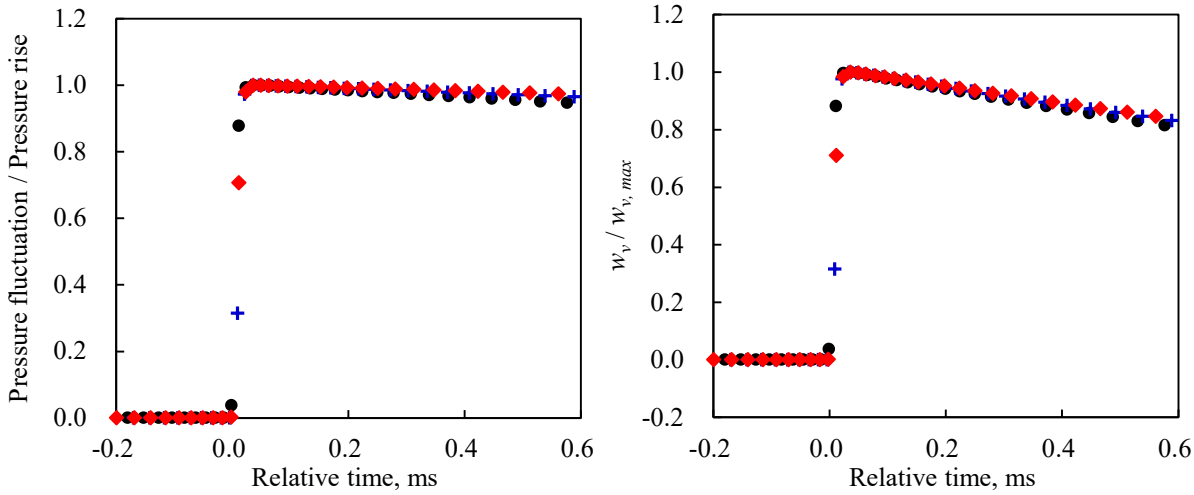

(b) Uniform atmosphere at h = 3 km

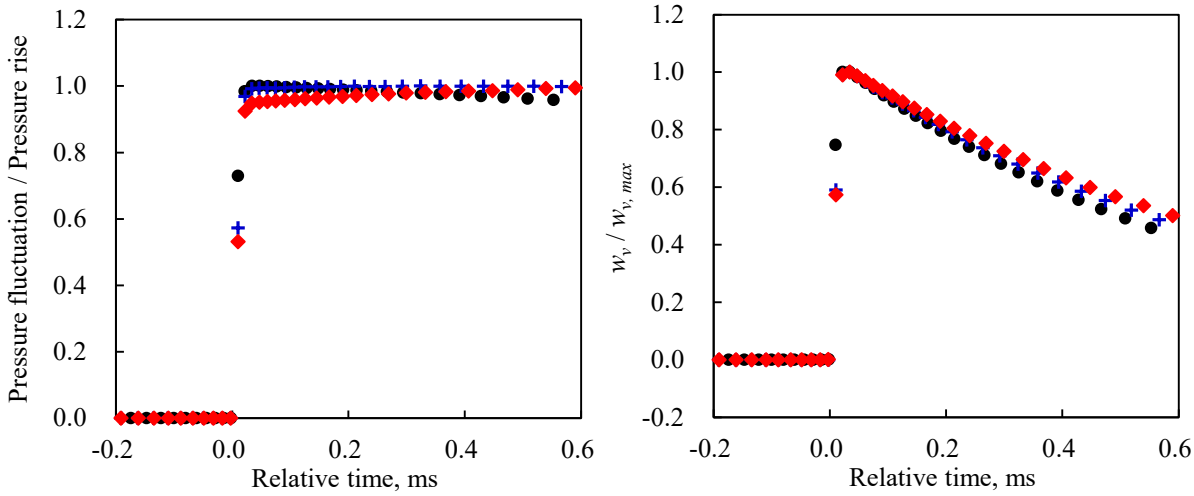

(c) Uniform atmosphere at h = 0 km

Fig. 4.8 Variation in pressure waveform and relaxation term of N_2 near front shock wave in Case F where molecular relaxation of N_2 is considered (Left: pressure, Right: relaxation term of N_2).

4.3.3 Classification of molecular relaxation according to relaxation time

As can be seen from the analyses above, the transition of the wave profile due to the molecular relaxation is classified by the length of the relaxation time. Figure 4.9 shows the classification of the transition of wave profile due to the molecular relaxation. Table 4.4 shows the results obtained by applying the classification method to the simulation results. As shown in Fig. 4.9(a), in the case of very long relaxation time (Type A), the wave profile does not change because the translational energy is hardly decreased by the molecular relaxation. The Type A holds in the transition of the wave profile due to the molecular relaxation of N_2 at h = 6.039 km as shown in Fig. 4.6(a). As shown in Fig. 4.9(b), in the case of long relaxation time (Type B), the pressure fluctuation is widely decreased, although the energy exchange just behind the shock wave is too small to form the rise time. The Type B holds in the transition of the wave profile due to the molecular relaxation of O_2 at h = 6.039 km as shown in Fig. 4.1(a) and that of N_2 at h = 3 km and 0 km as shown in Figs. 4.6(b) and 4.6(c). As shown in Fig. 4.9(c), in the case of short relaxation time (Type C), the

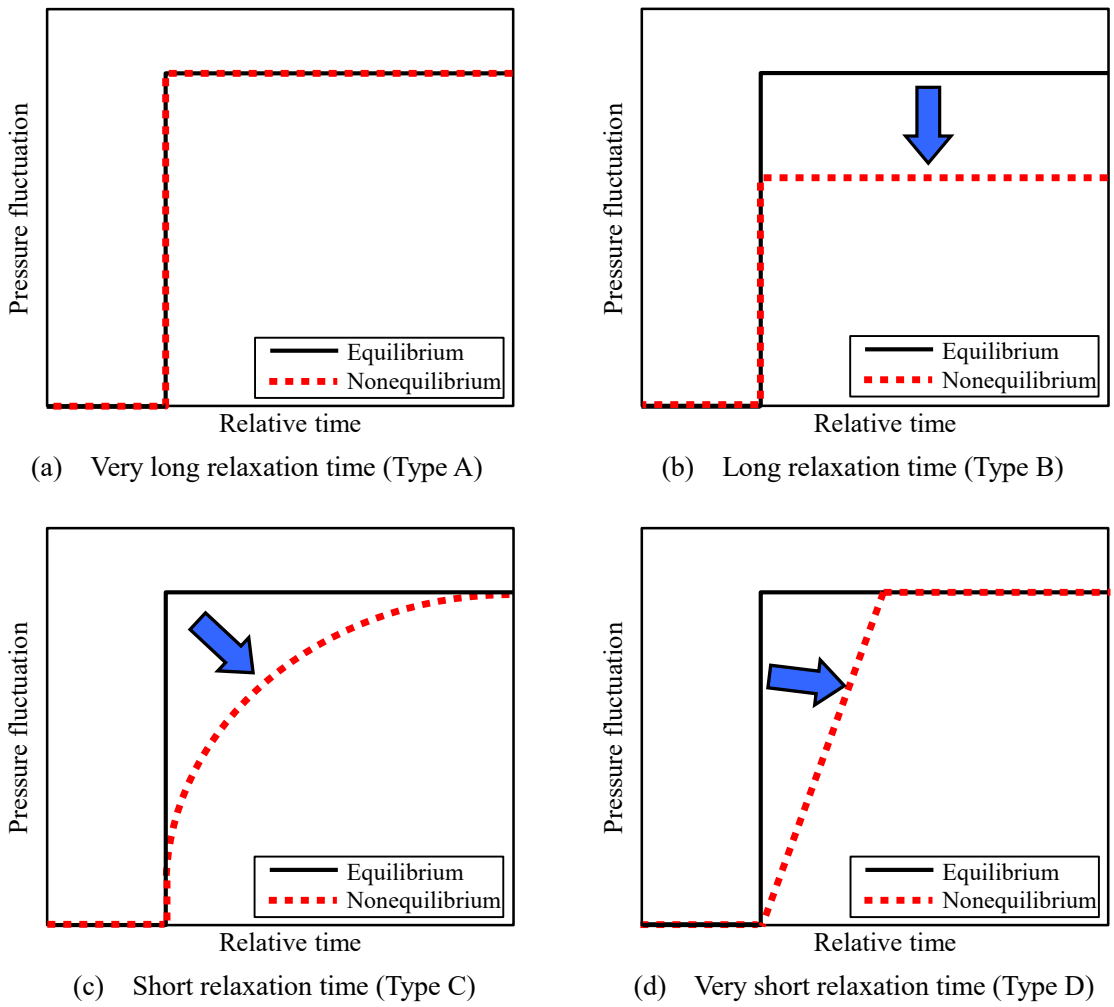

Fig. 4.9 Classification of transition of wave profile due to molecular relaxation.

Table 4.4 Classification of transition of wave profile obtained by simulation

Type	Computational condition	Relaxation time	Waveform
A	Molecular relaxation of N_2 at h = 6.039 km	24.1 ms	Fig. 4.6 (a)
	Molecular relaxation of N_2 at h = 3 km	4.49 ms	Fig. 4.6 (b)
B	Molecular relaxation of O_2 at h = 6.039 km	3.26 ms	Fig. 4.1 (a)
	Molecular relaxation of N_2 at h = 0 km	0.798 ms	Fig. 4.6 (c)
C	Molecular relaxation of O_2 at h = 3 km	0.0967 ms	Fig. 4.1 (b)
D	Molecular relaxation of O_2 at h = 0 km	0.00824 ms	Fig. 4.1 (c)

significant energy exchange converges just behind the shock wave, and as a result the pressure fluctuation is partially decreased behind the shock wave, and the long rise time is formed. The Type C holds in the transition of the wave profile due to the molecular relaxation of O_2 at h = 3 km as shown in Fig. 4.1(b). As shown in Fig. 4.9(d), in the case of very short relaxation time (Type D), the pressure gradient is significantly decreased. Consequently, the rise time is somewhat formed, although the pressure rise is hardly decreased. The Type D holds in the transition of the wave profile due to the molecular relaxation of O_2 at h = 0 km as shown in Fig. 4.1(c). Therefore, the transition of the wave profile due to the molecular relaxation was successfully classified by the full-field simulation with the thermal nonequilibrium, and this classification is quite helpful in understanding the transition of the wave profile. These results show that the formation mechanism of rise time according to the variation in the atmospheric conditions was well clarified.

4.3.4 Molecular relaxation of O_2 and N_2 in uniform atmosphere (Case G)

Figures 4.10 and 4.11 show the pressure waveforms and the magnitude of the translational-vibrational relaxation term, respectively, at r/L = 1078 in the Case G, as well as those shown in Figs. 4.1, 4.4, 4.6, and 4.7. In Fig. 4.11(c), numerical errors were generated because the relaxation time of O_2 in the uniform atmosphere at h = 0 km was much faster than the time scale of the flow, and the computational method was not robust enough to reduce numerical errors caused by the difference of the time scale between the translational-vibrational relaxation and the flow. However, because the pressure waveform in the uniform atmosphere at h = 0 km was not fluctuated, the error is assumed to have little effect on the pressure waveform. As can be seen in Fig. 4.10, the mixed effects of molecular relaxation with respect to O_2 and N_2 are approximately evaluated as the superposition of each effect; i.e., the pressure waveforms in the Case G can be approximately obtained as follows:

$$\Delta p_{Nonequilibrium(O_2+N_2)} \approx \Delta p_{Nonequilibrium(O_2)} + \Delta p_{Nonequilibrium(N_2)} - \Delta p_{Equilibrium} \tag{4.5}$$

Figure 4.12 shows the pressure waveforms in the Case G and those calculated by the right-hand side of Eq. (4.5) where the pressure fluctuation in all cases was periodically resampled by the linear interpolation in the sampling interval of 0.04 ms. As shown in Fig. 4.12, the pressure waveforms are in good agreement with each other regardless of the atmospheric conditions; thus, the approximation given by Eq. (4.5) seems quite reasonable. Therefore, the transition of wave profile due to the molecular relaxation of O_2 and N_2 is explained as follows. In the case of uniform atmosphere at h = 6.039 km, the molecular relaxation of O_2 is the dominant effect because that of N_2 hardly affects the pressure waveform, as shown in Figs. 4.10(a) and 4.11(a). Consequently, the pressure fluctuation is widely decreased by the effect of molecular relaxation of O_2, although the rise time is not formed. In the case of uniform atmosphere at h = 3 km, the translational energy is mainly converted to the vibrational energy of O_2 just behind the shock wave, and it is mainly converted to the vibrational energy of N_2 from the relative time of approximately 0.8 ms, as shown in Fig. 4.11(b). Consequently, the pressure fluctuation just behind the shock wave is significantly decreased by the molecular relaxation of O_2, and the rise time is formed, as shown in Fig. 4.10(b), because the effect of molecular relaxation of O_2 is stronger than the nonlinear effect. In addition, the pressure fluctuation behind the shock wave is widely decreased by the molecular relaxation of N_2. In the case of uniform atmosphere at h = 0 km, the translational energy is mainly converted to the vibrational energy of O_2 just behind the shock wave, and it is mainly converted to the vibrational energy of N_2 from the relative time of approximately 0.25 ms, as shown in Fig. 4.11(c). Consequently, the high pressure gradient caused by the shock wave is decreased by the molecular relaxation of O_2, and the pressure fluctuation behind the shock wave is widely decreased by the molecular relaxation of N_2, as shown in Fig. 4.10(c). These results show that the molecular relaxation of O_2 and N_2 must be simultaneously considered in the simulation. Moreover, it can be seen that the pressure rise in the uniform atmosphere at h = 6.039 km is the lowest in all cases, and the rise time in the uniform atmosphere at h = 3 km is the longest.

Figures 4.13 and 4.14 show the variation in the pressure and the magnitude of the translational-vibrational relaxation terms, respectively, near the front shock wave in the Case G, as well as those shown in Figs. 4.5 and 4.8. As shown in Fig. 4.14, the relaxation term of O_2 in the Case G is almost the same as that in the Case E shown in Fig. 4.5 because the molecular relaxation of O_2 is stronger than that of N_2. On the other hand, the relaxation term of N_2 in the Case G differs from that in the Case F shown in Fig. 4.8, because the rise time is formed by the effect of molecular relaxation of O_2, and the exchange velocity is decreased. As shown in Fig. 4.13, the wave profile in the Case G is almost the same as that in the Case E because it is mainly smoothed by the molecular relaxation of O_2, although the pressure fluctuation is decreased by the molecular relaxation of N_2.

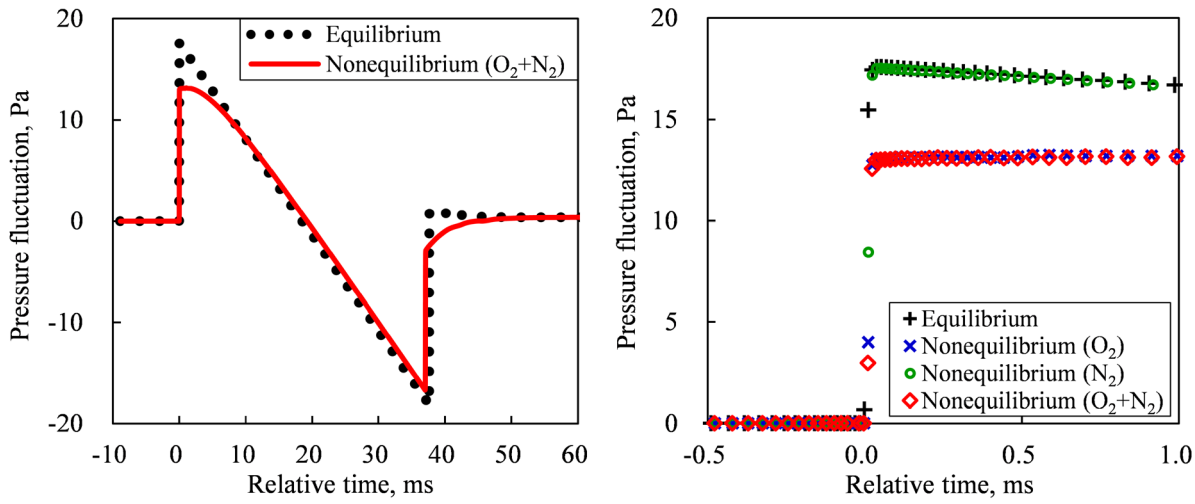

(a) Uniform atmosphere at h = 6.039 km

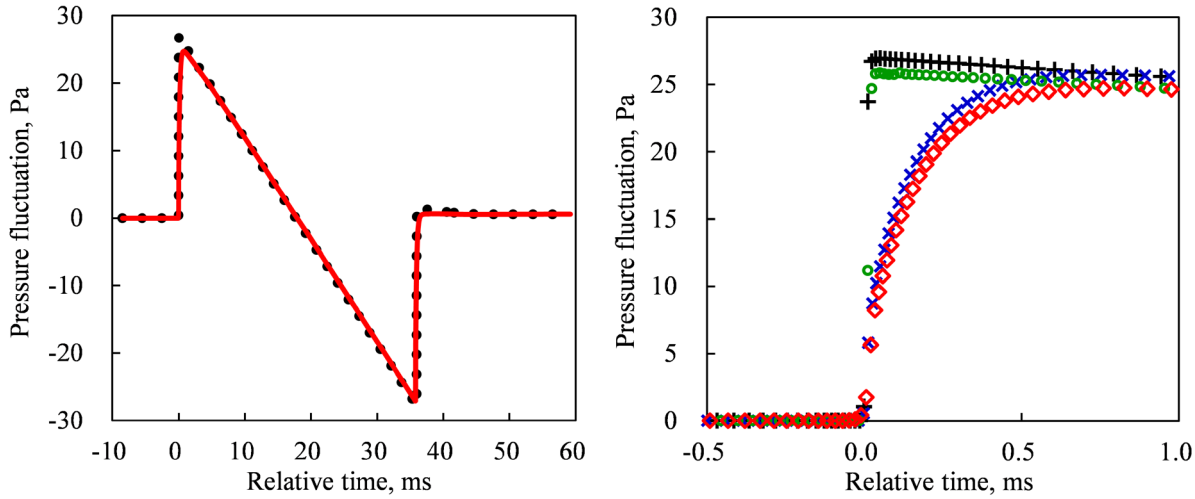

(b) Uniform atmosphere at h = 3 km

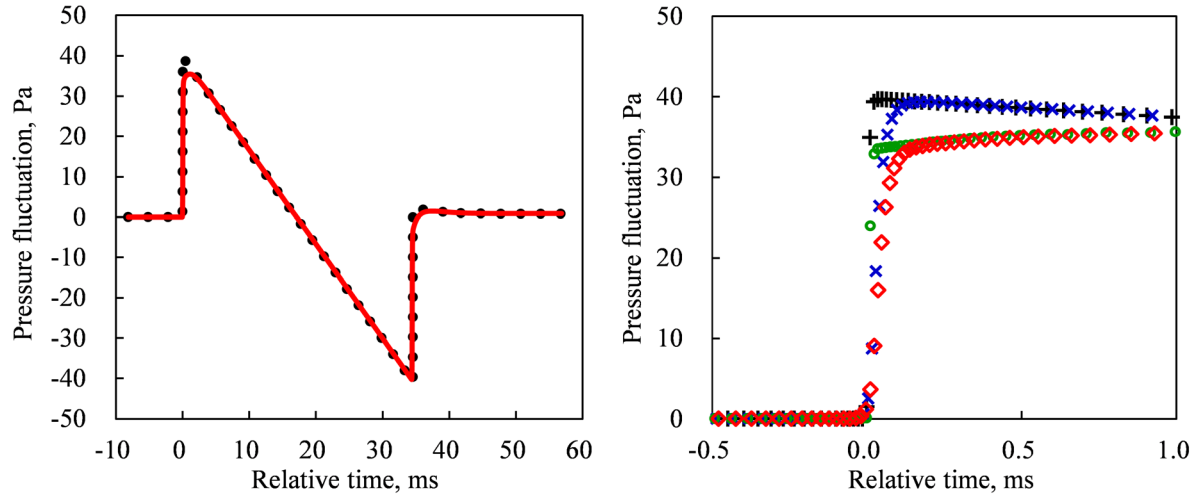

(c) Uniform atmosphere at h = 0 km

Fig. 4.10 Pressure waveforms at r/L = 1078 in Case G where molecular relaxation of O_2 and N_2 is considered (Left: overall view, Right: Closeup of front shock wave).

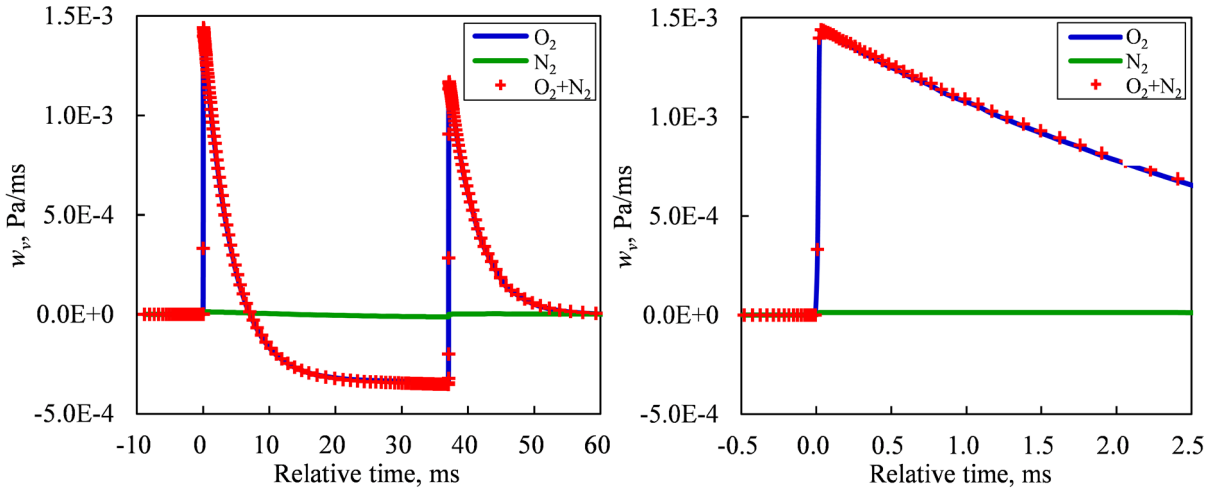

(a) Uniform atmosphere at h = 6.039 km

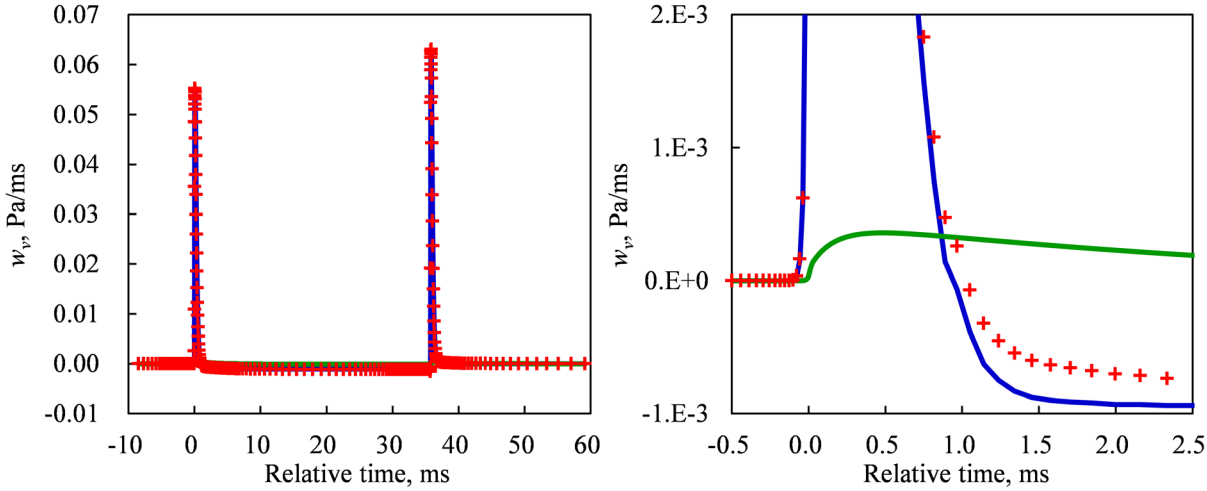

(b) Uniform atmosphere at h = 3 km

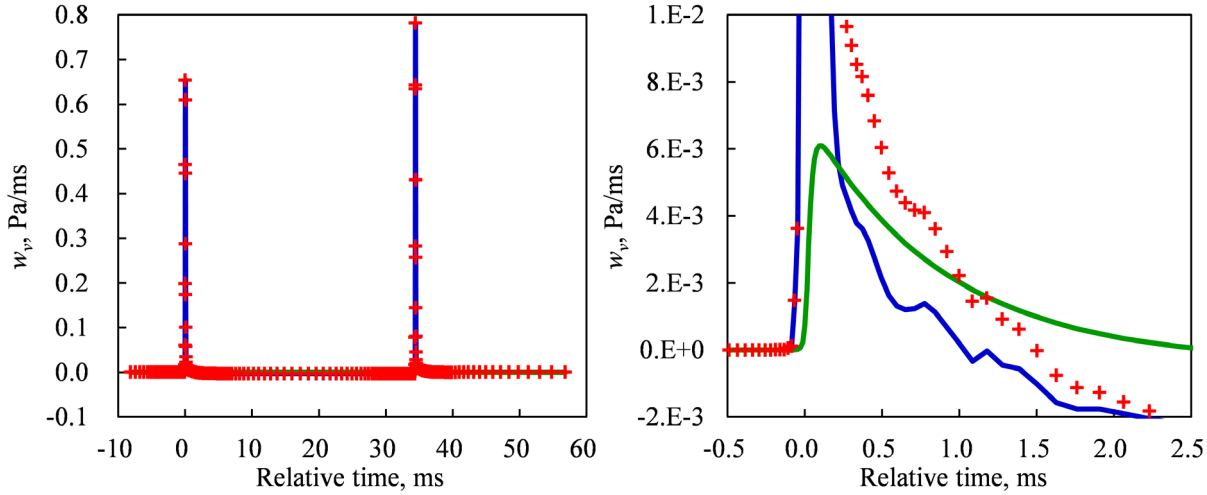

(c) Uniform atmosphere at h = 0 km

Fig. 4.11 Magnitude of relaxation term at r/L = 1078 in Case G where molecular relaxation of O_2 and N_2 is considered (Left: overall view, Right: Closeup of front shock wave).

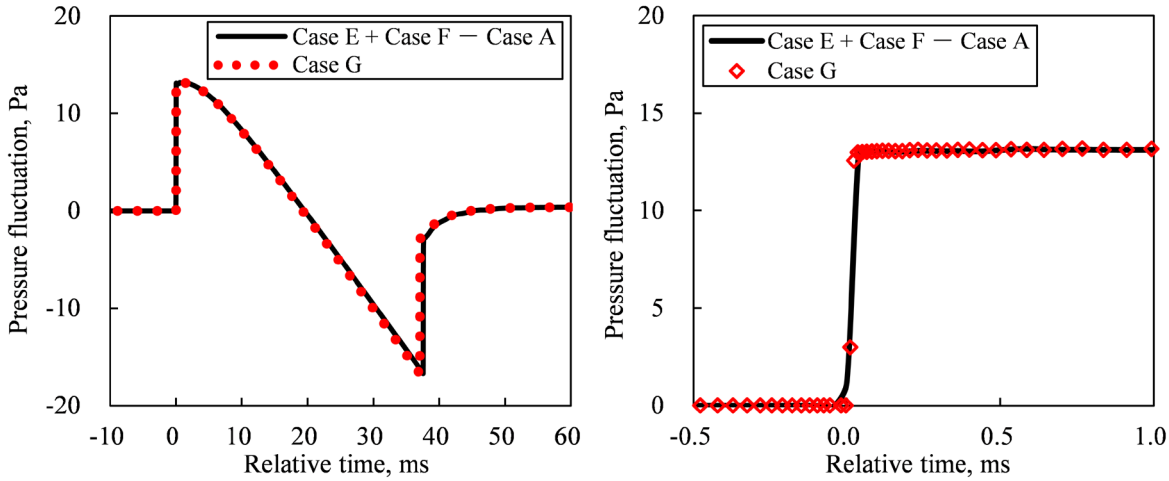

(a) Uniform atmosphere at h = 6.039 km

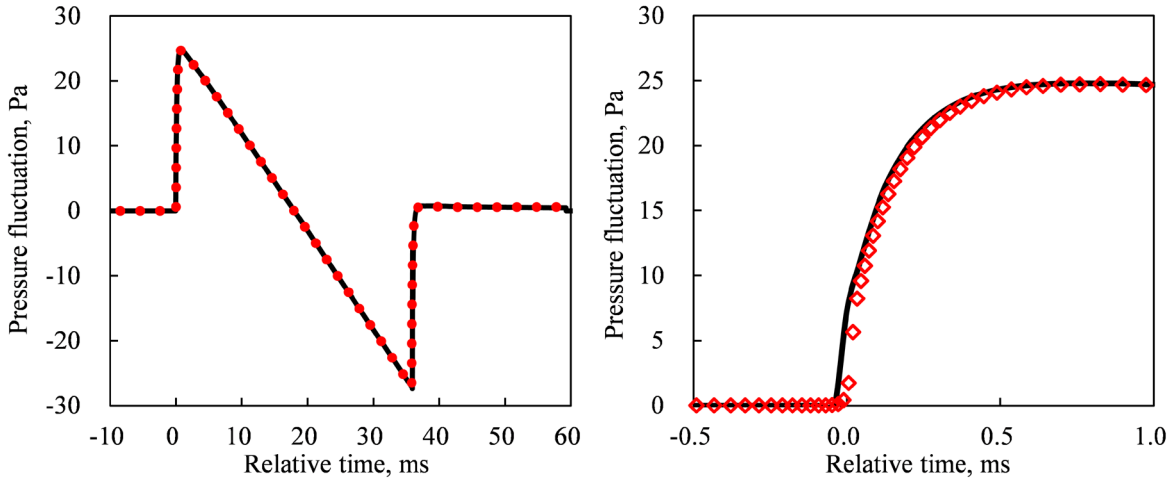

(b) Uniform atmosphere at h = 3 km

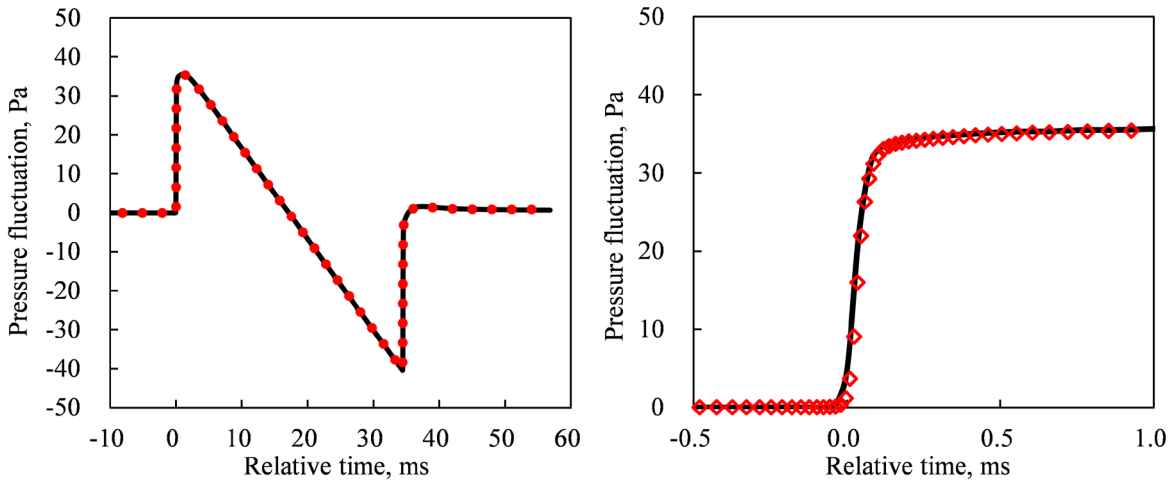

(c) Uniform atmosphere at h = 0 km

Fig. 4.12 Pressure waveforms at r/L = 1078 in Case G (nonequilibrium of O_2+N_2) and those calculated by combining results in Cases A (equilibrium), E (nonequilibrium of O_2), and F (nonequilibrium of N_2).

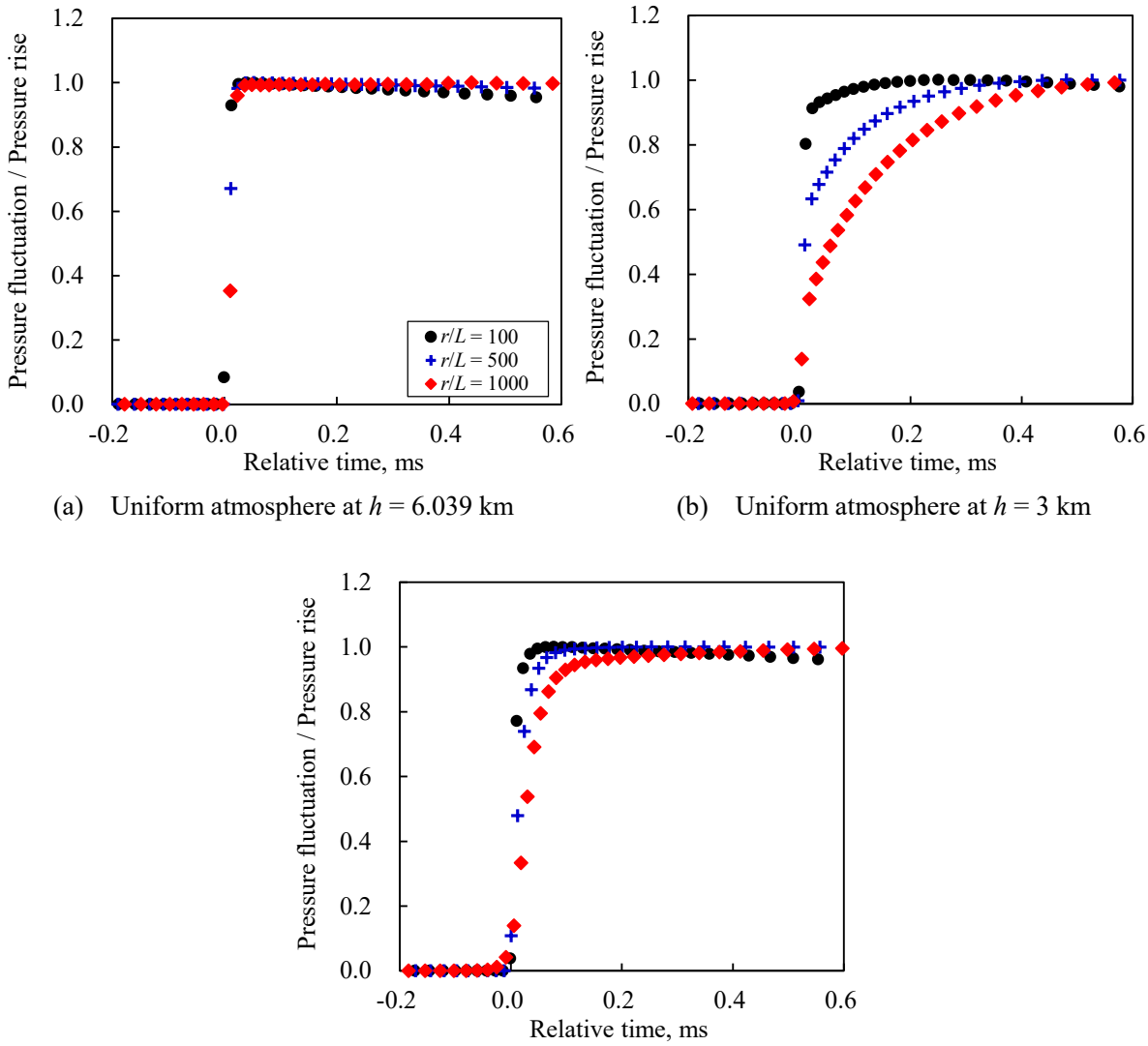

(a) Uniform atmosphere at h = 6.039 km

(b) Uniform atmosphere at h = 3 km

(c) Uniform atmosphere at h = 0 km

Fig. 4.13 Variation in pressure waveform near front shock wave in Case G where molecular relaxation of O_2 and N_2 is considered.

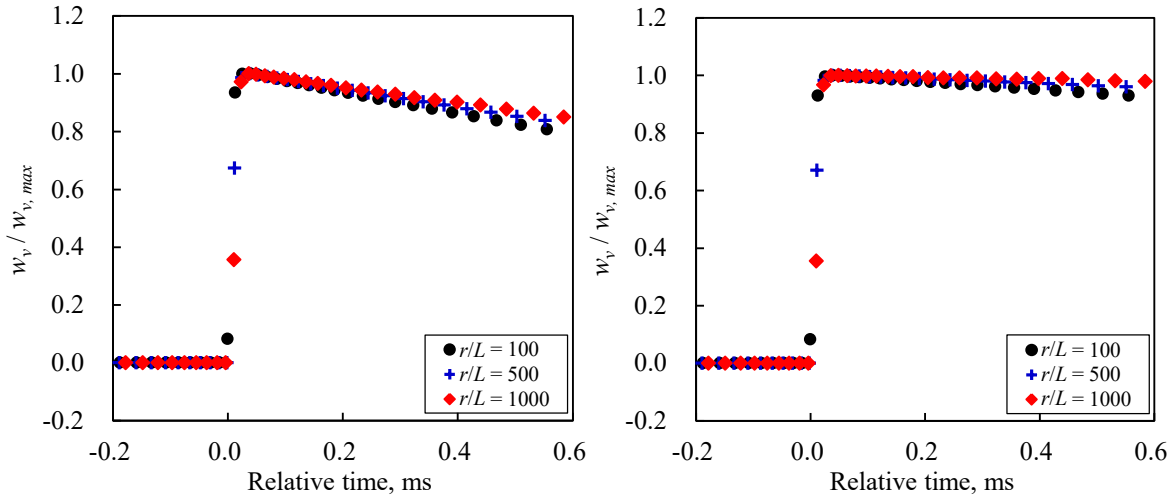

(a) Uniform atmosphere at h = 6.039 km

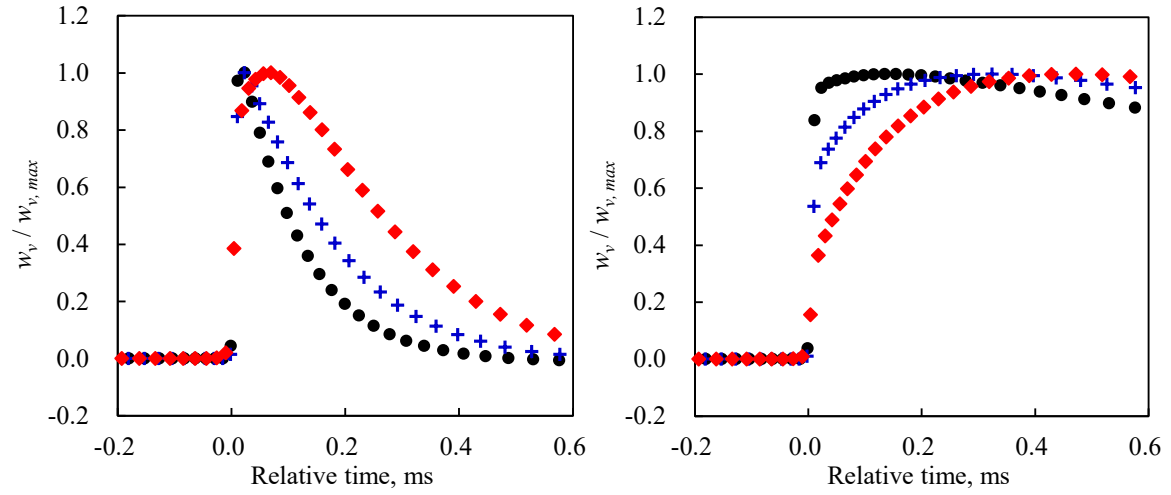

(b) Uniform atmosphere at h = 3 km

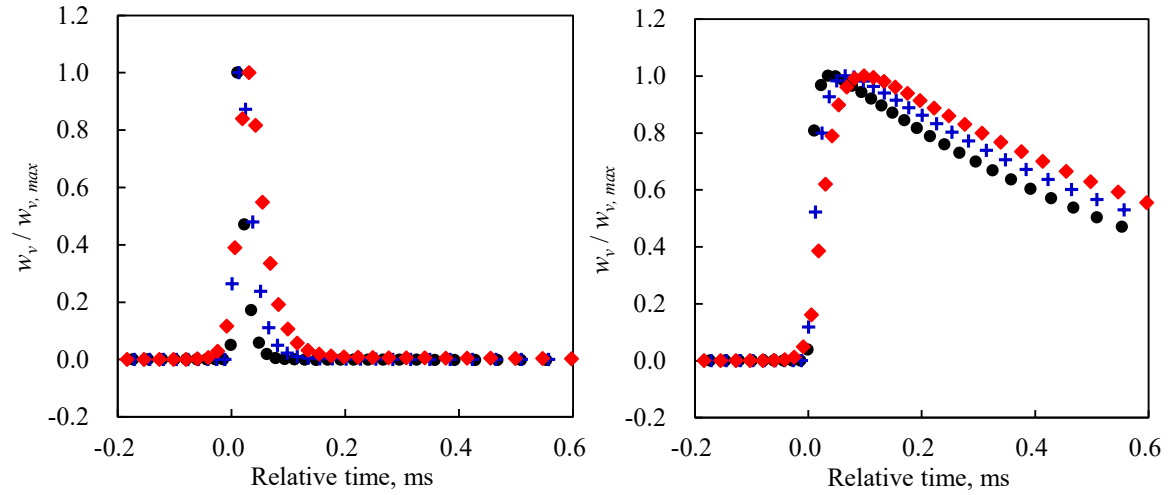

(c) Uniform atmosphere at h = 0 km

Fig. 4.14 Variation in relaxation term near front shock wave in Case G where molecular relaxation of O_2 and N_2 is considered (Left: O_2, Right: N_2).

4.3.5 Molecular relaxation of O_2 and N_2 in stratified atmosphere (Case C)

Figure 4.15 shows the pressure waveforms at h = 0 km on the symmetry plane beneath the body, which was obtained by the simulation with the molecular relaxation of O_2 and N_2 in the stratified atmosphere (Case C). To clarify the effect of molecular relaxation, the pressure waveform in the Case B, where the thermal equilibrium was assumed, is depicted in this figure. Because the accuracy of simulation was already validated by comparison with the D-SEND#1 flight test data in the previous chapter, it was adequate for evaluating the detailed effect of molecular relaxation in the stratified atmosphere. As can be seen in Fig. 4.15, the pressure fluctuation in the thermal nonequilibrium is lower than that in the thermal equilibrium, and the rise time is formed by the effect of molecular relaxation.

Figures 4.16 and 4.17 show the variation in the pressure waveforms and the magnitude of the translational-vibrational relaxation terms, respectively, near the front shock wave in the Case C, as well as those shown in Figs. 4.5, 4.8, 4.13, and 4.14. Note that the distributions shown in Figs. 4.13 and 4.14 are useful for understanding the transition of the pressure waveforms and the relaxation terms, and the exchange velocity of the translational-vibrational energy in the stratified atmosphere increases as the relaxation time decreases toward the ground, as shown in Fig. 3.4. As shown in Fig. 4.17(a), the rate of decrease in the relaxation term of O_2 behind the shock wave increases toward the ground, and as a result the magnitude of the relaxation term is enhanced just behind the shock wave as altitude decreases. On the other hand, as shown in Fig. 4.17 (b), the energy exchange caused by the relaxation term of N_2 hardly converges just behind the shock wave because the relaxation time of N_2 is longer than that of O_2. Therefore, the wave profile is mainly changed by the molecular relaxation of O_2 in the same way as the Case G, where the molecular relaxation of O_2 and N_2 is considered in the uniform atmosphere. As shown in Fig. 4.16(a), the wave profile at h = 5–3.5 km is smoothed in the order of the highest pressure to the lowest one, and the rise time is formed because the relaxation time of O_2 at the altitudes is short enough to make the significant energy exchange converge just behind the shock wave. As shown in Fig. 4.16(b), the wave profile at h = 3.5–0.5 km is dramatically changed by the variation in the atmospheric properties with altitude because of the following reason: the relaxation time at the low altitudes is too short to form the long rise time, and as a result the high pressure gradient is relaxed by the effect of molecular relaxation with respect to O_2, whereas the low pressure gradient is steepened by the nonlinear effect. Figure 4.18 shows the schematic of the variation in the wave profile toward the ground. As the wave profile is mainly changed by the molecular relaxation of O_2, it is assumed to be changed from the Types B to D shown in Fig. 4.9 toward the ground; thus, it can be seen that the wave profile at the high to middle altitudes is assumed to be changed from the Types B to C as shown in Fig. 4.18(a), and that at the middle to low altitudes is assumed to be changed from the Types C to D as shown in Fig. 4.18(b). These results show that the transitional process of the wave

profile in the stratified atmosphere was well clarified using the classification method of the transition of the wave profile shown in Fig. 4.9, although the complex change of the wave profile occurred.

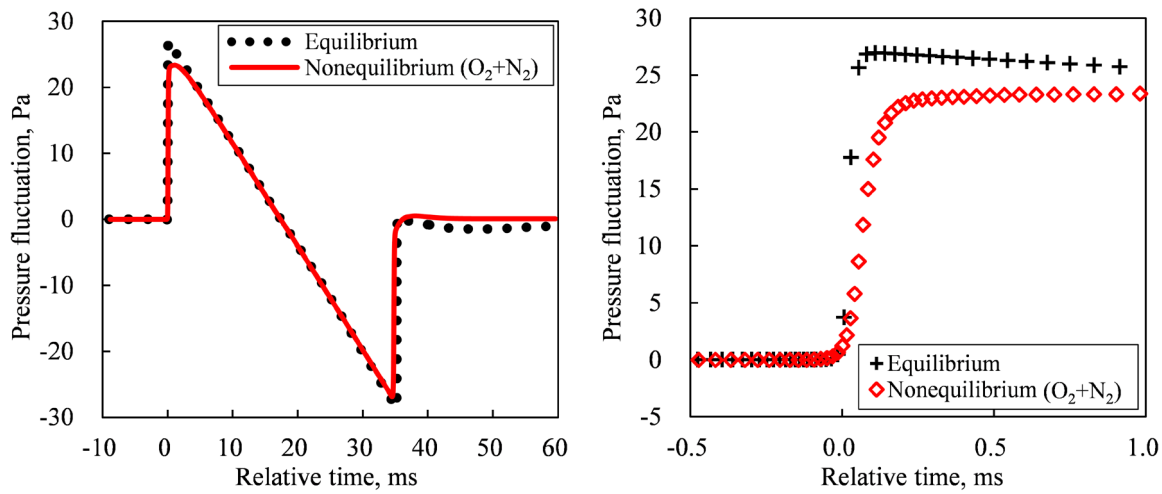

Fig. 4.15 Pressure waveforms at *h* = 0 km on the symmetry plane beneath the body in Case C where molecular relaxation of O_2 and N_2 in stratified atmosphere is considered (Left: overall view, Right: Closeup of front shock wave).

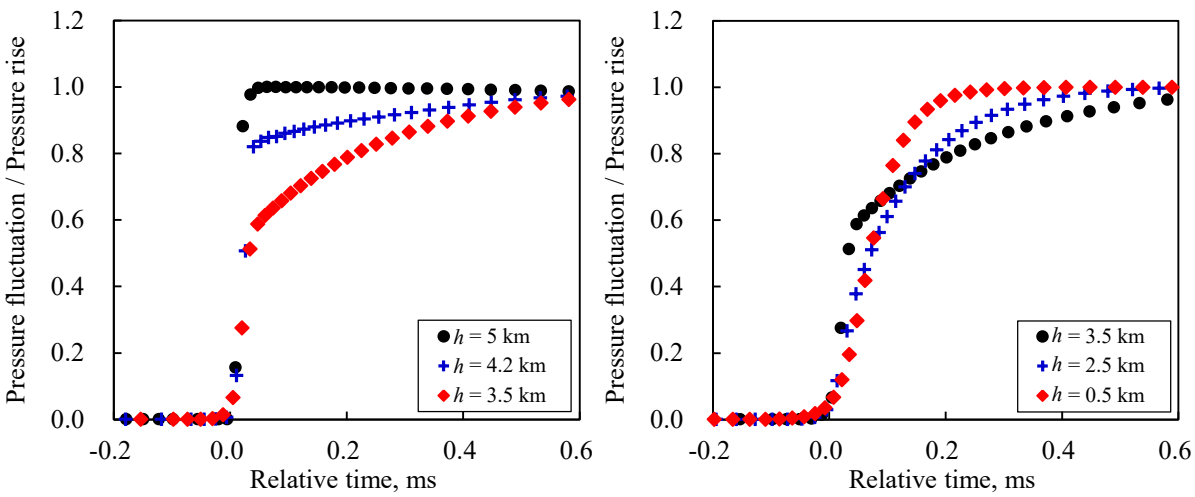

(a) High altitude (b) Low altitude

Fig. 4.16 Variation in pressure waveform on the symmetry plane beneath the body near front shock wave obtained by simulation with molecular relaxation of O_2 and N_2 in stratified atmosphere (Case C).

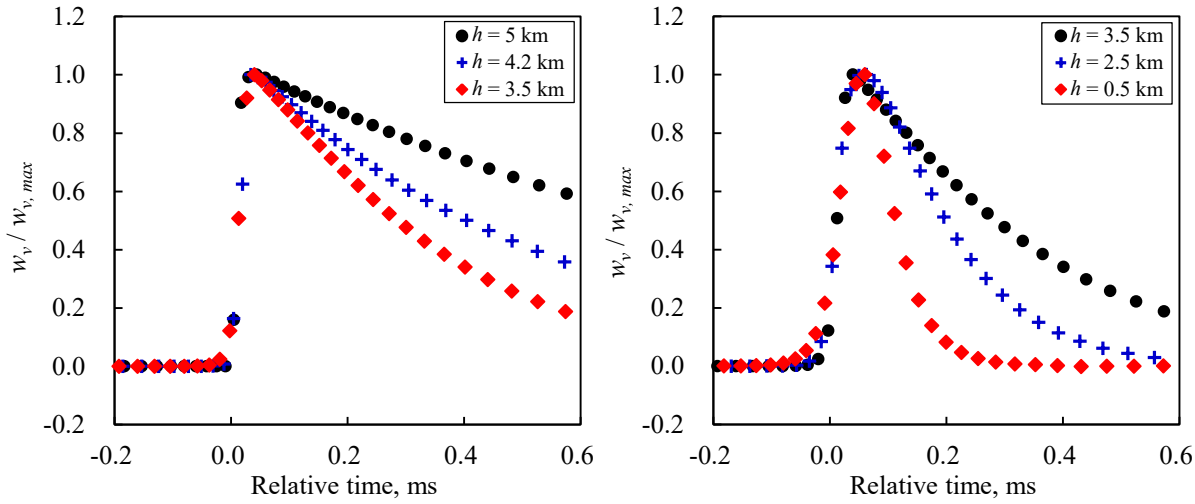

(a) Molecular relaxation of O_2

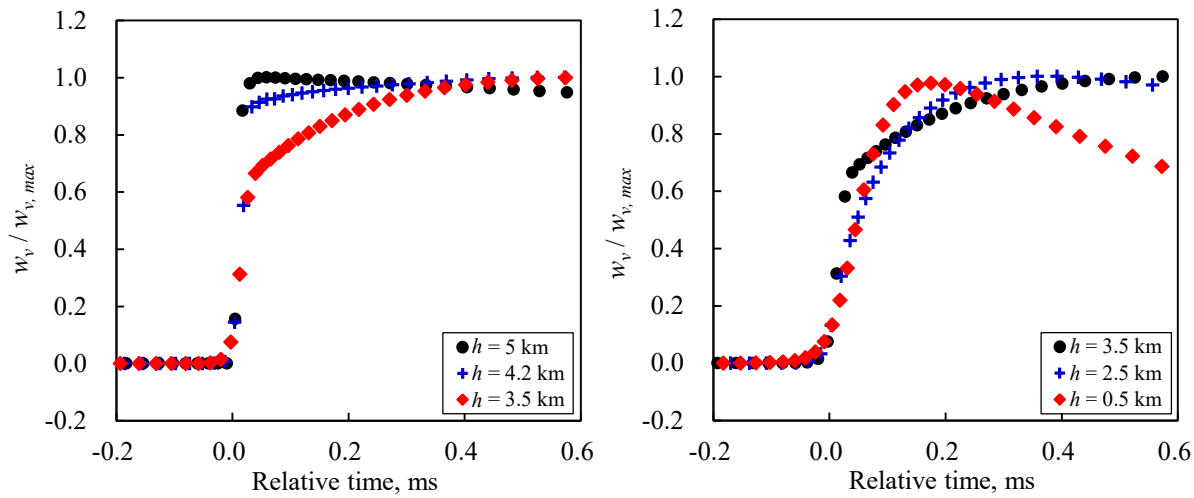

(b) Molecular relaxation of N_2

Fig. 4.17 Variation in relaxation term on the symmetry plane beneath the body obtained by simulation with thermal nonequilibrium of O_2 and N_2 in stratified atmosphere (Case C).

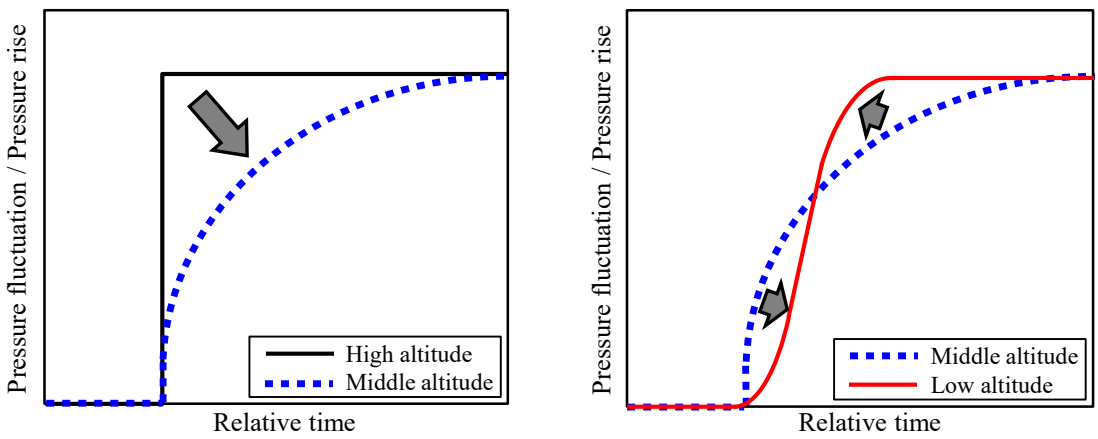

(a) High to middle altitudes (Types B to C) (b) Middle to low altitudes (Types C to D)

Fig. 4.18 Schematic of variation of wave profile in stratified atmosphere toward the ground.

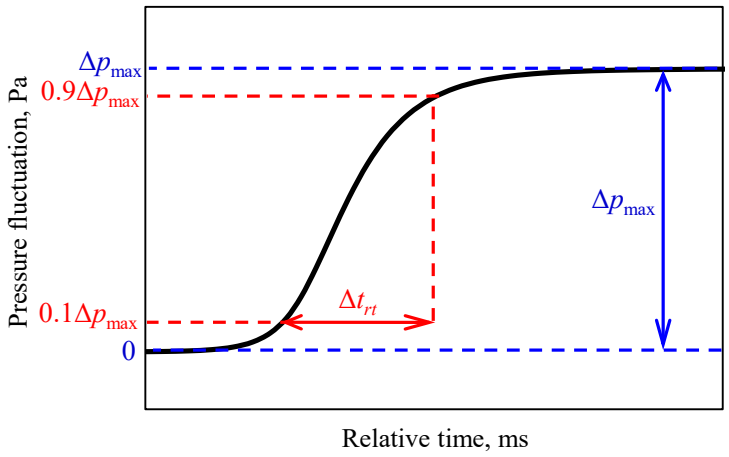

Fig. 4.19 Definition of pressure rise of front shock wave Δp_{max} and rise time Δt_{rt}.

4.3.6 Pressure rise and rise time

Pressure rise and rise time, which are the most important parameters for evaluating sonic boom intensity, are investigated in this section. Figure 4.19 shows the definition of the pressure rise Δp_{max} and its rise time Δt_{rt}. The rise time is defined as the time that it takes the pressure fluctuation to change from 10 % to 90 % of the pressure rise in this chapter.

Figure 4.20 shows the pressure rise of the front shock wave and the rise time in the uniform atmosphere. In the case of thermal equilibrium, the rise time in the far field is zero theoretically, although it was approximately 0.01 to 0.02 ms because the simulation was performed by the discrete grid points. However, there was little change of the rise time in the far field, and thus the rise time longer than the grid resolution is assumed to be reliable. Note that the distributions shown in Figs. 4.5, 4.8, and 4.13 are useful for understanding the variation in the pressure rise and rise time. As shown in Fig. 4.20, the pressure rise in the near field decreases rapidly, whereas that in the far field decreases slowly because the effect of geometrical spreading of the front shock wave weakens as the radial distance increases. The results show that the strength of nonlinearity decreases with increasing the radial distance because the effect of nonlinear wave steepening is caused by the difference of the propagation speed of waves that is correlated with the pressure rise. The pressure rise in the thermal nonequilibrium is smaller than that in the thermal equilibrium because it is decreased by the effect of molecular relaxation. Table 4.5 shows the difference in the pressure rise of the front shock wave at r/L = 1078 obtained by the simulation with the thermal nonequilibrium relative to the thermal equilibrium. As can be seen in this table, the decrease of the pressure rise in the Case G is expressed as the superposition of that in the Cases E and F as shown in Fig. 4.12. The largest decrease in the pressure rise is caused by the molecular relaxation of O_2 at h = 6.039 km, and the second largest decrease is caused by the molecular relaxation of N_2 at h = 0 km. The results show that the pressure rise is

significantly decreased when the relaxation time is approximately 0.8–3.3 ms as shown in Table 4.2. As shown in Fig. 4.20, the rise time in the near field decreases rapidly because the compression waves behind the front shock wave shown in Fig. 3.10 are integrated with the front shock wave, and it does not change until r/L = 110 because the nonlinear effect in the near field is much stronger than the effect of molecular relaxation. Thereafter, the variation in the rise time differs according to the atmospheric conditions. The rise time in the uniform atmosphere at h = 6.039 km hardly changes because the effect of molecular relaxation is weaker than the nonlinear effect, whereas that at h = 3 km and 0 km monotonically increases with increasing the radial distance because the effect of molecular relaxation is stronger than the nonlinear effect. The results show that the exchange rate of translational-vibrational energy is almost constant (see next section for details). The largest increase in the rise time is caused by the molecular relaxation of O_2 at h = 3 km. Hence, it can be seen that the long rise time is formed when the relaxation time is approximately 0.1 ms as shown in Table 4.2, and the rise time significantly depends on the atmospheric conditions.

Figure 4.21 shows the pressure rise of the front shock wave and the rise time in the stratified atmosphere. Although the rise time in the thermal equilibrium was approximately 0.01 to 0.05 ms in the far field, that in the thermal nonequilibrium longer than the grid resolution as well as Fig. 4.20 is assumed to be reliable. Note that the distributions shown in Fig. 4.16 are useful for understanding the variation in the pressure rise and rise time. In the case of stratified atmosphere, the pressure rise decreases more slowly than that in the uniform atmosphere because the atmospheric properties in the stratified atmosphere increase toward the ground. In the case of thermal nonequilibrium relative to the thermal equilibrium, the pressure rise decreased by 13.2 % at h = 0 km because of the molecular relaxation. The rise time in the near field changes in the same way as the case of uniform atmosphere shown in Fig. 4.20, because the nonlinear effect is stronger than the effect of molecular relaxation until h = 4.4 km. However, the rise time in the far field increases and decreases toward the ground. The rise time at h = 4.4–3.7 km increases rapidly because the effect of molecular relaxation is stronger than the nonlinear effect, whereas that at h = 3.7–0 km decreases gradually because the nonlinear effect is stronger than the effect of molecular relaxation. These results show that the rise time in the stratified atmosphere was dramatically changed because the strength of molecular relaxation and nonlinearity significantly changed with altitude.

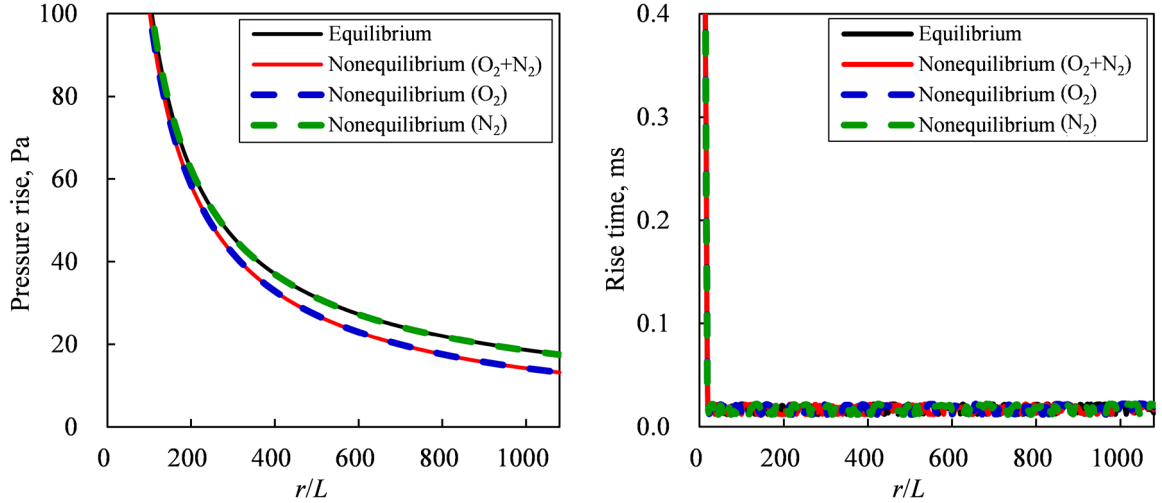

(a) Uniform atmosphere at h = 6.039 km

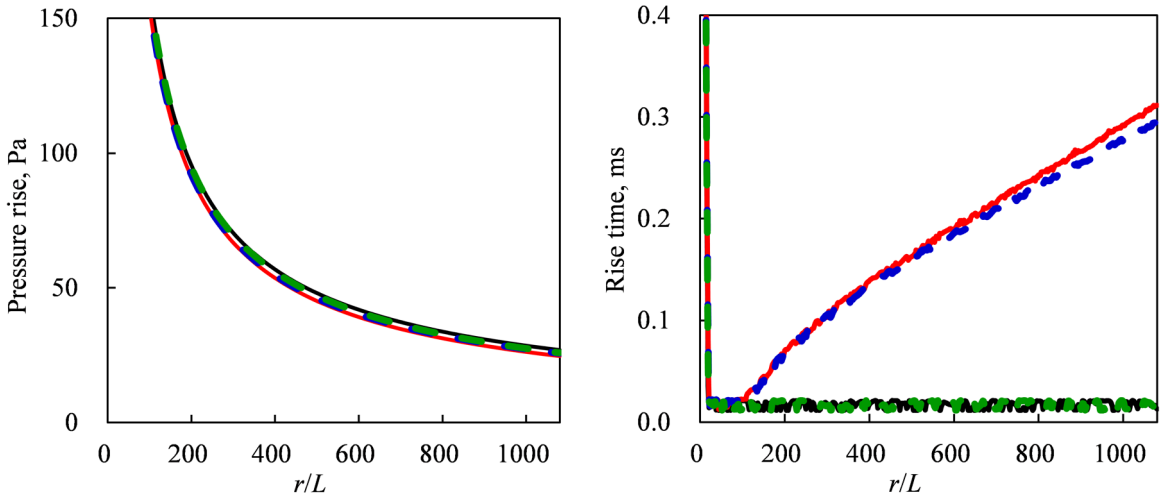

(b) Uniform atmosphere at h = 3 km

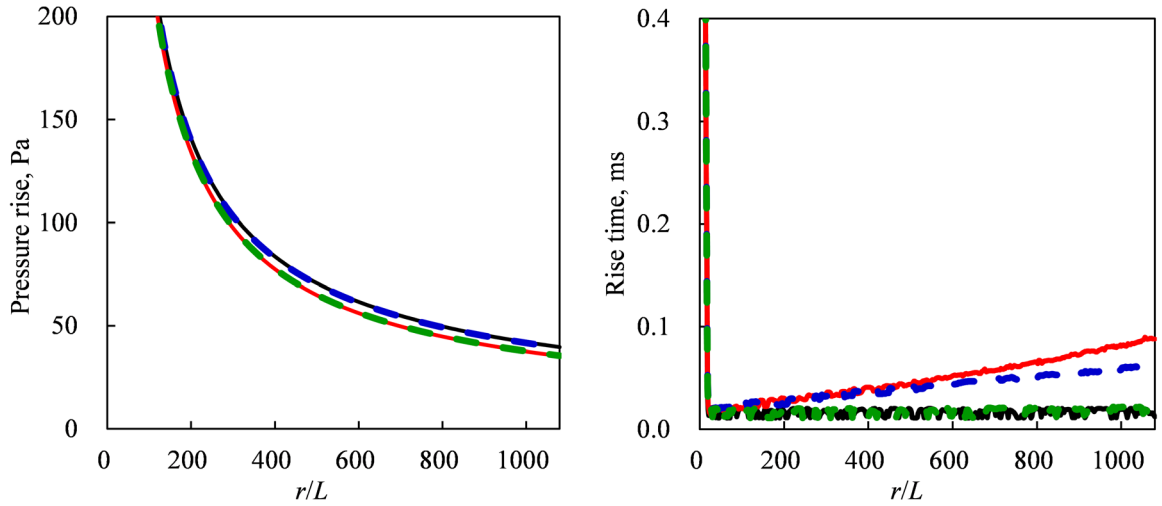

(c) Uniform atmosphere at h = 0 km

Fig. 4.20 Sonic boom intensity in uniform atmosphere (Left: pressure rise, Right: rise time).

Table 4.5 Difference in pressure rise of front shock wave at r/L = 1078 obtained by simulation with thermal nonequilibrium relative to thermal equilibrium (Case A)

	h = 6.039 km	h = 3 km	h = 0 km
Case E: Molecular relaxation of O_2	–24.7%	–4.6%	–0.8%
Case F: Molecular relaxation of N_2	–0.4%	–4.0%	–10.2%
Case G: Molecular relaxation of O_2+N_2	–25.0%	–8.3%	–10.6%

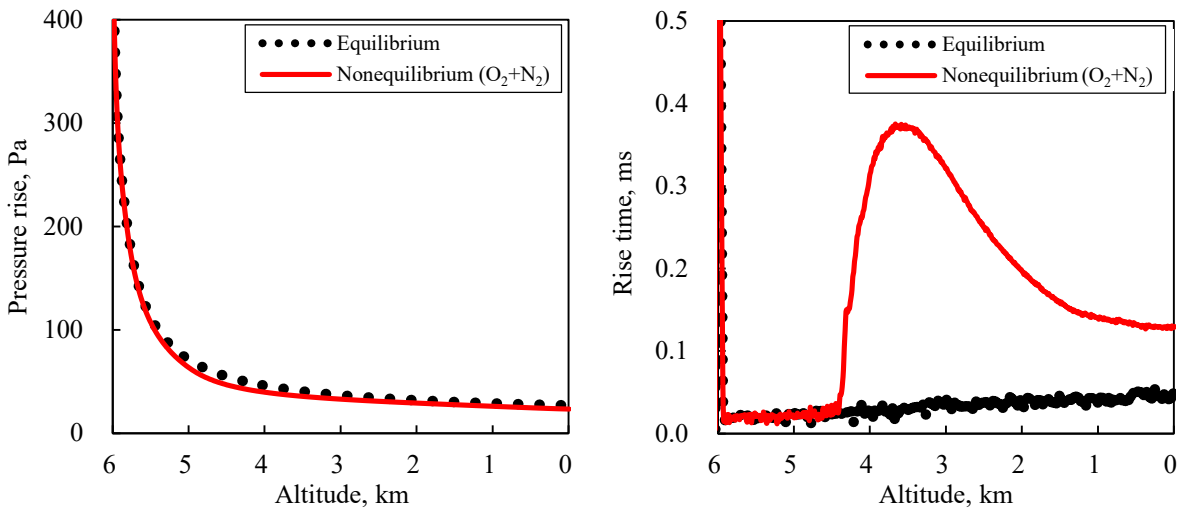

Fig. 4.21 Sonic boom intensity in stratified atmosphere (Left: pressure rise, Right: rise time).

4.3.7 Strength of molecular relaxation

Strength of molecular relaxation can be evaluated by two parameters: the maximum exchange rate of translational-vibrational energy and its exchange time. The maximum exchange rate is defined as the maximum value of the relaxation term $w_{v,\,\max}$ divided by the maximum increase in the translational energy per unit volume $\Delta e_{tr,\,\max}$ given by the following equation:

$$\Delta e_{tr,\max} = \frac{\Delta p_{\max}}{\gamma - 1} \tag{4.6}$$

As can be seen from Eq. (4.6), the maximum increase in the translational energy is proportional to the pressure rise of the front shock wave. The exchange time Δt_{ex} is defined as the relative time when the magnitude of the relaxation term becomes zero behind the front shock wave. Figure 4.22 shows the definition of the maximum value of the relaxation term and the exchange time.

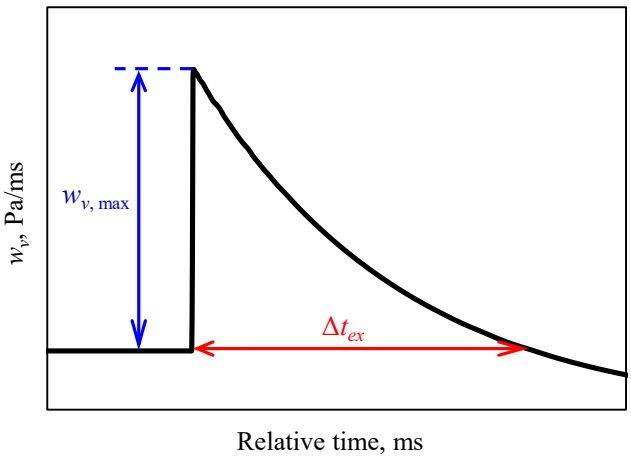

Fig. 4.22 Definition of maximum value of relaxation term $w_{v,\ max}$ and exchange time of translational-vibrational energy Δt_{ex}.

Maximum exchange rate of translational-vibrational energy

Figure 4.23 shows the variation in the maximum exchange rate of translational-vibrational energy in the uniform atmosphere (Cases E, F, and G). In the case of uniform atmosphere at h = 0 km, small numerical errors as well as Fig. 4.11 (c) were generated. Note that the distributions shown in Fig. 4.20 are useful for understanding the variation in the maximum exchange rate that depends on the pressure rise and rise time, and the relaxation time is almost constant when the uniform properties of atmosphere is assumed in the entire computational domain because of the following reason: Although the relaxation time given by Eqs. (2.12) and (2.13) depends on the pressure, temperature, and absolute humidity, the absolute humidity is set as the constant value in the entire computational domain, and the fluctuation of pressure and temperature caused by waves is much smaller than the atmospheric pressure and temperature, respectively. As shown in Fig. 4.23, the maximum exchange rate in the near field increases as the rise time decreases. In the uniform atmosphere at h = 6.039 km, the maximum exchange rate in the far field hardly changes because the rise time is not formed. In the cases of uniform atmospheres at h = 3 km and 0 km, the maximum exchange rate due to the molecular relaxation of O_2 decreases linearly with increasing the radial distance as shown in Fig. 4.23(a), because the rise time is formed, and the rapid increase in the translational energy caused by the shock wave is relaxed. As shown in Fig. 4.23(b), the maximum exchange rate due to the molecular relaxation of N_2 hardly changes with the radial distance because the rise time is not formed. As shown in Fig. 4.23(c), the maximum exchange rates due to the molecular relaxation of O_2 and N_2 in the Case G are almost the same as those in the Cases E and F, respectively. However, because the rise time is formed by the molecular relaxation of O_2, the maximum exchange rate of N_2 slightly decreases with the radial distance. As the relaxation time decreases with decreasing altitude, the translational-vibrational energy exchange converges just behind the shock wave, and as a result the maximum exchange rate increases with

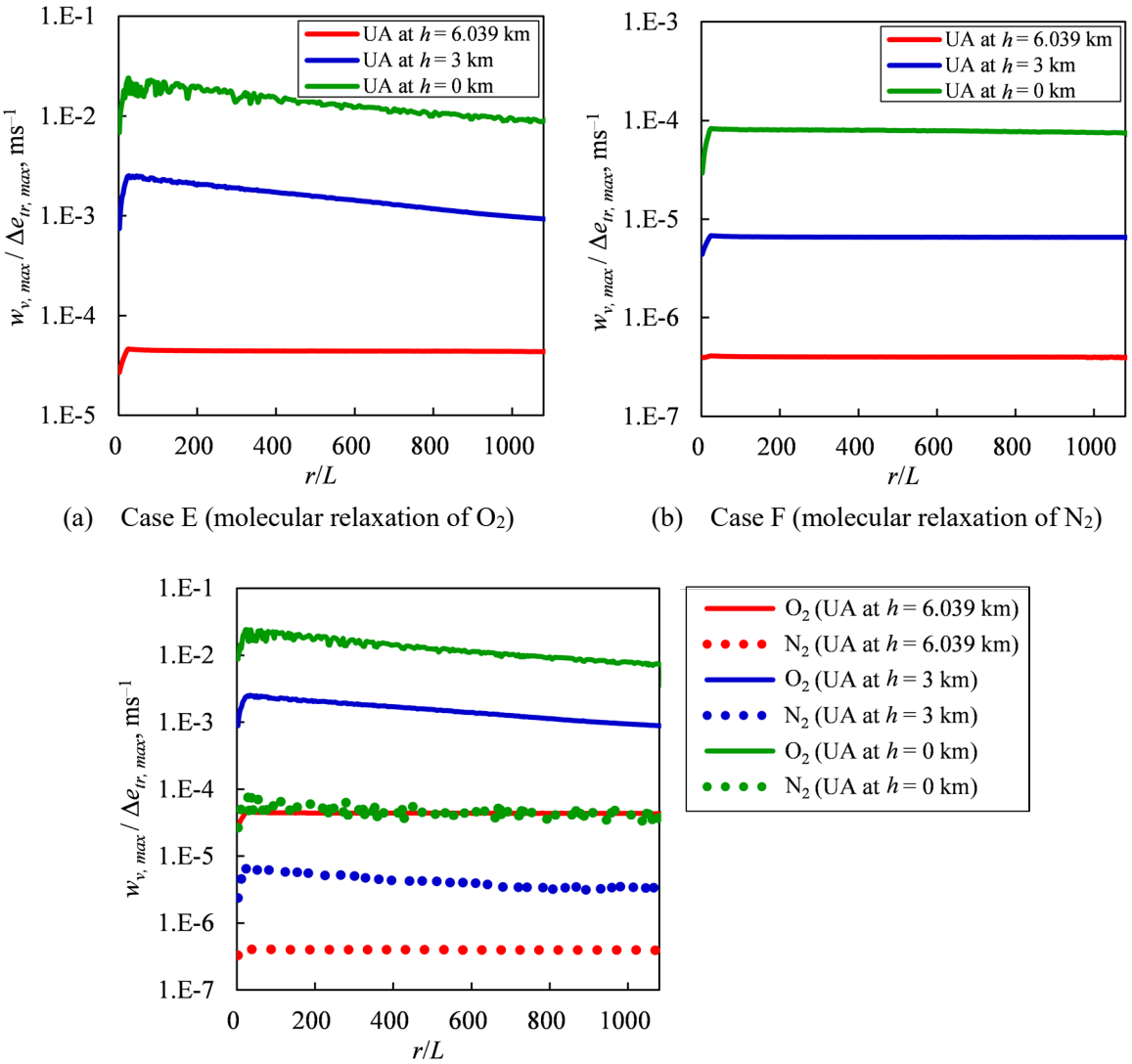

(a) Case E (molecular relaxation of O_2)

(b) Case F (molecular relaxation of N_2)

(c) Case G (molecular relaxation of O_2 and N_2)

Fig. 4.23 Maximum exchange rate of translational-vibrational energy in uniform atmosphere (UA).

decreasing altitude. These results show that strength of molecular relaxation can be evaluated by the maximum exchange rate depending on the relaxation time, and the transition of wave profile caused by the molecular relaxation can be well classified according to the relaxation time, as shown in Fig. 4.9.

Figure 4.24 shows the variation in the inverse of maximum exchange rate with relaxation time in the uniform atmosphere (Cases E, F, and G). As shown in this figure, the inverse of the maximum exchange rate increases linearly as the relaxation time increases; i.e., the inverse of the maximum exchange rate and the relaxation time obey the power law, which is convenient for understanding the strength of molecular relaxation. Tables 4.6 and 4.7 show the equations of the fitted curves on the inverse of the maximum exchange rate and the relaxation time. Note that the number of sampling points was only three, and it should be increased to obtain the more accurate relation. However, because the high degree of curve fit is

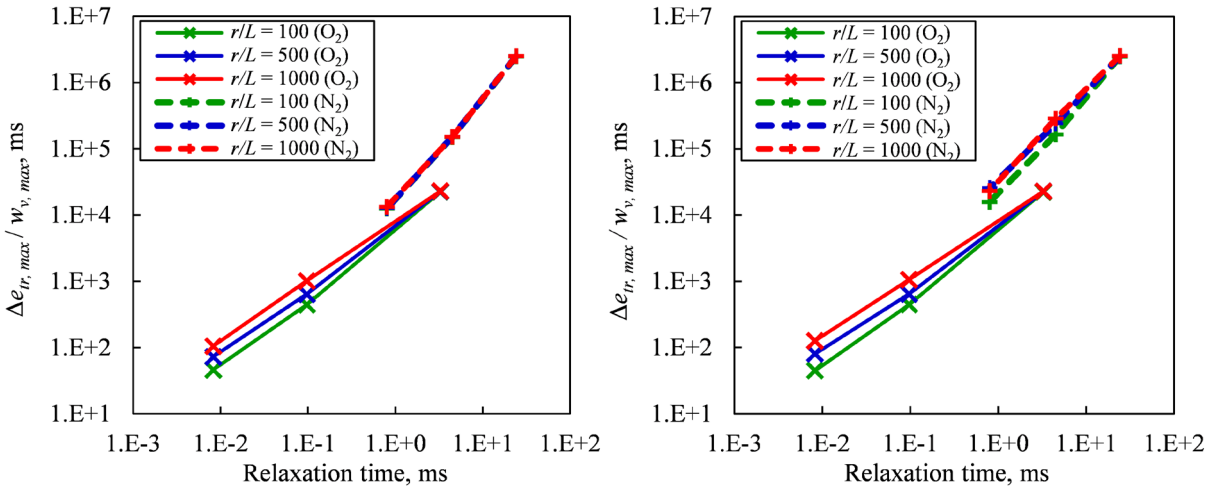

(a) Cases E and F (b) Case G

Fig. 4.24 Variation in inverse of maximum exchange rate of translational-vibrational energy relative to relaxation time in uniform atmosphere.

Table 4.6 Fitted curve on inverse of maximum exchange rate of translational-vibrational energy and relaxation time in Cases E and F

	O_2		N_2	
r/L	Fitted curve	Degree of curve fit	Fitted curve	Degree of curve fit
100	$y = 6{,}070\,x^{1.039}$	$R^2 = 0.9973$	$y = 16{,}545\,x^{1.554}$	$R^2 = 0.9982$
500	$y = 6{,}895\,x^{0.964}$	$R^2 = 0.9985$	$y = 16{,}798\,x^{1.552}$	$R^2 = 0.9982$
1000	$y = 8{,}028\,x^{0.899}$	$R^2 = 0.9999$	$y = 17{,}429\,x^{1.539}$	$R^2 = 0.9978$

obtained in all cases as shown in Tables 4.6 and 4.7, the fitted curves are quite helpful in understanding the variation in the effect of molecular relaxation with the relaxation time. As shown in Tables 4.6 and 4.7, the order of the power for the molecular relaxation of O_2 differs from that for the molecular relaxation of N_2 because the oxygen concentration in air is lower than the nitrogen concentration, and the characteristics vibrational temperature of O_2 is lower than that of N_2. In the Cases E and G, the order of the power decreases with increasing the radial distance because the rise time is formed by the molecular relaxation of O_2, and the maximum exchange rate decreases, as shown in Figs. 4.23(a) and 4.23(c). However, because the decrease in the order of the power is small, the translational-vibrational energy exchange just behind the shock wave is induced at an almost constant rate; thus, the maximum exchange rate can be approximately evaluated as the constant value in the entire computational domain. These results show the strength of molecular relaxation in the entire flow field can be comprehensively evaluated by the fitted curve, where the strength of molecular relaxation just behind the shock wave increases with decreasing the relaxation time.

Table 4.7 Fitted curve on inverse of maximum exchange rate of translational-vibrational energy and relaxation time in Case G

	O_2		N_2	
r/L	Fitted curve	Degree of curve fit	Fitted curve	Degree of curve fit
100	$y = 6{,}077\ x^{1.044}$	$R^2 = 0.9977$	$y = 20{,}462\ x^{1.485}$	$R^2 = 0.9975$
500	$y = 6{,}934\ x^{0.949}$	$R^2 = 0.9976$	$y = 33{,}797\ x^{1.344}$	$R^2 = 0.9995$
1000	$y = 8{,}171\ x^{0.870}$	$R^2 = 0.99999$	$y = 33{,}045\ x^{1.377}$	$R^2 = 0.9989$

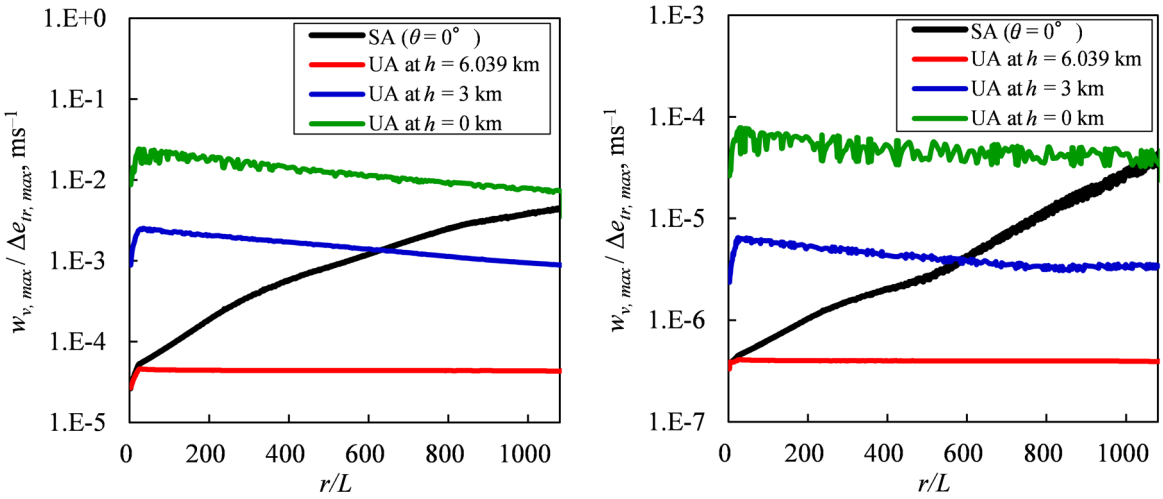

(a) O_2 (b) N_2

Fig. 4.25 Maximum exchange rate of translational-vibrational energy in Cases C (SA: stratified atmosphere) and G (UA: uniform atmosphere).

Figure 4.25 shows the maximum exchange rate in the stratified atmosphere (Case C). In this figure, the maximum exchange rate in the uniform atmosphere (Case G) is also depicted to facilitate analysis of the variation in the rate with altitude. The maximum exchange rate in the stratified atmosphere at h = 6.039 km is almost the same as that in the uniform atmosphere at the altitude. Because the relaxation time increases toward the ground, the maximum exchange rate in the stratified atmosphere increases toward the ground and approaches that in the uniform atmosphere at h = 0 km. In the stratified atmosphere, the rise time is dramatically increased at h = 4.4–3.7 km as shown in Fig. 4.21, and thus the maximum exchange rate is smaller than that in the uniform atmosphere at h = 0 km. Figure 4.26 shows the fitted curve on the inverse of the maximum exchange rate and the relaxation time. The degree of curve fit in the stratified atmosphere is lower than that in the uniform atmosphere, and the order of the power in the stratified atmosphere is lower than that in the uniform atmosphere because the rise time in the stratified atmosphere dramatically changes as shown in Fig. 4.21.

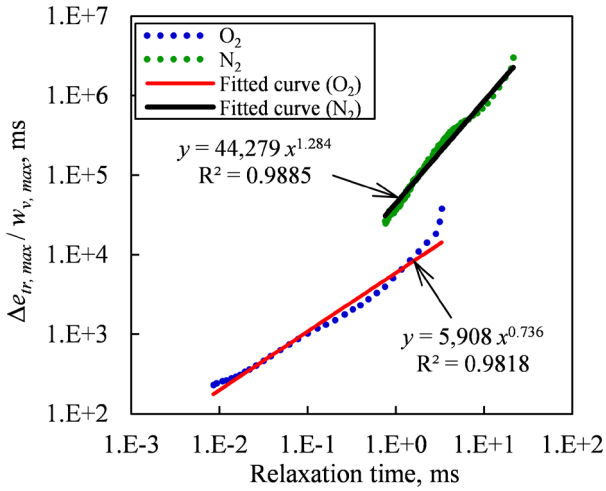

Fig. 4.26 Fitted curve on inverse of maximum exchange rate of translational-vibrational energy and relaxation time in stratified atmosphere (Case C).

Exchange time of translational-vibrational energy

Figure 4.27 shows the exchange time of translational-vibrational energy in the uniform atmosphere (Cases E, F, and G). As the radial distance increases, the exchange time in the near field decreases because the rise time decreases as shown in Fig. 4.20, and that in the far field increases. In the case of uniform atmosphere at low altitudes, the exchange time hardly changes because the exchange velocity is very fast. On the other hand, in the case of uniform atmosphere at high altitudes, the exchange time is mainly changed by the interval of the front and rear shock waves that increases with increasing radial distance. The exchange time in the uniform atmosphere at low altitudes is faster than that in the uniform atmosphere at high altitudes. Moreover, the exchange time in the molecular relaxation of O_2 at h = 6.039 km is in good agreement with that in the molecular relaxation of N_2 at h = 3 km. Hence, it can be seen that the exchange time is strongly related to the relaxation time, although the exchange time is hardly changed by the magnitude of the energy exchange. As described above, not only the maximum exchange rate but also the exchange time strongly depended on the relaxation time; thus, the classification of the transition of wave profile shown in Fig. 4.9 seems to be quite reasonable.

Figure 4.28 shows the exchange time in the stratified atmosphere (Case C). In this figure, the exchange time in the uniform atmosphere (Case G) is also depicted to facilitate analysis of the variation in the exchange time with altitude. As shown in this figure, the exchange time in the stratified atmosphere at h = 6.039 km is almost the same as that in the uniform atmosphere at the altitude, and it approaches that in the uniform atmosphere at h = 0 km as the radial distance increases, as well as the maximum exchange rate in Fig. 4.25. The results show that the strength of molecular relaxation can be investigated by the maximum exchange rate and exchange time not only in the uniform atmosphere but also in the stratified atmosphere.

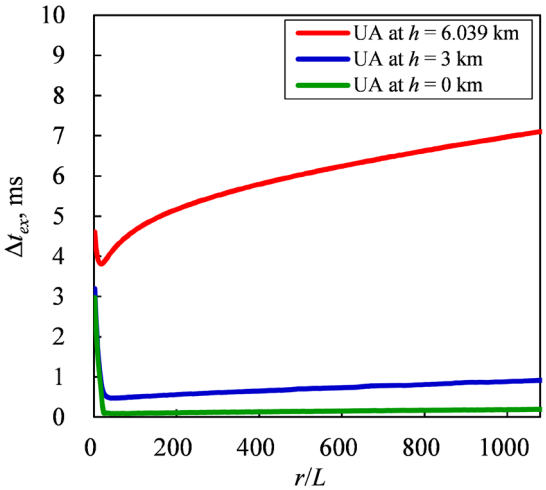

(a) Case E (molecular relaxation of O_2)

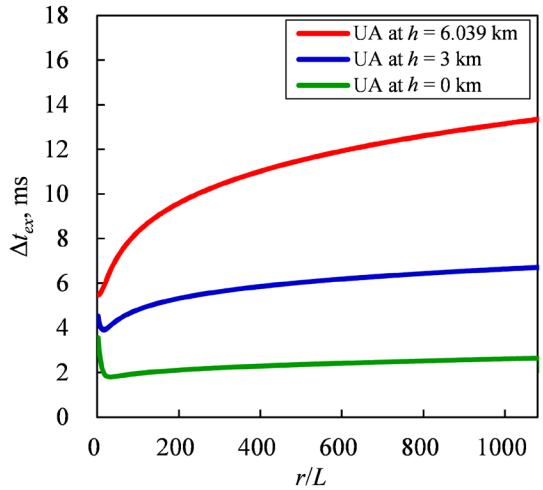

(b) Case F (molecular relaxation of N_2)

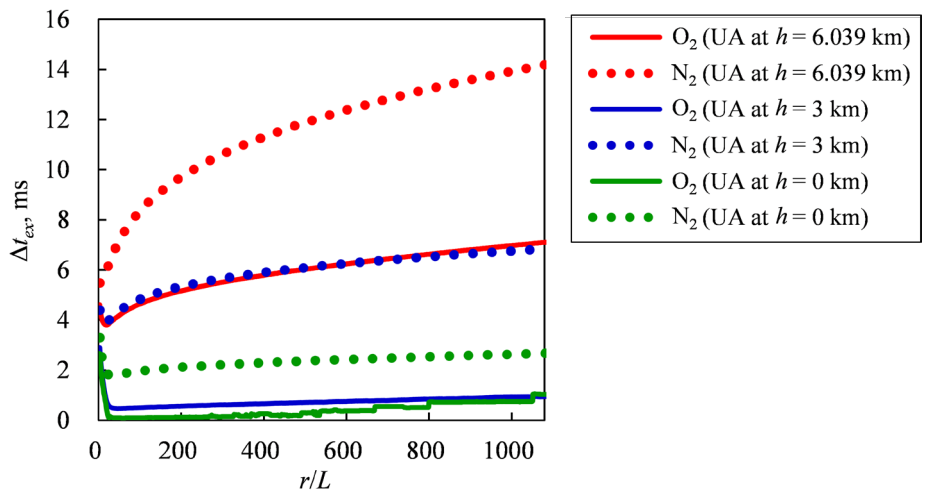

(c) Case G (molecular relaxation of O_2 and N_2)

Fig. 4.27 Exchange time of translational-vibrational energy in uniform atmosphere (UA).

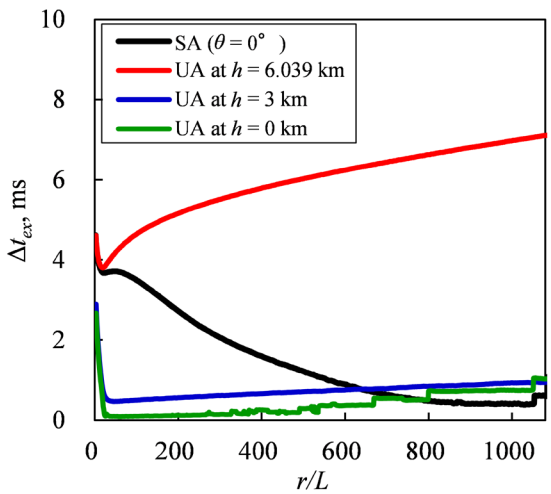

(a) O_2

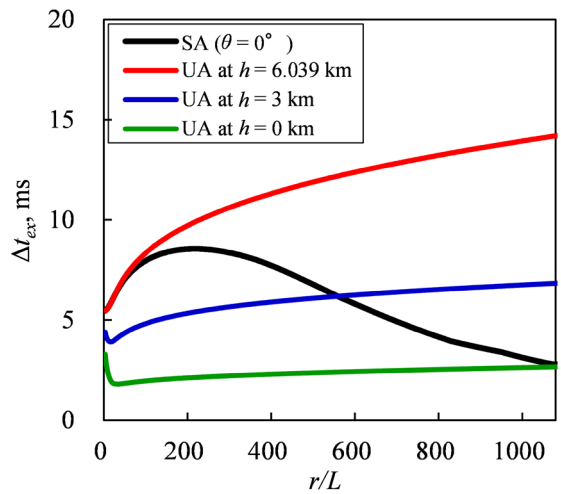

(b) N_2

Fig. 4.28 Exchange time of translational-vibrational energy in Cases C (SA: stratified atmosphere) and G (UA: uniform atmosphere).

4.4 Summary of this chapter

In this chapter, full-field simulation was performed to clarify the effect of molecular relaxation on the wave profile and the formation mechanism of rise time in the uniform and stratified atmospheres. The results are summarized as follows.

- The relation between the transition of the wave profile and the magnitude of translational-vibrational relaxation term was investigated, and as a result the effect of molecular relaxation on the wave profile was clarified as follows. In the case of long relaxation time, the energy exchange was induced slowly, and the pressure fluctuation behind the shock wave was widely decreased, although the energy exchange just behind the shock wave was too small to form the rise time. On the other hand, in the case of short relaxation time, the energy exchange was induced rapidly and converged just behind the shock wave. As a result, the pressure fluctuation just behind the shock wave was significantly decreased, and the rise time was formed. The mixed effects of molecular relaxation with respect to O_2 and N_2 were expressed as the superposition of each effect because the molecular relaxation of O_2 was the dominant effect on the formation of rise time. As the relaxation time decreased with decreasing altitude, the wave profile in the stratified atmosphere was significantly changed toward the ground.
- The rise time in the uniform atmosphere at low altitudes monotonically increased because the exchange rate of translational-vibrational energy hardly changed with the radial distance from the body axis. On the other hand, the rise time in the stratified atmosphere increased and decreased toward the ground because the strength difference between the molecular relaxation and the nonlinearity was dramatically changed according to the variation in the relaxation time with altitude.
- Strength of molecular relaxation was investigated by the maximum exchange rate of translational-vibrational energy and its exchange time. As the relaxation time decreased, the maximum exchange rate increased, whereas the exchange time decreased. Moreover, the maximum exchange rate and the relaxation time obeyed the power law; this is quite helpful in understanding the variation in the strength of molecular relaxation with the relaxation time. Therefore, it was shown that the strength of molecular relaxation was strongly related to the maximum exchange rate and the exchange time, and the transition of wave profile caused by the molecular relaxation can be well classified according to the relaxation time.

These results show that the effect of molecular relaxation on the wave profile and the formation mechanism of rise time were well clarified by the full-field simulation with the thermal nonequilibrium, in which the detailed model of molecular relaxation was considered.

Chapter 5

Full-Field Simulation at Low Supersonic Speed

5.1 Outline of this chapter

In this chapter, full-field simulation is performed to analyze sonic boom propagation at a low supersonic speed, including sonic boom cutoff phenomena, and to investigate the applicability to the analysis of focused sonic boom in the caustic-vicinity field. Thus far, focused sonic boom has been predicted by the simplified methods of solving the progressive wave equation [55], Khokhlov–Zabolotskaya (KZ) equation [56], nonlinear Tricomi equation [57] and so on. However, there are three big issues for the prediction methods as follows: First, even the latest prediction method of solving the lossy nonlinear Tricomi equation [58] does not consider the important effects such as geometrical spreading and atmospheric stratification. Second, the prediction accuracy of the evanescent wave is not necessarily adequate because the attenuation characteristics of the evanescent wave have not been fully clarified, although this wave is assumed to decay exponentially toward the ground. Third, classifying the three-dimensional structure of a caustic is difficult because the existing prediction methods cannot account for the variation in the circumferential direction around the body axis. To improve these problems, the full-field simulation method seems promising because it has the potential for incorporating various effects that cannot be considered in the existing prediction methods. Thus far, the predictions of focused sonic boom have been made mainly for transonic accelerations and maneuvers, not for cutoffs; thus, the cutoff phenomena have not been well clarified. Therefore, full-field simulation is applied to the analysis of cutoff phenomena in this chapter, and the results are analyzed to investigate the detailed mechanism of the cutoff phenomena, such as the waveform transition in the cutoff region, the three-dimensional structure of the cutoff surface, and the characteristics of the evanescent wave. Consequently, the usefulness of the full-field simulation method is investigated as an approach to analyze sonic boom propagation at low supersonic speeds and focused sonic boom in the caustic-vicinity field. The contents of this chapter were already published in [83].

5.2 Sonic boom cutoff phenomena

5.2.1 Sonic cutoff and lateral cutoff

Shock waves generated from a supersonic aircraft are refracted by variation in the atmospheric temperature, and the shock-wave angles differ in the propagation directions. In the case of ISO standard atmosphere [82], the atmospheric temperature increases from an altitude of 11 km to the ground as described in section 5.3.1, and the shock-wave angles to the ground surface increase toward the ground. Consequently, the shock waves are diffracted at the singularity zone where the shock-wave angles to the ground surface are equal to 90°, and they do not reach the ground. This phenomenon is known as sonic boom cutoff.

Figure 5.1 shows the schematic of sonic boom cutoff phenomena. The cutoff phenomena are grouped into two types: sonic and lateral cutoffs [93, 94]. The acoustic ray that is vertical to the shock wave indicates the propagation path of the wave, and the caustic indicates an envelope surface of the rays. As

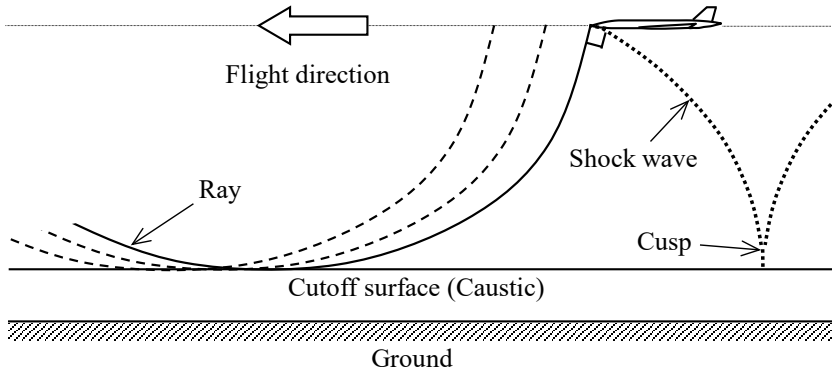

(a) Sonic cutoff

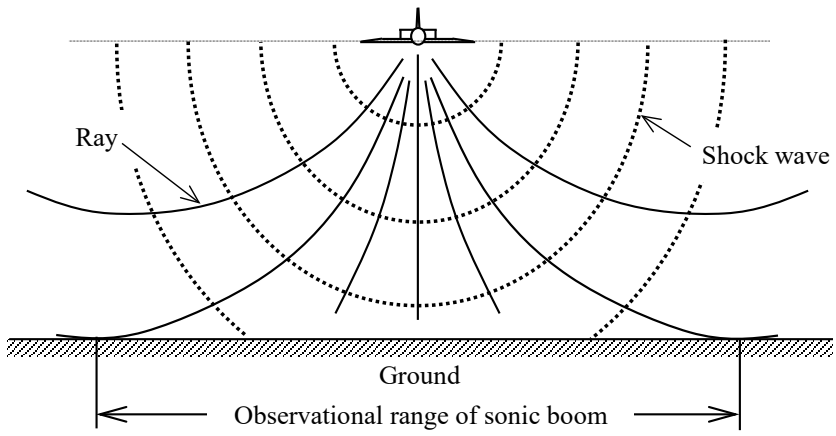

(b) Lateral cutoff

Fig. 5.1 Schematic of sonic boom cutoff phenomena.

shown in Fig. 5.1(a), sonic cutoff occurs beneath a supersonic aircraft flying at a relatively low supersonic speed of Mach 1.2 or less. When sonic cutoff occurs, all shock waves generated from an aircraft do not reach the ground. Therefore, the low supersonic aircraft [95] is of interest as a solution of the sonic boom problem, because it may be allowed to make a supersonic flight overland. However, several rays are integrated in the caustic region, i.e., the cutoff region, and the pressure rise in the region becomes approximately three times larger than that without the focusing of the rays. In addition, the evanescent wave, instead of the shock wave, propagates beneath the cutoff region. For these reasons, sonic cutoff must be avoided near the ground, and the flight conditions must be determined by considering the evanescent wave, even if the aircraft flies at relatively low supersonic speeds. As shown in Fig. 5.1(b), lateral cutoff occurs when the shock wave propagating obliquely downward is diffracted. The lateral cutoff occurs not only at low supersonic speeds but also at higher speeds, and the altitude of lateral cutoff is higher than that of sonic cutoff; thus, the lateral cutoff limits the observational range of sonic boom at the ground level normal to the flight direction.

5.2.2 Waveform transition in cutoff region

Figure 5.2 shows a schematic of the waveform transition in the sonic cutoff region. The shadow zone indicates the area beneath the caustic region. The incoming wave generated from an aircraft propagates in the downward direction and is divided into two waves by the diffraction effect. One is an outgoing wave in the upward direction, and the other is an evanescent wave in the downward direction. If the incoming waveform is an N-shaped waveform (N-wave), the outgoing waveform assumes a U-shaped waveform (U-wave) [96]. For sonic cutoff, the altitude of the caustic is equal to the sonic cutoff altitude, where the local Mach number is 1. Therefore, the upper area of the sonic cutoff region is aerodynamically a supersonic region, and the lower area (shadow zone) is a subsonic region; i.e., the flow field around the sonic cutoff region is in a transonic flow regime. Even if the cutoff phenomena occur, an evanescent wave, instead of a shock wave, propagates beneath the cutoff region. Thus, the flight altitude must be determined by considering the evanescent wave that cannot be precisely predicted in the existing prediction method. Because full-field simulation can analyze the evanescent wave in the subsonic region, it is a powerful tool for investigating sonic boom propagation in the caustic-vicinity field.

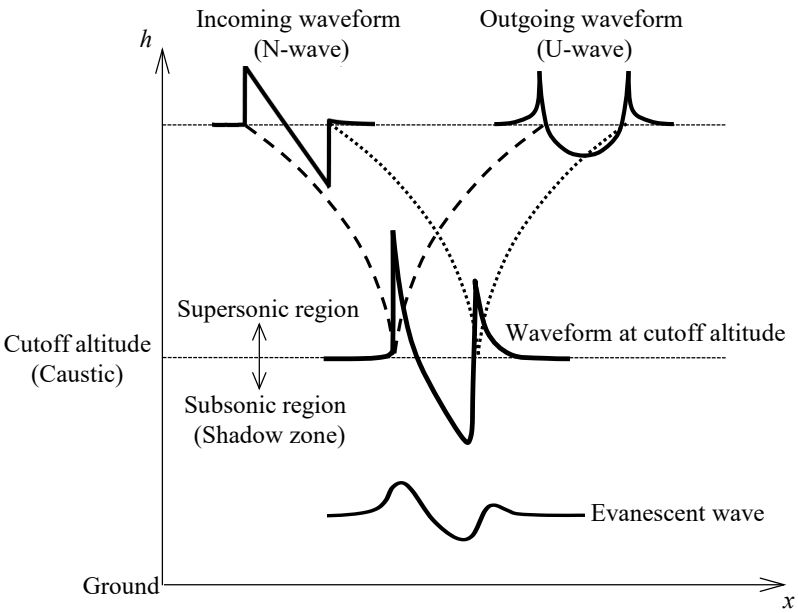

Fig. 5.2 Schematic of waveform transition in sonic cutoff region.

5.3 Computational methods

5.3.1 Computational conditions

A simple computational model is suitable not only for the simplicity of the analysis, but also for reducing the computational load. The computational model was set as an axi-symmetric paraboloid:

$$S(x)=4\pi D^2\left(\frac{x}{L}\right)^2\left(1-\frac{x}{L}\right)^2 \quad \left(0\le\frac{x}{L}\le 1\right) \tag{5.1}$$

where $S(x)$ is the cross-sectional area in the x coordinate. The length of the body is L = 100 m, and its maximum diameter is D = 10 m. The flight Mach number was M_∞ = 1.1, and the flight altitude was h = 10 km. The steady level flight was assumed in this simulation.

As the cutoff phenomena are caused by variation in the atmospheric temperature with altitude, the atmospheric stratification must be considered. Thus, the atmospheric model was set as the ISO standard atmosphere [82] shown in Fig. 5.3. In the case of ISO standard atmosphere, the atmospheric temperature is defined as

$$T_a = T_0 - \beta h \quad (0 \le h \le 11km) \tag{5.2}$$

$$T_a = const \quad (11 \le h \le 20km) \tag{5.3}$$

where the atmospheric temperature at the ground is T_0 = 288.15 K, and the temperature lapse rate is β = 6.5 K/km. The unit of h is kilometer. Moreover, the atmospheric pressure and density are calculated by the equation of the state of ideal gas as

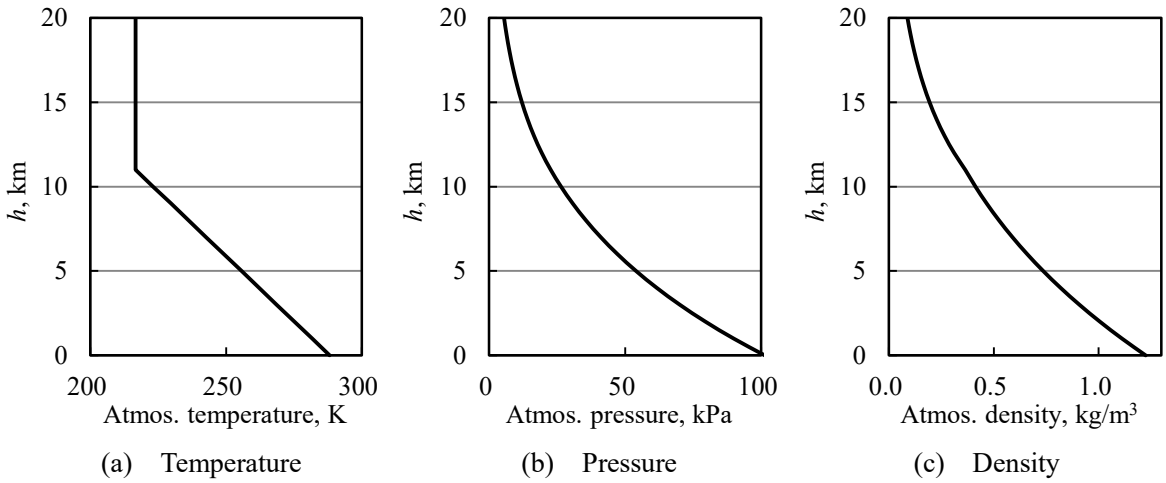

Fig. 5.3 ISO standard atmosphere.

Table 5.1 Computational conditions

Computational model	Axi-symmetric paraboloid (L = 100 m, D = 10 m)
Flight Mach number	$M_\infty = 1.1$
Flight altitude	h = 10 km
Flight condition	Steady level flight
Atmosphere	Stratification (ISO standard atmosphere)
Computational domain	r/L = 0–110

$$p_a = \rho_a R T_a \tag{5.4}$$

and the hydrostatic equation as

$$\frac{dp_a}{dh} = -g\rho_a \tag{5.5}$$

Consequently, the atmospheric pressure is obtained as follows:

$$\frac{p_a}{p_0} = \left(\frac{T_a}{T_0}\right)^{\frac{g}{\beta R}} \quad (0 \le h \le 11km) \tag{5.6}$$

$$\frac{p_a}{p_c} = \exp\left(-\frac{g}{RT_c}(h-11)\right) \quad (11 \le h \le 20km) \tag{5.7}$$

where the atmospheric pressure at the ground is p_0 = 101.325 kPa. Subscript c denotes the atmospheric property at h = 6.75 km, where the temperature lapse rate β changes.

Table 5.1 shows the computational conditions. The flow solver and the computational domain are described in sections 5.3.2 and 5.3.3, respectively.

5.3.2 Flow solver

The governing equations were the three-dimensional Euler equations with the gravity term as

$$\frac{\partial Q}{\partial t}+\frac{\partial E}{\partial x}+\frac{\partial F}{\partial y}+\frac{\partial G}{\partial z}=S_G \tag{5.8}$$

$$Q=\begin{bmatrix}\rho\\ \rho u\\ \rho v\\ \rho w\\ e\end{bmatrix}, E=\begin{bmatrix}\rho u\\ \rho u^2+p\\ \rho uv\\ \rho uw\\ (e+p)u\end{bmatrix}, F=\begin{bmatrix}\rho v\\ \rho uv\\ \rho v^2+p\\ \rho vw\\ (e+p)v\end{bmatrix}, G=\begin{bmatrix}\rho w\\ \rho uw\\ \rho vw\\ \rho w^2+p\\ (e+p)w\end{bmatrix}, S_G=\begin{bmatrix}0\\ 0\\ \rho g\\ 0\\ \rho g v\end{bmatrix} \tag{5.9}$$

$$e=\frac{\rho RT}{\gamma-1}+\frac{\rho}{2}\left(u^2+v^2+w^2\right) \tag{5.10}$$

where geometrical spreading, nonlinearity, and atmospheric stratification are considered. To reduce the computational load, viscosity and molecular relaxation were not considered. The computational approach of solving the governing equations is explained in section 2.3 of chapter 2. However, the flow field in the cutoff region was so complicated that the generation of nonphysical waves in the stratified atmosphere was not entirely avoided by the numerical correction method described in section 2.3.4 of chapter 2. Thus, the generation of nonphysical waves in the stratified atmosphere was avoided by setting the following threshold value in addition to the numerical correction method [83]. If the fluctuation component of the velocities u, v, and w is less than 10^{-15} times the flight velocity, each fluctuation component is set to zero. In addition, if the fluctuation component of the quantities p and ρ is less than 10^{-15} times the quantities of ISO standard atmosphere, each fluctuation component is set to zero. To determine the threshold value, preliminary calculations were performed, where the orders of the values differed. Consequently, the most appropriate value was set to avoid the generation of nonphysical waves.

5.3.3 Computational domain

Figure 5.4 shows the outline of the entire computational domain around the paraboloid. The computational domain was set from r/L = 0 to 110 (r = 0 km to 11 km). To reduce the computational load, the computational domain in the radial direction was split into several subdomains with extended regions (see section 2.5 of chapter 2 for details). Table 5.2 shows the range of the subdomains with the extended regions. In the case of stratified atmosphere, the boundary condition at the surface of the body must be evaluated by considering the change caused by atmospheric stratification and the fluctuation caused by waves in a compressible fluid. However, these two terms cannot be distinguished, and simple extrapolation such as that used in the unstratified atmosphere is not necessarily adequate. To improve this problem, the

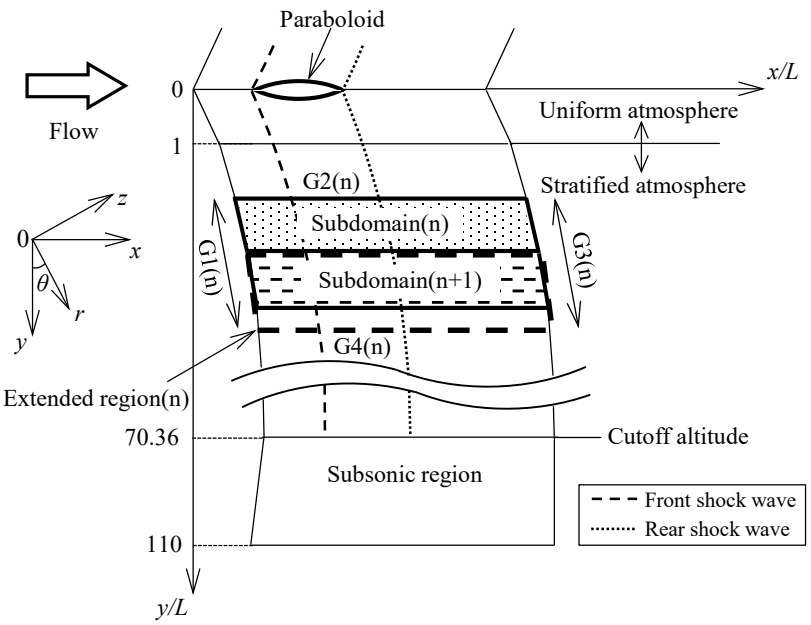

Fig. 5.4 Outline of computational domain.

Table 5.2 Range of subdomain(n) with extended region(n)

Atmosphere	n	*r/L*
Uniform	0	0–10.0
	1–7	1–5.8, 2.2–8, …, 15.6–27
Stratification	8–22	20–32, 25–37, …, 90–102
	23	95–110

uniform atmosphere at the flight altitude was assumed for the near field around the paraboloid, i.e., the subdomain (0) with the extended region (0). Assuming the uniform atmosphere, axi-symmetric analysis instead of three-dimensional analysis can be performed and is suitable for reducing the computational load. Therefore, axi-symmetric analysis was performed in the subdomain (0) with the extended region (0). The boundary conditions were the same as those used in chapter 3 (see section 3.2.4 for details), because the same grid type was used in both chapter 3 and this chapter.

5.3.4 Computational grid and computational load

Figure 5.5 shows the computational grid on the symmetry plane beneath the paraboloid. The computational grid was constructed to align the grid lines with the front and rear shock waves of the incoming waveform. The locations of these shock waves were set as follows: The locations of the highest and second-highest pressure gradients were derived, and the derived upstream and downstream locations

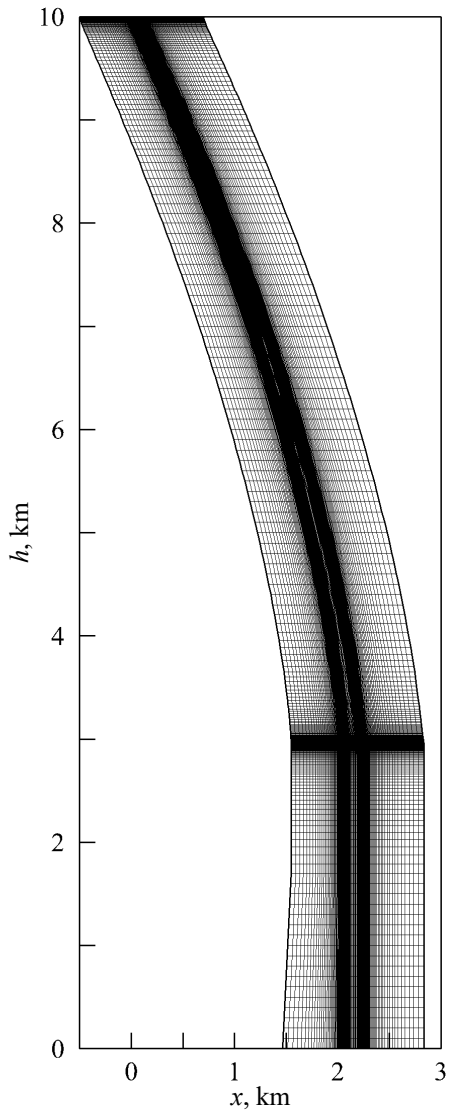

Fig. 5.5 Computational grid of Grids 2A and 3A on the symmetry plane beneath the body.

were identified as the locations of the front and rear shock waves, respectively. The minimum grid spacing in the streamwise direction was 0.1 m in the locations of the front and rear shock waves, and that in the radial direction was 0.1 m at the surface of the body. The grid spacing in the radial direction was increased with the radial distance in the region of $r/L < 20$, and the spacing normalized by the length of the body was 1 in the region of $r/L > 20$. For smoothing the grid lines, the grid angles were changed every 10 points in the region of $r/L < 5$ and every 5 points in the region of $r/L > 5$. Grid generation under the above conditions was conducted in the entire computational domain, as described in sections 2.4 and 2.6 of chapter 2. Thereafter, the grid number in the radial direction was increased in the cutoff region because the flow field around the region was very complex. Specifically, the location of the minimum grid spacing in the radial direction was 0.1 m at $r/L = 70.36$, where the pressure rise reached the local maximum value by the sonic cutoff. Finally, the computation in the entire domain from $r/L = 1$ to 110 was performed by the final

solution-adapted grid.

Table 5.3 shows the number of grid points. The grid convergence was confirmed by comparison with results using grids with twice the number of Grid 2A or 3A. Computational grids except for these two were constructed by adding the internal dividing points to Grid 2A or 3A. Table 5.4 shows the grid convergence. As shown in Table 5.4, the grid convergence was adequate for evaluating the characteristics of cutoff phenomena.

The computations were performed using the HITACHI SR16000 System (yayoi) [92] in the Information Technology Center, The University of Tokyo. The computational capability was 980.48 GFlops per node. It took approximately 10 hours for solution-adapted grid generation and approximately 24 hours for final computation using Grid 3A, when one node was used.

Table 5.3 Number of computational grid

Solver	Computational domain	Grid name	Streamwise direction	Radial direction	Rotational direction
2D (axi-symmetric)	r/L = 0–10	Grid 2A	241	87	–
		Grid 2B	481	87	–
		Grid 2C	241	173	–
3D (grid generation)	r/L = 1–110	Grid 3A0	241	136	53
3D (final grid)	r/L = 1–110	Grid 3A	241	296	53
		Grid 3B	481	296	53
		Grid 3C	241	591	53
		Grid 3D	241	296	103

Table 5.4 Difference in pressure rise of front shock wave relative to Grid 2A or 3A

Location	Grid name	Difference
r/L = 1	Grid 2B	0.2 %
	Grid 2C	–0.3 %
h = 2.96 km (θ = 0 °) in cutoff region	Grid 3B	6.3 %
	Grid 3C	–0.7 %
	Grid 3D	3.2 %

5.4 Computational results

Simulation results obtained from Grids 2B and 3B are analyzed in this section because the peak pressure rise in the cutoff region obtained for these grids was the highest among the results for all computational grids, as described in Table 5.4. In the analysis, the pressure distributions in the entire flow filed are investigated to clarify the detailed mechanism of the cutoff phenomena, such as the waveform transition in the cutoff region, the three-dimensional structure of the cutoff surface, and the characteristics of the evanescent wave.

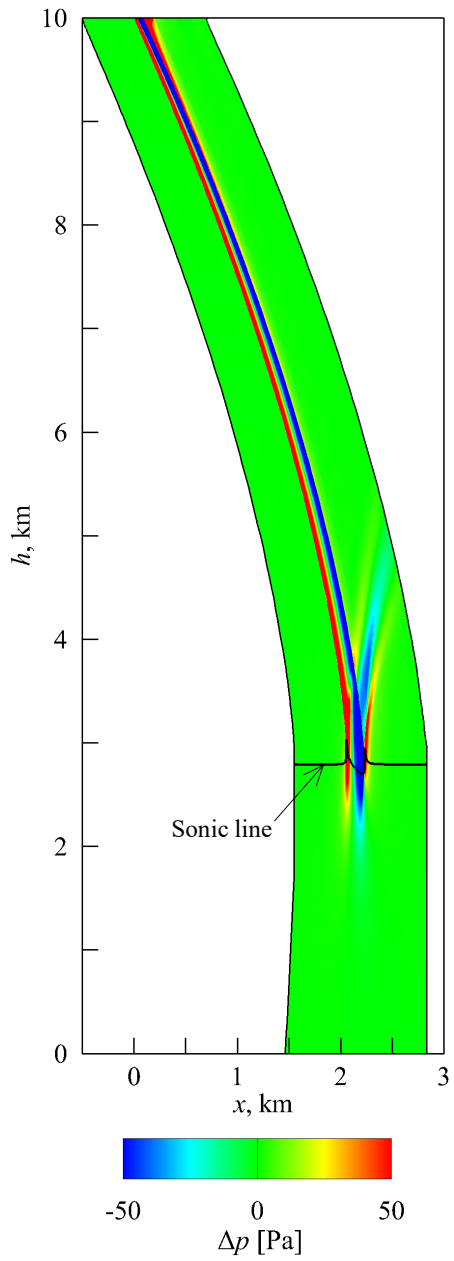

Fig. 5.6 Overall pressure distribution on the symmetry plane beneath the paraboloid.

5.4.1 Pressure distribution

Figures 5.6–5.8 show the distributions of the pressure fluctuation on the symmetry plane beneath the paraboloid. In Figs. 5.6 and 5.8, the sonic line, the boundary line between the supersonic and subsonic regions, is plotted as the black line. As shown in Fig. 5.7, physical phenomena around the paraboloid are composed of three waves: the front shock wave from the nose, the expansion wave from the convex surface of the body, and the rear shock wave from the tail. As shown in Fig. 5.6, these waves are refracted by variation in the atmospheric temperature with altitude, and a large variation in pressure fluctuation is confirmed at h = 2.5–4 km, indicating sonic cutoff. In the sonic cutoff region, the incoming wave generated from the paraboloid is divided into two waves, as shown in Fig. 5.8. One is an outgoing wave in the upward direction, and the other is an evanescent wave in the downward direction. Although the incoming wave appears to be simply reflected at the cutoff surface, the sonic cutoff should be interpreted as diffraction phenomena because of the following two reasons: First, the shock wave is vertical to the cutoff surface. Unless the angle between the reflection surface and shock wave is less than 90°, the reflection never occurs. Second, the caustic cusp [96] is confirmed in the cutoff region, although it cannot appear in the reflection. Therefore, it is reasonable to consider the sonic cutoff as diffraction phenomena. The cutoff altitude, where the local Mach number is equal to 1, was 2.79 km in the freestream conditions. In the cutoff region, the pressure fluctuation was enhanced by integration of the incoming and outgoing waveforms, and the focused

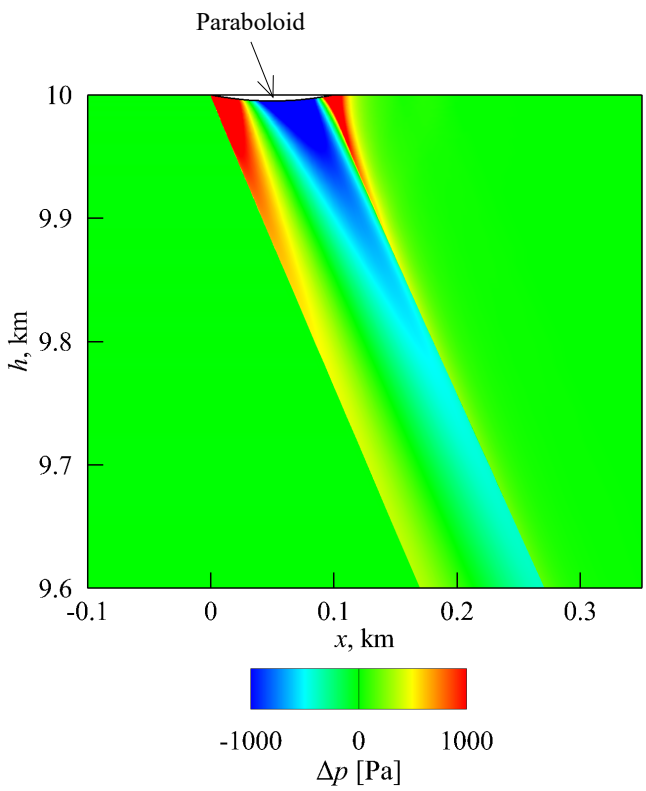

Fig. 5.7 Pressure distribution in the near field on the symmetry plane beneath the paraboloid.

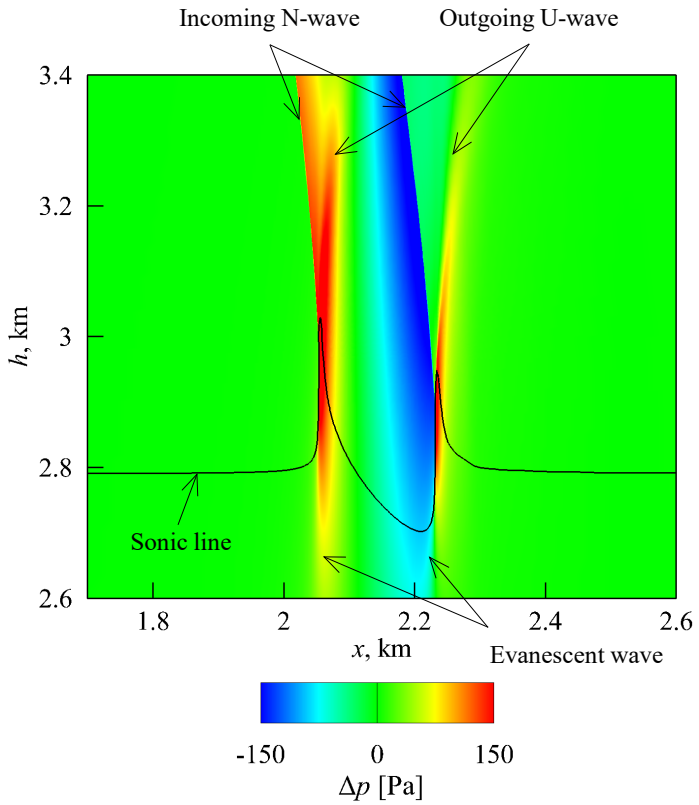

Fig. 5.8 Pressure distribution in the cutoff region on the symmetry plane beneath the paraboloid.

sonic boom was generated. The evanescent wave beneath the cutoff surface was rapidly attenuated in the downward propagation because the compression waves were not converged in the subsonic region. These results show that the full-field simulation successfully reproduced the cutoff phenomena including the evanescent wave.

The results of the SCAMP flight test [12] and the method of solving the lossy nonlinear Tricomi equation [58] demonstrated the three characteristics of focused sonic boom in the caustic-vicinity field as follows: First, the incoming wave is divided into an outgoing wave and an evanescent wave. Second, the pressure fluctuation in the caustic region is increased by the diffraction effect. Third, the evanescent wave is rapidly reduced. These characteristics were in good agreement with those obtained by the full-field simulation. Therefore, it can be seen that the full-field simulation method is applicable to the analysis of focused sonic boom in the cutoff region, i.e., the caustic-vicinity field.

Figure 5.9 shows the overall distribution of the pressure fluctuation from $\theta = -90°$ to $90°$, considering symmetry with respect to the x-y plane. In this figure, the distributions at $h = 10$ km, $z = 0$ km, $r = 10$ km, and the cutoff surface where the pressure rise of the front shock wave reaches the peak value in each rotational direction, are shown. As can be seen in Fig. 5.9, the three-dimensional configuration of the cutoff surface is a downward convex, and the altitude of lateral cutoff is higher than that of sonic cutoff. Moreover, the peak pressure rise in lateral cutoff decreases with increasing the horizontal distance from the x-y plane.

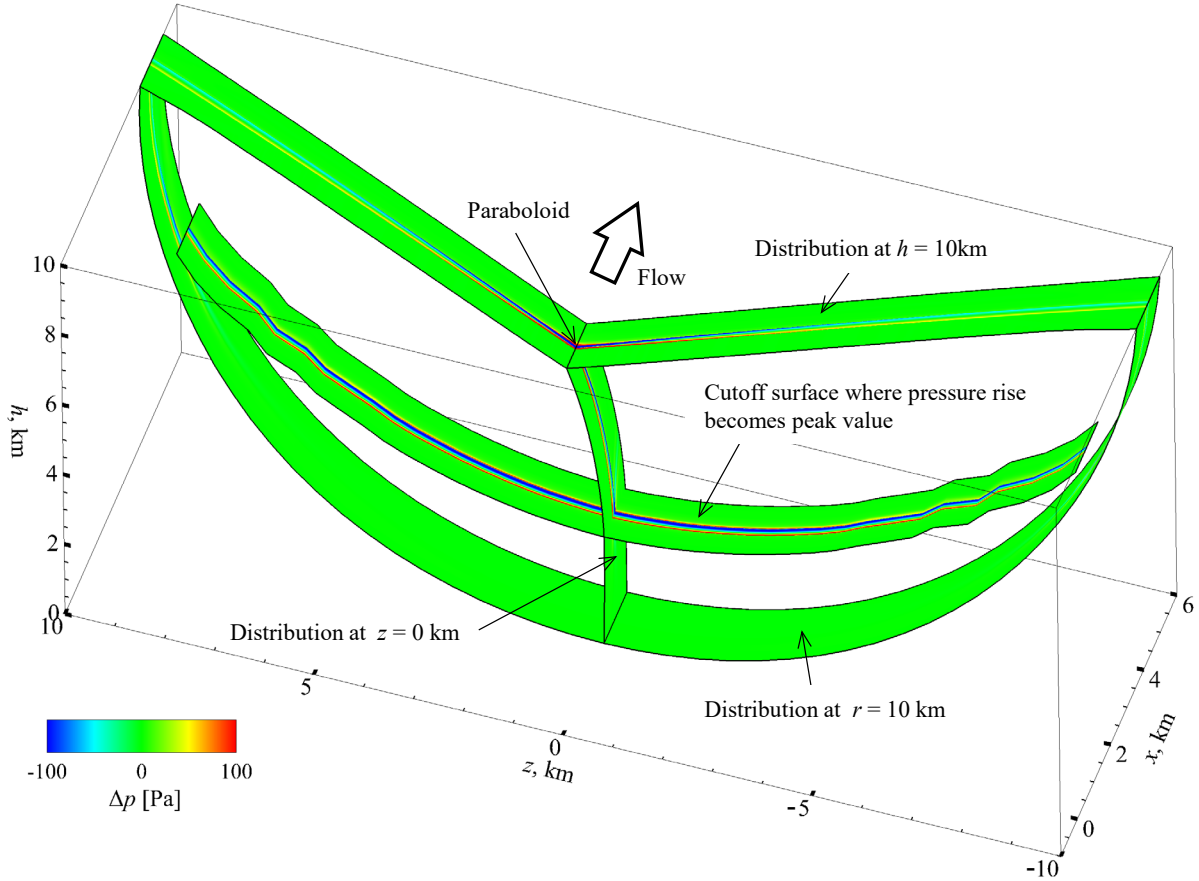

Fig. 5.9 Three-dimensional pressure distribution involving cutoff surface.

These results show that the three-dimensional structure of cutoff phenomena was successfully analyzed by the full-field simulation considering the variation in the circumferential direction around the body axis, which cannot be considered in the existing prediction methods; this is a specific advantage of the simulation.

5.4.2 Pressure waveform

Figure 5.10 shows the pressure waveforms on the symmetry plane beneath the paraboloid, where the horizontal axis represents the relative time calculated by the streamwise distance from the front shock wave and the flight velocity. Note that the pressure distributions shown in Figs. 5.6–5.9 are useful for understanding the waveform transition. As shown in Fig. 5.10(a), the pressure waveform at h = 6 km is shaped like an N (N-wave), where all of the waves generated from the paraboloid can be confirmed. As shown in Fig. 5.10(b), the incoming and outgoing waveforms at h = 4.3 km are confirmed in the upstream and downstream regions, respectively. As shown in Fig. 5.10(c), the rear shock wave of the incoming waveform and the front shock wave of the outgoing waveform are integrated at h = 3.76 km. As shown in Fig. 5.10(d), the incoming and outgoing waveforms at h = 3.19 km are close and overlap each other. As

shown in Fig. 5.10(e), the pressure rise of the front shock wave at h = 2.96 km reaches the peak value after integration of the front shock wave of incoming and outgoing waveforms. As shown in Fig. 5.10(f), the pressure rise of the rear shock wave at h = 2.87 km reaches the peak value after integration of the rear shock wave of incoming and outgoing waveforms. Figs. 5.10(e) and (f) show that the sonic boom intensity is dramatically increased by the diffraction effect in the cutoff region. As shown in Fig. 5.10(g), the pressure fluctuation under the sonic cutoff altitude decreases rapidly toward the ground because the compression waves do not converge in the subsonic region under the cutoff altitude, and the evanescent wave attenuates rapidly. These results show that the waveform transition in the cutoff region was successfully analyzed by the full-field simulation. Therefore, it can be seen that the full-field simulation is useful for investigating complex waveform transition in the caustic-vicinity field.

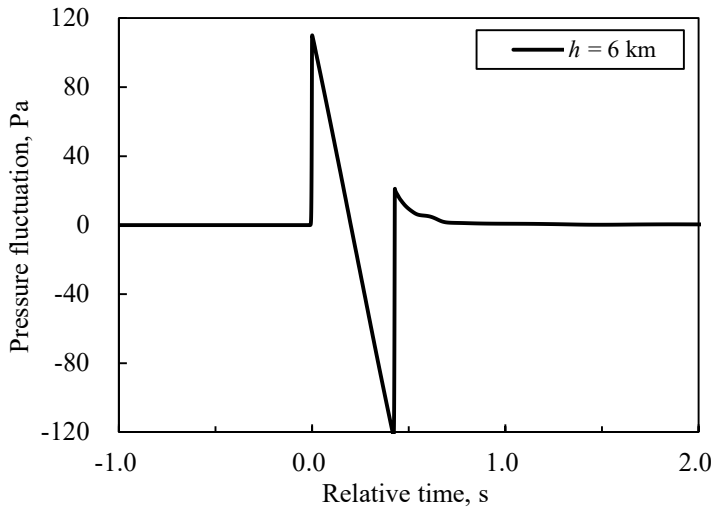

(a) h = 6 km

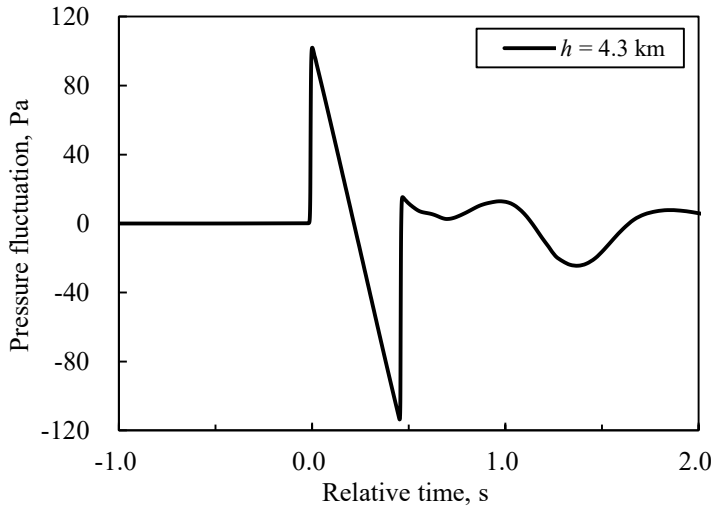

(b) h = 4.3 km

Fig. 5.10 Pressure waveforms on the symmetry plane beneath the paraboloid.

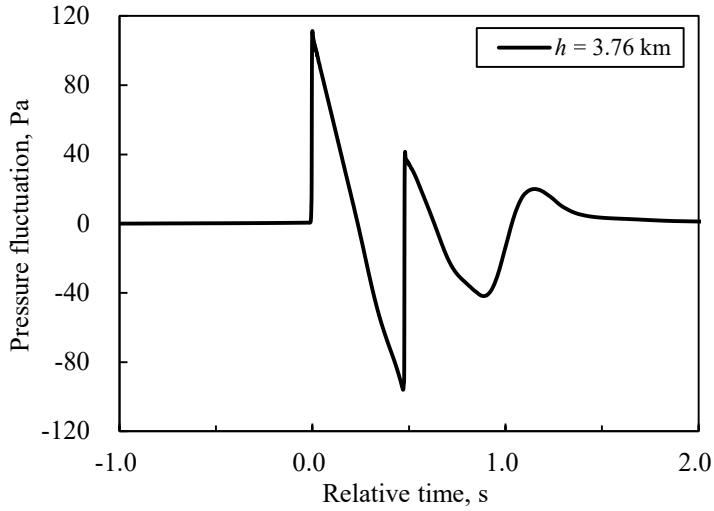

(c) h = 3.76 km

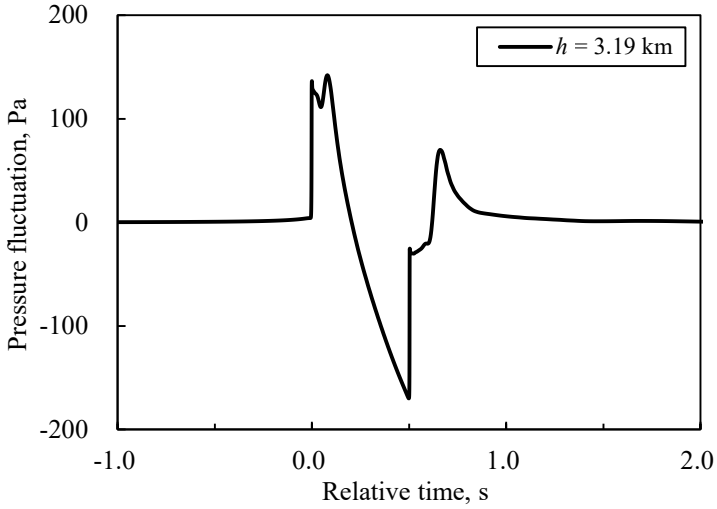

(d) h = 3.19 km

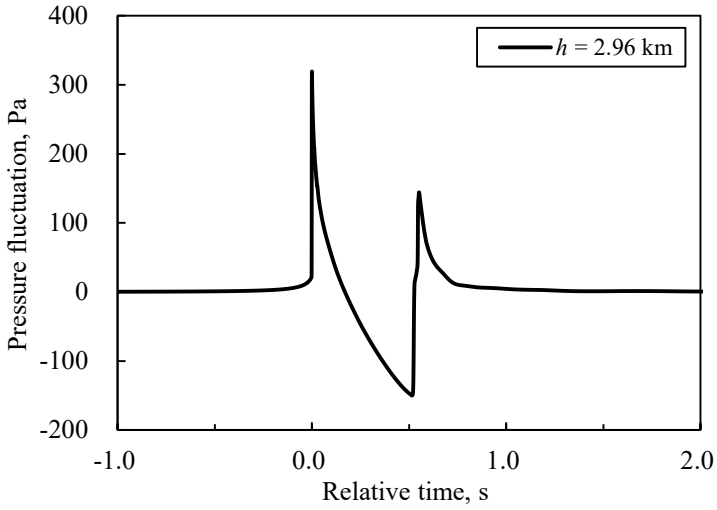

(e) h = 2.96 km

Fig. 5.10 Pressure waveforms on the symmetry plane beneath the paraboloid.

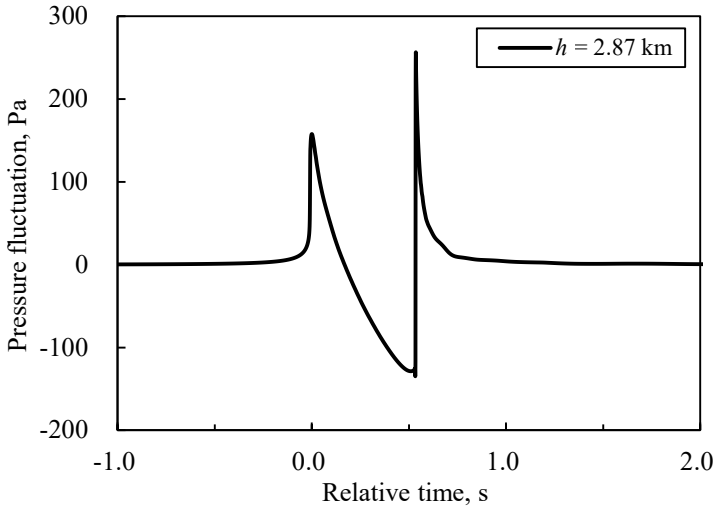

(f) h = 2.87 km

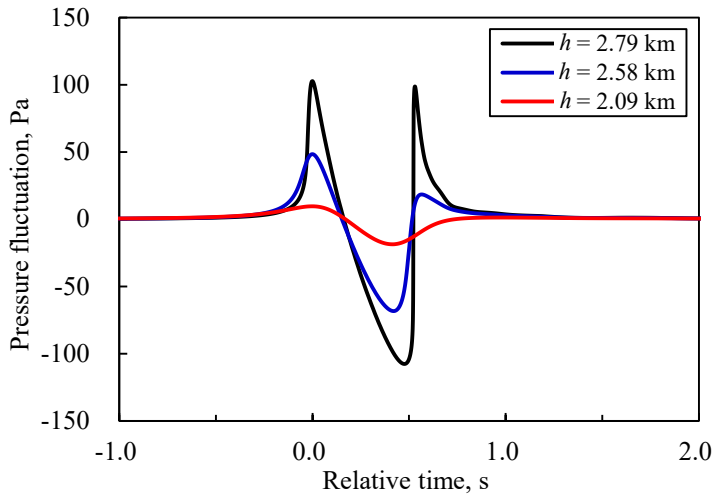

(g) h = 2.79, 2.58, and 2.09 km

Fig. 5.10 Pressure waveforms on the symmetry plane beneath the paraboloid.

5.4.3 Pressure rise at front shock-wave surface

Figure 5.11 shows the distribution of pressure rise at the front shock-wave surface from θ = 0° to 360°, considering symmetry with respect to the *x*-*y* plane. The change in pressure rise around an altitude of 11 km is influenced by variation in the atmospheric temperature gradient, as shown in Fig. 5.3. The pressure rise in the near field around the paraboloid decreases rapidly because of the strong effect of geometrical spreading of the shock wave with increasing distance from the axis of symmetry. Because the atmospheric properties in the stratified atmosphere vary with altitude, the pressure rise differs in the propagation directions and increases in the cutoff region. The cutoff shape is a downward convex, and the focusing strength in the cutoff region decreases with increasing the horizontal distance from the *x*-*y* plane. The pressure rise under the cutoff region decreases rapidly because the compression waves in the subsonic

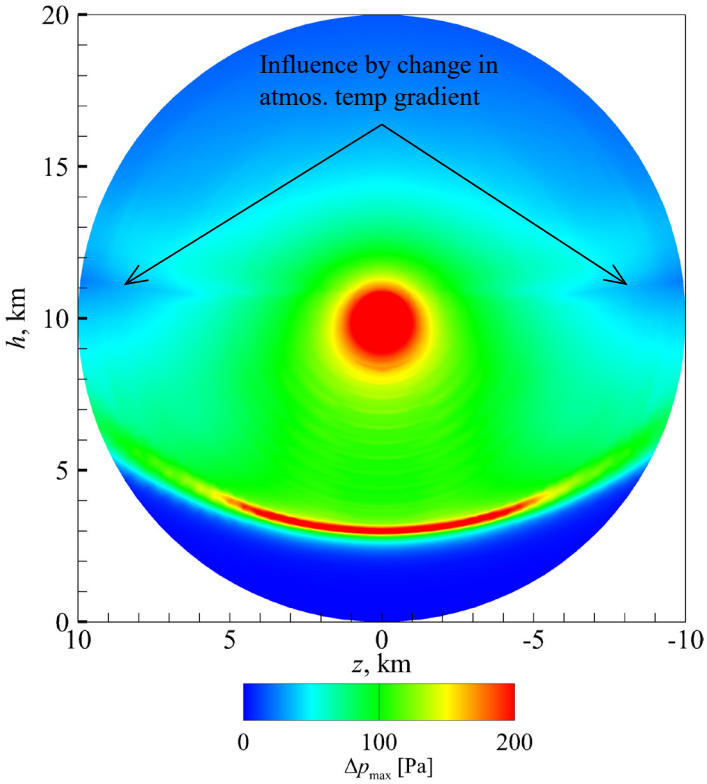

Fig. 5.11 Pressure rise at front shock-wave surface.

region are not integrated.

Figure 5.12 shows the pressure rise of the front shock wave on the symmetry plane beneath the paraboloid. Although the correction term and threshold values were set to simulate the flow field in the stratified atmosphere as described in section 5.3.2, small numerical errors were generated. As shown in Fig. 5.12, the pressure rise in the near field decreases rapidly and reaches the local minimum value of 102 Pa at h = 4.3 km. Thereafter, the pressure rise dramatically increases with approaching the cutoff region. When the focusing strength is strongest in the cutoff region, the pressure rise reaches the peak value. The peak pressure rise was 319 Pa at h = 2.96 km and 3.1 times larger than the local minimum value at h = 4.3 km. At the sonic cutoff altitude in the freestream conditions, the pressure rise was 103 Pa at h = 2.79 km. Thus, the altitude of the peak value was higher than the sonic cutoff altitude because the focused sonic boom was generated by integration of the incoming and outgoing waveforms. The pressure rise under the cutoff region decreases rapidly because the compression waves in the subsonic region are not integrated. The pressure rise at h = 2.09 km was approximately 10 Pa and the tenth part of that at h = 2.79 km, which is the sonic cutoff altitude. These results show that the influence of sonic boom can be ignored at the ground when the steady level flight is assumed to have a speed of Mach 1.1 at h = 10 km. Although there is no international standard in which the allowable level of sonic boom is defined, various standards have been proposed [2, 97]. Even if a strict standard, in which the maximum pressure rise must be below 0.3 psf

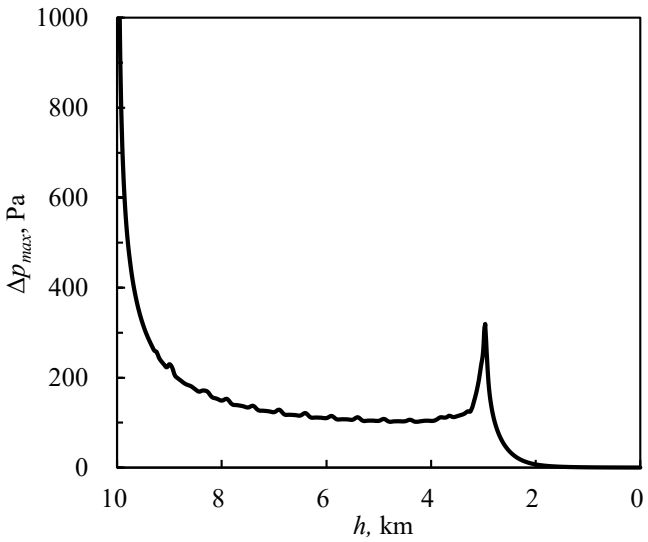

Fig. 5.12 Pressure rise of front shock wave with altitude on the symmetry plane beneath the paraboloid.

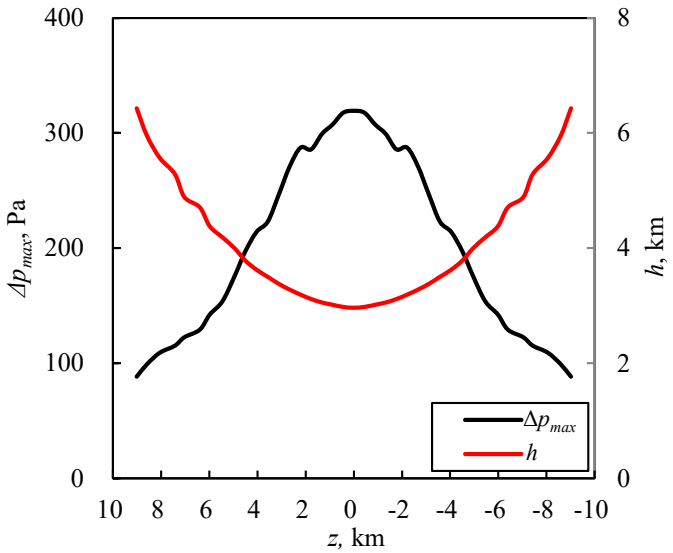

Fig. 5.13 Peak pressure rise of front shock wave and altitude in sonic and lateral cutoffs.

(approximately 14 Pa) [98], is applied, an aircraft will be allowed to fly at a relatively low supersonic speed by virtue of the presence of cutoff phenomena. Although the allowable flight Mach number is limited, the flight velocity of the aircraft is significantly higher than that of present transonic civil aircraft; thus, the transportation time can be significantly reduced by the aircraft. Then, the full-field simulation is of value in determining the appropriate flight conditions.

Figure 5.13 shows the peak pressure rise and altitude in both sonic and lateral cutoffs, where the pressure rise of the front shock wave reaches the peak value in each rotational direction. Small numerical errors, as

well as those shown in Fig. 5.12, were generated. Because all peak values were obtained at grid points, they were not necessarily the maximum in the cutoff region; thus, the curve of the peak pressure rise is not smooth. As shown in Fig. 5.13, the peak pressure rise in the lateral cutoff decreases as the distance from the *x*-*y* plane increases, and the lateral cutoff altitude increases. Thus, it can be seen that the focusing strength in the lateral cutoff is weaker than that in the sonic cutoff.

5.5 Summary of this chapter

In this chapter, the first ever direct simulation of cutoff phenomena was successfully performed. The results are summarized as follows.

- In the sonic cutoff region, the incoming wave generated from the body was divided into an outgoing wave in the upward direction and an evanescent wave in the downward direction. The sonic cutoff was considered as the diffraction phenomena because the shock wave was vertical to the cutoff surface, and the caustic cusp was confirmed in the cutoff region. The sonic boom intensity in the cutoff region was enhanced by integration of the incoming and outgoing waves.
- The evanescent wave under the cutoff altitude was successfully predicted by the full-field simulation without assuming that the evanescent wave decays exponentially. Consequently, it was shown that the evanescent wave propagated vertically downward direction and rapidly attenuated toward the ground, because the compression waves were not integrated in the subsonic region.
- The three-dimensional structure of cutoff surface was successfully obtained by the simulation accounting for the variation in the circumferential direction around the body axis. The shape of the cutoff surface was a downward convex, and the peak pressure rise in lateral cutoff decreased with increasing the distance from the vertical plane including the flight path.

These results show that the sonic boom cutoff phenomena was well clarified, and the full-field simulation was powerful for analyzing the sonic boom propagation at the low supersonic speed, including the focused sonic boom in the caustic-vicinity field.

Chapter 6

Full-Field Simulation at Hypersonic Speed

6.1 Outline of this chapter

In this chapter, full-field simulation is performed to analyze sonic boom propagation from a hypersonic flight object and to clarify a unique phenomenon in a hypersonic flow regime. Analysis of sonic boom propagation from a hypersonic flight object is essential for evaluating meteorite impacts and for developing hypersonic aircrafts. However, sonic boom characteristics at hypersonic speeds have been hardly investigated because sonic boom intensity cannot be precisely predicted by the existing prediction methods without accounting for the strong nonlinearity and thermochemical nonequilibrium [20]. As the full-field simulation method has the potential for considering the strong nonlinearity and thermochemical nonequilibrium, it seems promising to analyze sonic boom propagation from a hypersonic flight object. In this chapter, full-field simulation is applied to sonic boom analysis in a hypersonic flow regime, and the usefulness of this simulation is investigated.

In the Chelyabinsk meteorite event [24–27], strong shock waves were caused by not only the meteorite exploding but also their hypersonic flights, and the explosive sound occurred several times at an interval of several tens of seconds [27]. Generally, multiple shock waves generated from a supersonic aircraft are consolidated into an N-shaped waveform (N-wave) in the far field, and an explosive sound occurs twice at an interval of approximately 0.1 s [6]. Therefore, the interval of explosive sounds in the Chelyabinsk meteorites was much longer than that in a general supersonic aircraft, and it seems reasonable to consider that the explosive sound from each individual meteorite may have occurred only once. This speculation is supported by a previous computational analysis in a hypersonic flow regime [99], whererin the pressure waveform originating at a hypersonic spherical body was changed from a two-peaked waveform (N-wave) to a one-peaked waveform (caret-wave). However, the transitional process remains to be investigated. In this chapter, full-field simulation is applied to the flow field around a hypersonic spherical body, and the results are investigated to clarify the waveform transition from the N-wave type to the caret-wave type. Consequently, the usefulness of this simulation is investigated as an approach to analyze sonic boom

propagation from a hypersonic flight object. A part of the contents in this chapter was already published in [87].

6.2 Computational methods

6.2.1 Computational conditions

The computational conditions were set using the flight conditions of the Chelyabinsk meteorite as a reference. The Chelyabinsk meteorite is assumed to be approximately 17 m to 20 m in diameter [24]. Thus, the computational model was set as a sphere of 20 m in diameter. To investigate the waveform transition according to the flight Mach number, the flight Mach numbers were set as M_∞ = 2, 5, 6, 7, 8, 9, 9.5, 10, 10.5, and 11. All computational conditions excluding the flight Mach numbers were the same in all cases. In the Chelyabinsk meteorite event, the sonic boom reaching Chelyabinsk is assumed to be generated at an altitude of 24–30 km [24]. Thus, the atmospheric properties were set as the geometric mean of the properties of the ISO standard atmosphere [82] at an altitude of 25 km and those at the ground; i.e., the atmospheric temperature was 252.7 K, the atmospheric pressure was 15.95 kPa, and the atmospheric density was 0.2199 kg/m^3. The Reynolds number based on the diameter varied from 1.7×10^8 at $M_\infty = 2$ to 9.6×10^8 at $M_\infty = 11$. Table 6.1 shows the computational conditions. The flow solver and the computational domain are described in sections 6.2.2 and 6.2.3, respectively.

Table 6.1 Computational conditions

Computational model	Sphere (D = 20 m)
Flight Mach number	M_∞ = 2, 5, 6, 7, 8, 9, 9.5, 10, 10.5, and 11
Flight condition	Steady level flight
Atmosphere	Uniform (geometric mean of properties at h = 25 km and those at ground)
Computational domain	$r/D \approx$ 0–340 (M_∞ = 9), 0–190 (M_∞ = 9.5), and 0–130 (the others)

6.2.2 Flow solver

The governing equations were the axi-symmetric Navier–Stokes equations as

$$\frac{\partial Q}{\partial t} + \frac{\partial E}{\partial x} + \frac{\partial F}{\partial r} + H = \frac{\partial E_v}{\partial x} + \frac{\partial F_v}{\partial r} + H_v \tag{6.1}$$

$$Q=\begin{bmatrix}\rho\\ \rho u\\ \rho v\\ e\end{bmatrix},E=\begin{bmatrix}\rho u\\ \rho u^2+p\\ \rho uv\\ (e+p)u\end{bmatrix},F=\begin{bmatrix}\rho v\\ \rho uv\\ \rho v^2+p\\ (e+p)v\end{bmatrix},H=\begin{bmatrix}\rho v/r\\ \rho uv/r\\ \rho v^2/r\\ (e+p)v/r\end{bmatrix} \tag{6.2}$$

$$E_v=\begin{bmatrix}0\\ \tau_{xx}\\ \tau_{xr}\\ \beta_x\end{bmatrix},F_v=\begin{bmatrix}0\\ \tau_{rx}\\ \tau_{rr}\\ \beta_r\end{bmatrix},H_v=\begin{bmatrix}0\\ \tau_{xr}/r\\ 2\mu\left(\dfrac{\partial v}{\partial r}-\dfrac{v}{r}\right)\Big/r\\ \beta_r/r\end{bmatrix} \tag{6.3}$$

$$e=\frac{\rho RT}{\gamma-1}+\frac{\rho}{2}\left(u^2+v^2\right) \tag{6.4}$$

where geometrical spreading, nonlinearity, and viscosity are considered. Although viscosity is assumed to hardly affect the far-field waveform except on the formation of rise time, it must be considered to simulate the realistic wake flow behind the sphere, where the trailing shock wave is generated. To reduce the computational load, the real gas effects [20, 100] including thermochemical nonequilibrium and the turbulence effects were not considered. These effects on the waveform should be investigated in the future work. The computational approach of solving the governing equations is described in section 2.3 of chapter 2. To investigate the unsteady nature in the wake flow, the unsteady analyses at M_∞ = 2 and 10 were performed by the third-order total variation diminishing (TVD) Runge–Kutta scheme [101]. As a result, the unsteady nature in the separated region hardly affected the far-field waveform. Thus, the flow field was assumed to be steady, and the implicit time marching method was used.

6.2.3 Computational domain

Figure 6.1 shows the outline of the entire computational domain around the sphere. To detect the coalescence point of the bow and trailing shock waves, the computational domains were set from r/D = 0 to approximately 340 at M_∞ = 9, approximately 190 at M_∞ = 9.5, and approximately 130 at the other flight Mach numbers. In these domains, the extended regions were included to prevent the influence of the boundary condition at $x = x_{\max}$. To reduce the computational load, the computational domain was split into two regions: the semicircular region in the near field and the solution-adapted region in the far field. When the semicircular region was computed, a part of the solution-adapted region was simultaneously computed to prevent the influence of the boundary condition at $x = x_{\max}$.

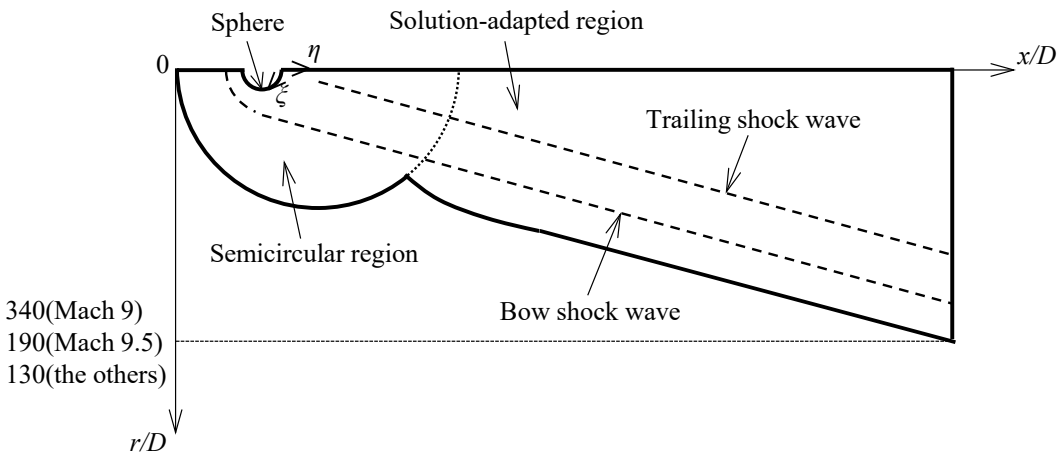

Fig. 6.1 Outline of computational domain around sphere.

6.2.4 Boundary conditions

No-slip and adiabatic wall boundary conditions

At the surface of the body, the no-slip and adiabatic wall conditions were set as

$$\begin{aligned} u = v = 0 \\ p_{j=1} = p_{j=2} \\ T_{j=1} = T_{j=2} \end{aligned} \tag{6.5}$$

where the subscript $j = 1$ denotes the index of grid points on the wall boundary. The density was calculated by the equation of the state of ideal gas given by Eq. (2.8).

Axi-symmetric boundary conditions

On the axis of symmetry at $r = 0$, the axi-symmetric boundary conditions were set as

$$Q_{ja=1} = Q_{ja=2}, \text{ but } v_{ja=1} = 0 \tag{6.6}$$

where the subscript $ja = 1$ denotes the index of grid points on the axis of symmetry.

Outflow boundary conditions

The outflow boundary at $x = x_{\max}$ was evaluated by the zeroth-order extrapolation as

$$Q_{j=j\max} = Q_{j=j\max-1} \tag{6.7}$$

where subscript $j = j\max$ denotes the index of grid points at $x = x_{\max}$.

Interpolating boundary conditions

For the simulation in the solution-adapted region, the boundary between the semicircular and solution-adapted regions was set by the results obtained by the simulation in the semicircular region.

Freestream boundary conditions in uniform atmosphere

The other boundaries were set as the freestream boundary conditions in the uniform atmosphere:

$$\begin{aligned} u &= u_\infty \\ v &= 0 \\ p &= p_\infty \\ T &= T_\infty \end{aligned} \tag{6.8}$$

where subscript ∞ denotes the freestream value. Note that the reflection of waves was not considered because the axi-symmetric analysis was performed.

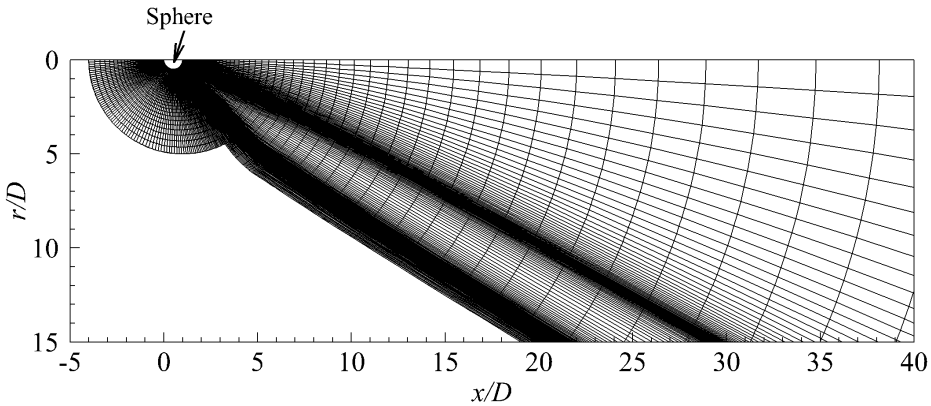

(a) $M_\infty = 2$ (shown every other point in ξ direction and every five points in η direction)

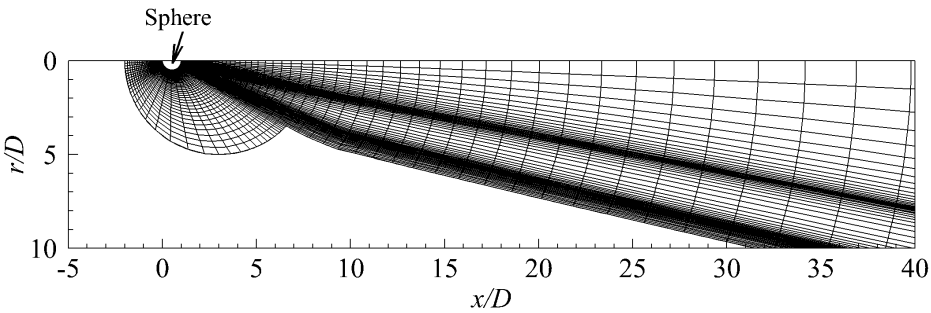

(b) $M_\infty = 5$ (shown every five points in each direction)

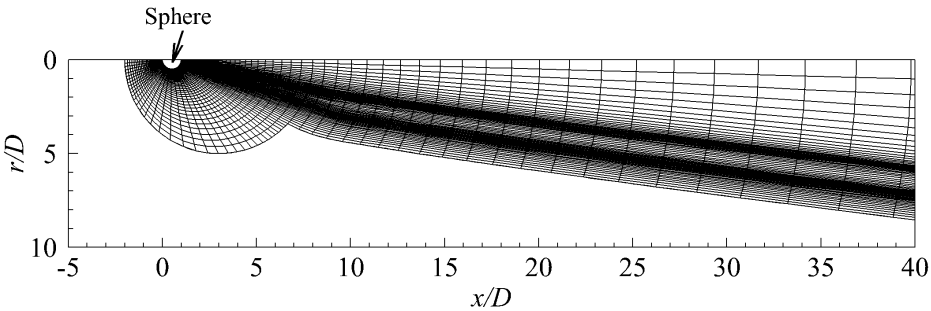

(c) $M_\infty = 10$ (shown every five points in each direction)

Fig. 6.2 Computational grids in the near fields.

6.2.5 Computational grid

Figure 6.2 shows the solution-adapted grids in the near field at M_∞ = 2, 5, and 10. The computational grids were constructed to align the grid lines with the bow and trailing shock waves, as described in section 2.4 of chapter 2. The locations of the bow and trailing shock waves were identified as those of the first and second local maximum pressures, respectively, viewed from the upstream. Because the boundary layer flow over the body was expected to have little effect on the far-field waveform, the minimum grid spacing was set to resolve the shock waves as follows. At the surface of the body, the minimum grid spacing in the ξ direction was set to 9.2 mm at M_∞ = 2 and 6.7 mm at the other flight Mach numbers, and that in the η direction was 2 mm at all flight Mach numbers. In the solution-adapted region, the minimum grid spacing in the ξ direction was 100 mm at all flight Mach numbers. Table 6.2 shows the number of grid points. As the flight Mach number increases, the shock-wave angles in the far field decreases, and the propagation distance of the shock waves to a specified r/D differs in different Mach numbers. Thus, the grid numbers were adjusted according to the flight Mach number. The procedure of the solution-adapted grid generation was described in sections 2.4 and 2.6 of chapter 2.

The grid convergence at M_∞ = 2 and 10 was confirmed by comparison with results using grids with four times the number of grid points, which were constructed by adding the internal dividing points to the computational grids in the ξ and η directions. Table 6.3 shows the grid convergence. The pressure waveforms and pressure rises in both cases were almost the same regardless of the minimum grid spacing and the number of grid points. Therefore, the grid convergence was adequate for evaluating the sonic boom waveform in both cases. Because the computational grids were constructed by the same method regardless of the flight Mach number, the grid convergence is assumed to be adequate for the other flight Mach numbers.

Table 6.2 Number of grid points

Region	Mach number	ξ direction	η direction
Semicircular region	All cases	501	401
Solution-adapted region	$M_\infty = 2$	321	211
	$M_\infty = 5, 6$	321	241
	$M_\infty = 7$	321	251
	$M_\infty = 8$	321	261
	$M_\infty = 9$	321	381
	$M_\infty = 9.5, 10, 10.5, 11$	321	271

Table 6.3 Difference in pressure rise of shock wave obtained by grids with four times the number of grid points relative to computational grids.

	Location	$M_\infty = 2$	$M_\infty = 10$
Bow shock wave	$r/D = 10$	–0.1 %	–0.2 %
	$r/D = 100$	0.04 %	–0.1 %
Trailing shock wave	$r/D = 10$	–0.2 %	–1.0 %
	$r/D = 100$	–0.2 %	–

6.3 Computational results

To clarify the waveform transition from an N-wave type to a caret-wave type in a hypersonic flow regime, simulation results are analyzed by the pressure waveform and the traces of bow and trailing shock waves generated from the sphere. The locations of these waves are identified as those of the first and second local maximum pressures, respectively, viewed from the upstream. As a result, the coalescence point of the bow and trailing shock waves are obtained, and the sonic boom waveform type generated from the hypersonic spherical body is classified according to the flight Mach number and the radial distance from the axis of symmetry. Moreover, the detailed mechanism of the waveform transition is investigated by analyzing the shock-wave angle.

6.3.1 Distributions of Mach number and pressure in the near field

Figure 6.3 shows the distributions of the Mach number and the pressure fluctuation in the near fields. In the Mach number distributions, the streamlines are depicted as black solid lines. In the pressure distribution, the traces of the bow and trailing shock waves are plotted as black solid and dashed lines, respectively. Physical phenomena around the sphere include four waves: the bow shock wave in front of the sphere, the expansion waves at the spherical surface, the trailing shock wave in the wake flow behind the sphere, and the expansion waves behind the trailing shock wave. All four waves are confirmed regardless of the flight Mach number. As the flight Mach number increases, the bow shock wave and the expansion waves behind the trailing shock wave strengthen, whereas the trailing shock wave weakens. The angle of the bow shock wave is 90° at the axis of symmetry and decreases with increasing the radial distance from the axis of symmetry because the bow shock wave in the near field is significantly attenuated by the expansion waves issued from the spherical surface. The change in the angle of the trailing shock wave with the radial distance is smaller than that in the angle of the bow shock wave because the strength of the trailing shock wave at the generation source of the wave is weaker than that of the bow shock wave. As the flight Mach number increases, the angles of the bow and trailing shock waves in the far fields decrease.

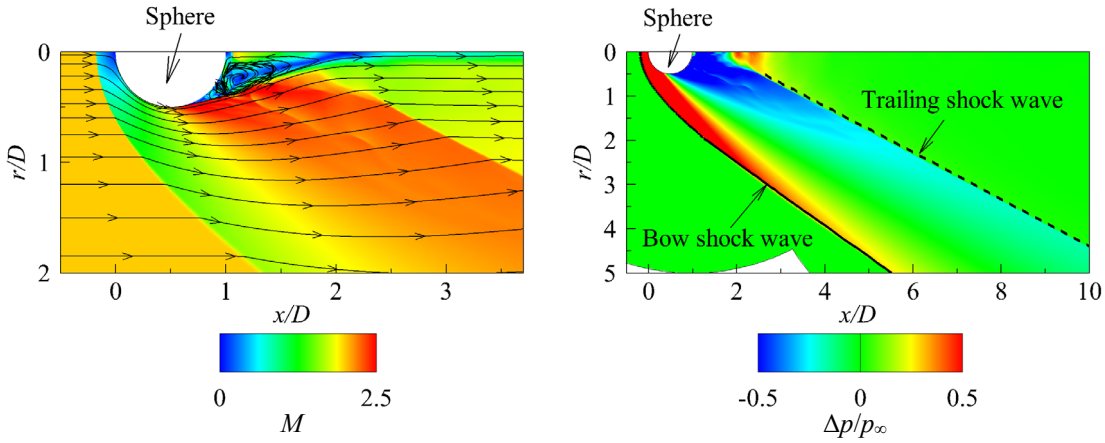

(a) $M_\infty = 2$

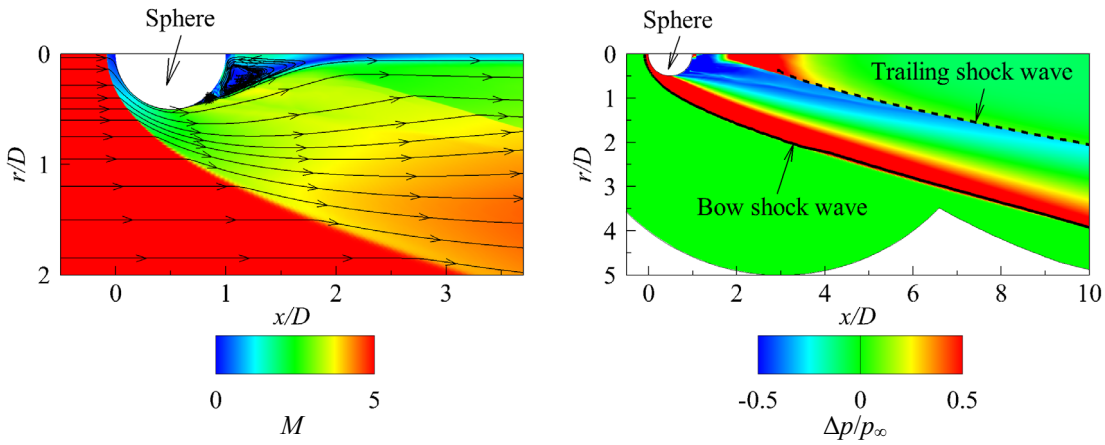

(b) $M_\infty = 5$

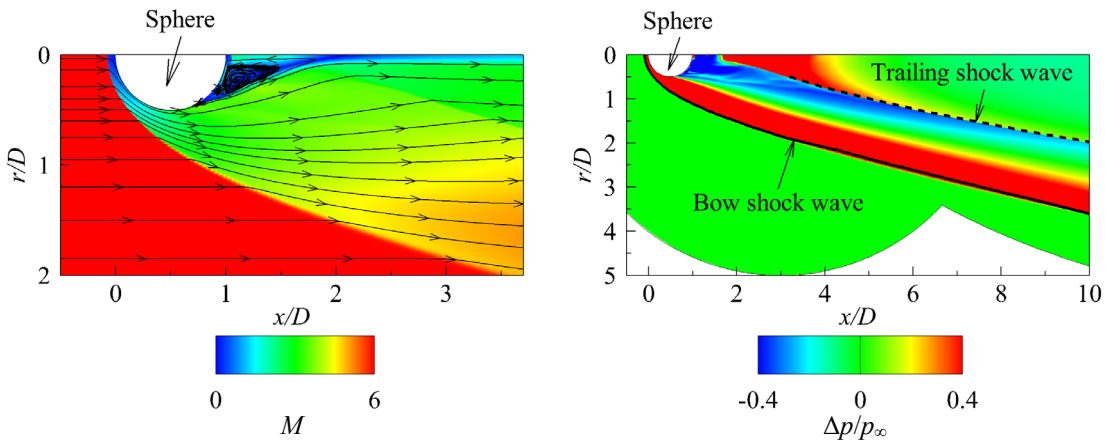

(c) $M_\infty = 6$

Fig. 6.3 Distributions of Mach number (left) and pressure fluctuation (right) in the near fields.

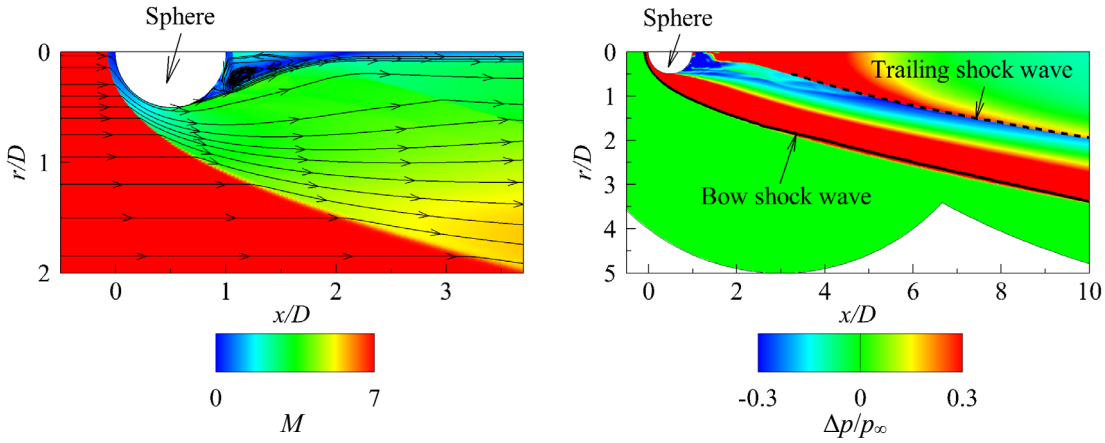

(d) $M_\infty = 7$

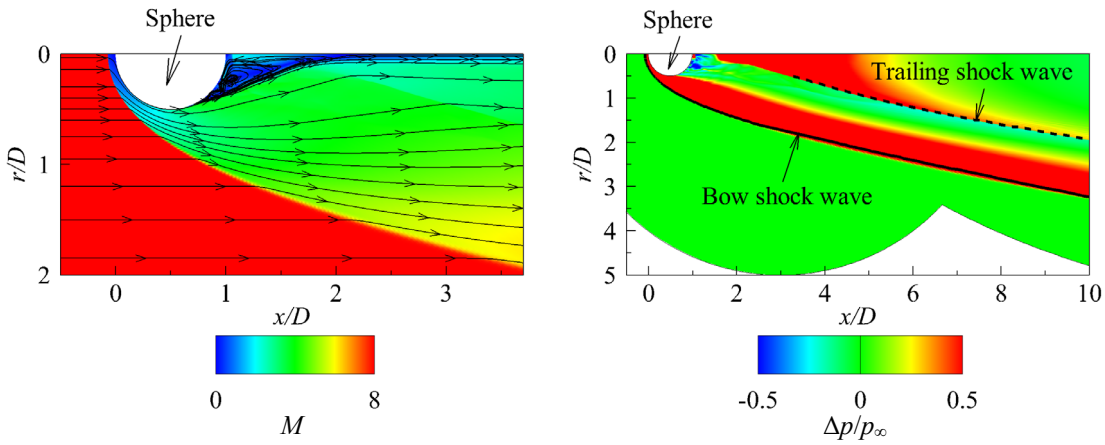

(e) $M_\infty = 8$

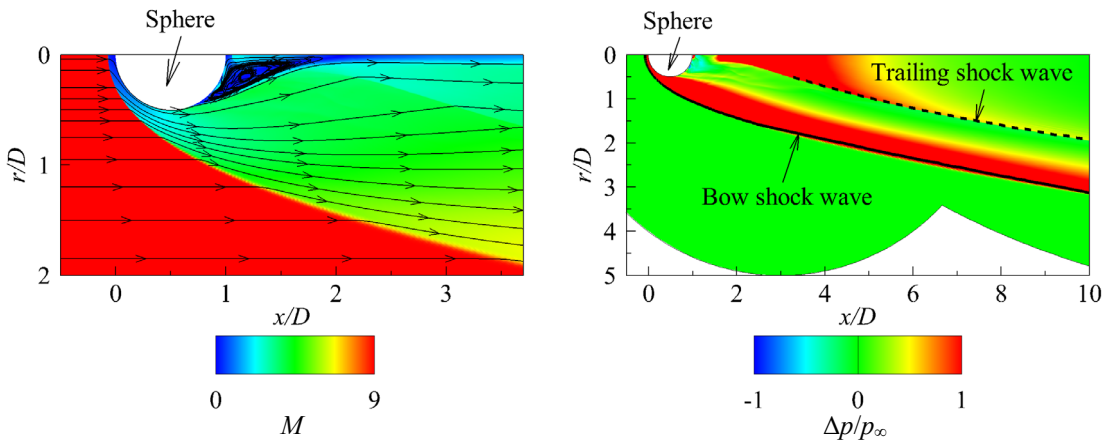

(f) $M_\infty = 9$

Fig. 6.3 Distributions of Mach number (left) and pressure fluctuation (right) in the near fields.

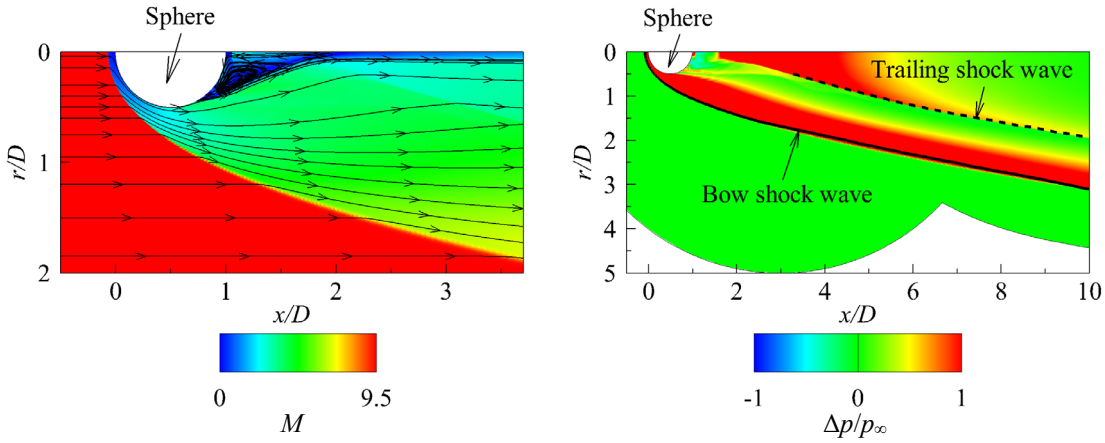

(g) $M_\infty = 9.5$

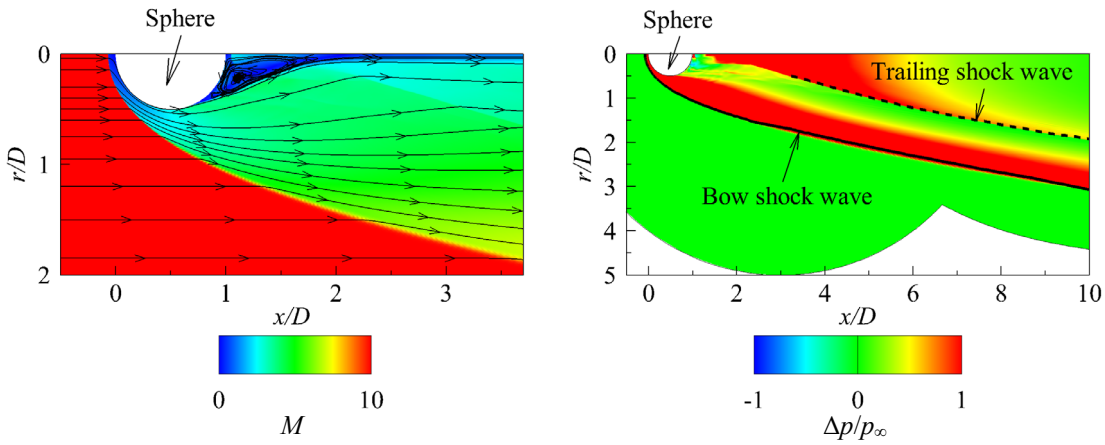

(h) $M_\infty = 10$

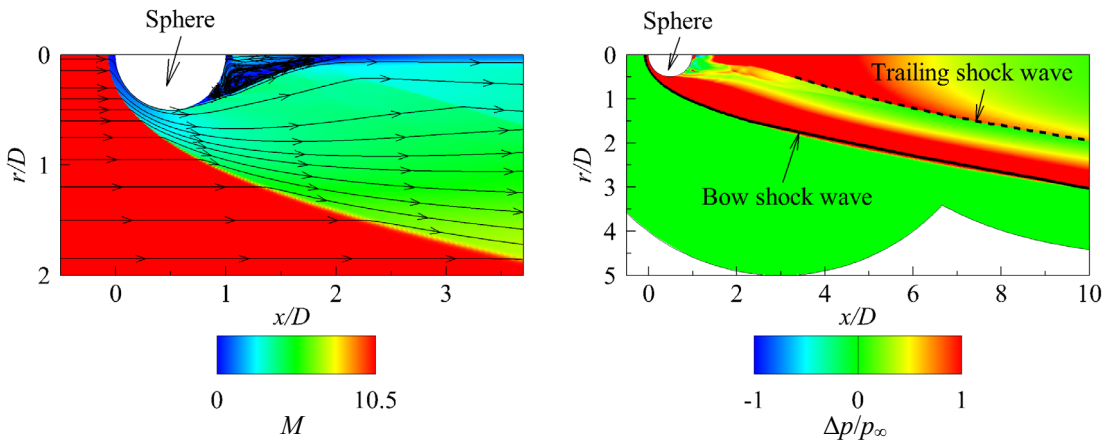

(i) $M_\infty = 10.5$

Fig. 6.3 Distributions of Mach number (left) and pressure fluctuation (right) in the near fields.

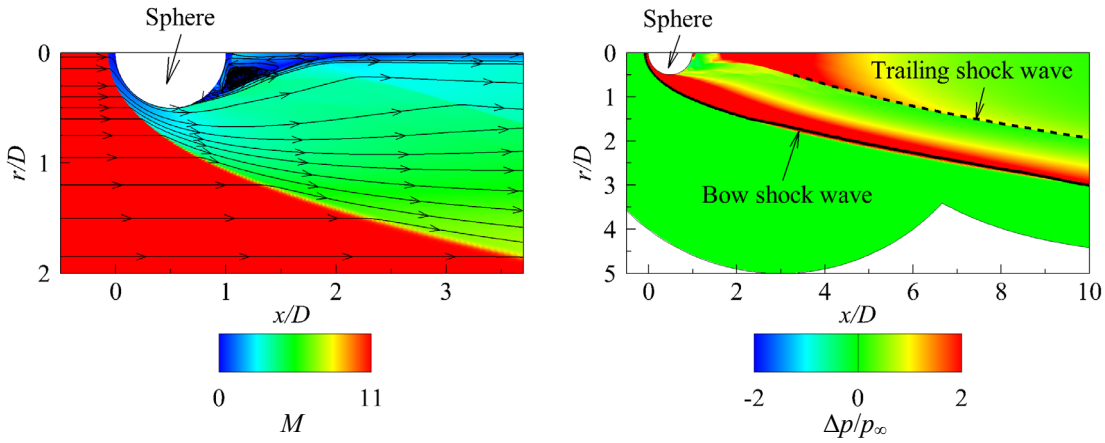

(j) $M_\infty = 11$

Fig. 6.3 Distributions of Mach number (left) and pressure fluctuation (right) in the near fields.

6.3.2 Pressure waveform in the far field

Figure 6.4 shows the pressure waveforms at r/D = 50 and 100. The horizontal axis represents the relative time calculated by the streamwise distance from the bow shock wave and the flight velocity. As shown in Fig. 6.4(a), the pressure rises of the bow and trailing shock waves at $M_\infty = 2$ are almost equivalent, and the waveform is two-peaked and shaped like an N (N-wave). As the flight Mach number increases, the bow shock wave and the expansion waves behind the trailing shock wave strengthen, whereas the trailing shock wave weakens, as shown in Fig. 6.4. Thus, the bow shock waves at the hypersonic speeds are stronger than the trailing shock waves, and the over-expanded flow regions behind the trailing shock waves are formed. The pressure behind the over-expansion is gradually restored to the atmospheric pressure. As the flight Mach number increases, the interval between the bow and trailing shock waves decreases because the difference in the angles of the bow and trailing shock waves decreases (see section 6.3.4 for details). In the case of flight Mach number less than or equal to 8, the interval increases with increasing radial distance from the axis of symmetry, although the rate of increase in the interval drops as the flight Mach number increases. On the other hand, in the case of flight Mach number greater than or equal to 9, the interval decreases with increasing the radial distance, resulting in the coalescence of these waves. As shown in Figs. 6.4(h)–(j), the waveforms at r/D = 100 are one-peaked and shaped like carets (caret-waves) after the coalescence of the bow and trailing shock waves. Therefore, the waveform changed from the N-wave to the caret-wave as the flight Mach number increased. An explosive sound occurs twice from an N-wave and only once from a caret-wave; thus, the number of explosive sounds varied with the flight Mach number. Although this waveform transition occurred in hypersonic flow regimes, it was well investigated by the full-field simulation considering the strong nonlinearity; this is a specific advantage of full field simulation. Therefore, it can be seen that the full-field simulation method is a powerful tool for analyzing sonic boom propagation from a hypersonic blunt body.

Figure 6.5 shows the closeup of the pressure waveforms before and after the coalescence of the bow and trailing shock waves at $M_\infty = 10$. As can be seen in this figure, the trailing shock wave becomes dull as the interval decreases because of the following reason: the trailing shock wave crosses into the grid lines between the bow and trailing shock waves before the coalescence of these waves. As a result, the number of grid points capturing the trailing shock wave is increased, and the resolution of the trailing shock wave is reduced. Thus, to precisely predict the pressure rise of the shock wave after the coalescence, the computational grid must be improved so that the trailing shock wave does not cross into grid lines (although the grid convergence including the number of grid points and the minimum grid spacing was confirmed, as described in section 6.2.5).

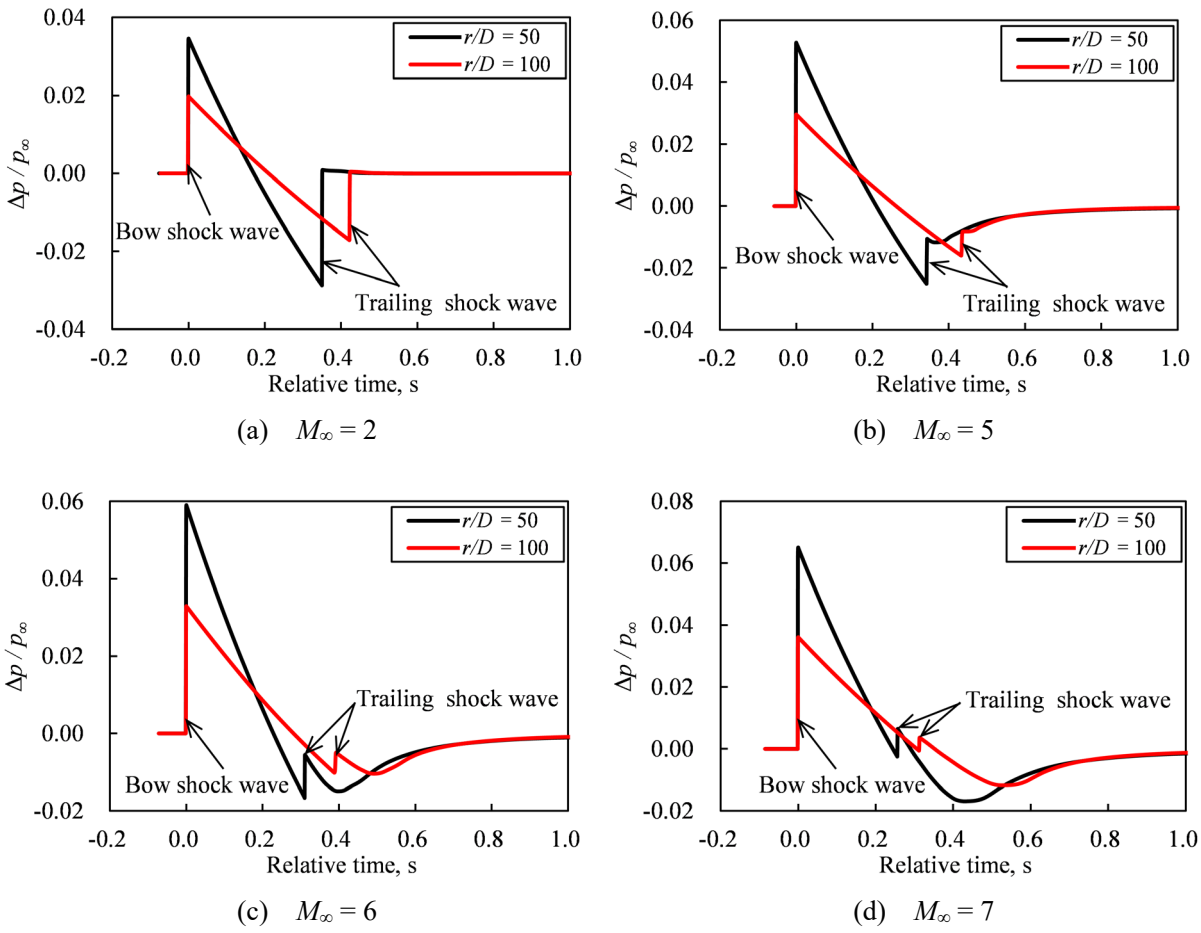

Fig. 6.4 Pressure waveforms in the far fields.

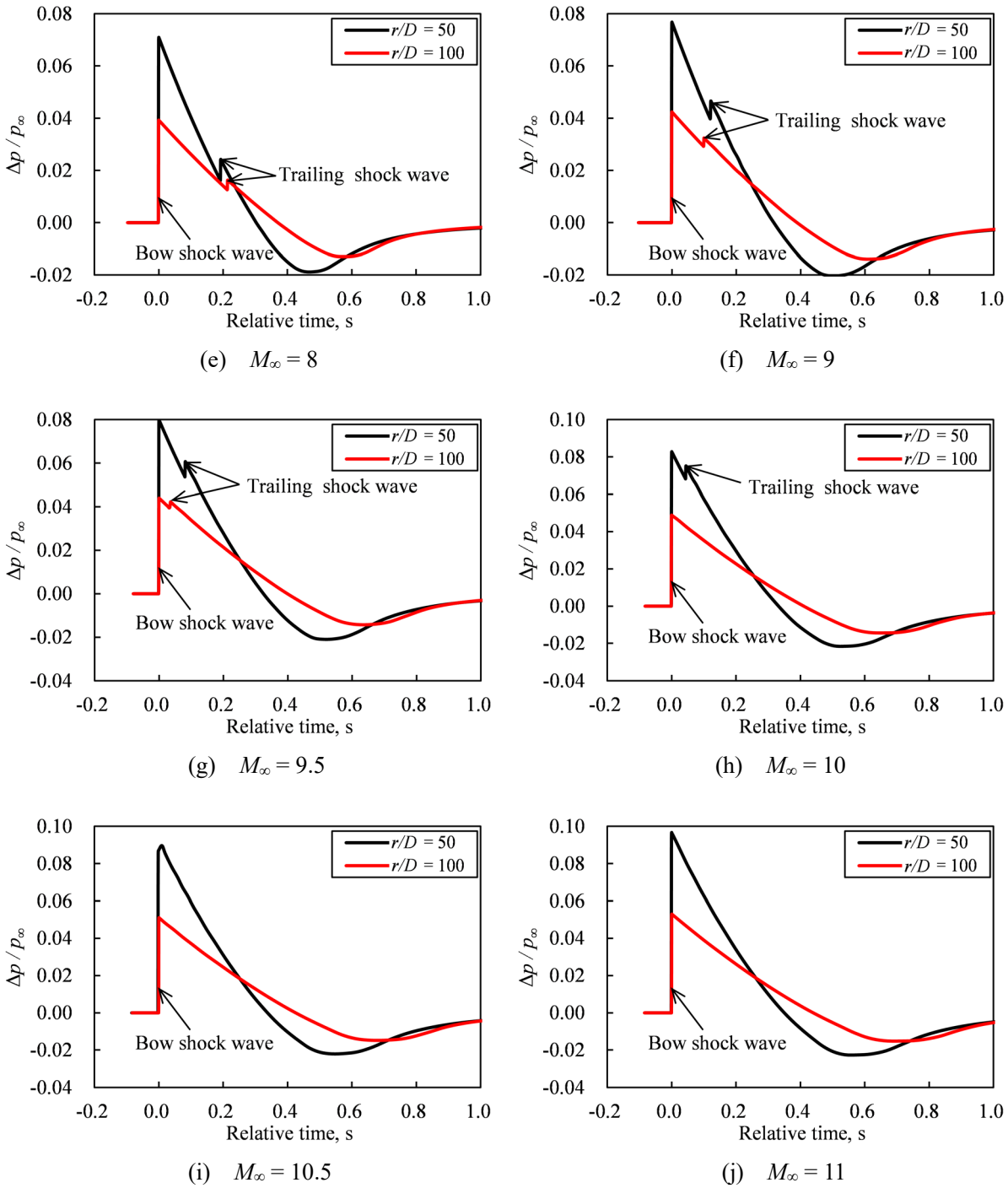

Fig. 6.4 Pressure waveforms in the far fields.

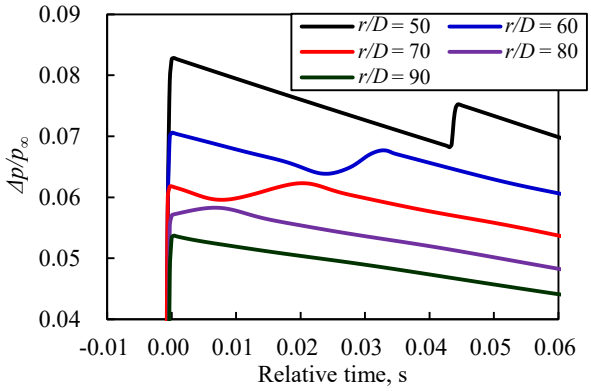

Fig. 6.5 Closeup of bow shock wave at M_∞ = 10.

6.3.3 Traces of bow and trailing shock waves

Figure 6.6 shows the traces of the bow and trailing shock waves with the radial distance. In Fig. 6.6, the aspect ratio is 4:1 to enhance the clarity of the traces. As can be seen in Fig. 6.6, the angle of the bow shock wave in the near field is higher than that of the trailing shock wave because it is 90° at the axis of symmetry and decreases gradually. As the flight Mach number increases, the shock-wave angles in the far fields decrease, and the propagation distance of the shock wave to a specified r/D decreases because the ray path is vertical to the shock wave. Figure 6.7 shows the interval between the bow and trailing shock waves. As shown in Fig. 6.7, the interval in the near field increases with increasing the radial distance, whereas that in the far fields differs according to the flight Mach numbers. In the case of flight Mach number less than or equal to 8, the interval between the bow and trailing shock waves increases with increasing radial distance from the axis of symmetry, although the rate of increase in the interval drops as the flight Mach number increases. On the other hand, in the case of flight Mach number higher than or equal to 9, the interval decreases with increasing radial distance, resulting in the coalescence of these waves. The results show that the critical Mach number deciding the coalescence of these waves exists between M_∞ = 8 and 9.

Figure 6.8 shows the transition curve, where the variation in the radial distance of the coalescence point with the flight Mach number is depicted. In the lower area of the transition curve, the waveform is the N-wave type, and the explosive sound occurs twice, whereas in the upper area, the waveform is the caret-wave type, and the explosive sound occurs only once. The waveform transition occurred when the radial distance from the axis of symmetry and/or the flight Mach number changed enough to cross the transition curve. As the flight Mach number increases, the coalescence point approaches the axis of symmetry. If a realistic flight of a meteorite with a diameter of 20 m at an altitude of 25 km is assumed, the waveform generated when the flight Mach number is higher than or equal to 9 is a caret-wave, and the explosive sound occurs only once at the ground.

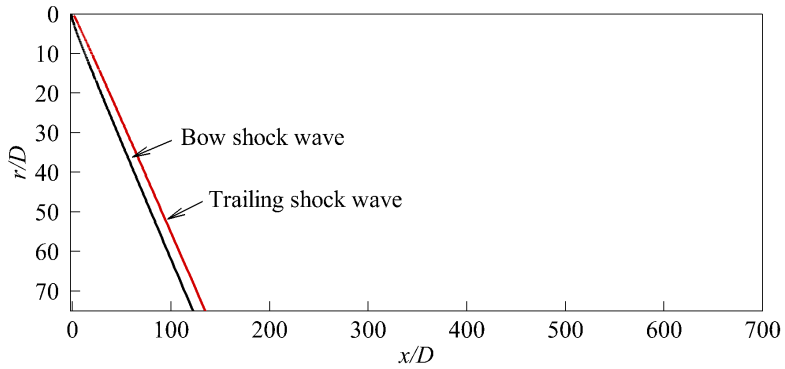

(a) $M_\infty = 2$

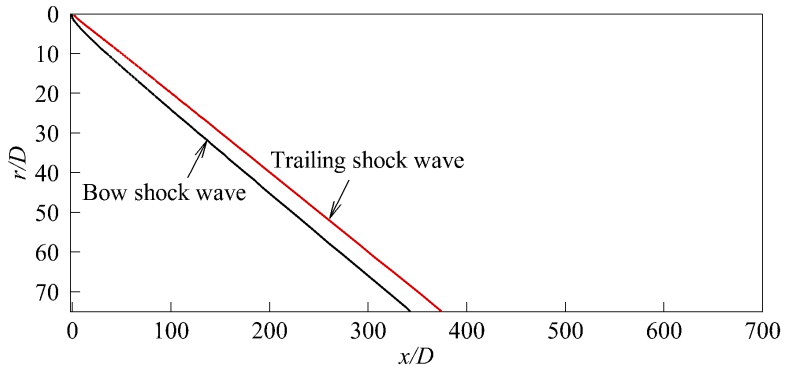

(b) $M_\infty = 5$

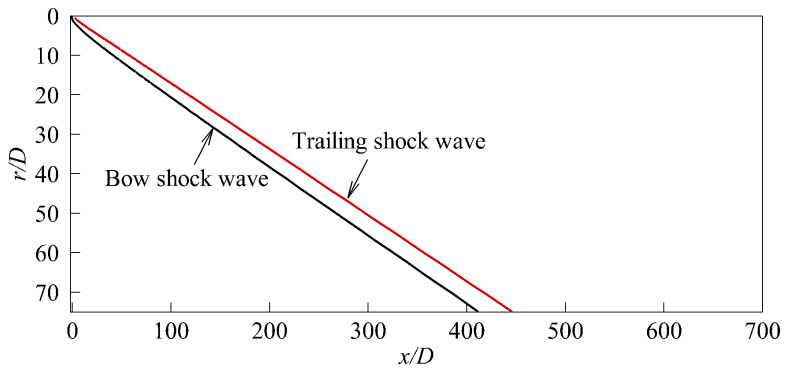

(c) $M_\infty = 6$

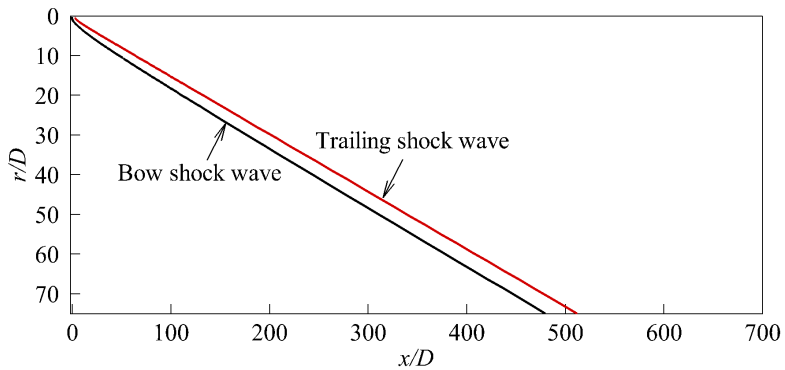

(d) $M_\infty = 7$

Fig. 6.6 Traces of bow and trailing shock waves with radial distance.

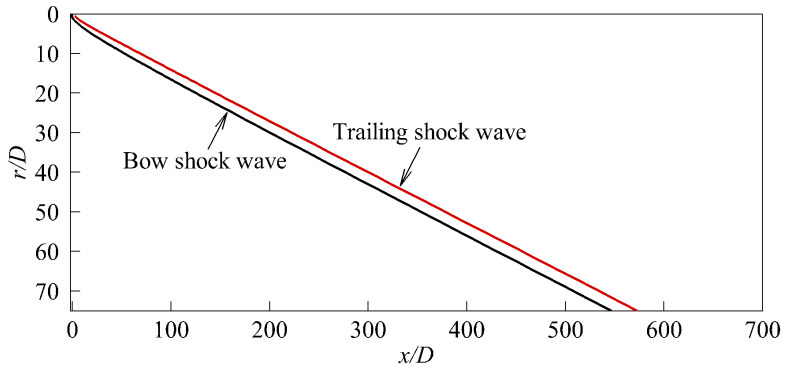

(e) $M_\infty = 8$

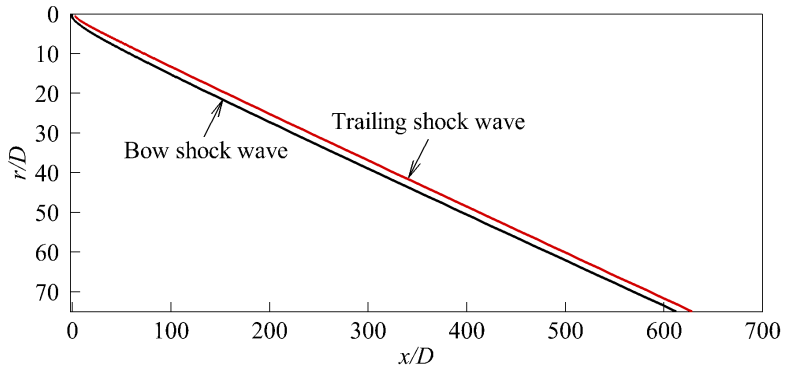

(f) $M_\infty = 9$

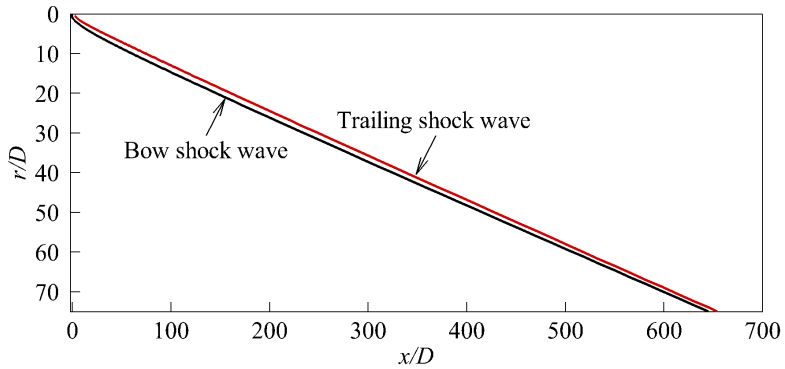

(g) $M_\infty = 9.5$

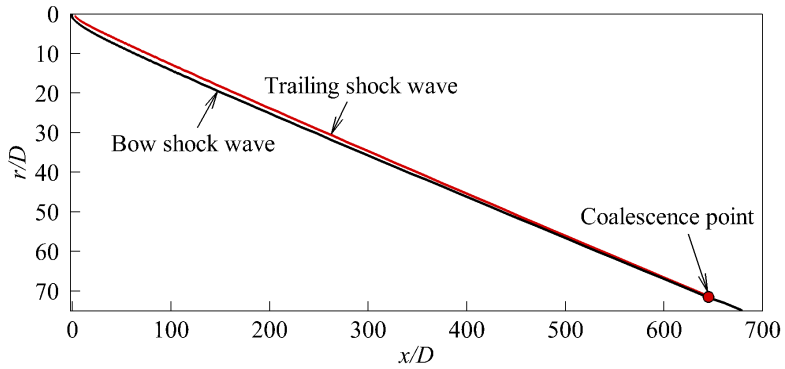

(h) $M_\infty = 10$

Fig. 6.6 Traces of bow and trailing shock waves with radial distance.

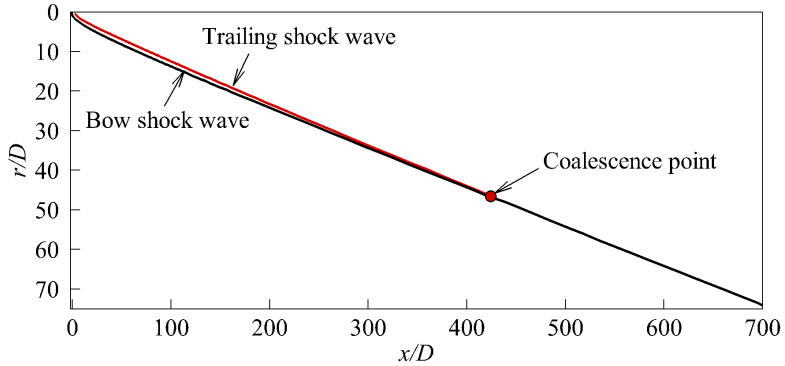

(i) $M_\infty = 10.5$

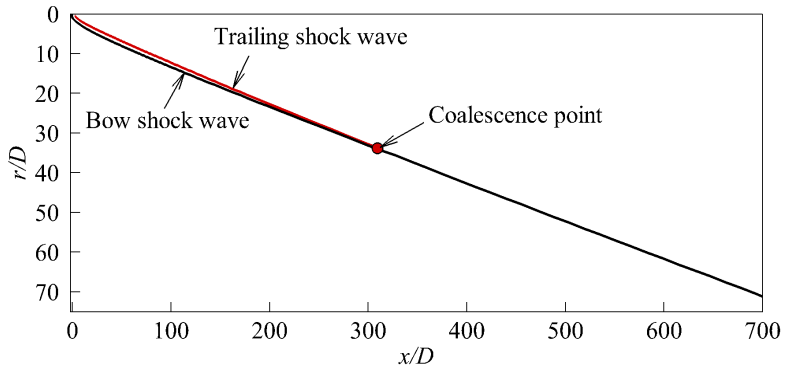

(j) $M_\infty = 11$

Fig. 6.6 Traces of bow and trailing shock waves with radial distance.

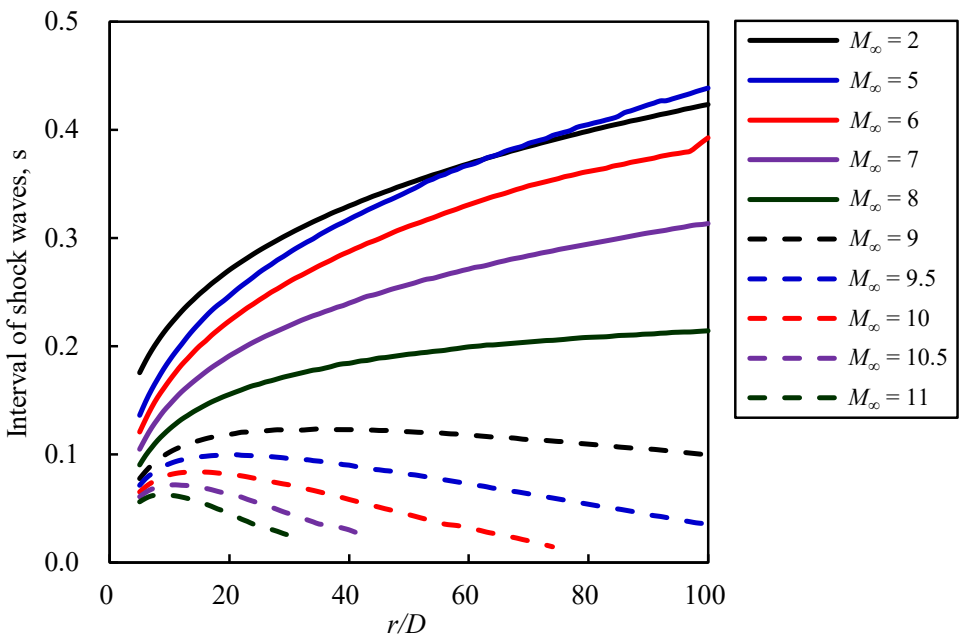

Fig. 6.7 Interval between bow and trailing shock waves.

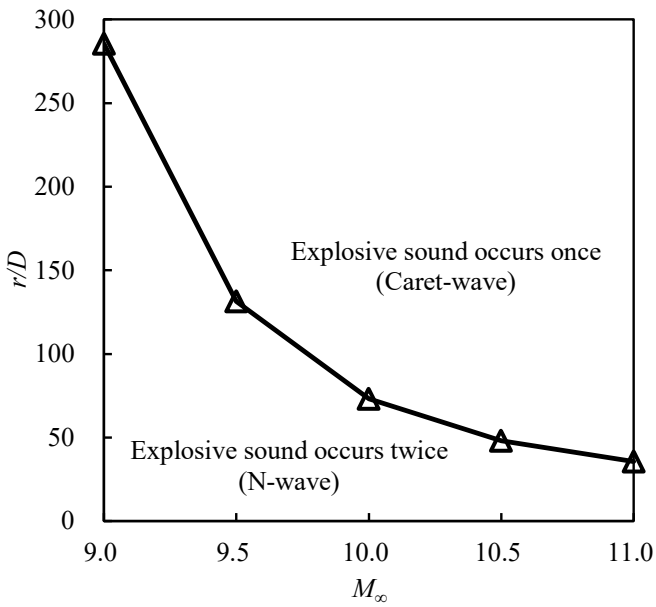

Fig. 6.8 Transition curve that divides N-wave from caret-wave.

6.3.4 Shock-wave angles of bow and trailing shock waves

In order to clarify the detailed mechanism of waveform transition, the shock-wave angles are investigated in this section. The real shock-wave angles from the streamwise direction are calculated using the traces of the bow and trailing shock waves described in Fig. 6.6. Moreover, to facilitate analysis of the variation in the shock-wave angle, the Mach angle μ_M is calculated as

$$\mu_M = \arcsin\frac{1}{M_1} \tag{6.9}$$

$$M_1 = \frac{\left|\vec{U}_1\right|}{c_1} = \sqrt{\frac{u_1^2 + v_1^2}{\gamma R T_1}} \tag{6.10}$$

where subscript 1 indicates the value just before the shock wave. For the bow shock wave, the Mach angle is calculated as $M_1 = M_\infty$; thus, this angle does not change in the entire flow field. For the trailing shock wave, the velocity vector just before the trailing shock wave is not parallel to the streamwise direction, as shown in Fig. 6.3. Because the Mach angle is defined as the angle between the Mach line and the velocity vector, the modified Mach angle $\mu_{M\,\mathrm{mod}}$ is calculated as

$$\mu_{M\,\mathrm{mod}} = \mu_M + \alpha_1 \tag{6.11}$$

$$\alpha_1 = \arctan\frac{v_1}{u_1} \tag{6.12}$$

where α is the angle of the flow velocity from the streamwise direction. Figure 6.9 shows the calculating method of the modified Mach angle. The modified Mach angle of the trailing shock wave changes with the radial distance because the local Mach number and the velocity vector just before the trailing shock wave

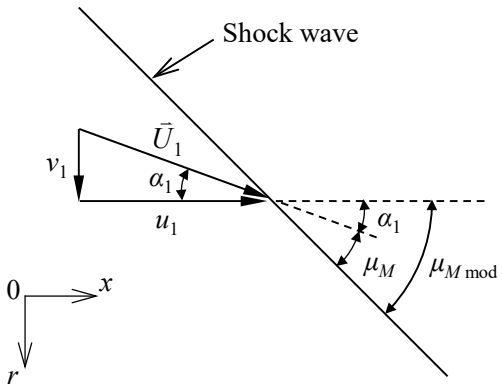

Fig. 6.9 Calculating method of modified Mach angle.

change with the distance. Generally, the real shock-wave angle depends on the following three parameters. The first parameter is the local Mach number just before the shock wave. In the case of weak shock wave, the shock-wave angle is assumed to be the Mach angle given by Eq. (6.9). As can be seen from Eq. (6.9), the Mach angle decreases with increasing the local Mach number just before the shock wave. The second parameter is the pressure rise of the shock wave, which indicates the strength of the shock wave. The angle of the strong shock wave is higher than that of the weak shock wave, although it approaches the Mach angle as the shock wave weakens. The third parameter is the angle of velocity vector just before the shock wave. The above three parameters are quite helpful in understanding the variation in the real shock-wave angles.

Figure 6.10 shows the variation in the angles of the bow and trailing shock waves with the radial distance. Although small numerical errors were generated in the real angles of the bow and trailing shock waves, the traces of these waves shown in Fig. 6.6 are macroscopically smooth; thus, the accuracy of the real angles is adequate for investigating the mechanism of the waveform transition. As shown in Fig. 6.10, in the case of flight Mach number higher than or equal to 9, the real angle of the trailing shock wave in the far field is higher than that of the bow shock wave; thus, the interval between the bow and trailing shock waves decreases with increasing the radial distance as shown in Fig. 6.7, resulting in the coalescence of these waves. The real angle of the bow shock wave decreases monotonically and approaches the Mach angle as the radial distance increases, regardless of the flight Mach number. On the other hand, the variation in the real angle of the trailing shock wave with the radial distance differs according to the flight Mach number. In the case of flight Mach number less than or equal to 6, the real angle of the trailing shock wave increases with increasing the radial distance, whereas in the case of flight Mach number higher than or equal to 7, it decreases with increasing the radial distance. However, the real angle of the trailing shock wave, as well as that of the bow shock wave, approaches the modified Mach angle and the Mach angle of the bow shock wave in the freestream conditions as the radial distance increases. The results show that the real angles of

the bow and trailing shock waves can be approximately evaluated by the Mach angle or the modified Mach angle that can be evaluated by two parameters: the local Mach number and the velocity vector just before the shock wave, as can be seen from Eq. (6.11).

Figures 6.11 and 6.12 show the differences of the angle between the bow and trailing shock waves, and Figure 6.13 shows the angle of flow velocity just before the trailing shock wave. As shown in Figs. 6.11–6.13, the angle of flow velocity just before the trailing shock wave changes in the same way as the difference of the Mach angle between the bow and trailing shock waves; thus, the angle of flow velocity just before the trailing shock wave is related to the Mach angle of the trailing shock wave because the Mach angle of the bow shock wave is constant at each flight Mach number. The result shows that the presence or absence of the coalescence of the bow and trailing shock waves can be approximately evaluated by the local Mach number just before the trailing shock wave. As shown in Fig. 6.12, the Mach angle of the trailing shock wave relative to that of the bow shock wave increases with increasing the flight Mach number; i.e., the local Mach number just before the trailing shock wave relative to the flight Mach number decreases with increasing the flight Mach number, because of the following reason: As the flight Mach number increases, the bow shock wave strengthens (see next section for details), and the interval between the bow and trailing shock waves decreases as shown in Fig. 6.7. Consequently, in the case of flight Mach number higher than or equal to 8, the local Mach number just before the trailing shock wave is smaller than the flight Mach number, and the Mach angle of the trailing shock wave is larger than that of the bow shock wave; i.e., the bow and trailing shock waves approach each other as the radial distance increases. These results show that the detailed mechanism of the waveform transition was well clarified by investigating the variation in the local Mach number just before the trailing shock wave. Note, however, that the real shock-wave angle is larger than the Mach angle until the shock wave weakens sufficiently as shown in Fig. 6.10; thus, in the case of flight Mach number less than or equal to 8, the real angle of the trailing shock wave is smaller than that of the bow shock wave in the entire computational domain, whereas in the case of flight Mach number higher than or equal to 9, the real angle of the trailing shock wave in the far field is higher than that of the bow shock wave.

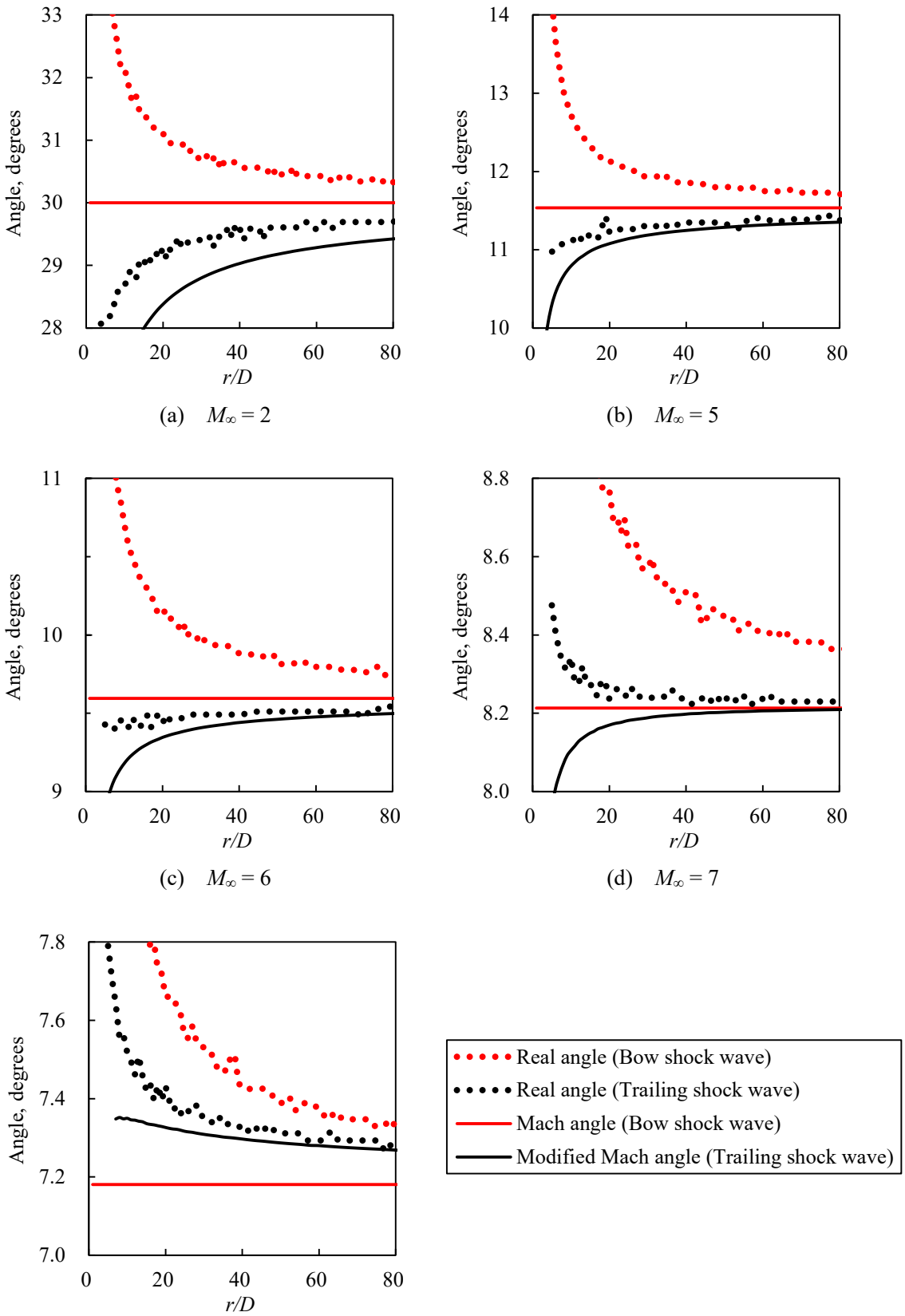

Fig. 6.10 Shock-wave angles and Mach angles of bow and trailing shock waves.

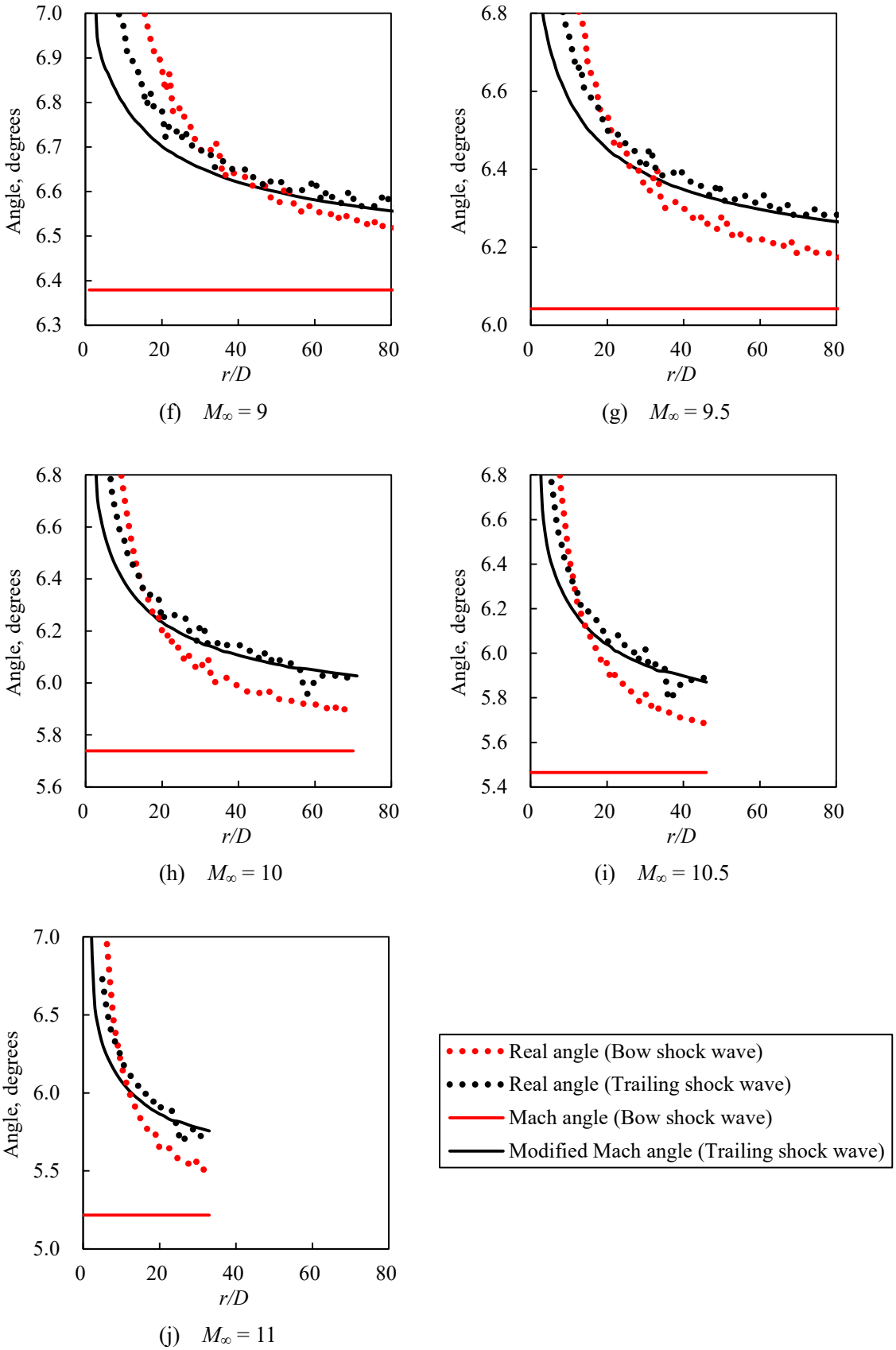

Fig. 6.10 Shock-wave angles and Mach angles of bow and trailing shock waves.

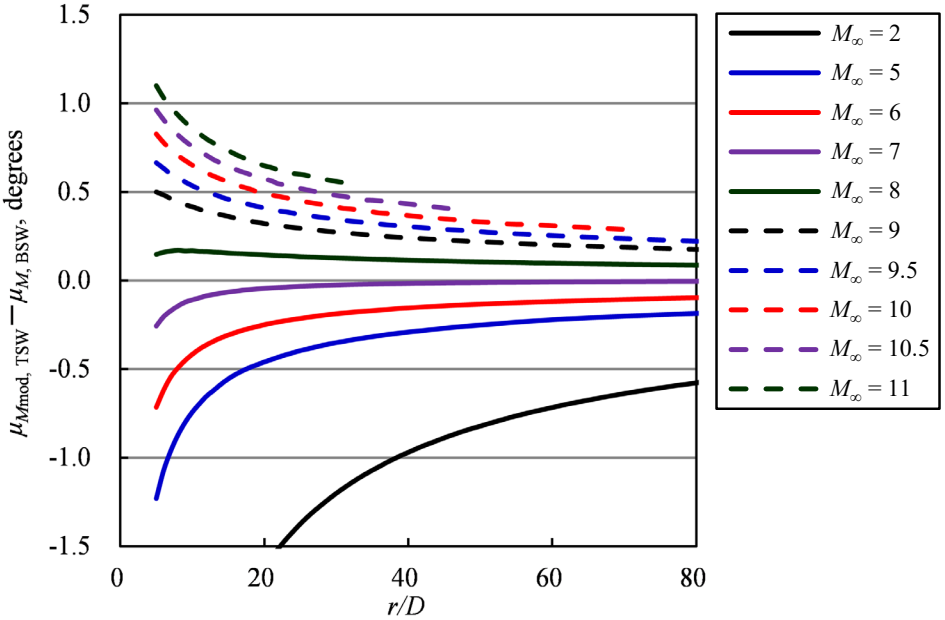

Fig. 6.11 Difference in Mach angle of bow shock wave (BSW) and modified Mach angle of trailing shock wave (TSW).

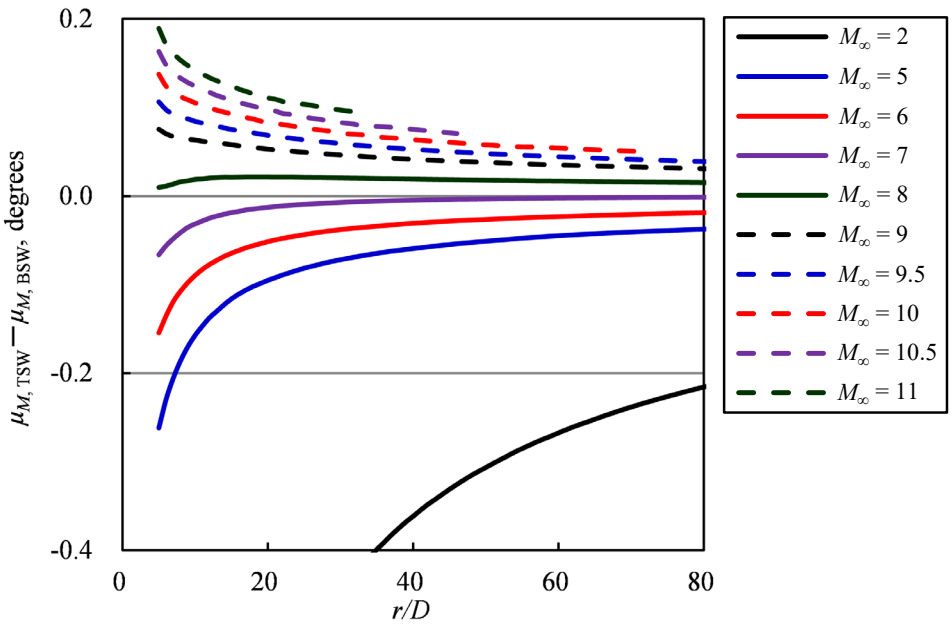

Fig. 6.12 Difference in Mach angle of bow (BSW) and trailing (TSW) shock waves.

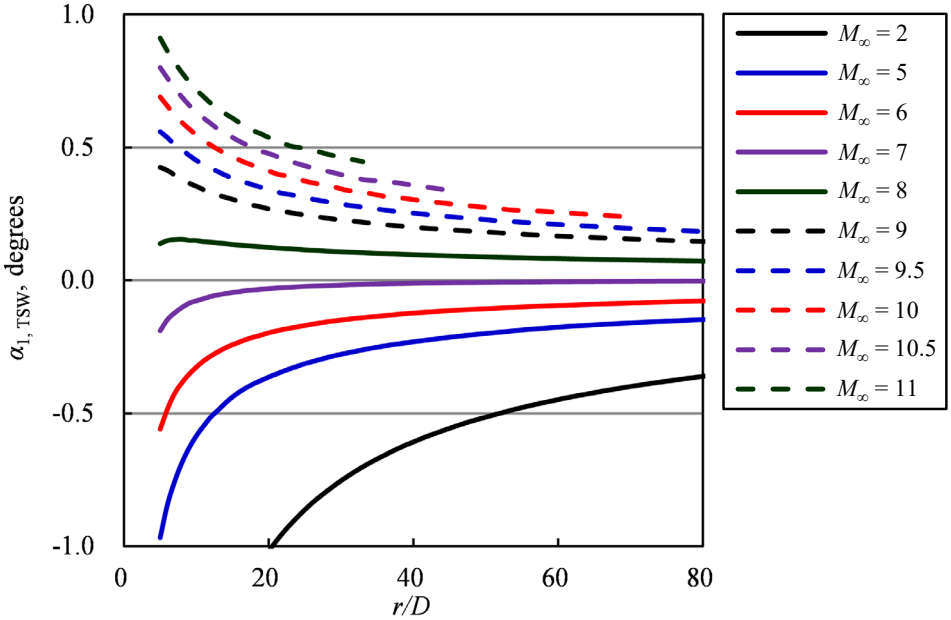

Fig. 6.13 Angle of velocity vector just before trailing shock wave (TSW).

6.3.5 Pressure rise of bow and trailing shock waves

The difference in the shock-wave angles described in the previous section is changed by the strength of the shock wave, which correlates highly with the pressure rise of the shock wave. Therefore, the investigation of the variation in the pressure rise is quite helpful in understanding the detailed mechanism of the waveform transition. Figure 6.14 shows the variation in the pressure rise with the radial distance. The pressure rise of the bow shock wave is defined as the first local maximum value of pressure fluctuation viewed from the upstream, and that of the trailing shock wave is calculated by subtracting the first local minimum pressure from the second local maximum pressure. Regardless of the flight Mach numbers, the pressure rises of the bow and trailing shock waves in the near fields decrease rapidly, whereas those in the far fields decrease slowly because the strength of geometrical spreading decreases with increasing radial distance from the axis of symmetry. As the flight Mach number increases, the bow shock wave strengthens, whereas the trailing shock wave weakens; thus, the bow shock wave becomes stronger than the trailing shock wave. Although the pressure rise of the bow shock wave is increased by the coalescence of the bow and trailing shock waves, the trailing shock wave becomes dull before the coalescence, because of the following reason: The trailing shock wave crosses into the grid lines between the bow and trailing shock waves before the coalescence, as shown in Fig. 6.5. Consequently, the number of grid points capturing the trailing shock wave is increased, and the resolution of the trailing shock wave is reduced; thus, the pressure rise of the trailing shock wave before the coalescence decreases, as shown in Fig. 6.14(b). To precisely predict the pressure rise of the shock wave after the coalescence, the computational grid must be improved so that the trailing shock wave does not cross into grid lines.

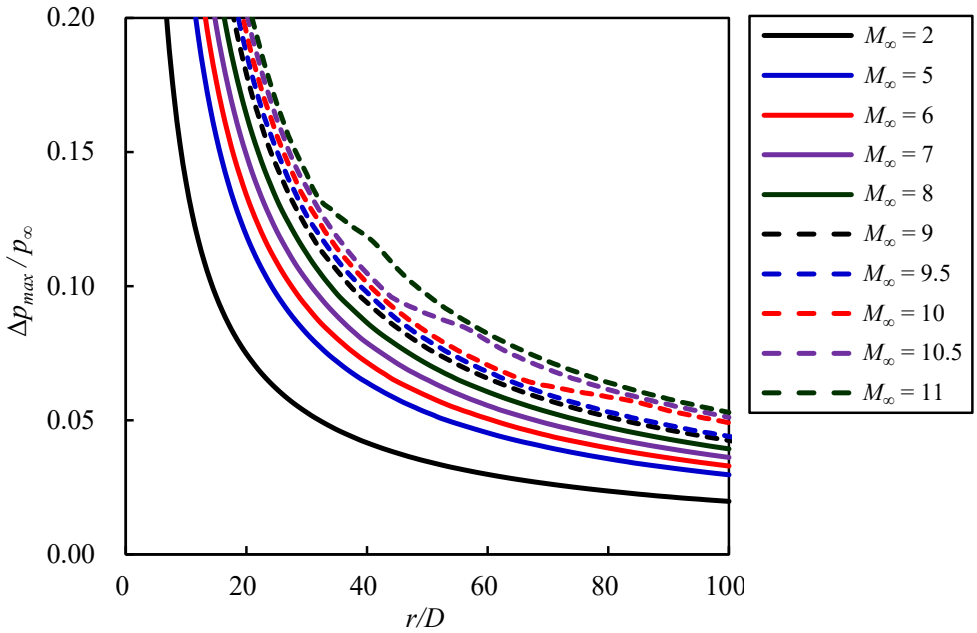

(a) Bow shock wave

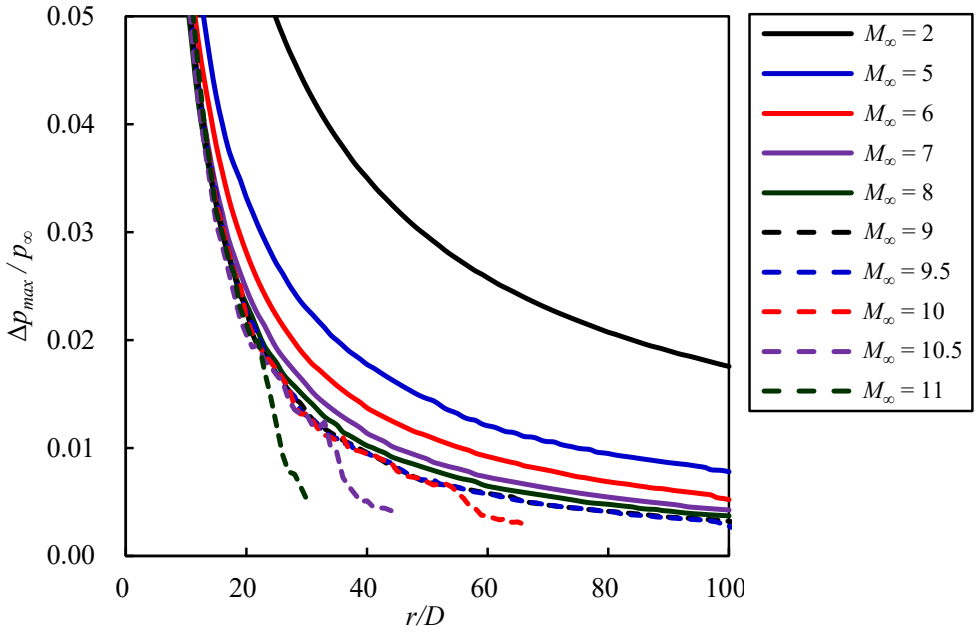

(b) Trailing shock wave

Fig. 6.14 Variation in pressure rise of shock wave with radial distance.

6.4 Summary of this chapter

In this chapter, full-field simulation was performed to analyze the waveform transition of sonic boom generated from a hypersonic spherical body. The results are summarized as follows.

- The pressure waveform was changed from an N-wave to a caret-wave as the flight Mach number increased. An explosive sound occurs twice in the case of the N-wave, whereas it occurs only once in the case of the caret-wave; i.e., the number of explosive sounds changed with the flight Mach number. The results show that there is the critical Mach number, at which the waveform transition occurs.
- The traces of the bow and trailing shock waves were investigated, and the coalescence point of the bow and trailing shock waves was obtained. The results show that the coalescence of these waves is a unique phenomenon in hypersonic flow regimes. Moreover, the transition curve that divided an N-wave type from a caret-wave type was obtained. This curve indicates that the number of explosive sounds changes with the flight Mach number, and the radial distance of the coalescence point decreases with increasing the flight Mach number.
- To analyze the detailed mechanism of the waveform transition, the variation in the real shock-wave angle was compared with the Mach angle. Consequently, the difference of the real angle between the bow and trailing shock waves strongly depended on the variation in the local Mach number just before the trailing shock wave. Thus, the detailed mechanism of the waveform transition was well clarified by investigating the variation in the local Mach number just before the trailing shock wave.

These results show that the waveform transition of sonic boom generated from a hypersonic spherical body was well clarified, and the full-field simulation was powerful for analyzing sonic boom characteristics in the hypersonic flow regime, including the strong bow shock wave.

Chapter 7

Conclusions

A framework of the full-field simulation method was formulated to reproduce sonic boom propagation through the real atmosphere and was used to clarify formation mechanism of rise time, sonic boom cutoff phenomena, and the waveform transition in hypersonic flow regimes. The results are summarized as follows.

Formulation of full-field simulation method (Chapters 2 and 3)

The full-field simulation method for sonic boom propagation through the real atmosphere was formulated by constructing three methods. First was the computational approach including the numerical correction method for considering atmospheric stratification. Second was the method of constructing the solution-adapted grid aligned with the shock waves in the entire flow field. Third was the segmentation method of a computational domain for reducing the computational load. Consequently, the first-ever direct reproduction of the flight test for sonic boom was successful. The simulation results reached the same level of accuracy as the waveform parameter method, which is the representative prediction method for sonic boom. Moreover, the pressure waveform of the full-field simulation with the thermal nonequilibrium was in good agreement with the D-SEND#1 flight test data. These results confirmed that the accuracy of full-field simulation in the real atmosphere was adequate for evaluating sonic boom intensity, including not only the pressure rise but also the rise time.

Full-field simulation for rise time prediction (Chapter 4)

Full-field simulation with the thermal nonequilibrium was performed to clarify the effect of molecular relaxation on the pressure waveform and the formation mechanism of rise time in the uniform and stratified atmospheres. The results show that the effect of molecular relaxation changed according to the variation in the relaxation time. In the case of long relaxation time, the energy exchange was induced slowly, and the pressure fluctuation behind the shock wave was widely decreased, although the energy exchange just behind the shock wave was too small to form the rise time. On the other hand, in the case of short

relaxation time, the energy exchange was induced rapidly and converged just behind the shock wave. As a result, the pressure fluctuation just behind the shock wave was significantly decreased, and the rise time was formed. The rise time in the uniform atmosphere increased monotonically, whereas that in the stratified atmosphere increased and decreased toward the ground because the difference of strength between the molecular relaxation and the nonlinearity was dramatically changed according to the variation in the relaxation time with altitude. Moreover, it was shown that the strength of molecular relaxation can be investigated by two parameters: the maximum exchange rate of translational-vibrational energy and its exchange time. Therefore, the effect of molecular relaxation and the formation mechanism of rise time were well clarified by the full-field simulation with the thermal nonequilibrium.

Full-field simulation at low supersonic speed (Chapter 5)

The full-field simulation method was applied to the analysis of sonic boom propagation generated from a low supersonic flight object, and the results were analyzed to investigate the following three characteristics of cutoff phenomena. First was the waveform transition of sonic boom in the cutoff region. The incoming wave generated from the body was divided into an outgoing wave in the upward direction and an evanescent wave in the downward direction by the diffraction phenomena. In addition, the focused sonic boom was generated by integration of the incoming and outgoing waves. Second was the characteristic of the evanescent wave under the cutoff altitude. The evanescent wave propagated vertically downward direction and rapidly attenuated toward the ground. Third was the three-dimensional structure of cutoff phenomena. The shape of the cutoff surface was a downward convex, and the lateral cutoff altitude was higher than the sonic cutoff altitude beneath the body. These results were quite helpful in clarifying the characteristics of cutoff phenomena that cannot be precisely predicted in the exiting prediction methods. Therefore, the full-field simulation method was a powerful tool for analyzing the sonic boom propagation generated from the low supersonic flight object, including the focused sonic boom in the caustic-vicinity field.

Full-field simulation at hypersonic speed (Chapter 6)

The full-field simulation method was applied to the analysis of sonic boom propagation generated from a hypersonic spherical body, and the results were investigated to clarify the waveform transition of sonic boom according to the flight Mach number. Consequently, the sonic boom waveform type was changed from an N-wave type to a caret-wave type as the flight Mach number increased. An explosive sound occurs twice in the case of the N-wave, whereas it occurs only once in the case of the caret-wave; i.e., the number of explosive sounds changed with the flight Mach number. The transition curve that divides an N-wave from a caret-wave was obtained by the full-field simulation, and there was the critical Mach number, at

which the waveform transition occurs. Moreover, the detailed mechanism of the waveform transition was clarified by comparison between the real shock-wave angle and the Mach angle. Consequently, the difference of the real angle between the bow and trailing shock waves strongly depended on the variation in the local Mach number just before the trailing shock wave, and the detailed mechanism of the waveform transition was well clarified by investigating the variation in the local Mach number just before the trailing shock wave. These results were quite helpful in clarifying sonic boom characteristics at hypersonic speeds. Therefore, the full-field simulation was powerful for analyzing the sonic boom propagation generated from the hypersonic flight object.

As mentioned above, the framework of the full-field simulation method was completely constructed because all three phases were completed, as shown in Fig. 7.1. Moreover, the formation mechanism of rise time, the sonic boom cutoff phenomena, and the waveform transition in hypersonic flow regimes were well clarified by the full-field simulation. Therefore, the objectives of this thesis were completed. Because the full-field simulation based on the CFD has the potential for considering various flight, atmospheric, and ground conditions, it seems promising for realizing high-accuracy numerical flight experiments for sonic boom.

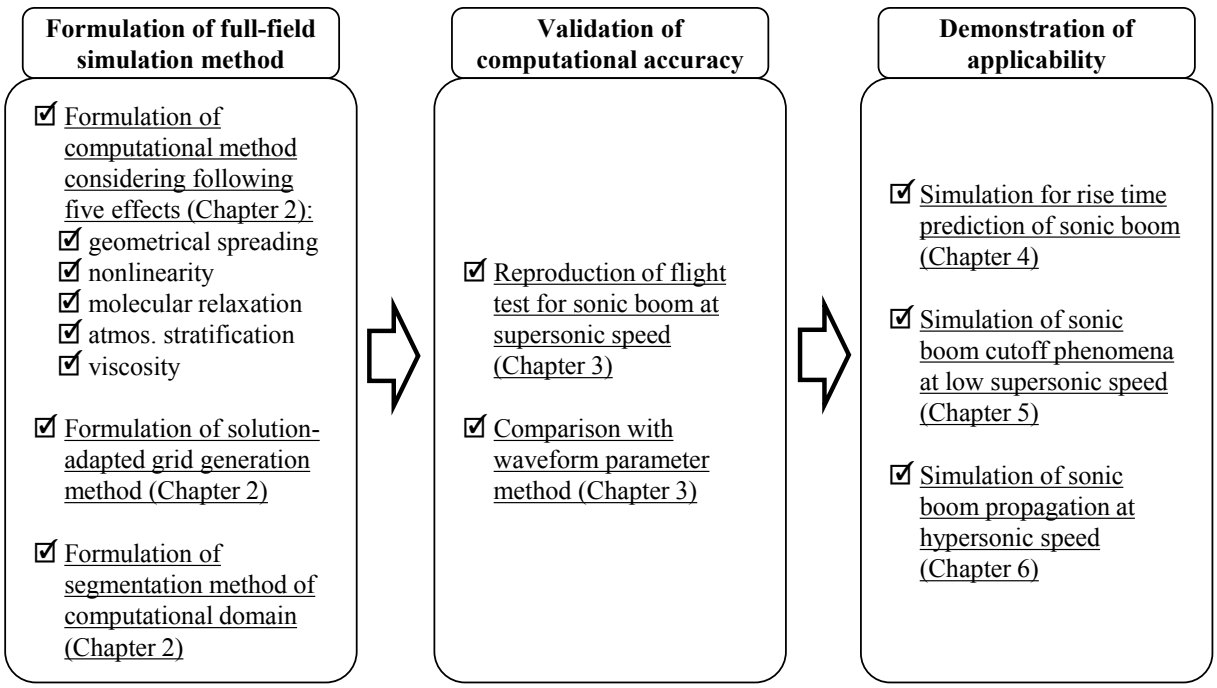

Fig. 7.1 Roadmap for constructing framework of full-field simulation method.

Appendix

Waveform Parameter Method

The waveform parameter method [45] invented by Thomas is the representative prediction method for sonic boom in the far field reaching the ground. In this method, the pressure fluctuation is derived from the conservation of the Blokhintsev energy invariant in the geometric acoustics, and the nonlinear effect on the waveform distortion is considered by the isentropic wave theory, in which the propagation speed is assumed to be a sum of the local speed of sound and the change of velocity. The entire pressure waveform is split into a sequence of segments, and the segmented waveform is described by the following three parameters. The first parameter m_i is the pressure gradient of segment i. The second parameter Δp_i is the pressure rise of the shock wave at the boundary of segments i and i–1. The third parameter λ_{Di} is the time duration of segment i. Figure A.1 shows the schematic of these parameters. These parameters along the ray path are computed by the three ordinary differential equations as

$$\frac{dm_i}{dt} = C_1 m_i^2 + C_2 m_i \tag{A.1}$$

$$\frac{d\Delta p_i}{dt} = \frac{1}{2} C_1 \Delta p_i \left(m_i + m_{i-1} \right) + C_2 \Delta p_i \tag{A.2}$$

$$\frac{d\lambda_{Di}}{dt} = -\frac{1}{2} C_1 \left(\Delta p_i + \Delta p_{i+1} \right) - C_1 m_i \lambda_{Di} \tag{A.3}$$

$$C_1 = \frac{\gamma + 1}{2\gamma} \frac{c_a}{p_a a_n} \tag{A.4}$$

$$C_2 = \left(\frac{1}{2\rho_a} \frac{d\rho_a}{dt} + \frac{3}{2c_a} \frac{dc_a}{dt} - \frac{1}{a_n} \frac{da_n}{dt} - \frac{1}{2A} \frac{dA}{dt} \right) \tag{A.5}$$

where p, ρ and c are the pressure, density, and speed of sound, respectively. a_n is the velocity normal to the wave front, and A is a ray tube area [102] as cut by the wave front. Subscript a means the atmospheric value. The derivation of the equations above is left out here (see reference 45 for details). The variables C_1 and C_2 in the nonuniform atmosphere change along the ray path. However, if these variables are assumed to

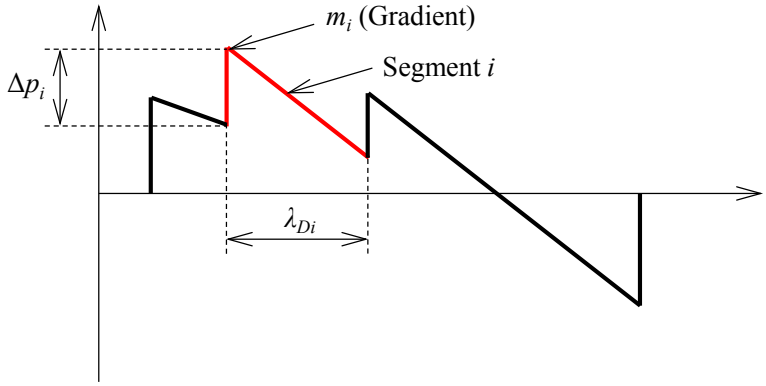

Fig. A.1 Three waveform parameters where red line indicates waveform of segment *i*.

be constant during the sufficiently small time, the equations above can be solved by the finite difference method. As the acoustic waves propagate along the ray paths, they are distorted by the nonlinear effect, resulting in the coalescence of the waves. In the waveform parameter method, λ_{Di} becomes zero when two waves coalesce into a single wave. In such a case, the coalescence point is computed, and the waveform parameters are redefined at this point.

References

[1] Hayes, W. D.: Sonic Boom, Annual Review of Fluid Mechanics, Vol. 3, 1971, pp. 269-290.

[2] Alonso, J. J., and Colonno, M. R.: Multidisciplinary Optimization with Applications to Sonic-Boom Minimization, Annual Review of Fluid Mechanics, Vol. 44, 2012, pp. 505-526.

[3] Garces, M., Bass, H., Drop, D., Hetzer, C., Hedlin, M., Pichon, A. L., Lindquist, K., North, R., and Olson, J.: Forensic Studies of Infrasound from Massive Hypersonic Sources, Eos, Vol. 85, No. 43, 2004.

[4] Chapman, C. R.: Calibrating Asteroid Impact, Science, Vol. 342, 2013, pp. 1051-1052.

[5] Menexiadis, G., and Varnier, J.: Long-Range Propagation of Sonic Boom from the Concorde Airliner: Analyses and Simulations, Journal of Aircraft, Vol. 45, No. 5, 2008, pp. 1612-1618.

[6] Maglieri, D. J., Bobbitt P. J., Plotkin, K. J., Shepherd, K. P., Coen P. G., and Richwine, D. M.: Sonic Boom Six Decades of Research, NASA SP-2014-622

[7] International Civil Aviation Organization (ICAO), http://www.icao.int/

[8] Rallabhandi, S. K., Nielsen, E. J., Diskin, B.: Sonic Boom Mitigation through Aircraft Design and Adjoint Methodology, Journal of Aircraft, Vol. 51, No. 2, 2014, pp. 502-510

[9] Ordaz, I., Geiselhart, K. A., and Fenbert, J. W.: Conceptual Design of Low-Boom Aircraft with Flight Trim Requirement, Journal of Aircraft, Vol. 52, No. 3, 2015, pp. 932-939.

[10] Park, M. A., and Morgenstern, J. M.: Summary and Statistical Analysis of the First AIAA Sonic Boom Prediction Workshop, Journal of Aircraft (Early edition), 2015.

[11] Park, M. A., Aftosmis, M. J., Campbell, R. L., Carter, M. B., Cliff, S. E., Bangert, L. S.: Summary of the 2008 NASA Fundamental Aeronautics Program Sonic Boom Prediction Workshop, Journal of Aircraft, Vol. 51, 2014, pp. 987-1001.

[12] Page, J. A., Plotkin, K. J., Haering Jr., E. A., Maglieri, D. J.,Cowart, R., Salamone, J., Elmer, K., Welge, B., and Ladd, J.: SCAMP: Superboom Caustic Analysis and Measurement Project Overview, AIAA Paper, 2013-0930, 2013.

[13] NASA FaINT project, http://www.nasa.gov/topics/aeronautics/features/faint_sonic_booms.html

[14] Naka, Y.: Sonic Boom Data from D-SEND#1, Japan Aerospace Exploration Agency Research and Development Memorandum, JAXA-RM-11-010E, 2012.

[15] D-SEND Database, http://d-send.jaxa.jp/d_send_e/index.html [cited 30 May 2012].

[16] Taguchi, H., Kobayashi, H., Kojima, T., Ueno, A., Imamura, S., Hongoh, M., and Harada, K.: Research on Hypersonic Aircraft Using Pre-Cooled Turbojet Engines, Acta Astronautica, Vol. 73, 2012, pp. 164–172.

[17] Roncioni, P., Natale, P., Marini, M., Langener, T., and Steelant, J.: Numerical Simulations and Performance Assessment of a Scramjet Powered Cruise Vehicle at Mach 8, Aerospace Science and Technology, Vol. 42, 2015, pp.218–228.

[18] Loubeau, A., and Coulouvrat, F.: Effects of Meteorological Variability on Sonic Boom Propagation from Hypersonic Aircraft, AIAA journal, Vol. 47, No. 11, 2009, pp. 2632-2641.

[19] Whitham, G. B.: The Flow Pattern of a Supersonic Projectile, Communications on Pure and Applied Mathematics, Vol.5, No. 3, 1952, pp. 301-348.

[20] Anderson, J. D., Jr.: Hypersonic and High Temperature Gas Dynamics, McGraw-Hill, New York, 1989.

[21] NASA, Ten Thousandth Near-Earth Object Unearthed in Space, http://www.nasa.gov/mission_pages/asteroids/news/asteroid20130624.html

[22] McCord, T. B. et al.: Detection of a Meteoroid Entry into the Earth's Atmosphere on February 1, 1994, Journal of Geophysical Research, Vol. 100, No. E2, 1995, pp. 3245–3249.

[23] Silber, E. A., Le Pichon, A., and Brown, P. G.: Infrasonic Detection of a Near-Earth Object Impact over Indonesia on 8 October 2009. Geophysical Research Letters, Vol. 38, L12201, 2011.

[24] Brown, P. G. et al.: A 500-kiloton Airburst over Chelyabinsk and an Enhanced Hazard from Small Impactors, Nature, Vol. 503, 2013, pp. 238-241.

[25] Borovicka, J., Spurny, P., Brown, P., Wiegert, P., Kalenda, P., Clark, D., and Shrbeny, L.: The Trajectory, Structure and Origin of the Chelyabinsk Asteroidal Impactor, Nature, Vol. 503, 2013, pp. 235-237.

[26] Popova, O. P. et al.: Chelyabinsk Airburst, Damage Assessment, Meteorite Recovery, and Characterization, Science, Vol. 342, No. 6162, 2013, pp. 1069-1073.

[27] Takahashi, N., and Yoshikawa, M.: Report on Field Survey in the Chelyabinsk Meteorite, Planetary People, Vol. 22, No. 4, 2013, pp. 228-233 (in Japanese).

[28] Ceplecha, Z.: Luminous Efficiency Based on Photographic Observations of the Lost City Fireball and Implications for the Influx of Interplanetary Bodies onto Earth, Astronomy and Astrophysics, Vol. 311, 1996, pp. 329-332.

[29] Lin, S. C.: Cylindrical Shock Waves Produced by Instantaneous Energy Release, Journal of Applied Physics, Vol. 25, No. 1, 1954, pp. 54–57.

[30] Revelle, D. O.: On Meteor Generated Infrasound, Journal of Geophysical Research, Vol. 81, No. 7,

1976, pp. 1217–1230.

[31] Hayes, W. D., and Runyan, H. L., Jr.: Sonic-Boom Propagation through a Stratified Atmosphere, Journal of the Acoustical Society of America, Vol. 51, No. 2C, 1972, pp. 695–701.

[32] Hammerton, P. W.: Effect of Molecular Relaxation on the Propagation of Sonic Booms through a Stratified Atmosphere, Wave Motion, Vol. 33, 2001, pp. 359–377.

[33] Plotkin, K. J.: State of the Art of Sonic Boom Modeling, Journal of Acoustical Society of America, Vol. 111, No. 1, 2002, pp. 530-536.

[34] Lipkens, B., and Blackstock, D. T.: Model Experiment to Study Sonic Boom Propagation through Turbulence. Part I: General results, Journal of Acoustical Society of America, Vol. 103, No. 1, 1998, pp. 148-158.

[35] Piacsek, A. A.: Atmospheric Turbulence Conditions Leading to Focused and Folded Sonic Boom Wave Fronts, Journal of Acoustical Society of America, Vol. 111, No. 1, 2002, pp. 520–529.

[36] Yamashita, H., and Obayashi, S.: Sonic Boom Variability Due to Homogeneous Atmospheric Turbulence, Journal of Aircraft, Vol. 46, No. 6, 2009, pp. 1886-1893.

[37] Coulouvrat, F.: Sonic Boom in the Shadow Zone: A Geometrical Theory of Diffraction, Journal of Acoustical Society of America, Vol. 111, No. 1, 2002, pp. 499–508.

[38] Morris, O. A., and Miller, D. S.: Sonic-Boom Wind-Tunnel Testing Techniques at High Mach Numbers, Journal of Aircraft, Vol. 9, No. 9, 1972, pp. 664-667.

[39] Cliff, S., Elmiligui, A., Aftosmis, M., Thomas, S., Morgenstern, J., Durston, D.: Design and Evaluation of a Pressure Rail for Sonic Boom Measurement in Wind Tunnels, Seventh International Conference on Computational Fluid Dynamics, ICCFD7-2006, 2012.

[40] Sasoh, A., Imaizumi, T., Toyoda, A., Ooyama, T.: In-Tube Catapult Launch from Rectangular-Bore Aeroballistic Range, AIAA journal, Vol. 53, No. 9, 2015, pp. 2781-2784.

[41] Cliff, S. E., and Thomas, S. D.: Euler/Experiment Correlation of Sonic Boom Pressure Signatures, Journal of Aircraft, Vol. 30, No. 5, 1993, pp. 669-675.

[42] Cheung, S. H., Edwards, T. A., and Lawrence S. L.: Application of Computational Fluid Dynamics to Sonic Boom Near- and Mid-field Prediction, Journal of Aircraft, Vo. 29, No. 5, 1992, pp. 920-926.

[43] Alauzet, F., and Loseille, A.: High-Order Sonic Boom Modeling Based on Adaptive Methods, Journal of Computational Physics, Vol. 229, 2010, pp. 561-593.

[44] S.Choi, J.J.Alonso, E.Van der Weide: Numerical and Mesh Resolution Requirements for Accurate Sonic Boom Prediction, Journal of Aircraft, Vol.46, No.4, 2009.

[45] Thomas, C. L.: Extrapolation of Sonic Boom Pressure Signatures by the Waveform Parameter Method, NASA TN D-6832, 1972.

[46] Thomas, Charles: Extrapolation of Wind-Tunnel Sonic Boom Signatures without Use of a Whitham F-Function, NASA SP-255, 1970, pp. 205-217.

[47] Pilon, A. R.: Spectrally Accurate Prediction of Sonic Boom Signals, AIAA Journal, Vol. 45, No. 9, 2007, pp. 2149–2156.

[48] Rallabhandi, S. K.: Advanced Sonic Boom Prediction Using the Augmented Burgers Equation, Journal of Aircraft, Vol. 48, No. 4, 2011, pp. 1245-1253.

[49] Naka, Y., Makino, Y., Hashimoto, A., Yamamoto, M., Yamashita, H., Uchida, T., and Obayashi, S.: Validation of Sonic-Boom Propagation Analysis Methods Using D-SEND#1 Data, JAXA-SP-12-010, 2012, pp. 95-99 (in Japanese).

[50] Johnson, M. E., and Hammerton, P. W.: Effect of Molecular Relaxation Processes on Travelling Wave Solutions of Sonic Boom Waveforms, Wave Motion, Vol. 38, 2003, pp. 229-240.

[51] Marchiano, R., Coulouvrat, F., and Grenon, R.: Numerical Simulation of Shock Wave Focusing at Fold Caustics, with application to sonic boom, Journal of Acoustical Society of America, Vol. 114, No. 4, 2003, pp. 1758-1771.

[52] Downing, M., Zamot, N., Moss, C., Morin, D., Wolski E., Chung S., Plotkin K., and Maglieri, D.: Controlled Focused Sonic Booms from Maneuvering Aircraft, Journal of Acoustical Society of America, Vol. 104, 1998, pp. 112–121.

[53] Friedman, M. P. and Chou, D. C.: Behavior of the Sonic Boom Shock Wave near the Sonic Cutoff Altitude, NASA CR-358, 1965.

[54] Maglieri, D. J., Bobbitt, P. J., Massey, S. J., Plotkin, K. J., Kandil, O. A., and Zheng, X.: Focused and Steady-State Characteristics of Shaped Sonic Boom Signatures: Prediction and Analysis, NASA CR–2011-217156.

[55] McDonald, B. E.: High-Angle Formulation for the Nonlinear Progressive-Wave Equation Model, Wave Motion, Vol. 31, No. 2, 2000, pp. 165-171.

[56] Pinton, G., Coulouvrat, F., Gennisson, J. L., and Tanter, M.: Nonlinear Reflection of Shock Shear Waves in Soft Elastic Media, Journal of Acoustical Society of America, Vol. 127, No. 2, 2010, pp. 683–691.

[57] Auger, T., and Coulouvrat, F.: Numerical Simulation of Sonic Boom Focusing, AIAA Journal, Vol. 40, No. 9, 2002, pp. 1726-1734.

[58] Salamone Ⅲ, J. A., Sparrow, V. W., and Plotkin, K. J.: Solution of the Lossy Nonlinear Tricomi Equation Applied to Sonic Boom Focusing, AIAA Journal, Vol. 51, No. 7, 2013, pp. 1745-1754.

[59] Lind, A. B., and Sparrow, V. W.: Including the Effects of Terrain Reflections and Post Boom Noise in Sonic Booms, AIAA Paper 2009-3385, 2009.

[60] Cho, S. T., and Sparrow, V. W.: Diffraction of Sonic Booms around Buildings Resulting in the

Building Spiking Effect, Journal of Acoustical Society of America, Vol. 129, No. 3, 2011, pp. 1250–1260.

[61] Yamashita, R., and Suzuki, K.: Full-Field Sonic Boom Simulation in Stratified Atmosphere, AIAA Journal, AIAA Journal, Vol. 54, No. 10, 2016, pp. 3223-3231.

[62] Yamashita, R., and Suzuki, K.: Sonic Boom Analysis for Hypersonic Vehicle by Global Direct Simulation, Journal of the Japan Society for Aeronautical and Space Sciences, Vol. 62, 2014, pp. 77-84 (in Japanese).

[63] Park, C.: Assessment of Two-Temperature Kinetic Model for Ionizing Air, Journal of Thermophysics and Heat Transfer, Vol. 3, No. 3, 1989, pp. 233–244.

[64] Prakash, A., Parsons, N., Wang, X., and Zhong, X.: High-Order Shock-Fitting Methods for Direct Numerical Simulation of Hypersonic Flow with Chemical and Thermal Nonequilibrium, Journal of Computational Physics, Vol. 230, 2011, pp. 8474-8507.

[65] Coratekin, T., van Keuk, J., and Ballmann, J.: Performance of Upwind Schemes and Turbulence Models in Hypersonic Flows, AIAA Journal, Vol. 42, No. 5, 2004, pp. 945–957.

[66] Peskin, C. S.: The Fluid Dynamics of Heart Valves: Experimental, Theoretical, and Computational Methods, Annual Review of Fluid Mechanics, Vol. 14, 1982, pp. 235-259.

[67] Ochi, A., Ueno, Y., and Hayama, K: A Validation Study of Higher Order CFD Analysis for Unsteady Flow around Landing Gear, Journal of the Japan Society for Aeronautical and Space Sciences, Vol. 59, 2011, pp. 7-15. (in Japanese)

[68] Sakai, T.: Real Gas Effects on Weak Shock Wave Propagation in an Atmosphere, AIAA paper 2010-1388, 2010.

[69] Honma H., and Glass, I. I.: Weak Shock-Wave Transitions of N-Waves in Air with Vibrational Excitation, Proceedings of the Royal Society of London. Series A., Mathematical and Physical, Vol. 391, 1984, pp.55-83.

[70] Potapkin, A.V., Korotaeva, T.A., Moskvichev, D.Yu., Shashkin, A.P., Maslov, A.A.: An Advanced Approach for Far-Field Sonic Boom Prediction, AIAA Paper 2009-1056, 2010.

[71] Roe, P. L.: Approximate Riemann Solvers, Parameter Vectors, and Difference Schemes, Journal of Computational Physics, Vol. 43, Issue 2, 1981, pp. 357-372.

[72] Park, M. A., and Darmofal, D. L.: Output-Adaptive Tetrahedral Cut-Cell Validation for Sonic Boom Prediction, AIAA Paper 2008-6594, 2008

[73] Park, C.: Nonequilibrium Hypersonic Aerothermodynamics, Wiley, New York, 1990.

[74] Bass, H. E., Sutherland, L. C., Zuckerwar, A. J., Blackstock, D. T. and Hester, D. M.: Atmospheric Absorption of Sound: Further Developments, Journal of Acoustical Society of America, Vol. 97, No. 1, 1995, pp. 680-683.

[75] Shima, E., and Jounouchi, T.: Role of CFD in Aeronautical Engineering (No.14) –AUSM Type Upwind Schemes–, Special Publication of National Aerospace Lab., Vol. 34, 1997, pp. 7–12.

[76] Liou, M. S., and Steffen, C. J., Jr.: A New Flux Splitting Scheme, Journal of Computational Physics, Vol. 107, No. 1, 1993, pp. 23–39.

[77] Warming, R. F., and Steger, J. L.: Flux Vector Splitting of the Inviscid Gasdynamic Equations with Application to Finite-difference Methods. Journal of Computational Physics, Vol. 40, 1981, pp. 263–293.

[78] van Leer, B.: Towards the Ultimate Conservative Difference Scheme. IV. A New Approach to Numerical Convection, Journal of Computational Physics, Vol. 23, No.3, 1977, pp. 276-299.

[79] van Albada, G. D., van Leer, B., and Roberts, Jr., W. W.: A Comparative Study of Computational Methods in Cosmic Gas Dynamics, Astronomy and Astrophysics, Vol. 108, No.1, 1982, pp. 76-84.

[80] Eberhardt, S., and Imlay, S.: Diagonal Implicit Scheme for Computing Flows with Finite Rate Chemistry, Journal of Thermophysics and Heat Transfer, Vol. 6, No. 2, 1992, pp. 208-216.

[81] Bussing, T. R. A. and Murman, E. M.: Finite-Volume Method for the Calculation of Compressible Chemically Reacting Flows, AIAA Journal, Vol. 26, No. 9 (1988), pp. 1070-1078.

[82] Standard Atmosphere, International Organization for Standardization, ISO 2533:1975, 1975.

[83] Yamashita, R. and Suzuki, K.: Full-Field Simulation for Sonic Boom Cutoff Phenomena, Transactions of the Japan Society for Aeronautical and Space Sciences, Vol.58, No.6, 2015, pp. 327-336.

[84] Shima, E.: A Simple Implicit Scheme for Structured/Unstructured CFD, Proceedings of the 29th Fluid Dynamics Conference, Japan Society for Aeronautical and Space Sciences, Tokyo, 1997, pp. 325-328 (in Japanese).

[85] Shima, E., and Kitamura, K.: Parameter-Free Simple Low-Dissipation AUSM-Family Scheme for All Speeds, AIAA Journal, Vol. 49, No. 8, 2011, pp. 1693-1709.

[86] S.Yoon, A.Jameson: Lower-Upper Symmetric-Gauss-Seidel Method for the Euler and Navier-Stokes Equations, AIAA Journal, Vol.26, No.9, 1988.

[87] Yamashita, R. and Suzuki, K.: Waveform Transition of Sonic Boom from N-wave to Caret-wave generated from a Sphere at Hypersonic Speed, AIAA Journal, Vol. 54, No. 2, 2016, pp. 766-769.

[88] Anderson, J. D., Jr.: Modern Compressible Flow with Historical Perspective, McGraw-Hill, New York, 1990.

[89] Yamashita, R., and Suzuki, K.: Rise Time Prediction of Sonic Boom by Full-Field Simulation, Journal of Aircraft, Vol. 55, No.3, 2018, pp. 1305-1310.

[90] Yamashita, R. and Suzuki, K.: Effects of Vibrational Relaxation on Sonic Boom Waveforms in a Stratified Atmosphere, AIAA Journal, Vol. 58, No. 9, 2020, pp. 3987-4002.

[91] Thompson, K. W.: Time Dependent Boundary Conditions for Hyperbolic Systems, Journal of Computational Physics, Vol.68, 1987, pp. 1–24.

[92] HITACHI SR16000 System (yayoi), the Information Technology Center, The University of Tokyo, http://www.cc.u-tokyo.ac.jp/index-e.html

[93] Plotkin, K. J., and Matisheck, J. R., and Tracy, R. R.: Sonic Boom Cutoff Across the United States, AIAA 2008-3033.

[94] Lee, R. A., and Downing, M.: Comparison of Measured and Predicted Lateral Distribution of Sonic Boom Overpressures from the United States Air Force Sonic Boom Database, Journal of Acoustical Society of America, Vol. 99, No. 2, 1996, pp. 768-776.

[95] Aerion AS2, http://www.aerionsupersonic.com/

[96] Coulouvrat, F.: Focusing of Weak Acoustic Shock Waves at a Caustic Cusp, Wave Motion, Vol. 32, 2000, pp.233-245.

[97] Welge, H. R. et al.: N+3 Advanced Concept Studies for Supersonic Commercial Transport Aircraft Entering Service in the 2030-2035 Period, NASA/CR–2011-217084, 2011.

[98] Jung, T. P., Starkey, R. P., and Argrow, B.: Lobe Balancing Design Method to Create Frozen Sonic Booms Using Aircraft Components, Journal of Aircraft, Vol. 49, No. 6, 2012, pp. 1878-1893.

[99] Henneton, M., Gainville, O., and Coulouvrat, F.: Numerical Simulation of Sonic Boom from Hypersonic Meteoroids, AIAA Journal, Vol. 53, No. 9, 2015, pp. 2560–2570.

[100] Tchuen, G., and Zeitoun, D. Z.: Effects of Chemistry in Nonequilibrium Hypersonic Flow Around Blunt Bodies, Journal of Thermophysics and Heat Transfer, Vol. 23, No. 3, 2009, pp. 433–442.

[101] Shu, C. W., and Osher, S.: Efficient Implementation of Essentially Non-Oscillatory Shock-Capturing Schemes, Journal of Computational Physics, Vol. 77, No. 2, 1988, pp. 439-471.

[102] Hayes, W.D., Haefeli, R.C., and Kulsrud, H.E.: Sonic Boom Propagation in a Stratified Atmosphere with Computer Program, NASA CR-1299, 1969.

Publications

Journal articles

- Yamashita, R., and Suzuki, K.: Sonic Boom Analysis for Hypersonic Vehicle by Global Direct Simulation, Journal of the Japan Society for Aeronautical and Space Sciences, Vol. 62, No. 3, June, 2014, pp. 77-84 (in Japanese).
- Yamashita, R. and Suzuki, K.: Full-Field Simulation for Sonic Boom Cutoff Phenomena, Transactions of the Japan Society for Aeronautical and Space Sciences, Vol.58, No.6, November, 2015, pp. 327-336.
- Yamashita, R. and Suzuki, K.: Waveform Transition of Sonic Boom Generated from a Sphere at Hypersonic Speed, AIAA Journal, Vol. 54, No. 2, February, 2016, pp. 766-769.
- Yamashita, R. and Suzuki, K.: Full-Field Sonic Boom Simulation in Stratified Atmosphere, AIAA Journal, Vol. 54, No. 10, October, 2016, pp. 3223-3231.
- Yamashita, R. and Suzuki, K.: Rise Time Prediction of Sonic Boom by Full-Field Simulation, Journal of Aircraft, Vol. 55, No.3, May-June, 2018, pp. 1305-1310.
- Yamashita, R. and Suzuki, K.: Effects of Vibrational Relaxation on Sonic Boom Waveforms in a Stratified Atmosphere, AIAA Journal, Vol. 58, No. 9, September, 2020, pp. 3987-4002.

Domestic conferences (in Japanese)

- Yamashita, R., and Suzuki, K.: Numerical Analysis of Sonic Boom Generated by Meteorite at Hypersonic Speeds, 57th Space Sciences and Technology Conference, JSASS-2013-4396, October, 2013 (in Japanese).
- Yamashita, R., and Suzuki, K.: Sonic Boom Analysis of Meteorite at Hypersonic Speeds in Earth Atmosphere, Japan Geoscience Union Meeting 2014, PPS21-P01, April, 2014 (in Japanese).
- Yamashita, R., and Suzuki, K.: Numerical Study on Rise Time Prediction of Sonic Boom with Thermal Nonequilibrium, 46th Fluid Dynamics Conference, JSASS-2014-2027-F/A, July, 2014 (in Japanese). (published in JAXA Special Publication, JAXA-SP-14-010, March, 2015, pp. 35-40.)
- Yamashita, R., and Suzuki, K.: Thermal Nonequilibrium Flow Analysis for Sonic Boom Propagation in Stratified Atmosphere, 47th Fluid Dynamics Conference, JSASS-2015-2080-F/A, July, 2015 (in Japanese).

International conferences (in English)

- Yamashita, R. and Suzuki, K.: Numerical Analysis of Sonic Boom Cutoff Phenomena by Direct Simulation in Whole Domain Extending to Ground Level [Peer-reviewed], 2013 Asia-Pacific International Symposium on Aerospace Technology (APISAT), No.02-05-3, November, 2013.
- Yamashita, R. and Suzuki, K.: Full-Field Sonic Boom Simulation in Real Atmosphere, 32nd AIAA Applied Aerodynamics Conference, AIAA Paper 2014-2269, June, 2014.
- Yamashita, R. and Suzuki, K.: Rise Time Prediction of Sonic Boom by Full-Field Simulation with Thermal Nonequilibrium, 33rd AIAA Applied Aerodynamics Conference, AIAA Paper 2015-2583, June, 2015.

Acknowledgement

I would like to express the deepest appreciation to Prof. Kojiro Suzuki who gave me a chance to push back the frontiers of aeronautics and astronautics. His comments, suggestions and encouragements were invaluable in progressing my research. Without his continuous support, this research would not have been possible.

I would like to thank Prof. Kenji Yoshida of JAXA, Associate Prof. Koji Okamoto, Associate Prof. Hiroyuki Koizumi, and Associate Prof. Taro Imamura for their valuable comments and suggestions on the thesis. I also thank Dr. Masashi Kanamori of JAXA for his useful advice on my research.

I would like to express my gratitude to all of the members in Suzuki laboratory, especially Assistant Prof. Yasumasa Watanabe, Dr. Yuya Ohmichi, Dr. Katsutoshi Hamasaki, and Mr. Hisaichi Shibata. Thanks to them, I was able to spend a valuable time.

Last, I would like to offer my special thanks to my family for their support.

February, 2016

Rei Yamashita